AWARD NUMBER: **W81XWH-15-1-0043**

TITLE:**New Epigenetic Therapeutic Intervention for Metastatic Breast Cancer**

PRINCIPAL INVESTIGATOR: **Ming-Ming Zhou**

CONTRACTING ORGANIZATION: **Icahn School of Medicine at Mount Sinai**
New York, NY 10029

REPORT DATE: **April 2017**

TYPE OF REPORT: **Annual**

PREPARED FOR: U.S. Army Medical Research and Materiel Command
Fort Detrick, Maryland 21702-5012

DISTRIBUTION STATEMENT: Approved for Public Release;
Distribution Unlimited

REPORT DOCUMENTATION PAGE

Form Approved
OMB No. 0704-0188

1. REPORT DATE	2. REPORT TYPE	3. DATES COVERED
April 2017	Annual	15 Mar 2016 - 14 Mar 2017

4. TITLE AND SUBTITLE
New Epigenetic Therapeutic Invention for Metastatic Breast Cancer

5a. CONTRACT NUMBER

5b. GRANT NUMBER
W18XWH-15-1-0043

5c. PROGRAM ELEMENT NUMBER

6. AUTHOR(S)
Ming-Ming Zhou, PhD
Professor
Icahn School of Medicine at Mount Sinai

E-Mail: ming-ming.zhou@mssm.edu

5d. PROJECT NUMBER

5e. TASK NUMBER

5f. WORK UNIT NUMBER

7. PERFORMING ORGANIZATION NAME(S) AND ADDRESS(ES)

Icahn School of Medicine at Mount Sinai
One Gustave L Levy Place
New York, NY 10029-6504

8. PERFORMING ORGANIZATION REPORT NUMBER

9. SPONSORING / MONITORING AGENCY NAME(S) AND ADDRESS(ES)

U.S. Army Medical Research and Materiel Command
Fort Detrick, Maryland 21702-5012

10. SPONSOR/MONITOR'S ACRONYM(S)

11. SPONSOR/MONITOR'S REPORT NUMBER(S)

12. DISTRIBUTION / AVAILABILITY STATEMENT

Approved for Public Release; Distribution Unlimited

13. SUPPLEMENTARY NOTES

14. ABSTRACT

Triple-negative breast cancer (TNBC) distinguishes from other forms of breast cancer in origination and progression. Likely originated from undifferentiated cancer stem cells, TNBC tumor cells possess many epithelial-mesenchymal transition (EMT) characteristics including invasion, resistance to apoptosis, and cancer stem cell-like traits that permit tumor dissemination and growth at distant sites. The Wnt pathways are important for EMT. We recently discovered that *Wnt5a* and its transcription factor Twist are markedly over-expressed in TNBC but not luminal breast cancer cells. We also discovered that constitutively activated NF-kB in TNBC sustains prolonged activation of pro-inflammatory cytokines, enabling rapid spread (metastasis) of TNBC tumors. *Notably*, the functions of both transcription factors Twist and NF-kB in gene activation require lysine acetylation, which signs to activate the transcriptional machinery in chromatin. This chemical modification enables them to recruit the major transcriptional regulatory co-activator proteins to coordinate target gene activation in the human genome. In this study, we will investigate the underlying mechanism of gene activation in TNBC. We are developing novel small molecule compounds to render the transcription factor/co-activator activity in gene activation, a key function required for the prolonged expression of inflammatory cytokines that fuel TNBC cells proliferation and spreading. Our study should have a major impact on new targeted therapy development to fight against the aggressive TNBC.

15. SUBJECT TERMS

16. SECURITY CLASSIFICATION OF:			17. LIMITATION OF ABSTRACT	18. NUMBER OF PAGES	19a. NAME OF RESPONSIBLE PERSON
a. REPORT	b. ABSTRACT	c. THIS PAGE			USAMRMC
Unclassified	Unclassified	Unclassified	Unclassified	86	19b. TELEPHONE NUMBER *(include area code)*

Table of Contents

Page

1. Introduction

Breast cancer is the most commonly occupying cancer among women. While great stride is made in the recent years in disease diagnosis and treatment, we still don't have effective means to treat a major sub-population of metastatic breast cancer patients, particularly those who suffer from *triple-negative breast cancer* (TNBC). The average time to live after documentation of metastasis is only about two years. Unlike other subtypes, TNBC lacks the expression of three receptors: estrogen receptor (ER), progesterone receptor (PR) and human epidermal growth factor receptor 2 (Her2/neu), hence the name. The available treatments targeting these receptors do not work for TNBC patients. Studies show that inflammatory genes drive rapid progression of TNBC, and epithelial-mesenchymal transition (EMT), a process of massive cell movement required for morphogenesis in embryonic development, is responsible for cancer cell invasion and metastasis. The major challenge in TNBC research is to identify the factors within the cell that initiate and promote tumor metastasis. Our goal is to determine the role of gene transcriptional regulation in the development of metastatic TNBC. We focus on the function of lysine acetylation in gene activation to attain both mechanistic insights and rational design of small molecules that modulate the acetyl-lysine binding activity of the bromodomain (BrD), which function was first discovered by the M.-M. Zhou lab (*Nature,* 1999) (PI of this project). BrDs are embedded in many transcription-associated proteins such as the BET (bromo and extra-terminal domain) proteins important for transcriptional activation of pro-inflammatory and oncogenesis genes in TNBC. Our recent study between the labs of Drs. M.-M. Zhou and B.P. Zhou (an expert investigator on TNBC; also Partnering PI of this project) has attributed rapid tumor growth and metastasis of TNBC cells to tumor initiating, undifferentiated stem cell properties, and to over-activation of oncogenes (*Cancer Cell,* 2014). We show that a new class of BrD inhibitors (BrDis), we developed, effectively down-regulate expression of cancer stem cell (CSC) factors, inhibit oncogenic gene expression, and suppress rapid growth and invasion properties of TNBC cells.

We hypothesize that the inflammatory, EMT and CSC properties of TNBC tumor are caused and fueled by transcriptional over-activation of inflammatory and oncogenic genes; chemical inhibition of such aberrant transcriptional activities can circumvent the aggression of metastatic TNBC tumor. To reach the goal of our proposed study, we will achieve the three Specific Aims: (1) Determine the role of BET proteins in gene transcriptional activation in TNBC; (2) Develop selective BrD inhibitors targeting oncogene–activation; and (3) Characterize the mechanism of the transcriptional program in TNBC cells.

EMT and CSC properties play a critical role in invasion, drug resistance, and tumor recurrence and are often associated with poor prognosis in TNBC patients. Our findings will contribute greatly toward the understanding of induction of EMT at metastasis. Our study also explores the therapeutic potential of targeting this initiating event for the treatment of metastatic breast cancer.

2. Keywords

BET – bromodomain and extra-terminal domain

BLBC – basal-like breast cancer

BrD – Bromodomain

ChIP – chromatin immunoprecipitation

ChIP-seq – chromatin immunoprecipitation sequencing

CSC – cancer stem cell

EMT – epithelial-mesenchymal transition

ER – estrogen receptor

FA – fluorescence anisotropy

FACS – flow cytometry analysis

Her2/neu – human epidermal growth factor receptor 2

ITC – isothermal titration calorimetry

NMR – nuclear magnetic resonance

PR – progesterone receptor

RNA-seq – RNA sequencing

TAMs – tumor-associated macrophages

TMA – tissue microarray

TNBC – triple-negative breast cancer

3. Accomplishments

3.1. What were the major goals of the project?

In this past 12 months of this project, i.e. the second year of this grant's funding period, we have focused our efforts in this study as outlined in the major Tasks 1-3 of our research proposal.

Task 1:

a. Determine binding specificity of the BrDs of the BET proteins to lysine-acetylated peptides derived from histones and major transcription proteins including Twist, NF-kB and STAT3.

b. Define the molecular basis of the BET BrDs' selective interactions with effector proteins through structure-guided analysis, and determining the key residues using site-directed mutagenesis.

c. Validate the selective molecular interactions of the BET BrDs with transcription proteins in luminal and basal-like breast cancer cell lines, with and without treatment of new BET BrD inhibitors.

Task 2:

a. Design and synthesize new diazobenzene analogs to optimize lead compounds with high affinity (K_d <100 nM) and selectivity (>100:1 for a target over closely related proteins). This is an iterative process, and is coupled to **task 2.2b-c** and **task 3.1a-c**.

b. Determine the detailed molecular basis of ligand recognition by the BET BrDs by obtaining SAR data of lead series, and by solving new crystal structures of new ligands bound to BET BrDs.

c. Validate the cellular efficacy (EC_{50} < 1 μM) of new BrD inhibitors in multiple TBNC cell lines.

Task 3:

a. Elucidate BRD4 functions in EMT and CSC properties as well as tumorigenicty of TNBC cells *in vitro* and *in vivo* using the newly developed selective BrD inhibitors.

b. Identify direct target genes of BRD4 in TNBC cell lines through ChIP-seq and RNA-seq analysis.

c. Determine the transcriptional expression levels of target genes of BRD4 in human TNBC samples.

3.2. What was accomplished under these goals?

We have made major progress in the past 12 months in this collaborative study between Dr. M.-M. Zhou's Lab at Icahn School of Medicine at Mount Sinai and Dr. B.H. Zhou's Lab at Kentucky University College of Medicine, as planned in our proposal. Specifically, Dr. M.-M. Zhou's lab has conducted extensive structural and biochemical analyses of interactions of the bromodomains of BET proteins, particularly BRD4 with lysine-acetylated histones and transcription factors including Twist, NF-kb, STAT3, and FOXO3a, as well as BRD2 with STAT3, and conduced structure-based rational design and synthesis of new chemical inhibitors for BET BrDs. At the same time, Dr. B.H. Zhou's lab has performed detailed functional characterization of BET proteins interactions with histones and key transcriptional factors using the new structural insights generated from Dr. M.-M. Zhou lab's study. In addition, Dr. B.H. Zhou's lab has been evaluating the mechanistic linkage between TNBC and obesity, which should be helpful to our efforts in the development of novel targeted therapy for TNBC (see below). Specifically, in the past year, we have completed most of the studies organized as ***subtask 1b***, and ***subtasks 2a*** and ***2b*** (M.-M. Zhou), ***subtasks 1c*** and ***3c*** (B.H. Zhou), and ***subtasks 2c***, ***3a*** and ***3b*** (M.-M. Zhou and B.H. Zhou). Below, we highlight some of our new key discoveries in this joint project.

(A) Structural Mechanism of Stat3/BRD2 in Control of Gene Transcription

The BET proteins are major transcriptional regulators and have emerged as new drug targets, but their functional distinction has remained elusive. Recently, we have characterized the mechanistic functions of BET proteins Brd2 and Brd4 in the context of lineage-specific differentiation of T-helper 17 (Th17) that are derived from murine primary naïve $CD4^+$ T cells isolated from mouse spleen and lymph nodes. Given the widely implicated functions of pro-inflammatory Th17 cells in cancer and inflammatory disorders, our study is highly relevant to our goal to better understand the transcriptional mechanism that contributes to the onset and development of TNBC in humans that has been suggested as cancer driven by inflammation.

Specifically, in this study, we show that Brd2 and Brd4 exert distinct genomic functions at genes whose transcription they co-regulate during Th17 cell differentiation. Brd2 is associated with the chromatin insulator CTCF and the cohesin complex to support *cis*-regulatory enhancer assembly for gene transcriptional activation. In this context, Brd2 binds the transcription factor Stat3 in an acetylation-sensitive manner via its second bromodomain (BD2) recognition of K87ac site in Stat3, which we have established through detailed structural mechanism analysis using combined NMR spectroscopy and molecular/cell biology methods (**Figure 1**) (PDB code: 5U5S). We further demonstrate that this Stat3/Brd2-BD2 interaction facilitates Stat3 recruitment to active enhancers occupied with transcription factors Irf4 and Batf. In parallel, Brd4 temporally controls RNA polymerase II (Pol II) processivity during transcription elongation through cyclinT1/Cdk9 recruitment and Pol II Ser2 phosphorylation. Collectively, our study uncovers both separate and interdependent Brd2 and Brd4 functions in potentiating the genetic program required for Th17 cell development in inflammation and cancer, particularly TNBC.

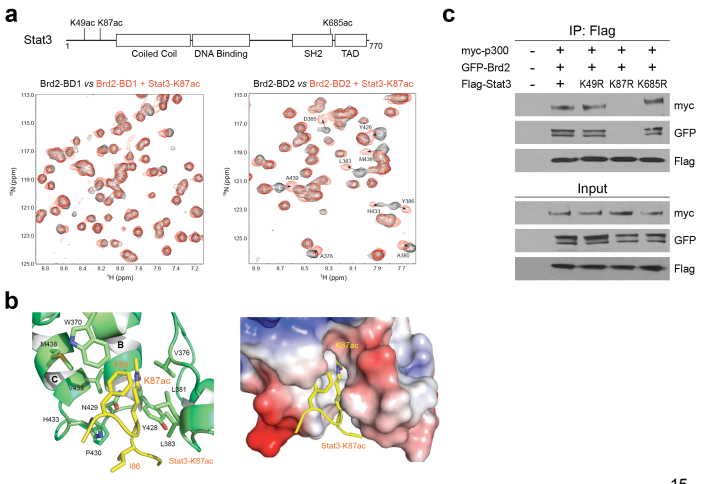

Figure 1. Structural basis of Brd2/Stat3 recognition. (a) 2D ^{15}N-HSQC spectra of Brd2-BD1 or BD2 illustrating changes of the protein backbone amide resonances in the free form (black), and in the presence of Stat3-K87ac peptide (red). Upper panel, the main lysine acetylation sites (K49ac, K87ac and K685ac) are depicted in Stat3 protein. **(b)** 3D NMR structure of Brd2-BD2 bound to Stat3-K87ac peptide (yellow), illustrating Stat3-K87ac recognition by the key residues at the Kac binding site. Right, electrostatic potential representation of Brd2-BD2 depicts Stat3-K87ac recognition in the Kac binding pocket. **(c)** Assessing site-specific Kac in Stat3/Brd2 association. Immuno-precipitation of Flag-tagged Stat3 wild-type, or point mutants of the three known lysine acetylation sites in HEK293 cells co-transfected with myc-300, and immunoblotting with specific antibodies to examine Brd2 interactions with Stat3.

(B) Twist Regulates ATX and LPAR1 Expression

The rapid tumor growth as well as aggressive metastasis of TNBC heavily relies on aberrant up-regulation of pro-oncogenic inflammatory pathways. Elucidation of the transcriptional program regulated by Twist helps us better understand the mechanistic linkage between TNBC and obesity. From numerous studies, we learn that ATX a secreted enzyme (encoded by *ENPP2*) produces most of the extracellular lysophosphatidic acid (LPA), which signals through its receptors (LPAR1-6) to mediate a wide range of inflammatory processes including wound healing, fibrosis and metastasis. Aberrant expression of ATX and LPARs has been linked to invasion, migration and metastasis of many types of cancers, including TNBC. Our current study indicates that Twist activation intensifies the inflammatory ATX-LPAR1 signaling to promote the development and progression of obesity-associated TNBC (see **Figure 2a**). We generated stable human normal breast epithelial cell lines MCF10A and HMLE, as well as luminal breast cancer cell line T47D with ectopic overexpression of Twist, and performed cDNA microarray screen to identify potential Twist target genes. It was revealed that the mRNA levels of Autotaxin (ATX) and LPAR1 were dramatically increased upon Twist over-expression (**Figure 2b**). Consistently, we found that ATX and LPAR1 are highly expressed in TNBC cells, and their expression correlates

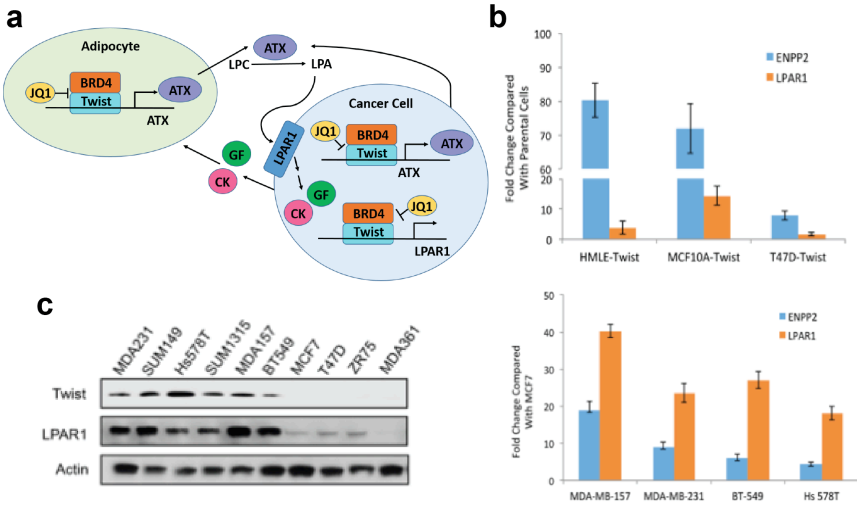

Figure 2. The role of Twist-ATX-LPAR1 signaling axis during TNBC cell-adipocyte crosstalk. (a) Scheme depiction of the Twist-ATX-LPAR1 signaling axis in TNBC. **(b)** ENPP2 and LPAR1 are potential target genes of Twist. Upper panel, Twist overexpression increased mRNA levels of ENPP2 and LPAR1. Lower panel, fold change of ENPP2 and LPAR1 mRNA levels in TNBC cells compared to MCF7 cells. **(c)** Western blotting showing expression of Twist and LPAR1 in TNBC cells and luminal subtype cells.

with that of Twist (**Figure 2c**). Notably, aberrant expression of ATX and LPARs has been linked to invasion, migration and metastasis of many types of cancers, including TNBC. Importantly, AT is a major source for the synthesis and secretion of ATX; dysregulation of ATX level/activity is involved in diet-induced obesity, with the underlying mechanism remaining contentious. Currently, we focus our efforts to elucide in details the mechanistic features underlying Twist-ATX-LPAR1 signaling axis in the development of TNBC. We are addressing questions including the function of Twist in regulation of ATX and LPAR1 expression, the role of Twist-ATX-LPAR1 axis during TNBC cell-adipocyte crosstalk in cells and in TNBC tumor growth *in vivo*.

(C) MS402, a Novel BRD4 Selective Inhibitor that Controls in Gene Transcription in Th17 cells

Our previous studies show that two BrDs in BET proteins have distinct, context-dependent molecular functions in transcription in that the first BrD (BD1) of BRD4 is dedicated to binding acetylated histone H4 whereas the 2nd BrD (BD2) is versatile and binds acetylated TFs and cyclin T1 of pTEFb. Using structure-based design, we recently developed a new class of cyclic vinylogous amide BrDis, of which a lead MS402 displays nM activity against BD1 (K_i =106±10 nM) with 8-fold selectivity over BD2 (**Figure 3a**) (see details in Cheung *et al, PNAS* 2017). This selectivity is consistent for BrDs of BRD2 or BRD3. MS402 has a 20-100-fold selectivity over BrDs of other sub-groups of the BrD family, and is >200 times more potent than H4K5ac/K8ac (**Figure 3a**). Given that pro-inflammatory Th17 cells have been implicated in TNBC tumor development, we next evaluated MS402 in *ex vivo* Th cell differentiation, in which murine primary naïve $CD4^+$ T cells isolated from mouse spleen and lymph nodes were treated with distinct cytokines to promote Th1, Th2, Th17 or Treg cell differentiation over 3.5 days with or without MS402 (**Figure 3b**). *Strikingly*, MS402 markedly inhibited Th17 cell differentiation (18.6% to 8.0%), as shown by flow cytometry, and to a lesser extent Th1 differentiation, and little effects on Th2 or Treg cell differentiation (**Figure 3c**). *Notably*, MS417, a potent pan-BET BrDi (K_i <10 nM) (also JQ1 and I-BET762), block broadly *ex vivo* differentiation of mouse primary naïve $CD4^+$ T cells to Th17, Th1, Th2, and to a lesser extent, Treg under the same conditions (**Figure 3b**). MS402 selectivity for Th17 cells is illustrated by its inhibition of transcription of Th17 signature genes *rorc* and *il17a* in mouse Th17 cells, but has minimal effects on *gata3* and *il4* in Th2 cells, which contrasts sharply to the much more broad effects of pan-BET BrDi MS417 on these Th17 and Th2 signature genes (**Figure 3c**). MS402 treatment resulted in a marked reduction of Brd4 and Cdk9 occupancy in Th17 cells, and RNA Pol-II Ser2 phosphorylation level at the Stat3 binding sites in *rorc* and *il17a* loci, but has minimal effects on genomic occupancy of Brd2 (**Figure 3d**), indicating MS402 as a selective inhibitor for Brd4 over Brd2 in Th17 cells. We have initiated a set of biological experiments to functionally evaluate MS402 activity in blocking TNBC in *in vivo* mouse model study.

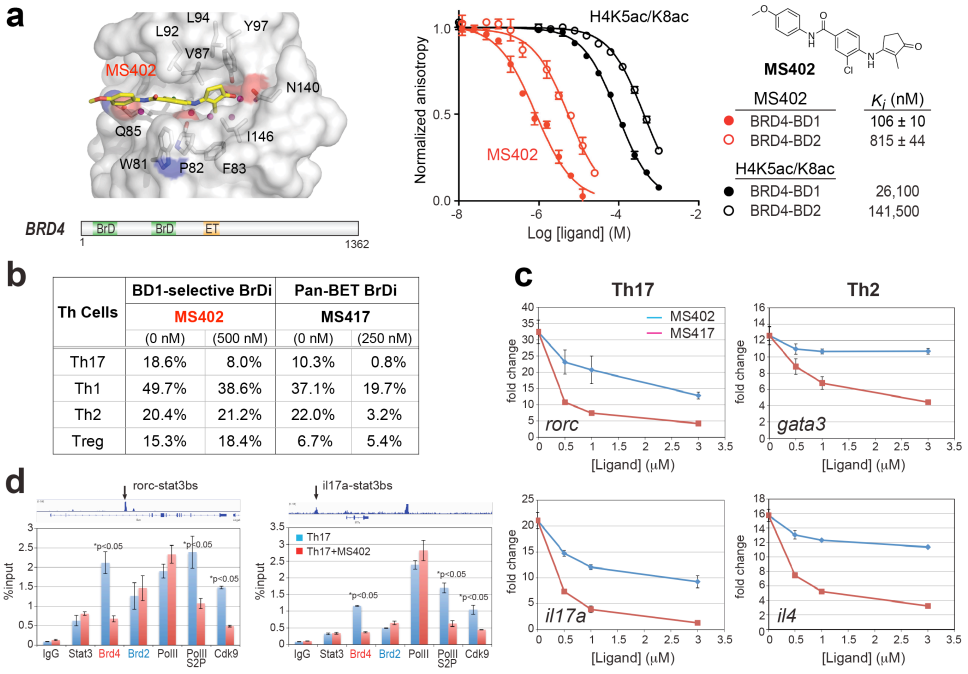

Th Cells	BD1-selective BrDi		Pan-BET BrDi	
	MS402		MS417	
	(0 nM)	(500 nM)	(0 nM)	(250 nM)
Th17	18.6%	8.0%	10.3%	0.8%
Th1	49.7%	38.6%	37.1%	19.7%
Th2	20.4%	21.2%	22.0%	3.2%
Treg	15.3%	18.4%	6.7%	5.4%

Figure 3. MS402 selectively inhibits Th17 cell differentiation. (a) Rational design of MS402, a BET BD1-specific inhibitor. *Note* that (i) inhibitory activity K_i was calculated from IC_{50} of FP competition data using a FITC-MS417 probe (Cheung, *PNAS* 2017); (ii) MS402 data represent three independent experiments, whereas H4K5ac/K8ac data were calculated from IC_{50} of 95% confidence intervals from sigmoidal curve fitting to triplicate data. **(b)** Table summarizing effects of MS402 or MS417 on *ex vivo* Th cell differentiation derived from murine primary naïve $CD4^+$ T cells isolated from mouse spleen and lymph nodes. See text for details. **(c)** Effects of MS402 *vs.* MS417 on mRNA levels of Th17 and Th2 signature TFs and cytokines in Th17 cells differentiated from mouse primary naïve $CD4^+$ T cells. **(c)** ChIP-seq tracks of Stat3 on *rorc* and *il17a* gene loci in Th17 cells (left) and ChIP-qPCR analysis of Stat3, Brd4, Brd2, PolII, PolIIS2P and Cdk9 in Th17 cells treated with and without MS402 (3 mM) (right). *Note* that (i) statistically significant (*p<0.05) results are annotated as in ***c***; (ii) all results presented here are representative of more than two independent experiments.

3.3. What opportunities for training and professional development has the project provided?
In the last funding period, the professional development of both Drs. Ming-Ming Zhou and Binhua P. Zhou was further strengthened and broaden as indicated in their active participation of breast cancer-related grant review at the NCI, DoD and Komen Cancer Foundation, as well as professional activities in reviewing scientific journals, and the presentation at several meetings and institutes, as shown below:

A. Grant Review:
Ming-Ming Zhou
2014 - Regular Member, NIH - "Macromolecular Structure and Function B" (MSFB)
2016 National Science Foundation
2016 NIH - New Innovator Award
2017 NIH - *"Cancer Drug Development & Therapeutics"* (CDDT)
2017 NIH/NIAID - Special Emphasis Panel, ZAI1 CB-A(M1) 1
2017 Wellcome Trust, UK

Binhua P. Zhou
2016 Reviewer (ad hoc), Susan G. Komen Foundation
2015-19 Reviewer (standing member), TPM study section, National Cancer Institute (NCI)

B. Editor/Service on Editorial Boards:
Ming-Ming Zhou
2009 - Editorial Board, *Journal of Molecular Cell Biology*
2010 - Editorial Board, *ACS Medicinal Chemistry Letters*
2010 - *Faculty of 1000* on *"Structure, and Transcription and Translation"*
2012 - Editorial Board, *Journal of Cancer Immunology*
2016 Guest Editor (w/ Steven Smith), *"Drug Discovery Today: Technologies", Elsevier*
2017 Guest Editor (with Evripidis Gavathiotis), *"Current Opinion in Chemical Biology", Elsevier*

Binhua P. Zhou
2010 - Editorial board member: *Scientific Reports*, *Cancer Hallmarks, Journal of Cancer Science & Therapy, American Journal of Cancer Biology, International Journal of Biological Chemistry*
2011 - Editor, *Cancer Reports, Pancreatic Disorders & Therapy*
2015 - Associate Editor, *Molecular and Cellular Oncology* (sections of Frontiers in Cell and Developmental Biology and Oncology)
2015 - Consulting Editors, *JCI Insight*

3.4. How were the results disseminated to communities of interest?
We have been disseminating the results of our study to the research community through invited talks at the universities and scientific conferences in the past 12 months, as well as publications:

A. Presentations
Ming-Ming Zhou
05/03/2016 Mayo Clinic, Department of Biochemistry & Molecular Biology, Rochester, MN, *"From Epigenetic Mechanism to New Targeted Therapy"*
06/11/2016 Chemical Biology Session at the ACS 44th Middle Atlantic Regional Meeting (MARM 2016), The College of Mount Saint Vincent in Riverdale, NY, *"From Epigenetic Structural Mechanism to Targeted Therapy"*
11/09/2016 University of Wisconsin-Madison, Cancer Biology Seminar Series, Madison, WI, *"From Epigenetic Mechanism to Targeted Therapy"*
12/22/2016 The First Bethune Hospital, Jilin University School of Medicine, Changchun, China, *"New Structural Mechanisms of Epigenetic Control of Gene Transcription"*
02/16/2017 Purdue University Cancer Center, West Lafayette, IN, *"From Epigenetic Structural Mechanism to Targeted Therapy"*

Binhua P. Zhou

04/13/2016 Department of Experimental Therapeutics, MD Anderson Cancer Center, Houston; *"Epithelial-mesenchymal transition in Breast Cancer Progression and Metastasis"*

06/12/2016 The Wistar Cancer Institute, Philadelphia, PA, *"Role and Regulation of Epithelial-mesenchymal transition in Breast Cancer"*

11/12/2016 Stanley S. Scott Cancer Center, Louisiana State University, New Orleans, LA, *"Distinct Roles of Snail and Twist in Epithelial-mesenchymal transition"*

02/23/2017 Department of Pharmacology, University of California at San Diego, CA, *"Epithelial-mesenchymal transition in Breast Cancer Progression and Metastasis"*

03/14/2017 Departments of Pathology, UT Southwestern Medical Center, Dallas, TX, *"Distinct Roles of Snail and Twist in Breast Cancer Progression and Metastasis"*

04/13/2017 Indiana University Melvin and Bren Simon Cancer Center, Indianapolis, IN, *"Epithelial-mesenchymal transition in Breast Cancer Progression and Metastasis"*

04/20/2017 Distinguished Scientist Speaker, University of Southern Alabama Mitchell Cancer Institute, Mobile, AL, *"Role and Regulation of Epithelial-mesenchymal transition in Breast Cancer"*

B. Publications relevant to this project

Cheung, K.L., Zhang, F., Jaganathan, A., Sharma, R., Zhang, Q., Konuma, T., Shen, T., Lee, J.-Y., Ren, C.Y., Chen, C.-H., Lu, G., Olson, M.R., Zhang, W., Kaplan, M.H., Littman, D.R., Walsh, M.J., Xiong, H., Zeng, L., & **Zhou, M.-M.** (2017) Distinct Roles of Brd2 and Brd4 in Potentiating the Transcriptional Program for Th17 Cell Differentiation. ***Molecular Cell,*** 65(6): 1068-1080. PMID: 28262505, PMCID: PMC5357147. Epub 2017 March 3.

Cheung, K.L., Lu, G.M., Sharma, R., Vincek, A.S., Zhang, R.H., Plotnikov, A.N., Zhang, F., Zhang, Q., Ju, Y., Hu, Y., Zhao, L., Han, X., Meslamani, J., Xu, F., Jaganathan, A., Shen, T., Zhu, H., Rusinova, E., Zeng, L., Zhou, J.C., Yang, J.C., Peng, L., Ohlmeyer, M., Walsh, M.J., Zhang, D.Y., Xiong, H.B., & **Zhou, M.-M.** (2017) Selective BET Bromodomain Inhibition Blocks Th17 Cell Differentiation and Ameliorates Colitis in Mice. ***PNAS.*** 114(11): 2952-2957. PMID: 28265070. Epub 2017 March 6.

Wang Y, Liu J, Ying X, Lin PC, and **Zhou BP***, (2016) Twist-mediated Epithelial-mesenchymal Transition Promotes Breast Tumor Cell Invasion via Inhibition of Hippo Pathway. ***Scientific Reports*** 6:24606.

Wu Y, Wang Y, Lin Y, Liu Y, Wang Y, Jia J, Singh P, Chi Y-I, Wang C, Dong C, Li W, Tao M, Napier D, Shi Q, Deng J, Evers BM, and **Zhou BP***, (2017) Dub3 Inhibition Suppresses Breast Cancer Invasion and Metastasis by Promoting Snail1 Degradation. ***Nature Communications*** 8:14228.

3.5. What do you plan to do during the next reporting period to accomplish the goals?

We are continuing our efforts in dissecting the molecular mechanism of gene transcriptional regulation or mis-regulation underlying metastatic breast cancer. Given that the major questions remained are on how lysine acetylation-mediated protein-protein interactions work in combinatorial fashions in gene transcription in chromatin, our ongoing efforts focus on the structural mechanism-guided rationally designed functional study in order to obtain deep functional and mechanistic underpinning of different transcription factors and regulatory proteins in their functions in control of gene transcription in the disease state and in response to pharmacological inhibition. *In summary,* we have made major progress in the past 12 months (i.e. the second year of this grant) towards addressing most aspects of the proposed studies as stated in the major tasks in the Statement of Work. We are continuing our efforts to achieve the goals of the remaining aims on the investigation of new therapeutic strategy that targets mis-regulation of oncogene transcriptional activation in metastatic breast cancer.

4. Impact

Triple-negative breast cancer (TNBC) is the most aggressive subtype of breast cancer that is associated with early metastasis to brain and lung, poor prognosis and short survival. About 240,000 women were diagnosed worldwide in 2012 with breast cancer, of which ~20-25% are of TNBC. TNBC disproportionally affects women of African and Hispanic descent, and occurs more often in younger women, affecting women

as early as in their 20s. 80% of breast cancer in people with an inherited BRCA1 mutation is found to be TNBC. TNBC lacks expression of three receptors, i.e. estrogen receptor (ER), progesterone receptor (PR) and human epidermal growth factor receptor 2 (Her2/neu), hence its name. Most available breast cancer treatments target these receptors. Unfortunately, given their triple negative status, TNBC tumors generally do not respond to receptor-targeted treatments. Depending on the stage of its diagnosis, TNBC is very aggressive, highly metastatic, and much more likely to recur than other breast cancer subtypes. Currently, there is no targeted therapy for TNBC. The standard of care for TNBC is surgery with adjuvant chemotherapy and radiation therapy, which is not effective once the tumor is spread.

Recent studies suggest that TNBC is inflammation-associated cancer - its rapid tumor growth and metastasis is heavily dependent upon and fueled by markedly elevated transcriptional activation of pro-inflammatory cytokines and EMT program. As such, chemical inhibitors that target epigenetic proteins whose functions are required for over-expression of these oncogenes offer an exciting opportunity to develop a new targeted epigenetic therapy to fight triple-negative breast cancer. Therefore, the funding provided by the DoD Breast Cancer Breakthrough Award will greatly accelerate our ongoing efforts to test our hypothesis, and validate our novel lead chemical compounds as a potentially new targeted epigenetic therapy to fight against this aggressive and devastating disease.

5. Changes/Problems

Nothing to Report

6. Products

Nothing to Report

7. Participants & Other Collaborating Organizations

What individuals have worked on the project?
Provide the following information for: (1) PDs/PIs; and (2) each person who has worked at least one person month per year on the project during the reporting period, regardless of the source of compensation (a person month equals approximately 160 hours of effort). If information is unchanged from a previous submission, provide the name only and indicate "no change."

Name:	Ming-Ming Zhou
Project role:	PI
Researcher identifier:	#1 at ISMMS
Nearest person months worked:	1
Contribution to project:	Directing the project
Name:	Adam Vincek
Project role:	Chemist
Researcher identifier:	#2 at ISMMS
Nearest person months worked:	6
Contribution to project:	Synthesis of new chemical compounds for BrDs
Name:	Steven Smith
Project role:	Chemist
Researcher identifier:	#3 at ISMMS
Nearest person months worked:	5
Contribution to project:	Synthesis of new chemical compounds for BrDs

Name:	Rajal Sharma
Project role:	Biochemist
Researcher identifier:	#4 at ISMMS
Nearest person months worked:	8
Contribution to project:	SAR study of BET BrD/ligand binding
Name:	Chunyan Ren
Project role:	Biochemist
Researcher identifier:	#5 at ISMMS
Nearest person months worked:	7
Contribution to project:	Characterization of BET inhibitors in TNBC cells
Name:	Jamel Meslamani
Project role:	Structural Chemist
Researcher identifier:	#6 at ISMMS
Nearest person months worked:	5
Contribution to project:	Structure-based design and analysis of BRD4 BrDs
Name:	Binhua P. Zhou
Project role:	PI
Researcher identifier:	#1 UKSoM
Nearest person months worked:	1
Contribution to project:	Directing the project
Name:	Yuting Zhou
Project role:	Graduate Student
Researcher identifier:	#2 UKSoM
Nearest person months worked:	4
Contribution to project:	Conducted identification of the interaction of BRD4 with Twist and characterization of the Twist-ATX-LPAR1 signaling axis in TNBC cells.

Has there been a change in the active other support of the PD/PI(s) or senior/key personnel since the last reporting period?

In the past 12 months, Drs. Ming-Ming Zhou and Binhua Zhou have some changes in their group's research grants, as listed below:

New Research Support

R01GM119189-01A1 (mPIs: M.-M. Zhou, & M. Walsh) 07/01/2016 – 06/30/20210 2.0 cal. mon.
NIH/NIGMS $240,000/yr, d.c.
"New Epigenetic Gene Silencing Technology"
This project aims to develop new transcriptional gene silencing technology based on H3K27 methylation.

1R41CA203067-01 (PI: M.-M. Zhou) 04/01/2016 – 03/31/2017 1.2 cal. mon. (*no salary support)
NIH/NCI $122,061/yr, d.c.
"Targeted Epigenetic Therapy for Triple-Negative Breast Cancer"
This project is to evaluate *in vivo* toxicity and efficacy of new compounds in blocking TNBC tumor growth in mouse models.

P20 GM121327 (MPI: St. Clair, D [contact]; Zhou, BP) 03/01/2017-12/31/2021 3.6 cal. mon.
NIH/NIGMS $2,220,230/yr
"University of Kentucky Center for Cancer and Metabolism"
Goals: To strengthen UK's cancer research enterprise by providing a thematically focused multidisciplinary infrastructure dedicated to defining the contribution of metabolism in the development and treatment of cancer and to use this novel multidisciplinary platform to develop promising early-stage investigators with enhanced skills in an exciting new area of cancer research.
Role: Co-PI and Mentor

Completed Research Support

R01CA87658-11 (PI: M.-M. Zhou) 04/02/2012 – 02/28/2017 1.0 cal. mon.
NIH/NCI $171,284/yr, d.c.
"Structure and Mechanism of Protein Modules in Chromatin Biology"
This project aims to conduct structural and biochemical analyses of epigenetic proteins including CBP in histone-mediated chromatin biology.

8. Special Reporting Requirements

N/A

9. Appendices

4 papers as listed in 3.4B.

Article

Molecular Cell

Distinct Roles of Brd2 and Brd4 in Potentiating the Transcriptional Program for Th17 Cell Differentiation

Graphical Abstract

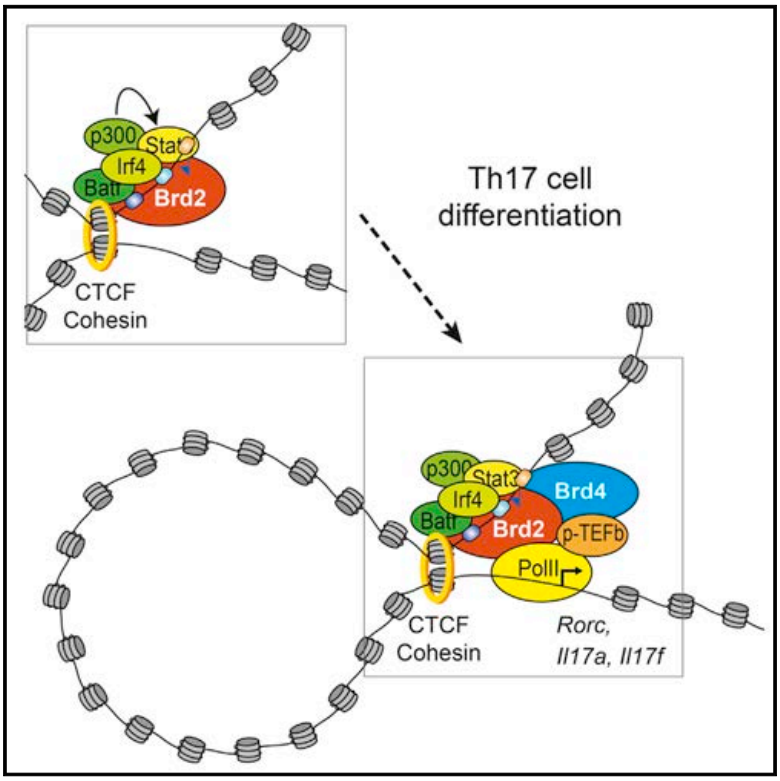

Authors

Ka Lung Cheung, Fan Zhang, Anbalagan Jaganathan, ..., Huabao Xiong, Lei Zeng, Ming-Ming Zhou

Correspondence

ming-ming.zhou@mssm.edu

In Brief

Cheung et al. uncover both separate and interdependent Brd2 and Brd4 genomic functions in potentiating the genetic program required for Th17 cell development and adaptive immunity. Brd2 interacts with the transcription factor Stat3 and the chromatin insulator CTCF-cohesin complex to support enhancer assembly, whereas Brd4 temporally controls RNA polymerase II for transcription elongation.

Highlights

- Brd2 and Brd4 have distinct genomic occupancy in Th17 cells
- Brd2 interacts with the CTCF-cohesin complex and the Stat3-Irf4-Batf complex
- Brd2-BD2 recruits Stat3 to chromatin through interaction with Stat3-K87ac
- Brd2 and Brd4 coordinate functionally to regulate gene transcription in chromatin

Cheung et al., 2017, Molecular Cell 65, 1–13
March 2, 2017
http://dx.doi.org/10.1016/j.molcel.2016.12.022

CellPress

Please cite this article in press as: Cheung et al., Distinct Roles of Brd2 and Brd4 in Potentiating the Transcriptional Program for Th17 Cell Differentiation, Molecular Cell (2017), http://dx.doi.org/10.1016/j.molcel.2016.12.022

Molecular Cell
Article

Distinct Roles of Brd2 and Brd4 in Potentiating the Transcriptional Program for Th17 Cell Differentiation

Ka Lung Cheung,[1,10] Fan Zhang,[2,3,10] Anbalagan Jaganathan,[1,10] Rajal Sharma,[1] Qiang Zhang,[1,4] Tsuyoshi Konuma,[1] Tong Shen,[1] June-Yong Lee,[5] Chunyan Ren,[1] Chih-Hung Chen,[6] Geming Lu,[2,7] Matthew R. Olson,[8] Weijia Zhang,[2] Mark H. Kaplan,[8] Dan R. Littman,[5,9] Martin J. Walsh,[1,6] Huabao Xiong,[2,7] Lei Zeng,[1,4] and Ming-Ming Zhou[1,11,*]
[1]Department of Pharmacological Sciences
[2]Department of Medicine
Icahn School of Medicine at Mount Sinai, New York, NY 10029, USA
[3]HIT Center for Life Sciences, School of Life Science and Technology, Harbin Institute of Technology, Harbin 150080, China
[4]The First Hospital and Institute of Epigenetic Medicine, Jilin University, Changchun 130061, China
[5]The Kimmel Center for Biology and Medicine of the Skirball Institute, New York University School of Medicine, New York, NY 10016, USA
[6]Department of Pediatrics
[7]Institute of Immunology
Icahn School of Medicine at Mount Sinai, New York, NY 10029, USA
[8]Department of Pediatrics and Herman B Wells Center for Pediatric Research, Indiana University School of Medicine, Indianapolis, IN 46202, USA
[9]Howard Hughes Medical Institute, New York, NY 10016, USA
[10]Co-first author
[11]Lead Contact
*Correspondence: ming-ming.zhou@mssm.edu
http://dx.doi.org/10.1016/j.molcel.2016.12.022

SUMMARY

The BET proteins are major transcriptional regulators and have emerged as new drug targets, but their functional distinction has remained elusive. In this study, we report that the BET family members Brd2 and Brd4 exert distinct genomic functions at genes whose transcription they co-regulate during mouse T helper 17 (Th17) cell differentiation. Brd2 is associated with the chromatin insulator CTCF and the cohesin complex to support *cis*-regulatory enhancer assembly for gene transcriptional activation. In this context, Brd2 binds the transcription factor Stat3 in an acetylation-sensitive manner and facilitates Stat3 recruitment to active enhancers occupied with transcription factors Irf4 and Batf. In parallel, Brd4 temporally controls RNA polymerase II (Pol II) processivity during transcription elongation through cyclin T1 and Cdk9 recruitment and Pol II Ser2 phosphorylation. Collectively, our study uncovers both separate and interdependent Brd2 and Brd4 functions in potentiating the genetic program required for Th17 cell development and adaptive immunity.

INTRODUCTION

T helper (Th) cells such as Th1, Th2, and Th17 and T regulatory (Treg) subsets that are characterized by producing signature cytokines have important functions in adaptive immunity (Harrington et al., 2005; Park et al., 2005; Takahama, 2006) and have been implicated in inflammatory and autoimmune diseases as well as cancer (Rubin et al., 2012; Saleh and Trinchieri, 2011; Tabas and Glass, 2013). Of these, Th17 cells produce interleukin 17a (IL-17a) and IL-17f to protect mucosa from bacterial and fungal infection (Murphy and Reiner, 2002; Wilson et al., 2009) and are linked to inflammatory disorders, including multiple sclerosis, rheumatoid arthritis, and inflammatory bowel disease (Dong, 2008; Ghoreschi et al., 2011; Littman and Rudensky, 2010; Miossec and Kolls, 2012). Th17 cell development from naive $CD4^+$ T cells is tightly regulated in gene transcription (Kanno et al., 2012; Medzhitov and Horng, 2009) by Th17-specific orphan nuclear receptor RORγT (Ivanov et al., 2006) and key transcription factors, including Stat3, Batf, Irf4, and IkBζ (Brüstle et al., 2007; Hirahara et al., 2015; Mathur et al., 2007; Okamoto et al., 2010; Schraml et al., 2009; Yang et al., 2007), that work in concert with chromatin-modifying enzymes and effector proteins to ensure proper timing, duration, and amplitude for ordered gene transcription during Th17 cell differentiation (Ciofani et al., 2012; Yosef et al., 2013).

Among the chromatin regulatory proteins are a family of transcription regulator proteins (Brd2, Brd3, Brd4, and testis-specific Brdt) that consist of two tandem acetyl-lysine binding bromodomains (BrDs) followed by an extra-terminal domain (BET) (Chiang, 2009; Dhalluin et al., 1999; Sanchez and Zhou, 2009). BET family proteins function to regulate gene transcription by modulating chromatin opening, facilitating transcription factor recruitment to target gene promoter and enhancer sites, and promoting activation of paused RNA polymerase II (Pol II) transcriptional machinery for gene transcription elongation (Chiang,

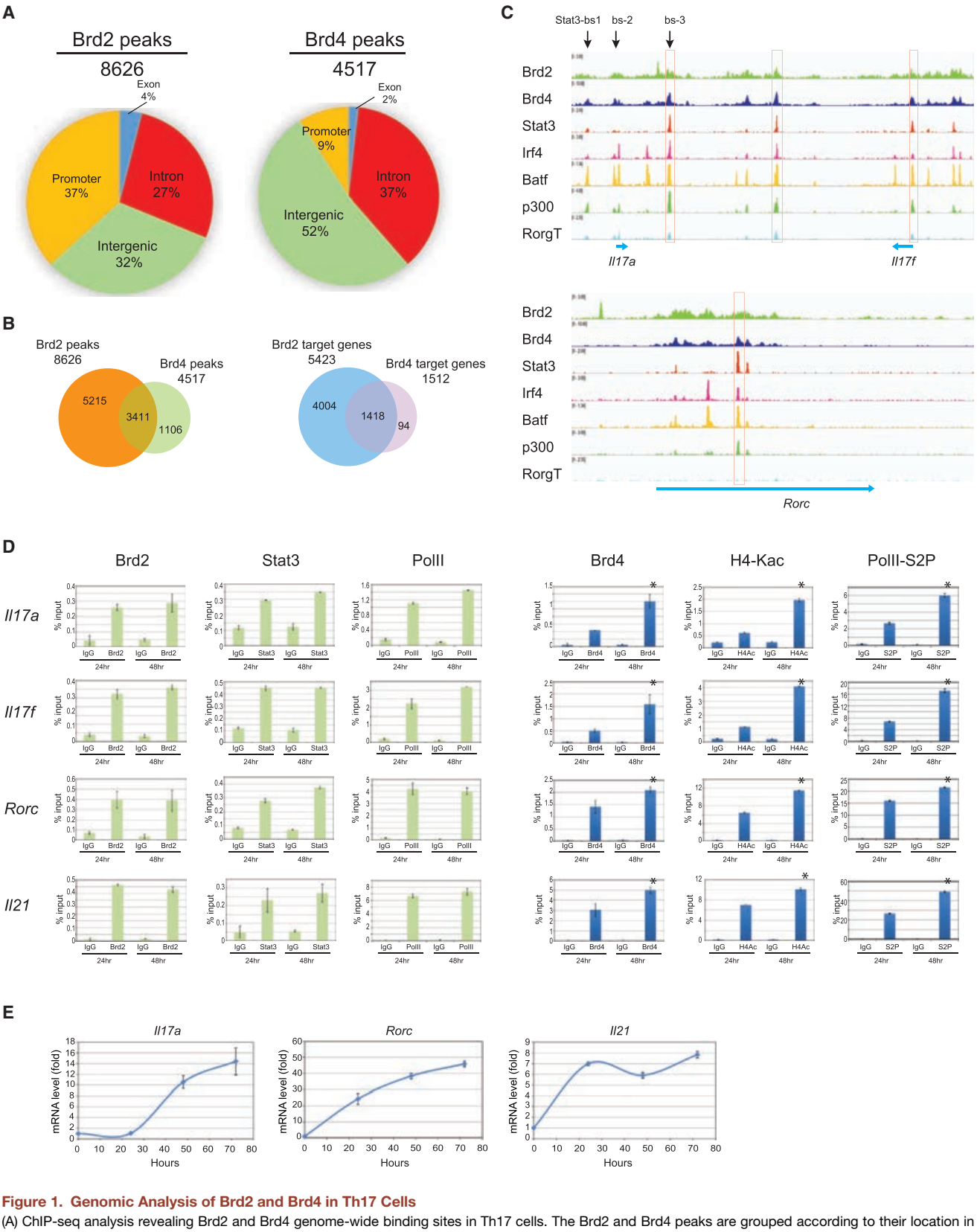

Figure 1. Genomic Analysis of Brd2 and Brd4 in Th17 Cells

(A) ChIP-seq analysis revealing Brd2 and Brd4 genome-wide binding sites in Th17 cells. The Brd2 and Brd4 peaks are grouped according to their location in promoter, exon, intron, or intergenic regions.

(legend continued on next page)

2009; Hargreaves et al., 2009; Hnisz et al., 2013; Kanno et al., 2014). Pharmacological inhibition of the BET BrDs downregulates transcriptional activation of genes required for rapid tumor cell growth (Dawson et al., 2011; Filippakopoulos et al., 2010; Puissant et al., 2013; Zuber et al., 2011) and also reduces cytokine production and autoimmunity in mouse $CD4^+$ T cells (Bandukwala et al., 2012; Mele et al., 2013; Zhang et al., 2012b).

Despite their prominent importance in biology, key questions regarding the separate or redundant functions of BET proteins in the control of gene transcription in chromatin, such as Brd2 and Brd4, which have been implicated in Th17 cell differentiation and Th17 cell-mediated pathology (Bandukwala et al., 2012; Mele et al., 2013), have not been addressed mechanistically. The lack of clear understanding of functional distinction of the BET proteins has seriously hampered their potential as viable epigenetic drug targets for new disease treatment (Shi and Vakoc, 2014). In this study, we sought to address this important problem by determining the mechanistic role of Brd2 and Brd4 in gene transcription during formation of the Th17 cell population derived from murine primary naive $CD4^+$ T cells.

RESULTS AND DISCUSSION

Genomic Analysis of Brd2 and Brd4 in Th17 Cells

To determine Brd2 and Brd4 functions in genome-wide regulation of gene transcription, we first performed a chromatin immunoprecipitation sequencing (ChIP-seq) study of Brd2 and Brd4 in Th17 cells that are differentiated from murine primary naive $CD4^+$ T cells isolated from mouse spleen and lymph nodes with treatment of transforming growth factor beta (TGF-β) plus IL-6 over 3.5 days. Contrary to the general assumption that Brd2 and Brd4 are functionally redundant in gene transcription (Bandukwala et al., 2012; Mele et al., 2013), our ChIP-seq data revealed that Brd2 and Brd4 have very different genome-wide occupancy in Th17 cells. These ChIP-seq data were highly reproducible, as shown by principal component analysis (PCA) clustering analysis, and high-quality peaks with quantitative difference were identified and analyzed by MAnorm (Shao et al., 2012) (Figure S1, available online). In total, 32% of 8,626 Brd2 peaks and 52% of 4,517 Brd4 peaks detected in Th17 cells were located in the intergenic region (Figure 1A; Tables S1 and S2). Brd2 demonstrated a greater enrichment in promoters (37%) than Brd4 (9%). Notably, a majority of Brd2 peaks do not overlap with those of Brd4 (Figure 1B), indicating non-redundant genomic functions. When Brd2 and Brd4 peaks are aligned with the nearest genes, we found that more than 90% of Brd4-associated genes (1,418/1,512) were associated with Brd2 (Figure 1B), suggesting that Brd4 functions jointly with Brd2 to regulate gene transcription. This is evident by co-localization of Brd4 and Brd2 with major transcription factor and transcriptional co-activator proteins such as Stat3, Irf4, Batf, RORγt, and p300 in *cis*-regulatory enhancer regions of the Th17 cell signature genes, including *Il17a*, *Il17f*, and *Rorc* (Ciofani et al., 2012) (Figure 1C), confirming the importance of Brd4 and Brd2 in gene transcription in Th17 cell differentiation. Indeed, the genes co-occupied by Brd4 and Brd2 are enriched in the JAK-STAT pathway (data not shown). Remarkably, Brd2 targets a large set of distinct genes (4,004/5,423)—more than twice number of genes that it co-targets with Brd4 (Figure 1B). These results strongly indicate that Brd2 works together with Brd4 but also has separate functions for gene transcription in Th17 cells.

To investigate their distinct functions in gene transcription, we evaluated Brd2 and Brd4 occupancy at the Th17 genes *Il17a-f*, *Rorc*, and *Il21* in murine primary naive $CD4^+$ T cells during Th17 cell differentiation. We observed that as demonstrated by ChIP-qPCR, Brd2 binding at the known enhancer sites along with Stat3 and Pol II in these gene loci (Ciofani et al., 2012) appeared to plateau after 24 hr of differentiation, whereas Brd4, together with lysine-acetylated H4 and Pol II phosphorylation at Ser2, continued to increase, correlating with the timing and extent of its target gene expression (Figure 1D). This difference is particularly obvious for late-stage Th17-specific genes, such as *Il17a*, whose transcription starts ~24 hr after the initiation of Th17 cell differentiation, as compared to early expressing genes, such as *Rorc* and *Il21* (Figure 1E). These results suggested that the kinetics of Brd2 and Brd4 recruitment to their target gene enhancer sites is different and that Brd4 occupancy is likely temporally coupled to the transcriptional activation of these signature genes in Th17 cell differentiation.

Brd2, but Not Brd4, Is Associated with the CTCF-Cohesin Complex in Th17 Cells

A consensus binding sequence analysis using the Homer program revealed that a major binding motif of Brd2 matches that of the chromatin architectural barrier protein CTCF, whereas Brd4 binding motifs include ETS (TTCCT), ATF3 (TGAnTCA), Stat3 (TTCCnGGAA), and p65 (GGGGnnnCCCC) (Figure 2A). Indeed, Brd2 is distinct from Brd4 in its co-localization with CTCF, with ~3-fold more peaks and higher intensity (Figure 2B), and conversely, Brd4 displays higher intensity with Stat3 than Brd2 (Figure S2A), as illustrated at *Il17a*, *Rorc*, *Il9*, and *Il12rb1* (Figures 2C and S2B). Our ChIP-seq data of the key cohesin proteins Nipbl, Smc1, and Smc3 confirmed Brd2 co-localization with the CTCF-cohesin complex in Th17 cells (Figures 2C, S2B, and S2C). Immunoprecipitation results verified Brd2's association with CTCF as well as the cohesin subunits Nipbl, Rad21, and Stag1 (Figure 2D); such interactions were almost absent for Brd4, although a very weak interaction was observed for Rad21.

(B) Venn diagrams showing the number of overlapping peaks of Brd2 and Brd4 (left) and genes co-bound by Brd2 and Brd4 (right) in Th17 cells.

(C) ChIP-seq tracks of Brd2, Brd4, and transcription factors revealing co-localization on *Il17* and *Rorc* gene loci in Th17 cells.

(D) Brd2, Stat3, PolII, Brd4, H4Ac, and PolII-S2P occupancy at *Il17a*, *Il17f*, *Rorc*, and *Il21* gene loci after 24 and 48 hr of Th17 cell differentiation from murine primary naive $CD4^+$ T cells isolated from mouse spleen and lymph nodes, as determined by ChIP-qPCR. The primer target site is indicated as Stat3-bs1 in (C). Data are presented as mean ± SEM of n = 3. $^*p < 0.05$.

(E) mRNA expression levels of *Il17a*, *Rorc*, and *Il21* during 72-hr lineage-specific differentiation of murine Th17 cells as described in (D), normalized to their corresponding expression levels in mouse primary naive $CD4^+$ T cells.

See also Figure S1 and Tables S1 and S2.

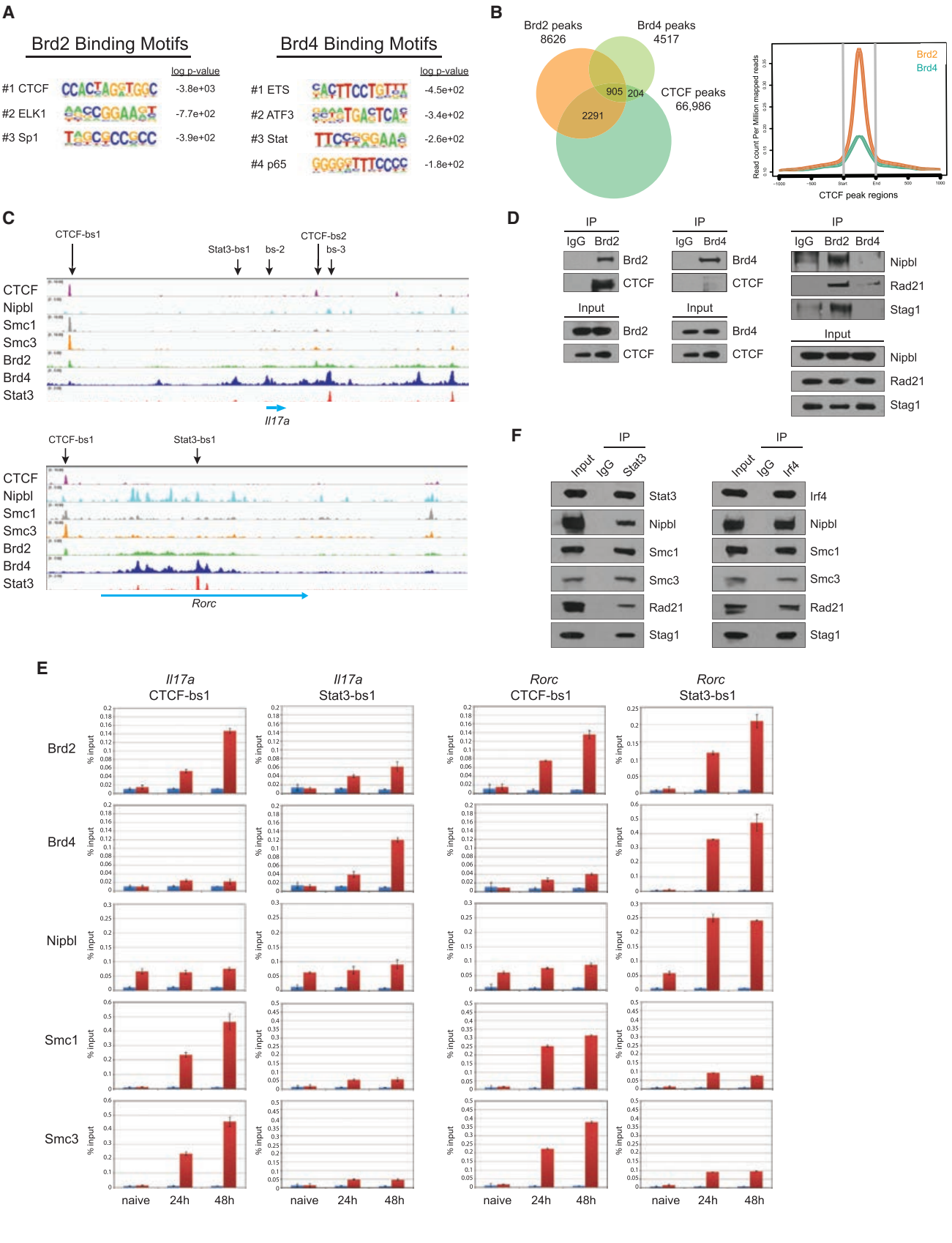

(legend on next page)

The CTCF-cohesin complex is known to have enhancer-blocking or insulator activity at *cis*-regulatory elements, where they work with transcription factors to establish chromatin-looping interaction between gene promoters and enhancers to regulate gene transcription (Bell et al., 1999; Dorsett and Merkenschlager, 2013; Kagey et al., 2010; Merkenschlager and Odom, 2013). Indeed, our ChIP analysis confirmed that Brd2, Nipbl, Smc1, and Smc3 are co-present at the CTCF and Stat3 binding sites in *Il17a* and *Rorc* gene loci in Th17 cells (Figure S2D). Brd2's association with cohesin components was further confirmed by their co-occupancy at the CTCF and Stat3 binding sites in *Il17a* and *Rorc* gene loci 24 and 48 hr after Th17 cell differentiation, as shown by ChIP analysis (Figure 2E). These results also revealed that Brd4 has a minimal presence at the CTCF binding sites but a major presence along with Brd2 and Nipbl at the Stat3 binding and enhancer sites. Notably, Brd2 occupancy at the CTCF sites and Brd4 at the enhancer sites increases as target gene expression increases in Th17 cell differentiation, indicative of dynamic and coordinated interactions between the CTCF-cohesin and the Stat3-enhancer complexes. Finally, Stat3 and the Th17 factor Irf4 interact with the cohesin components Nipbl, Smc1, Smc3, Rad21, and Stag1, as supported by immunoprecipitation of Stat3 or Irf4 (Figure 2F). Taken together, these results show that Brd2 is associated with the CTCF-cohesin complex in chromatin, possibly facilitating the assembly of *cis*-regulatory enhancers that include the transcription factors Stat3 and Irf4 that are necessary for gene transcription in Th17 cells.

To further evaluate differences in their genomic association with the CTCF-cohesion complex, we clustered Brd2 and Brd4 peaks ±1.5 kb from the center of Smc1 peaks in four groups: high in both Brd2 and Brd4 signals (a), high in Brd2 or Brd4 signals only (b and c), and low in both Brd2 and Brd4 signals (d) (Figure 3A). Given the enrichment of Brd2 and Brd4 signals is statistically significant over the background signals (Figure 3B), the difference in Brd2 and Brd4 peak intensity is likely not due to an affinity difference between their antibodies. Notably, Brd2-Brd4 co-bound genes exhibit the highest expression levels, while Brd2-only bound genes show modestly higher expression than genes without Brd2-Brd4 binding (Figure 3C). Clustering of Stat3 and enhancer marks such as H3K27Ac and H3K4me1 further revealed that Brd2-Brd4 co-bound peaks are enriched with Stat3 and even more enriched with H3K27Ac and H3K4me1 signals, confirming enhancer features (Figures 3D–3F). Similarly, peaks bound only by Brd2 are also enriched with Stat3, H3K27Ac, and H3K4me1, correlating with the modest increase in gene expression compared to genes without Brd2-Brd4 binding. As an example, the differential binding of Brd2 and Brd4 in relationship to the enhancer features is illustrated with the ChIP-seq tracks for *Il21* and *Rock2*, two important genes in Th17 cell differentiation (Figure 3G). Further, the functional differences of Brd2 and Brd4 in gene transcription are also reflected by differences in sensitivity of their genomic occupancy to chemical inhibition BET BrD and acetyl-lysine binding, illustrated at the *Il17a* and *Il17f* gene loci (Figures S3A–S3C). Collectively, these data indicate that Brd4 binding is required for substantial enhancement of gene expression in Th17 cells and that Brd2 alone also can confer transcriptional activity to genes.

Brd2's Interaction with Endogenous Stat3 Is Dependent upon Lysine Acetylation by p300

We next examined and confirmed interaction of Brd2, but not Brd4, with Stat3 by immunoprecipitation of endogenous Stat3 in Th17 cell lysates (Figure 4A). Stat3's association with Brd2, Irf4, and p300 is dependent on acetylation, which was increased in Th17 cells pre-treated with trichostatin A (TSA), a histone deacetylase inhibitor (Figure 4A). Reciprocal immunoprecipitation of Brd2 or Brd4 validated these interactions (Figure 4B). We also observed an interaction (albeit weak) between Brd2 and Brd4 (Figure 4B). The acetylation-dependent Stat3-Brd2 interaction is mostly DNA independent, as we detected only a slight decrease in interaction following ethidium bromide (EtBr) treatment (Figure 4C). The Stat3-Brd2 interaction is mediated by BrD and acetyl-lysine binding, as it is susceptible to disruption by MS417, a potent BET BrD inhibitor (Zhang et al., 2012a) (Figure 4D). Finally, co-transfection revealed that the Stat3-Brd2 interaction is dependent on Stat3 acetylation by p300 and that both BrDs (BD1 and BD2) of Brd2 are required and sufficient for the Stat3-Brd2 interaction, as acetyl-lysine-binding-deficient mutations of either BD1 or BD2 in Brd2 (Y154F or Y427F, respectively) abolished its association with Stat3 (Figure 4E).

We confirmed that Brd2 interacts with p300 and the Stat3-Irf4-Batf complex, whereas Brd4 interacts with Pol II and Cdk9 strongly but lacks direct interactions with Stat3, Irf4, or Batf (Figure 4F). Like Brd4, Brd2 also interacts with Pol II and to a lesser extent with Cdk9 in this context. These results suggest that Brd2 functions together with the CTCF/cohesin chromatin organizers to anchor the Stat3-Pol II complex at *cis*-regulatory enhancer regions occupied by p300, Irf4, and Batf. This model is supported by strong signals of the transcriptional activation marks H3K27ac, H3K4me1, and H3K4me3, but weak signals of the

Figure 2. Brd2, but Not Brd4, Is Associated with the CTCF-Cohesin Complex in Th17 Cells

(A) DNA binding motifs identified for Brd2 and Brd4 with their ChIP-seq data from Th17 cells.

(B) Venn diagrams showing the number of overlapping peaks of Brd2, Brd4, and CTCF (left) and normalized Brd2 and Brd4 ChIP signals centered on CTCF peak regions (right).

(C) ChIP-seq tracks of CTCF, Nipbl, Smc1, Smc3, Brd2, Brd4, and Stat3 on *Il17a* and *Rorc* gene loci in Th17 cells. The ChIP-seq data for CTCF and Stat3 were reported previously (Ciofani et al., 2012), whereas the others were generated in this study.

(D) Immunoprecipitation of Brd2 and Brd4 and immunoblotting with various specific antibodies to assess Brd2 or Brd4 interactions with CTCF and cohesin components (Nipbl, Rad21, and Stag1) in Th17 cells differentiated for 48 hr.

(E) Occupancy of Brd2, Brd4 and cohesin components (Nipbl, Smc1, and Smc3) at the CTCF and Stat3 binding sites in *Il17a* and *Rorc* gene loci in Th17 cells differentiated for 24 and 48 hr, as determined by ChIP. Data are presented as mean ± SEM of n = 3. The primer target sites are indicated in (C).

(F) Immunoprecipitation of Stat3 and Irf4 and immunoblotting with specific antibodies to examine Stat3 and Irf4 interactions with cohesin components (Nipbl, Smc1, Smc3, Rad21, and Stag1) in Th17 cells.

See also Figure S2.

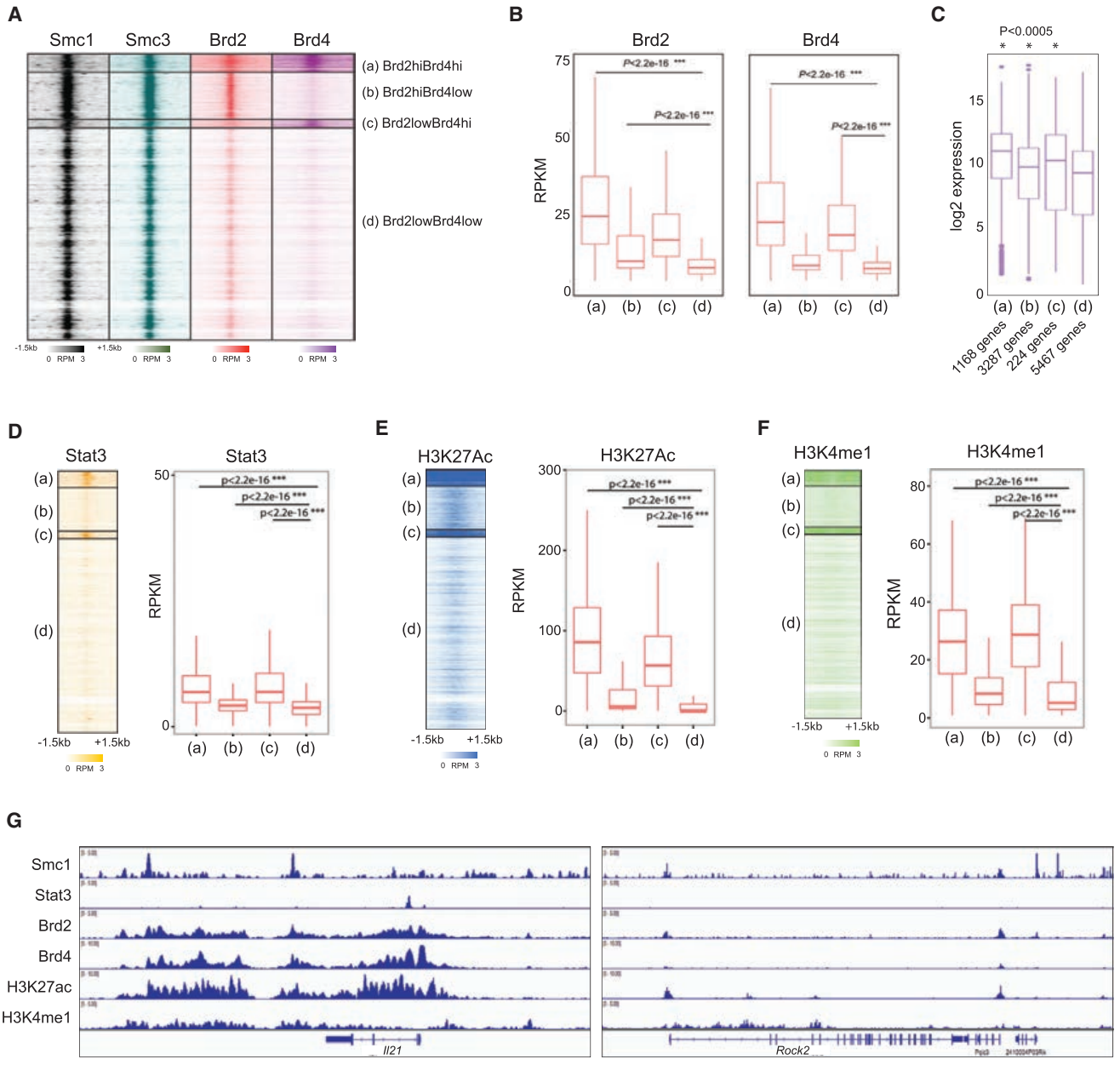

Figure 3. Brd2-Brd4 Co-bound Genes Mark Super-enhancers with the Highest Transcriptional Expression Levels in Th17 Cells

(A) Heatmap for ChIP-seq signals of Brd2 and Brd4 marked by the indicated antibodies ±1.5 kb from the center of Smc1 peaks.

(B) Boxplots of normalized counts of Brd2 and Brd4 signals illustrated at the four clusters of peaks.

(C) Boxplot indicating transcriptional expression levels of genes associated with the clustered peaks in Th17 cells.

(D) Heatmap of ChIP-seq signals of Stat3 located ±1.5 kb from the center of Smc1 peaks (left), and boxplots of normalized counts of these signals at the four clusters of peaks (right).

(E) Heatmap of ChIP-seq signals of H3K27Ac located ±1.5 kb from the center of Smc1 peaks (left), and boxplots of normalized counts of these signals at the four clusters of peaks (right).

(F) Heatmap of ChIP-seq signals of H3K4me1 located ±1.5 kb from the center of Smc1 peaks (left), and boxplots of normalized counts of these signals at the four clusters of peaks (right).

(G) ChIP-seq tracks representing examples of Brd2-Brd4 co-bound genes (such as *Il21*) and Brd2-only bound genes (such as *Rock2*).

See also Figure S3.

transcriptional repression mark H3K27me3 at the CTCF and Stat3 binding sites in the *Il17a* and *Rorc* gene loci (Figure S2E). ChIP-seq analysis suggested that Brd2 facilitates Stat3 binding on Irf4 binding sites. Almost 80% of Stat3 peaks (3,122/4,007) are co-localized with Irf4 peaks, bound or unbound by Brd2 (Figure 4G). Genomic analysis of the Irf4-Stat3 co-bound peaks

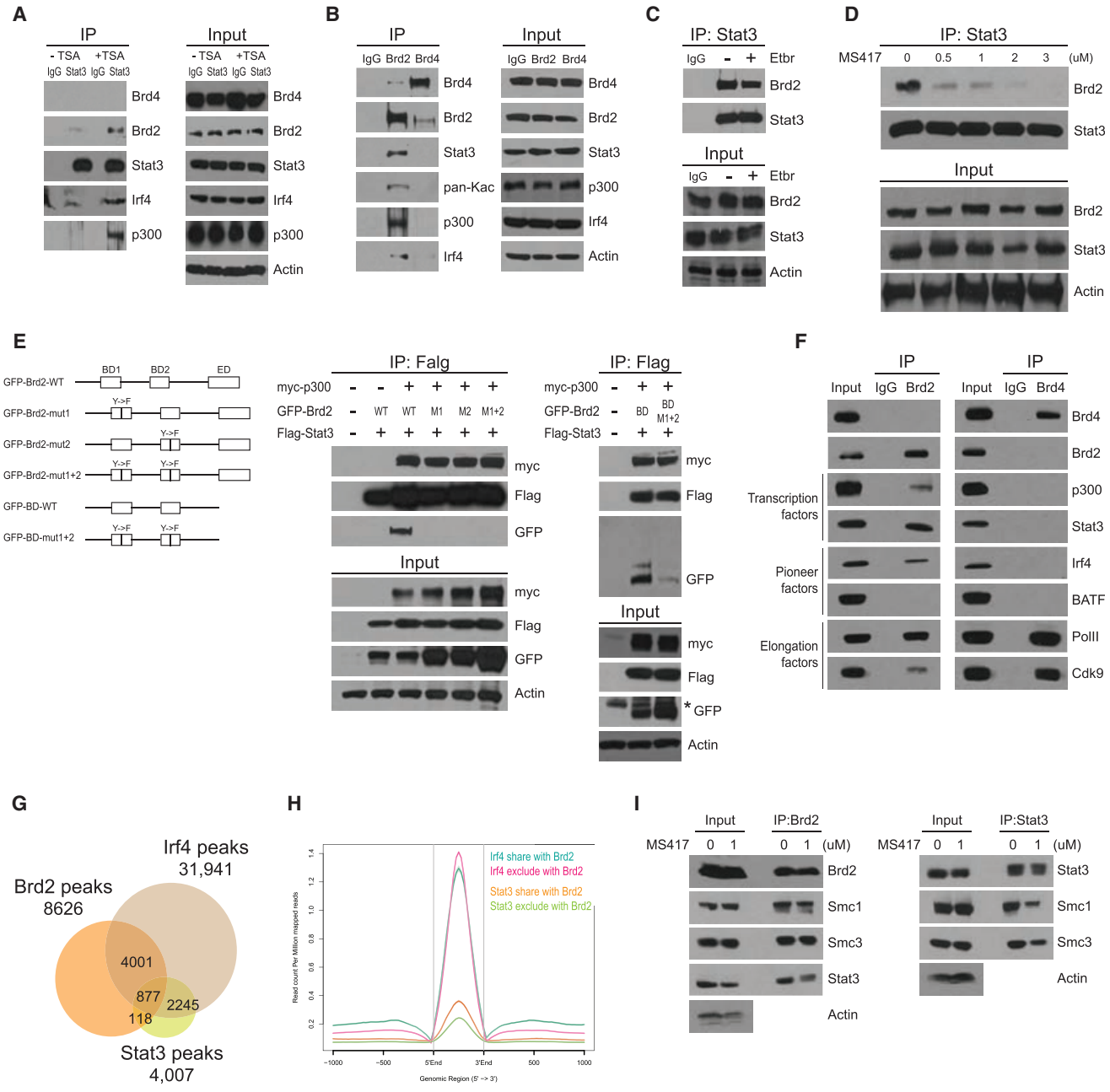

Figure 4. Brd2's Interaction with Endogenous Stat3 Is Dependent upon Its Acetylation by p300

(A) Immunoprecipitation of Stat3 and immunoblotting with specific antibodies to assess Stat3's interactions with Brd2, Brd4, Irf4, or p300 in Th17 cell lysates treated with or without TSA.

(B) Immunoprecipitation of Brd2 or Brd4 and immunoblotting with specific antibodies to examine the interactions of Brd2 or Brd4 with Stat3, p300, or Irf4 in Th17 cell lysates treated with TSA.

(C) Th17 cells lysates treated with TSA immunoprecipitated with Stat3 and then treated with or without ethidium bromide (EtBr) followed by western blot with antibodies against Brd2 and Stat3.

(D) Dose-dependent effects of BET BrD inhibition by MS417 on the Brd2-Stat3 association in Th17 cell lysates treated with TSA, as assessed when immunoprecipitated with Stat3, and then treated with MS417, followed by western blot with antibodies against Brd2 and Stat3.

(E) Assessing the role of lysine acetylation in the Brd2-Stat3 association. Left: schematic representations of various Brd2 plasmids used in the study. Middle: HEK293 cells overexpressed with FLAG-Stat3, GFP-Brd2, and myc-p300 were lysed and immunoprecipitated with antibody against FLAG to detect Brd2-Stat3 interactions with or without p300. Right: HEK293 cells overexpressed with FLAG-Stat3, GFP-Brd2-BD, and GFP-Brd2-BDMut1+2 were lysed and immunoprecipitated. The acetyl-lysine-binding-deficient mutations in BD1 and BD2 of Brd2 are Y154F and Y427F, respectively.

(legend continued on next page)

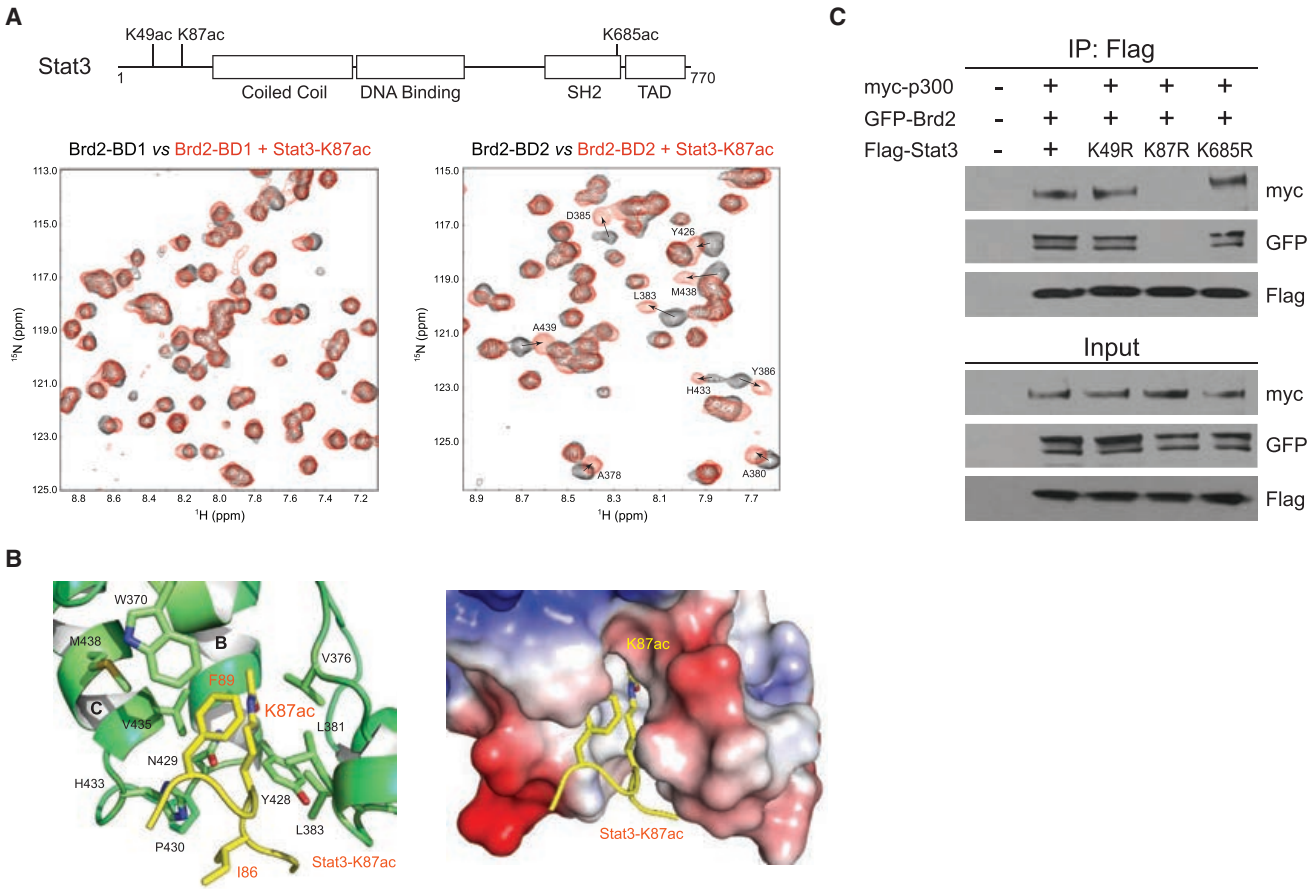

Figure 5. Structural Analysis of the Brd2-Stat3 Interaction

(A) 2D ^{15}N-HSQC spectra of Brd2-BD1 or BD2 illustrating changes of the protein backbone amide resonances in the free form (black) and in the presence of Stat3-K87ac peptide (red). Top: the three main lysine acetylation sites (K49ac, K87ac, and K685ac) in Stat3 are indicated in the protein domain organization diagram.

(B) 3D NMR structure of Brd2-BD2 bound to Stat3-K87ac peptide (yellow), illustrating Stat3-K87ac recognition by the key residues at the acetyl-lysine binding pocket as indicated in green. Bottom: electrostatic potential representation of the protein depicts the acetyl-lysine binding pocket for Stat3-K87ac recognition.

(C) Assessing the site-specific lysine acetylation in the Stat3-Brd2 association. Immunoprecipitation of FLAG-tagged wild-type Stat3 or point mutants of the three known lysine acetylation sites in HEK293 cells co-transfected with myc-300, as well as immunoblotting with specific antibodies to examine Brd2's interactions with Stat3.

See also Figure S5 and Table S3.

revealed that Irf4 binding is independent of Brd2, while Stat3 binding on Irf4 sites decreases in the absence of Brd2 (Figure 4H). Finally, BrD-acetylated lysine binding is key to enhancer assembly leading to transcriptional activation, as the Brd2-Stat3-cohesin (Smc1 and Smc3) association is sensitive to BrD inhibition by MS417 (Figure 4I). However, blocking of transcriptional elongation or processivity by small-molecule inhibitors for Cdk9 of pTEFb or RNA Pol II does not affect either Brd2 or Brd4 genomic occupancy at their target gene loci, as illustrated by ChIP-qPCR for *Il17a*, *Il17f*, and *Rorc* (Figures S4A–S4C).

Structural Basis of Brd2-Stat3 Recognition

To determine the molecular basis of lysine-acetylation-dependent Brd2 binding to Stat3, we performed a nuclear magnetic resonance (NMR) binding study of ^{15}N-labeled Brd2 BD1 or BD2 with Stat3 peptides derived from three known lysine acetylation sites (Hou et al., 2008; Yu et al., 2014; Yuan et al., 2005): K49ac (AYAAS-Kac-ESHAT, residues 44–54), K87ac (HNLLRI-Kac-QFLQS, residues 71–82), and K685ac (PKEEAFG-Kac-YCPE, residues 678–690) (Figure 5A). Our detailed NMR ^{15}N heteronuclear single quantum correlation (HSQC) spectral analysis

(F) Immunoprecipitation of Brd2 or Brd4 in Th17 cell lysates and immunoblotting with specific antibodies to assess their interactions with p300, Stat3, Irf4, Batf, PolII, or Cdk9.

(G) Venn diagrams showing the number of overlapping peaks of Brd2, Stat3, and Irf4 identified from ChIP-seq datasets collected in Th17 cells.

(H) Normalized Irf4 and Stat3 ChIP-signal centered around Irf4-Stat3 co-bound peak regions stratified by the presence of Brd2.

(I) Assessing effects of BET BrD inhibition by MS417 on Brd2-cohesin-Stat3 association, as determined by immunoprecipitation of Brd2 from Th17 cell lysates and immunoblotting with specific antibodies to Smc1, Smc3, and Stat3 with or without MS417 treatment.

See also Figure S4.

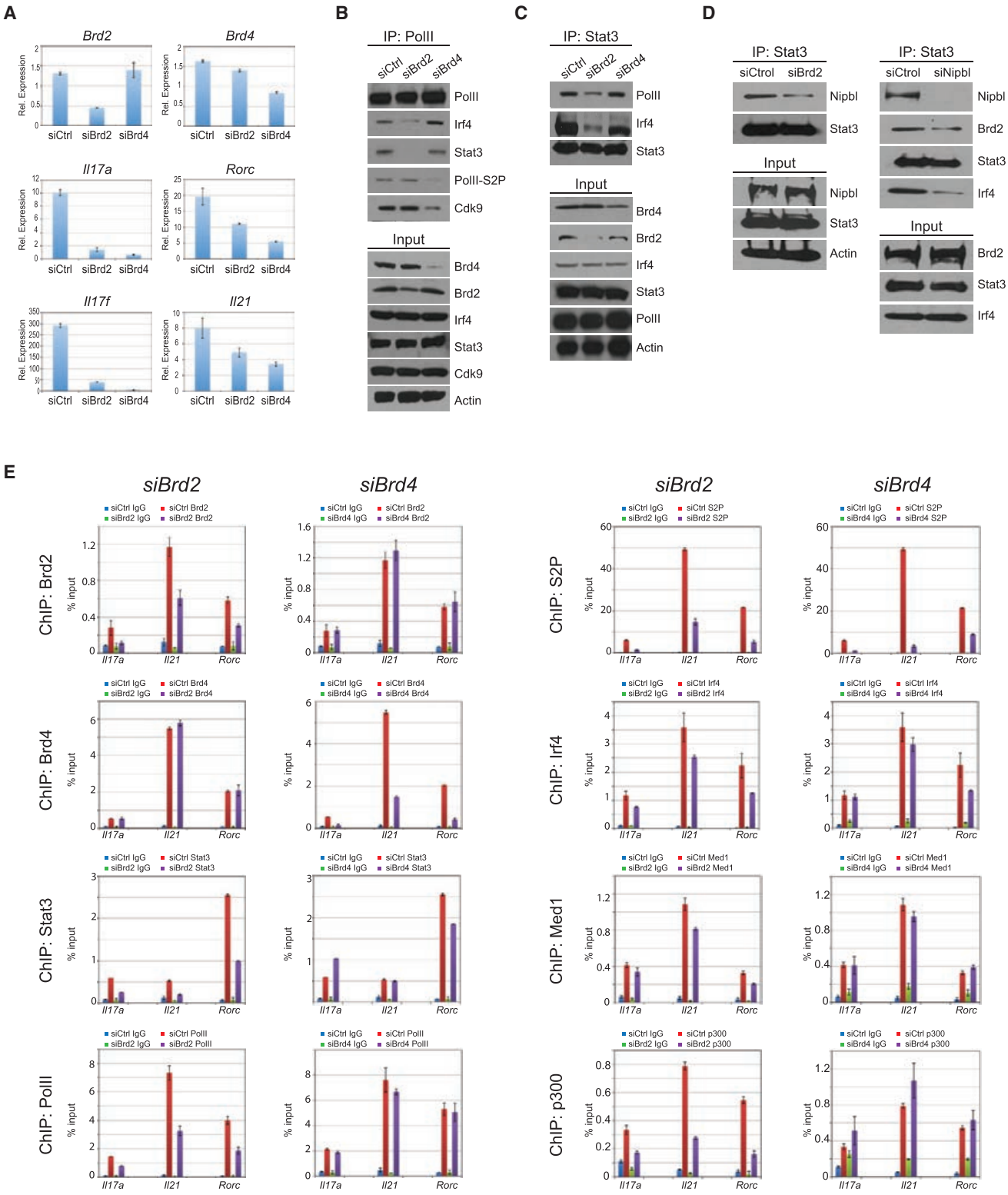

Figure 6. Brd2 and Brd4 Functionally Cooperate to Regulate Gene Transcription in Th17 Cells

(A) mRNA expression levels of *Brd2*, *Brd4*, *Il17a*, *Il17f*, *Rorc*, and *Il21* determined in mouse CD4$^+$ T cells transfected with siControl, siBrd2, or siBrd4 RNA and after 24 or 48 hr of Th17 cell differentiation. All results are statistically significant ($p < 0.05$), and data represent mean ± SEM of more than two independent experiments.

(legend continued on next page)

revealed that Brd2 BD2 binding to Stat3-K87ac peptide is likely to be the major molecular interaction for the Brd2-Stat3 association, as other pairwise protein-peptide titration showed little if any chemical shift perturbations of protein NMR resonances upon addition of the individual Stat3 peptides (Figure 5A and S5A).

We next solved the three-dimensional solution structure of Brd2-BD2 bound to the Stat3-K87ac peptide by using NMR spectroscopy (Figure S5B; Table S3) to discern the molecular basis of this selective interaction. As shown in the structure of the Brd2-BD2/Stat3-K87ac complex (Figure 5B), the Stat3 peptide is bound in the protein across an elongated cavity formed between the ZA and BC loops of this left-handed four-helical bundle structure, similar to a lysine-acetylated histone H4 peptide when bound to Brd2-BD2 (Figure S5C). Specifically, the acetylated K87 forms a hydrogen bond between its carbonyl oxygen and side-chain nitrogen of the conserved Asn429. In addition, F89 of Stat3 forms aromatic and hydrophobic interactions with side chains of Val435, Met438, and Trp370, while I86 interacts with Pro430 and His433. Importantly, the backbone carbonyl oxygen of K87ac establishes a hydrogen bond to the imidazole nitrogen of His433, a unique residue in the conserved acetyl-lysine binding pocket in Brd2-BD2, corresponding to Asp160 in Brd2-BD1. Notably, the amino acid residues at the Kac−1 and Kac+2 positions of the K49ac and K685ac sites in Stat3 are very different from those found at the K87ac site (see above) and likely cannot form the same interactions of Stat3-K87ac with Brd2-BD2. We further evaluated and confirmed the Brd2-BD2/Stat3-K87ac interaction by immunoprecipitation of FLAG-tagged wild-type Stat3 or point mutants of K49R, K87R, or K685R in HEK293 cells that were co-transfected with GFP-Brd2 and myc-300 (Figure 5C). Collectively, our results clearly demonstrated that direct interactions of I86 (Kac−1) and F89 (Kac+2) with the Brd2-BD2 conforms its selective recognition of the K87ac site over the other acetylation sites in Stat3.

Brd2 and Brd4 Functionally Cooperate to Regulate Gene Transcription in Th17 Cells

We further investigated the role of the distinct functions of Brd2 and Brd4 in Th17 cells by small interfering RNA (siRNA) knockdown of *Brd2* or *Brd4* (with >50% efficiency), which resulted in an inhibition of Th17 cell differentiation (Figure S6A) and a marked decrease in mRNA levels of *IL17a*, *Il17f*, *Il21*, and *Rorc* in Th17 cells after 48-hr cell differentiation (Figure 6A). *Brd2* knockdown resulted in decreased interactions of Pol II with Stat3 and Irf4 (Figure 6B) and Stat3 with Pol II and Irf4 (Figure 6C), supporting our notion that Brd2 is important for the Pol II-Stat3-Irf4 association. *Brd4* knockdown led to reduced Pol II-Cdk9 interaction and Pol II phosphorylation at Ser2, with minimal disruption of the Pol II's interactions with the transcription factors Stat3 and Irf4 (Figure 6B). Further, disruption of the Brd2-CTCF-cohesin association by *Brd2* or *Nipbl* knockdown resulted in reduced interactions of Brd2 with Nipbl, as well as Stat3 with Brd2 and Irf4, respectively (Figure 6D). siRNA knockdown of Nibpl, Smc1, or Smc3 resulted in a markedly reduced transcript level of *Il17a* in Th17 cells (Figure S6B).

To determine possible functional cooperativity between Brd2 and Brd4 in transcription, we analyzed by ChIP-qPCR the occupancy of Brd2, Brd4, Stat3, Irf4, p300, Med1, Pol II, and Pol II-S2P at the key Th17 gene loci in Th17 cells after siRNA knockdown of *Brd2* or *Brd4*. We observed that selective Brd4 deficiency has almost no effect on the abundance of Brd2 at the regulatory regions of these gene loci, or vice versa, indicating their independent mechanism of binding to target gene loci (Figure 6E). Notably, Stat3 binding at these gene loci is dependent on Brd2 abundance but is almost independent of Brd4 (Figure 6E), confirming a mutual stabilization of the Stat3-Brd2 complex on target genes during Th17 differentiation. Pol II binding is also dependent on Brd2, but not Brd4, which could be explained by reduced interaction of Pol II and Stat3 in the absence of Brd2. Pol II transcription factor recruitment to the regulatory region is independent of Brd4, but Brd4 is important for Pol II Ser2 phosphorylation and hence its activation. We observed a stable complex of Stat3, Brd2, p300, and Irf4 upon TSA treatment (Figure 4A), raising the question of whether the absence of Brd2 leads to reduced occupancy of p300 and Irf4 as well. Indeed, our ChIP-qPCR data revealed that while Irf4 occupancy decreased noticeably, p300 occupancy decreased dramatically upon *Brd2* knockdown. Taken together, our data suggest that Brd2 functions as a chromatin organizer to facilitate the assembly of enhancer regulatory elements and support transcription elongation, whereas Brd4 functions largely to activate paused RNA Pol II through phosphorylation, thereby sustaining productive gene transcriptional activation.

In summary, in this study, we report the previously unknown distinct functions of Brd2 and Brd4 in regulating gene transcription during Th17 cell differentiation. We discovered that although both Brd2 and Brd4 are important for transcription of Th17 genes, their mechanisms of binding to chromatin and functions in regulating gene transcriptional activation clearly differ (Figure 7). Specifically, Brd2 likely functions through the CTCF-cohesin complex (Bell et al., 1999; Dorsett and Merkenschlager, 2013; Hnisz et al., 2013; Merkenschlager and Odom, 2013) to sustain protein-complex interactions on *cis*-regulatory enhancer elements of target genes. Specifically, Brd2 directly binds to lysine 87-acetylated Stat3 via its second bromodomain, facilitates Stat3's association with other Th17

(B) Th17 cell lysates transfected with siControl, siBrd2, or siBrd4 RNA immunoprecipitated with Pol II and western blot with antibodies against Irf4, Stat3, PolII-S2P, and Cdk9.

(C) Th17 cell lysates transfected with siControl, siBrd2, or siBrd4 RNA immunoprecipitated with Stat3 and western blot with antibodies against PolII and Irf4.

(D) Th17 cell lysates transfected with siControl, siBrd2 (left), or siNipbl (right) RNA immunoprecipitated with Stat3 and western blot with antibodies against Nipbl, Brd2, Stat3, and Irf4.

(E) Brd2, Brd4, Stat3, PolII, PolII-S2P, Irf4, MED1 and p300 occupancy at gene loci of IL17a, IL21 and Rorc in Th17 cell lysates transfected with siControl, siBrd2 or siBrd4 RNA, as determined by ChIP-qPCR. Data are represented as mean ± SEM of n = 3.

See also Figure S6.

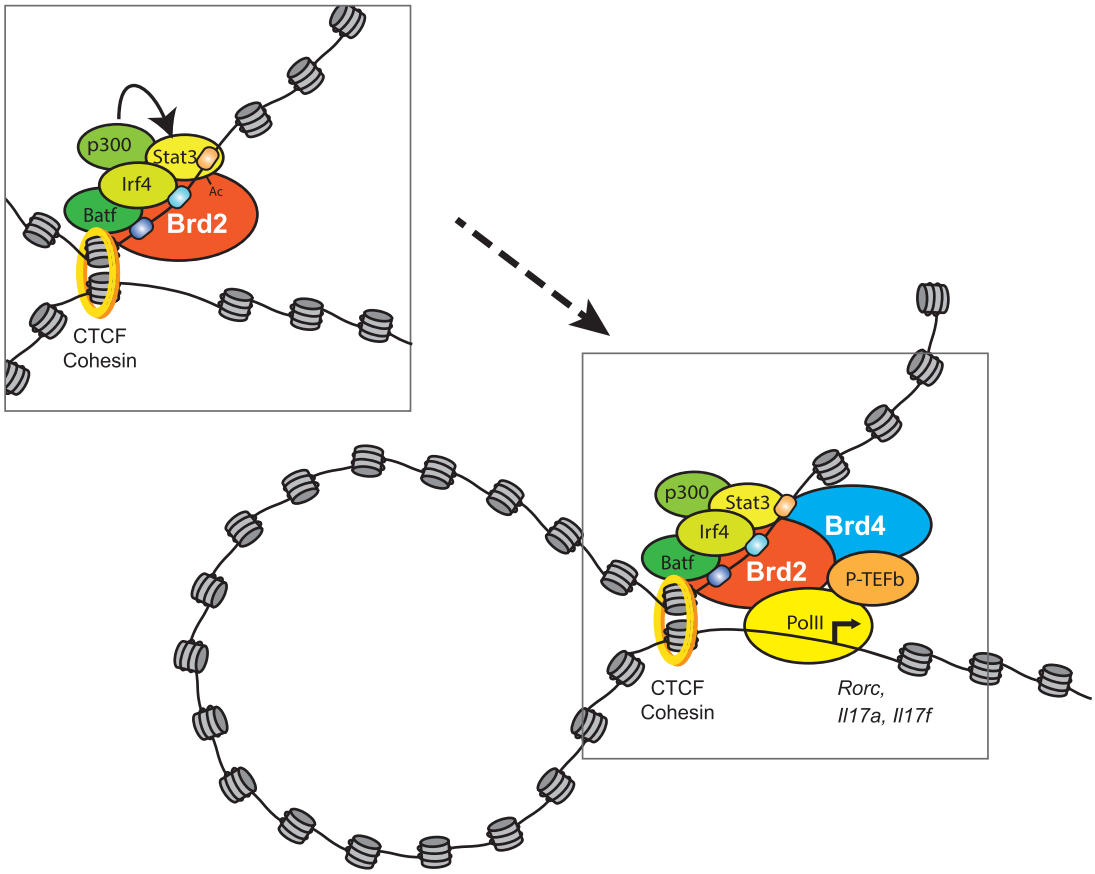

Figure 7. Distinct Roles of Brd2 and Brd4 in Potentiating the Gene Transcriptional Program for Th17 Cell Differentiation
Schematic diagram illustrating how Brd2 and Brd4 functionally cooperate with each other to regulate gene transcription in chromatin in Th17 cells.

factors (including Irf4 and Batf), and enhances the recruitment of RNA Pol II. In contrast, Brd4 binding to target gene loci such as *Il17* is temporally correlated with transcriptional elongation, suggesting a role for Brd4 in the control of the timing and amplitude of ordered gene transcription during Th17 cell differentiation. Therefore, the ability of Brd4 to trigger RNA Pol II transcription elongation for productive Th17 gene expression is a result of integration of enhancer assembly arranged by the Brd2-CTCF-cohesin complex and coordinated through Th17-inducing transcription factors (such as Stat3 and RORγt) and key chromatin regulatory proteins. Finally, through our demonstration of the distinct functions of Brd2 and Brd4 in gene transcription exerted through their bromodomain-acetyllysine-binding-mediated interactions with transcription factors and regulators, our study provides a rational direction for precise chemical modulation of Brd2 and/or Brd4 functions to render Th17 cell development as a new potential treatment for inflammatory disorders.

STAR★METHODS

Detailed methods are provided in the online version of this paper and include the following:

SUPPLEMENTAL INFORMATION

Supplemental Information includes six figures and four tables and can be found with this article online at http://dx.doi.org/10.1016/j.molcel.2016.12.022.

AUTHOR CONTRIBUTIONS

K.L.C. and M.-M. Z. conceived and designed the study and wrote the manuscript. K.L.C., F.Z., A.J., R.S., Q.Z., T.K., T.S., J.-Y.L., C.R., C.-H.C., G.L., M.R.O., W.Z., M.H.K., D.R.L., M.J.W., H.X., and L.Z. conducted experiments, and discussed and interpreted the data together with K.L.C. and M.-M.Z.

ACKNOWLEDGMENTS

We wish to thank the members of the L.Z., H.X., and M.-M.Z. laboratories for helpful technical suggestions and discussion, as well as the New York Structural Biology Center for the use of the NMR facilitates. This work was supported in part by research funds from the First Hospital of Jilin University (Changchun, China) and the Open Project of State Key Laboratory for Supramolecular Structure and Materials at Jilin University (L.Z.) and by research grants from the NCI (CA87658) and the NIAID (AI124465) (to M.-M.Z.).

Received: January 4, 2016
Revised: October 20, 2016
Accepted: December 22, 2016
Published: March 2, 2017

REFERENCES

Bandukwala, H.S., Gagnon, J., Togher, S., Greenbaum, J.A., Lamperti, E.D., Parr, N.J., Molesworth, A.M., Smithers, N., Lee, K., Witherington, J., et al. (2012). Selective inhibition of CD4+ T-cell cytokine production and autoimmunity by BET protein and c-Myc inhibitors. Proc. Natl. Acad. Sci. USA *109*, 14532–14537.

Bell, A.C., West, A.G., and Felsenfeld, G. (1999). The protein CTCF is required for the enhancer blocking activity of vertebrate insulators. Cell *98*, 387–396.

Brünger, A.T., Adams, P.D., Clore, G.M., DeLano, W.L., Gros, P., Grosse-Kunstleve, R.W., Jiang, J.S., Kuszewski, J., Nilges, M., Pannu, N.S., et al. (1998). Crystallography & NMR system: a new software suite for macromolecular structure determination. Acta Crystallogr. D Biol. Crystallogr. *54*, 905–921.

Brüstle, A., Heink, S., Huber, M., Rosenplänter, C., Stadelmann, C., Yu, P., Arpaia, E., Mak, T.W., Kamradt, T., and Lohoff, M. (2007). The development of inflammatory T(H)-17 cells requires interferon-regulatory factor 4. Nat. Immunol. *8*, 958–966.

Chiang, C.M. (2009). Brd4 engagement from chromatin targeting to transcriptional regulation: selective contact with acetylated histone H3 and H4. F1000 Biol. Rep. *1*, 98.

Ciofani, M., Madar, A., Galan, C., Sellars, M., Mace, K., Pauli, F., Agarwal, A., Huang, W., Parkhurst, C.N., Muratet, M., et al. (2012). A validated regulatory network for Th17 cell specification. Cell *151*, 289–303.

Clore, G.M., and Gronenborn, A.M. (1994). Multidimensional heteronuclear nuclear magnetic resonance of proteins. Methods Enzymol. *239*, 349–363.

Dawson, M.A., Prinjha, R.K., Dittmann, A., Giotopoulos, G., Bantscheff, M., Chan, W.I., Robson, S.C., Chung, C.W., Hopf, C., Savitski, M.M., et al. (2011). Inhibition of BET recruitment to chromatin as an effective treatment for MLL-fusion leukaemia. Nature *478*, 529–533.

Dhalluin, C., Carlson, J.E., Zeng, L., He, C., Aggarwal, A.K., and Zhou, M.M. (1999). Structure and ligand of a histone acetyltransferase bromodomain. Nature *399*, 491–496.

Dong, C. (2008). TH17 cells in development: an updated view of their molecular identity and genetic programming. Nat. Rev. Immunol. *8*, 337–348.

Dorsett, D., and Merkenschlager, M. (2013). Cohesin at active genes: a unifying theme for cohesin and gene expression from model organisms to humans. Curr. Opin. Cell Biol. *25*, 327–333.

Filippakopoulos, P., Qi, J., Picaud, S., Shen, Y., Smith, W.B., Fedorov, O., Morse, E.M., Keates, T., Hickman, T.T., Felletar, I., et al. (2010). Selective inhibition of BET bromodomains. Nature *468*, 1067–1073.

Ghoreschi, K., Laurence, A., Yang, X.P., Hirahara, K., and O'Shea, J.J. (2011). T helper 17 cell heterogeneity and pathogenicity in autoimmune disease. Trends Immunol. *32*, 395–401.

Hargreaves, D.C., Horng, T., and Medzhitov, R. (2009). Control of inducible gene expression by signal-dependent transcriptional elongation. Cell *138*, 129–145.

Harrington, L.E., Hatton, R.D., Mangan, P.R., Turner, H., Murphy, T.L., Murphy, K.M., and Weaver, C.T. (2005). Interleukin 17-producing CD4+ effector T cells develop via a lineage distinct from the T helper type 1 and 2 lineages. Nat. Immunol. *6*, 1123–1132.

Hirahara, K., Onodera, A., Villarino, A.V., Bonelli, M., Sciumè, G., Laurence, A., Sun, H.W., Brooks, S.R., Vahedi, G., Shih, H.Y., et al. (2015). Asymmetric action of STAT transcription factors drives transcriptional outputs and cytokine specificity. Immunity *42*, 877–889.

Hnilicova, J., Hozeifi, S., Stejskalova, E., Duskova, E., Poser, I., Humpolickova, J., Hof, M., and Stanek, D. (2013). The C-terminal domain of Brd2 is important for chromatin interaction and regulation of transcription and alternative splicing. Mol. Biol. Cell. *24*, 3557–3568.

Hnisz, D., Abraham, B.J., Lee, T.I., Lau, A., Saint-André, V., Sigova, A.A., Hoke, H.A., and Young, R.A. (2013). Super-enhancers in the control of cell identity and disease. Cell *155*, 934–947.

Hou, T., Ray, S., Lee, C., and Brasier, A.R. (2008). The STAT3 NH2-terminal domain stabilizes enhanceosome assembly by interacting with the p300 bromodomain. J. Biol. Chem. *283*, 30725–30734.

Ivanov, I.I., McKenzie, B.S., Zhou, L., Tadokoro, C.E., Lepelley, A., Lafaille, J.J., Cua, D.J., and Littman, D.R. (2006). The orphan nuclear receptor RORgammat directs the differentiation program of proinflammatory IL-17+ T helper cells. Cell *126*, 1121–1133.

Kagey, M.H., Newman, J.J., Bilodeau, S., Zhan, Y., Orlando, D.A., van Berkum, N.L., Ebmeier, C.C., Goossens, J., Rahl, P.B., Levine, S.S., et al. (2010). Mediator and cohesin connect gene expression and chromatin architecture. Nature *467*, 430–435.

Kanno, Y., Vahedi, G., Hirahara, K., Singleton, K., and O'Shea, J.J. (2012). Transcriptional and epigenetic control of T helper cell specification: molecular mechanisms underlying commitment and plasticity. Annu. Rev. Immunol. *30*, 707–731.

Kanno, T., Kanno, Y., LeRoy, G., Campos, E., Sun, H.W., Brooks, S.R., Vahedi, G., Heightman, T.D., Garcia, B.A., Reinberg, D., et al. (2014). BRD4 assists elongation of both coding and enhancer RNAs by interacting with acetylated histones. Nat. Struct. Mol. Biol. *21*, 1047–1057.

Landt, S.G., Marinov, G.K., Kundaje, A., Kheradpour, P., Pauli, F., Batzoglou, S., Bernstein, B.E., Bickel, P., Brown, J.B., Cayting, P., et al. (2012). ChIP-seq guidelines and practices of the ENCODE and modENCODE consortia. Genome Res. *22*, 1813–1831.

Laskowski, R.A., Rullmannn, J.A., MacArthur, M.W., Kaptein, R., and Thornton, J.M. (1996). AQUA and PROCHECK-NMR: programs for checking the quality of protein structures solved by NMR. J. Biomol. NMR *8*, 477–486.

Littman, D.R., and Rudensky, A.Y. (2010). Th17 and regulatory T cells in mediating and restraining inflammation. Cell *140*, 845–858.

Marinov, G.K., Kundaje, A., Park, P.J., and Wold, B.J. (2014). Large-scale quality analysis of published ChIP-seq data. G3 (Bethesda) *4*, 209–223.

Mathur, A.N., Chang, H.C., Zisoulis, D.G., Stritesky, G.L., Yu, Q., O'Malley, J.T., Kapur, R., Levy, D.E., Kansas, G.S., and Kaplan, M.H. (2007). Stat3 and Stat4 direct development of IL-17-secreting Th cells. J. Immunol. *178*, 4901–4907.

Medzhitov, R., and Horng, T. (2009). Transcriptional control of the inflammatory response. Nat. Rev. Immunol. *9*, 692–703.

Mele, D.A., Salmeron, A., Ghosh, S., Huang, H.R., Bryant, B.M., and Lora, J.M. (2013). BET bromodomain inhibition suppresses TH17-mediated pathology. J Exp Med. *210*, 2181–2190.

Merkenschlager, M., and Odom, D.T. (2013). CTCF and cohesin: linking gene regulatory elements with their targets. Cell *152*, 1285–1297.

Miossec, P., and Kolls, J.K. (2012). Targeting IL-17 and TH17 cells in chronic inflammation. Nat. Rev. Drug Discov. *11*, 763–776.

Murphy, K.M., and Reiner, S.L. (2002). The lineage decisions of helper T cells. Nat. Rev. Immunol. *2*, 933–944.

Nilges, M., and O'Donoghue, S. (1998). Ambiguous NOEs and automated NOE assignment. Prog. Nucl. Magn. Reson. Spectrosc. *32*, 107–139.

Okamoto, K., Iwai, Y., Oh-Hora, M., Yamamoto, M., Morio, T., Aoki, K., Ohya, K., Jetten, A.M., Akira, S., Muta, T., and Takayanagi, H. (2010). IkappaBzeta regulates T(H)17 development by cooperating with ROR nuclear receptors. Nature *464*, 1381–1385.

Park, H., Li, Z., Yang, X.O., Chang, S.H., Nurieva, R., Wang, Y.H., Wang, Y., Hood, L., Zhu, Z., Tian, Q., and Dong, C. (2005). A distinct lineage of CD4 T cells regulates tissue inflammation by producing interleukin 17. Nat. Immunol. *6*, 1133–1141.

Puissant, A., Frumm, S.M., Alexe, G., Bassil, C.F., Qi, J., Chanthery, Y.H., Nekritz, E.A., Zeid, R., Gustafson, W.C., Greninger, P., et al. (2013). Targeting MYCN in neuroblastoma by BET bromodomain inhibition. Cancer Discov. *3*, 308–323.

Rubin, D.C., Shaker, A., and Levin, M.S. (2012). Chronic intestinal inflammation: inflammatory bowel disease and colitis-associated colon cancer. Front. Immunol. *3*, 107.

Saleh, M., and Trinchieri, G. (2011). Innate immune mechanisms of colitis and colitis-associated colorectal cancer. Nat. Rev. Immunol. *11*, 9–20.

Sanchez, R., and Zhou, M.M. (2009). The role of human bromodomains in chromatin biology and gene transcription. Curr. Opin. Drug Discov. Devel. *12*, 659–665.

Schraml, B.U., Hildner, K., Ise, W., Lee, W.L., Smith, W.A., Solomon, B., Sahota, G., Sim, J., Mukasa, R., Cemerski, S., et al. (2009). The AP-1 transcription factor Batf controls T(H)17 differentiation. Nature *460*, 405–409.

Shao, Z., Zhang, Y., Yuan, G.C., Orkin, S.H., and Waxman, D.J. (2012). MAnorm: a robust model for quantitative comparison of ChIP-seq data sets. Genome Biol. *13*, R16.

Shi, J., and Vakoc, C.R. (2014). The mechanisms behind the therapeutic activity of BET bromodomain inhibition. Mol. Cell *54*, 728–736.

Stark, R., and Brown, G. (2011). DiffBind: differential binding analysis of ChIP-seq peak data. R package version 100 (University of Cambridge).

Tabas, I., and Glass, C.K. (2013). Anti-inflammatory therapy in chronic disease: challenges and opportunities. Science *339*, 166–172.

Takahama, Y. (2006). Journey through the thymus: stromal guides for T-cell development and selection. Nat. Rev. Immunol. *6*, 127–135.

Wei, L., Vahedi, G., Sun, H.W., Watford, W.T., Takatori, H., Ramos, H.L., Takahashi, H., Liang, J., Gutierrez-Cruz, G., Zang, C., et al. (2010). Discrete roles of STAT4 and STAT6 transcription factors in tuning epigenetic modifications and transcription during T helper cell differentiation. Immunity *32*, 840–851.

Wilson, C.B., Rowell, E., and Sekimata, M. (2009). Epigenetic control of T-helper-cell differentiation. Nat. Rev. Immunol. *9*, 91–105.

Yang, X.O., Panopoulos, A.D., Nurieva, R., Chang, S.H., Wang, D., Watowich, S.S., and Dong, C. (2007). STAT3 regulates cytokine-mediated generation of inflammatory helper T cells. J. Biol. Chem. *282*, 9358–9363.

Yosef, N., Shalek, A.K., Gaublomme, J.T., Jin, H., Lee, Y., Awasthi, A., Wu, C., Karwacz, K., Xiao, S., Jorgolli, M., et al. (2013). Dynamic regulatory network controlling TH17 cell differentiation. Nature *496*, 461–468.

Yu, H., Lee, H., Herrmann, A., Buettner, R., and Jove, R. (2014). Revisiting STAT3 signalling in cancer: new and unexpected biological functions. Nat. Rev. Cancer *14*, 736–746.

Yuan, Z.L., Guan, Y.J., Chatterjee, D., and Chin, Y.E. (2005). Stat3 dimerization regulated by reversible acetylation of a single lysine residue. Science *307*, 269–273.

Zhang, G., Liu, R., Zhong, Y., Plotnikov, A.N., Zhang, W., Zeng, L., Rusinova, E., Gerona-Nevarro, G., Moshkina, N., Joshua, J., et al. (2012a). Down-regulation of NF-κB transcriptional activity in HIV-associated kidney disease by BRD4 inhibition. J. Biol. Chem. *287*, 28840–28851.

Zhang, W., Prakash, C., Sum, C., Gong, Y., Li, Y., Kwok, J.J., Thiessen, N., Pettersson, S., Jones, S.J., Knapp, S., et al. (2012b). Bromodomain-containing protein 4 (BRD4) regulates RNA polymerase II serine 2 phosphorylation in human CD4+ T cells. J. Biol. Chem. *287*, 43137–43155.

Zuber, J., Shi, J., Wang, E., Rappaport, A.R., Herrmann, H., Sison, E.A., Magoon, D., Qi, J., Blatt, K., Wunderlich, M., et al. (2011). RNAi screen identifies Brd4 as a therapeutic target in acute myeloid leukaemia. Nature *478*, 524–528.

STAR★METHODS

KEY RESOURCES TABLE

REAGENT or RESOURCE	SOURCE	IDENTIFIER
Antibodies		
Brd2	Bethyl Laboratory	IHC-00612; RRID: AB_10755275
Brd4	Bethyl Laboratory	IHC-00396; RRID: AB_1604188
Stat3	Invitrogen	13-7000
PolII	Bethyl Laboratory	A304-405A; RRID: AB_2620600
PolII-S2P	Abcam	Ab5095; RRID: AB_304749
H4Kac	Millipore	06-866
CTCF	Active Motif	61312
Nipbl	Bethyl Laboratory	A301-779A; RRID: AB_1211232
Rad21	Active Motif	39384
Stag1	Active Motif	61562
Irf4	Santa Cruz	Sc-6059; RRID: AB_2127145
Batf	Santa Cruz	Sc-100974; RRID: AB_1119410
Smc3	Active Motif	61132
Smc1	Active Motif	61068
H3K27ac	Abcam	Ab4729; RRID: AB_2118291
H3K4me1	Abcam	Ab8895
P300	Santa Cruz	Sc-584
Flag	Abcam	Ab49763
GFP	Abcam	Ab1218
myc	Abcam	Ab9132
Cdk9	Bethyl Laboratory	A-303-493A
Med1	Santa Cruz	Sc-5334
Biological Samples		
Th17 primary cells	The Jackson Lab	C57B/6 (6–8 weeks)
Chemicals, Peptides, and Recombinant Proteins		
Cd3	BD Bioscience	553058
Cd28	BD Bioscience	553295
Recombinant mouse IL6	BD Bioscience	554582
Human TGFb1	R&D	240-B/CF
CD4(L3T4)Microbeads	Miltenyi Biotech	130-049-201
Stat3-K49ac peptide	Mimotopes	N/A
Stat3-K87ac peptide	Mimotopes	N/A
Stat3-K685ac peptide	Mimotopes	N/A
MS417	Mount Sinai	N/A
Critical Commercial Assays		
NEBNext ChIP-seq Library Prep Master Mix Set for Illumina	New England Biolabs Inc.	E6240L
Neon Transfection System	ThermoFisher Scientific	MPK5000
Deposited Data		
Brd2, Brd4, Smc1, Smc3, Nipbl, H3K27ac, H3K4me1 ChIP-seq data	This paper	GEO: GSE90788 and GSE63778
Other ChIP-seq data	Ciofani et al., 2012	GEO: GSE40918
Solution structure of Brd2-BD2 in complex with Stat3K87ac peptide	Protein Data Bank(PDB)	PDB: 5U5S

(*Continued on next page*)

Continued

REAGENT or RESOURCE	SOURCE	IDENTIFIER
NMR spectral data	BioMagResBank(BMRB)	BMRB: 30206
Experimental Models: Cell Lines		
Th17 primary cells	The Jackson Laboratory	C57B/6 (6-8 weeks)
Recombinant DNA		
GFP-Brd2 plasmids	David Stanek	Hnilicova et al., 2013
pCMV-p300-myc	Addgene	#30489
pCMV-Flag-Stat3	This paper	N/A
6xHis-Brd2-BD1	SGC Oxford	N/A
6xHis-Brd2-BD2	SGC Oxford	N/A
Sequence-Based Reagents		
siGENOME Control Pool Non-Targeting #2	Dharmacon	D-001206-14-05
siGENOME SMART Pool Mouse Brd2	Dharmacon	M-043404-01
siGENOME SMART Pool Mouse Brd4	Dharmacon	M-041493-00
siGENOME SMART Pool Mouse Nipbl	Dharmacon	M-048662-00
siGENOME SMART Pool Mouse Smc1	Dharmacon	M-049483-00
siGENOME SMART Pool Mouse Smc3	Dharmacon	M-064492-01
Primers for qPCR, ChIP-qPCR	This paper	Table S4
Software and Algorithms		
MAnorm	Shao et al., 2012	N/A
Phantompeakqualtools	Marinov et al., 2014	N/A
DiffBind Bioconductor package	Stark and Brown, 2011	N/A
X-PLOR	Brünger et al., 1998	N/A
ARIA	Nilges and O'Donoghue, 1998	N/A
Procheck-NMR	Laskowski et al., 1996	N/A
FlowJo	FLOWJO, LLC	https://www.flowjo.com/solutions/flowjo/downloads

CONTACT FOR REAGENT AND RESOURCE SHARING

Further information and requests for reagents may be directed to, and will be fulfilled by the corresponding author, Dr. Ming-Ming Zhou (ming-ming.zhou@mssm.edu).

EXPERIMENTAL MODEL AND SUBJECT DETAILS

C57BL/6 mice were obtained from Jackson Laboratory. All animals were housed and maintained in a conventional pathogen-free facility at the Icahn School of Medicine at Mount Sinai (ISMMS). The animal study protocols in this study were approved by the Institutional Animal Care and Use Committees of ISMMS. Mice of 6-8 weeks were sacrificed for T cell isolation.

METHOD DETAILS

Preparation of Protein and Peptides

The Brd2 BD1 domain (residues 73-194) and Brd2-BD2 domain (residues 348-455) fused with an N-terminal 6xHis tag were expressed in *E. Coli* BL21(DE3) codon plus RIL strain cells induced by isopropyl-β-D-thiogalactopyranoside (0.3 mM) at 25°C. The Brd2-BD1 or BD2 domain was purified with HiTrap IMAC FF column (GE Healthcare) followed by the removal of His-Tag via thrombin cleavage, and the protein was further applied to a Superdex 75 column and eluted with PBS buffer of pH 7.4 containing 2.0 mM EDTA, 2.0 mM DTT and 500 mM NaCl. Uniformly ^{15}N- and $^{15}N/^{13}C$-labeled proteins were prepared from cells grown in the minimal medium containing $^{15}NH_4Cl$ with or without $^{13}C_6$-glucose in H_2O.

Protein/Peptide Binding Study and Protein Structure Determination by NMR

The Brd2-BD1 or BD2 domain binding to lysine-acetylated Stat3 peptides containing K49ac (AYAAS-Kac-ESHAT, residues 44-54), K87ac (HNLLRI-Kac-QFLQS, residues 71-82), or K685ac (PKEEAFG-Kac-YCPE, residues 678-690) was assessed by

monitoring ^{15}N-labeled protein backbone amid resonance perturbations as a function of ligand concentration in 2D ^{1}H-^{15}N HSQC spectra. NMR samples of the Brd2-BD2 domain (0.5 mM) in complex with Stat3-K87ac (residues 71-82) peptide of 1.0 mM were prepared in PBS buffer of pH 7.4 containing 2.0 mM perdeuterated DTT and 2.0 mM EDTA in $H_2O/^2H_2O$ (9/1) or ^2H_2O. All NMR spectra were collected at 298K on NMR spectrometers of 800, 600, or 500 MHz. The ^{1}H, ^{13}C, and ^{15}N resonances of a protein of the complex were assigned by triple-resonance NMR spectra collected with a ^{13}C/^{15}N-labeled protein bound to an unlabeled peptide (Clore and Gronenborn, 1994). The distance restraints were obtained in three-dimensional ^{13}C- or ^{15}N-NOESY spectra. Slowly exchanging amides, identified in 2D ^{15}N-HSQC spectra recorded after a H_2O buffer was changed to a ^2H_2O buffer, were used with structures calculated with only NOE distance restraints to generate hydrogen-bond restraints for final structure calculations. The inter-molecular NOEs were detected in ^{13}C-edited (F_1), ^{13}C/^{15}N-filtered (F_3), three-dimensional NOESY spectrum.

Structure Calculations

3D Structures of the Brd2-BD2/Stat3-K87ac complex were calculated with a distance geometry-simulated annealing protocol using the X-PLOR program (Brünger et al., 1998) Manually assigned NOE-derived distance restraints were used to calculate initial structures. ARIA (Nilges and O'Donoghue, 1998) assigned distance restraints agree with structures calculated using only the manually determined NOE restraints. Ramachandran plot analysis of the final structures was performed using Procheck-NMR program (Laskowski et al., 1996).

Cell Sorting and T-Helper Cell Differentiation

CD4$^+$ T cells were purified from spleen and lymph nodes using anti-CD4 microbeads (Miltenyi Biotech). Naive CD4$^+$ T cells were activated with plate-bound anti-CD3 (1.5 μM/ml) and anti-CD28 (1.5 μM/ml) plus cytokines. IL-12 (20 ng/mL) and anti-IL4 (10 μM/ml) for Th1 conditions, IL4 (20 ng/mL), anti-IL12 (10 μM/ml) and anti-IFNγ (10 μM/ml) for Th2 conditions, IL6 (20 ng/mL), TGFβ (2.5 ng/mL) for Th17 conditions, TGFβ (2.5 ng/mL) for Treg conditions. The cells were cultured for two to three days before harvesting for further analysis. All cytokines were purchased from R&D, and neutralizing antibodies were purchased from BD Pharmigen.

Real-Time Quantitative PCR (qPCR)

Total RNA was extracted with RNeasy Mini Kit (QIAGEN) and reverse transcribed using the Superscript III Reverse Transcriptase (Life Technologies). All qPCR analysis were performed using Brilliant III Ultra Fast SYBR Green QPCR Master Mix (Agilent Technologies). In gene expression analysis, all data were normalized with Actin/Gapdh and represented relative to the control sample (fold change). For ChIP-qPCR relative occupancies were calculated as ratio of the amount of immunoprecipitated DNA to that of the input sample (%input). Measurements were performed in duplicate, and error bars denote experimental standard deviations. Results are representative of more than two independent experiments. Primer sequences are available in Table S4.

Gene Knockdown Using siRNA and Intracellular Staining and Flow Cytometry Analysis

All siRNAs (siCtrl, siBrd2, siBrd4, siNipbl, siSmc1, siSmc3) were purchased from Dharmacon. Briefly, naive T cells were activated under the Th0 condition overnight, re-suspended and transfected with Neon Transfection System (Invitrogen). The transfected cells were added to plates with CD3$^+$CD28 IMDM medium. After four hours of recovery, IL6 (20 ng/mL) and TGFβ (2.5 ng/mL) were added to induce Th17 differentiation. Supernatants and mRNA were collected for analysis after 48 hr. Phenotypic analysis of the gene knockdown by siRNA was performed in in vitro Th17 cell culture as follows. Naive CD4+ T cells (CD4$^+$CD25$^-$CD62L$^+$CD44^{low}) were isolated from lymph nodes and spleens of six to eight week old B6 mice using a FACSAria (BD) and activated by anti-CD3 and anti-CD28 stimulation in plates pre-coated with goat anti-hamster IgG. Cells were cultured in IMDM (Sigma) supplemented with 10% heat-inactivated FBS (Hyclone), 50 U penicillin-streptomycin (Invitrogen), 4 mM glutamine, and 50 μM β-mercaptoethanol. For T cell polarization, cells were cultured for 2 days under Th17 polarizing condition (0.1 ng/mL TGF-β, 20ng/mL IL-6) or Th0 condition (100U/mL IL-2) after 24 hr activation. For cytokine analysis, cells were incubated for 3 hr with phorbol PMA (50 ng/mL; Sigma), ionomycin (500 ng/mL; Sigma) and GolgiStop (BD). Intracellular cytokine staining was performed according to the manufacturer's protocol (FoxP3 staining buffer set from eBioscience). A LSR II flow cytometer (BD Biosciences) and FlowJo (Tree Star) software were used for flow cytometry and analysis. Dead cells were excluded using the Live/Dead fixable aqua dead cell stain kit (Invitrogen).

Chromatin Immunoprecipitation (ChIP)

Cells were chemically cross-linked with 1% formaldehyde solution for 10 min at room temperature followed by the addition of 2.5 M glycine (to a final concentration of 125 mM) for 5 min. Cells were rinsed twice with cold 1xPBS and then lysed in Szak's RIPA buffer (150 mM NaCl, 1% Nonidet P-40, 0.5% deoxycholate, 0.1% SDS, 50 mM Tris-HCl pH 8, 5 mM EDTA, Protease Inhibitor Cocktail (Roche), 10mM PMSF). Cells were then sonicated using sonicator (QSonica) for 10 pulses of 15 s at a voltage of 70V, followed by 1 min rest on ice. Sonicated chromatin was cleared by centrifugation. The resulting chromatin extract was incubated overnight at 4°C with appropriate primary antibodies and 25 μL of Protein A/G magnetic beads (Dynabeads, Life Technologies). Beads were washed 2 times with Szak's RIPA buffer (without PMSF and Protease Inhibitor cocktail), four times with Szak's IP Wash Buffer (100 mM Tris HCl pH 8.5, 500 mM LiCl, 1% Nonidet P-40, 1% deoxycholate), then twice again with incomplete RIPA buffer and twice with cold 1X TE. Complexes were eluted from beads in Talianidis Elution Buffer by heating at 65°C for 10 min and then by adding NaCl to a final concentration of 200 mM and reverse crosslinking was performed overnight at 65°C. Input DNA was concurrently treated for

crosslink reversal. Samples were then treated with RNaseA and Proteinase K for an hour, extracted with Phenol/Chloroform and ethanol precipitated. The pellet was resuspended in water and used for subsequent ChIP-seq library preparation or analyzed by qPCR as described above.

Immunoprecipitation (IP)

Pierce IP lysis buffer were used for cell lysis and washing. Briefly, cells were lysed and protein concentration was determined. 500ug of cleared protein lysates were incubated with IP antibodies overnight under rotation at 4°C and then incubated with 30ul of Protein G Sepharose beads for additional 2 hr. The beads were then washed extensively with IP lysis buffer, and eluted with Laemmli Sample Buffer heated under 95°C for 10 min. The supernatants then were collected for western blotting.

Chromatin Immunoprecipitation-sequencing (ChIP-Seq)

ChIPed-DNA was end repaired with T4 DNA polymerase and polynucleotide kinase. An A-base was added to the end-repaired DNA fragments. Solexa adaptors were ligated to the DNA fragments and 200-300bp size fractions were obtained using E-gel (Life Technologies). Adaptor-modified fragments were enriched by 18 cycles of PCR amplification. The DNA library prep was validated in Bioanalyzer for quantity and size. The input- and ChIPed-DNA libraries were sequenced on the Illumina HiSeq2000 platform with 50bp read length in a single end mode. Brd2 and Brd4 ChIP-seq were performed and analyzed in triplicate. H3K27ac and H3K4me1 ChIP-seq were performed in duplicate. Smc1, Smc3 and Nipbl were performed once. All ChIP-seq data described in this study have been deposited in GEO under the accession numbers GEO: GSE90788 and GSE63778.

QUANTIFICATION AND STATISTICAL ANALYSIS

Bioinformatics Analysis

For ChIP-seq analysis, the input and ChIP samples were sequenced by Illumina HiSeq200. After QC filtering by FASTAX (http://hannonlab.cshl.edu/fastx_toolkit/), only the reads with a quality score Q20 in at least 90% bases were included for analysis. The reads from both Input and ChIP samples were first aligned to mm9 reference genome using Bowtie. The peaks in the ChIP sample in reference to the input sample were called from read alignments by MACS algorithm and then the distance to the closest TSS was annotated from genome mapping information of RefSeq transcripts. Genes associated with peaks were annotated (http://amp.pharm.mssm.edu/Enrichr/). The Brd2, Brd4, Nipbl, Smc1, Smc3 peaks were compared to peaks from previously published Th17 (CTCF, p300, RorgT, Stat3, Irf4 and BATF) ChIP-seq datasets (Ciofani et al., 2012; Wei et al., 2010). Finally, the alignment and coverage of ChIPseq data were visualized by integrative genomics viewer (IGV) program (https://www.broadinstitute.org/igv/). Gene annotation and pathway analysis of the identified genes was performed using The Database for Annotation, Visualization and Integrated Discovery (DAVID) (http://david.abcc.ncifcrf.gov/). For replicates analysis, we followed guidelines recommended by ENCODE (Landt et al., 2012). Specifically, Brd2 and Brd4 ChIP-seq were performed in triplicate and analyzed. Quality of ChIP-seq data were analyzed with phantompeakqualtools. PCA clustering analysis was performed to determine the reproducibility of replicates and MAnorm (Shao et al., 2012) was used to analyze quantitative difference of peaks identified.

Analysis of ChIP-Seq Quality and Reproducibility

ChIP-seq samples were analyzed in triplicates. For data QC (quality control), Phantompeakqualtools (Marinov et al., 2014) was used to generate two quality metrics: NSC and RSC. The NSC (Normalized strand cross-correlation) and RSC (Relative strand cross-correlation) metrics use cross-correlation of stranded read density profiles to measure enrichment independently of peak calling. Samples with NSC > 1.05 and RSC > 0.8 were considered as high quality samples. Reproducibility of datasets was checked using PCA and clustering, using the *DiffBind Bioconductor* package (Stark and Brown, 2011).

Analysis of Quantitative Difference of ChIP-Seq Peaks Using MAnorm

MAnorm was used for normalization and quantitative comparison of Brd2 and Brd4 peaks. MAnorm was used to analyzed triplicates for Brd2 and Brd4 and takes the coordinate of all peaks and aligned reads in both Brd2 and Brd4 samples as input. The (M, A) value of each common peak is then calculated and plotted, where M = log2 (Read density in Brd2/Read density in Brd4) and A = 0.5 × log2 (Read density in Brd2 × Read density in Brd4). Robust regression is subsequently applied to the (M, A) values of all common peaks and a linear model is derived. Finally, the linear model is extrapolated to all peaks for normalization. A P value is also calculated for each peak to describe the statistical significance of read intensity difference between the two samples being compared. The normalized M value was then used as a quantitative measure of differential binding in each peak region between two samples, with peak regions associated with larger absolute M values exhibiting greater differences in binding. In the Venn diagram, Brd2 unique peaks (non-concordant peaks) are peaks with M-values greater than 1 and that have a log base 10(p value) greater than 5. Similarly, Brd4 unique peaks (non-concordant peaks) are peaks with M-values less than (−1) that have a log base 10(p value) greater than 5. Unbiased peaks (concordant peaks) are peaks with M-values between (−0.5) and (+0.5). Final Venn diagram was generated to incorporate results from triplicates. Peaks were considered positive if present in at least two out of three samples.

Statistical Analysis

Statistical analysis was performed using Student's t-Test. *P values* < 0.05 were considered statistically significant. Measurements were performed in duplicate, and error bars denote experimental standard deviations.

DATA AND SOFTWARE AVAILABILITY

The Brd2, Brd4, H3K27ac, H3K4me1, Smc1, Smc3, and Nipbl ChIP-seq data have been deposited in GEO under accession numbers GEO: GSE90788 and GSE63778. The solution structure of the Brd2-BD2 in complex with Stat3-K87ac peptide and for the NMR spectral data have been deposited in Protein Data Bank (PDB) under ID code PDB: 5U5S, and BioMagResBank (BMRB) ID code BMRB: 30206, respectively.

Molecular Cell, Volume *65*

Supplemental Information

Distinct Roles of Brd2 and Brd4 in Potentiating the Transcriptional Program for Th17 Cell Differentiation

Ka Lung Cheung, Fan Zhang, Anbalagan Jaganathan, Rajal Sharma, Qiang Zhang, Tsuyoshi Konuma, Tong Shen, June-Yong Lee, Chunyan Ren, Chih-Hung Chen, Geming Lu, Matthew R. Olson, Weijia Zhang, Mark H. Kaplan, Dan R. Littman, Martin J. Walsh, Huabao Xiong, Lei Zeng, and Ming-Ming Zhou

A

Cell	Target	Identifier	N_Unique map reads	MACS FDR 0.01	NSC (>1.05)	RSC (>0.8)	Quality Tag
Th17	Brd2	Brd2_rep1	63,129,695	14,485	1.36	1.17	high
Th17	Brd2	Brd2_rep2	28,803,910	31,133	1.88	1.44	high
Th17	Brd2	Brd2_rep3	34,325,785	38,491	1.62	1.56	very high
Th17	Brd4	Brd4_rep1	65,164,125	8,831	1.18	1.07	high
Th17	Brd4	Brd4_rep2	30,995,977	39,543	1.58	1.04	high
Th17	Brd4	Brd4_rep3	34,168,148	8,195	1.21	3.9	very high

B

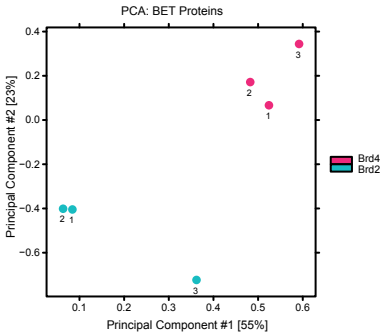

C

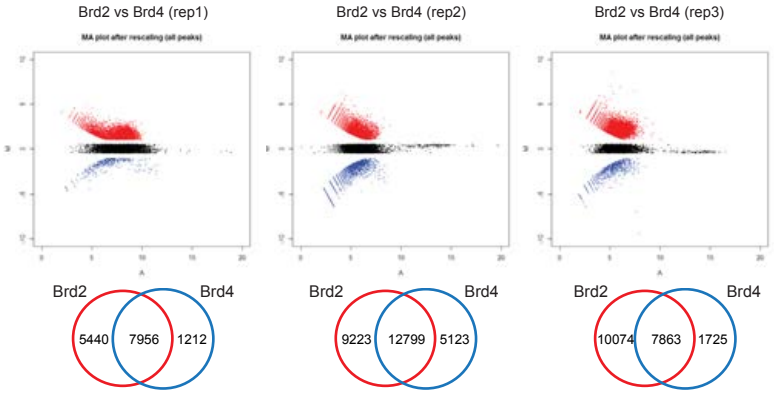

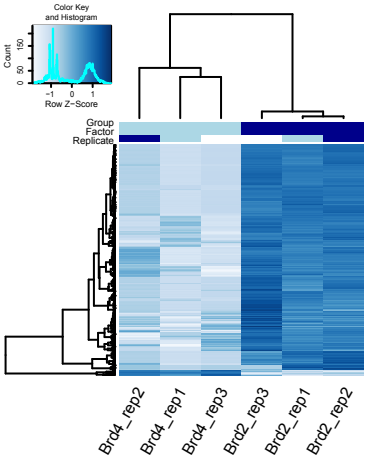

D

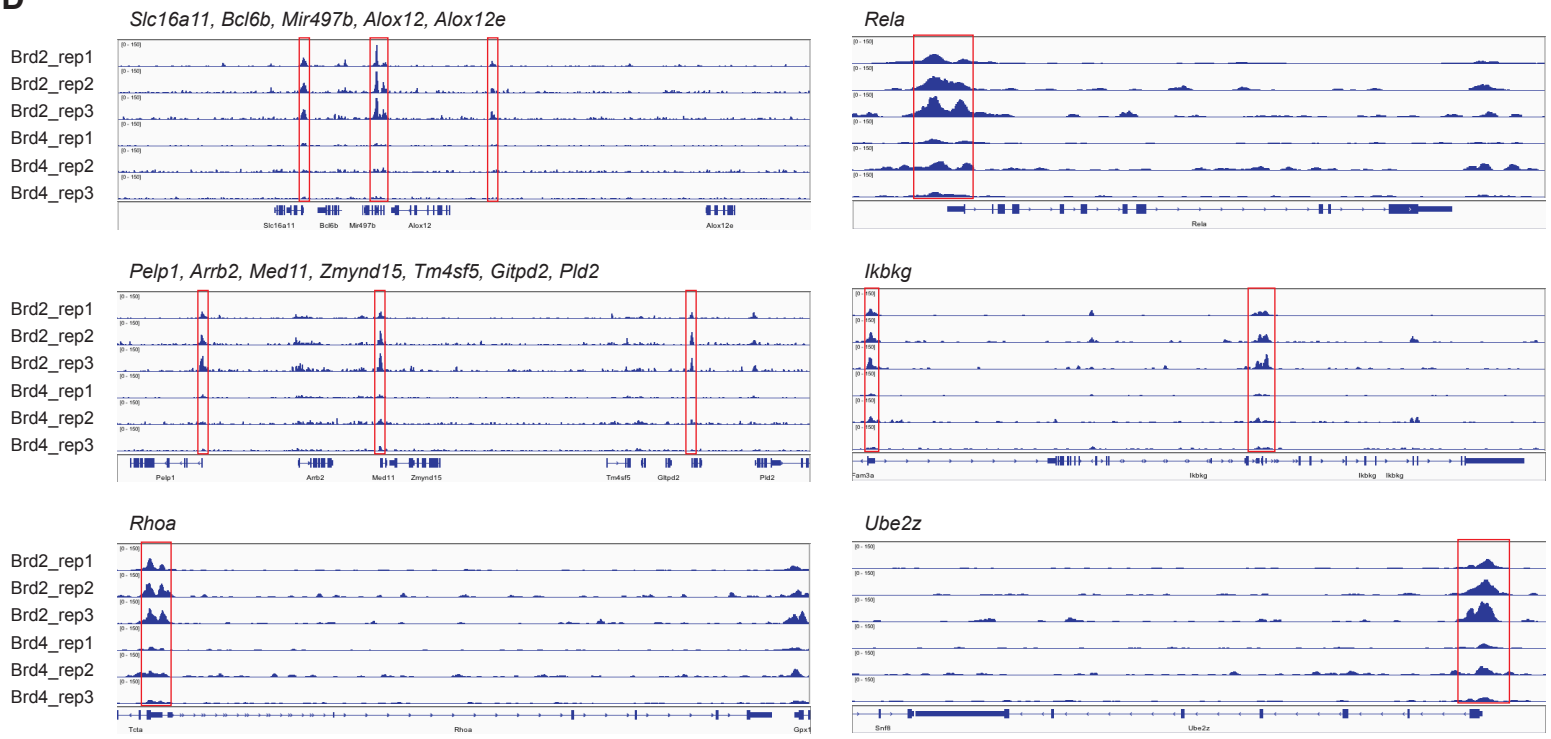

Figure S1. Analysis of quality and reproducibility of Brd2 and Brd4 ChIP-seq data in triplicates, related to Figure 1.
(A) Quality metrics for ChIP-seq triplicate. NSC and RSC values were calculated using phantompeakqualtools. Libraries with NSC >1.05 and RSC>0.8 were considered to be high quality.
(B) PCA plot of the Brd2 and Brd4 ChIP-seq data in triplicates ofmouse Th17 cells showing that the replicates for the corresponding BET proteins resemble each other well. *Lower panel,* hierachical clustering analysis of the Brd2 and Brd4 ChIP-seq data showing genome-wide occupancy of Brd2 and Brd4 at differentially bound sites in the triplicates.
(C) MAnorm was used for normalization and quantitative comparison of Brd2 and Brd4 ChIP-seq datasets. Each replicate is used for comparison and a MAplot is provided (upper panels). The Brd2 unique peaks, Brd4 unique peaks, and common peaks with statistical significance were shown in Venn diagrams (lower panels).
(D) ChIP-seq tracks showing selected gene loci occupanied with Brd2 binding, but not Brd4 in Th17 cells.

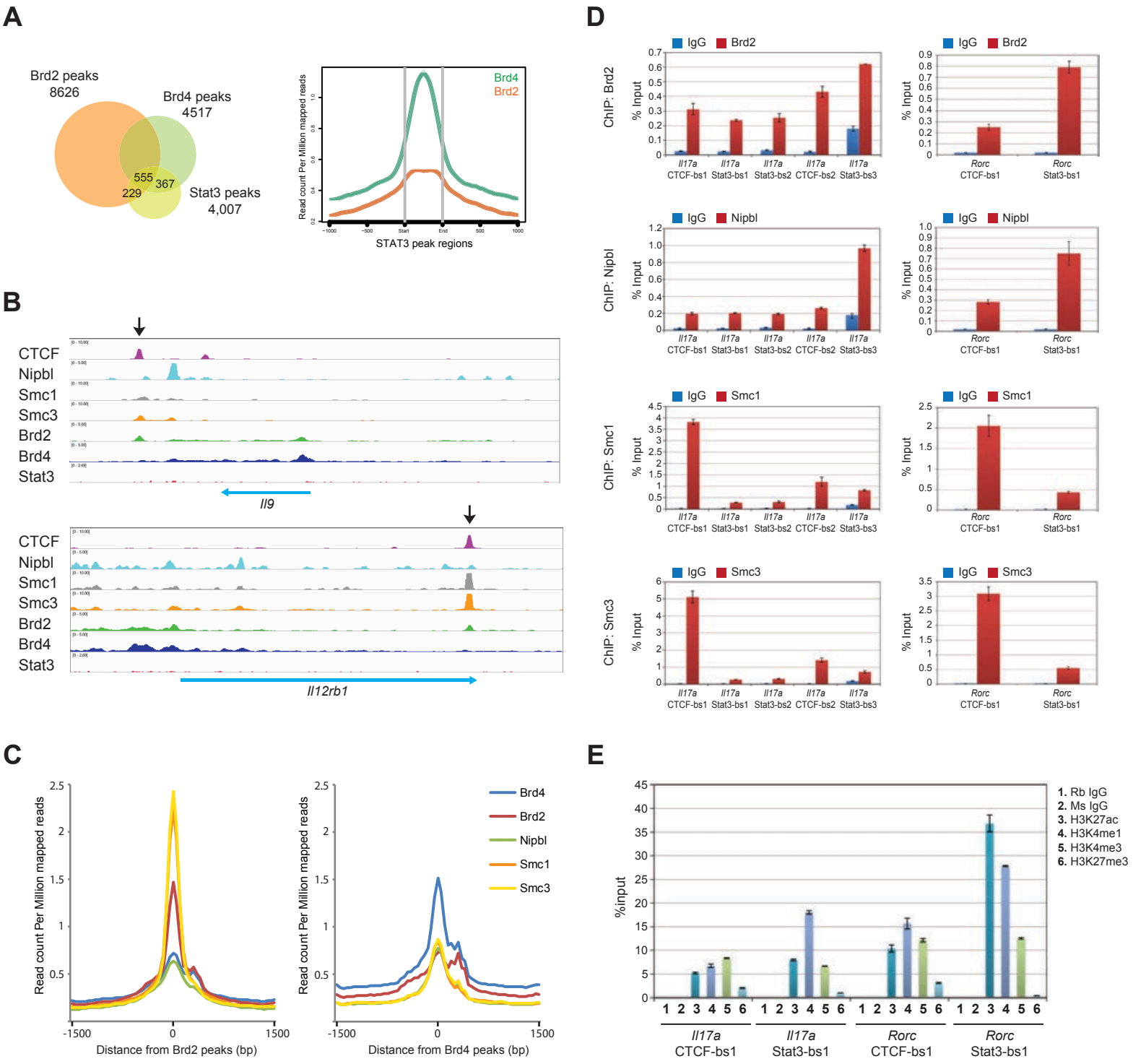

Figure S2. Brd2 , but not Brd4, is associated with CTCF/Cohesin complex in Th17 cells, related to Figure 2.
(A) Venn diagrams showing the number of overlapping peaks of Brd2, Brd4 and Stat3 (Left); and normalized Brd2 and Brd4 ChIP-signal centered around Stat3 peak regions (Right).
(B) ChIP-seq tracks of CTCF, Nipbl, Smc1, Smc3, Brd2, Brd4 and Stat3 on *Il9* and *Il12rb1* gene loci in Th17 cells.
(C) Normalized Brd2, Brd4, Nippbl, Smc1 and Smc3 ChIP-signal centered around Brd2 and Brd4 peak regions**.**
(D) ChIP-analysis showing occupancy of Brd2, and cohesin components (Nipbl, Smc1 and Smc3) at the CTCF and Stat3 binding sites in the *Il17a* and *Rorc*gene loci, respectively.
(E) ChIP analysis showing levels of hisotne modificaiotns including H3K27ac, H3K4me1, H3K4me3, and H3K27me3 at the CTCF and Stat3 binding sites along the *Il17a* and *Rorc*gene loci. The primer target sites are indicated in **Figure 2C**.

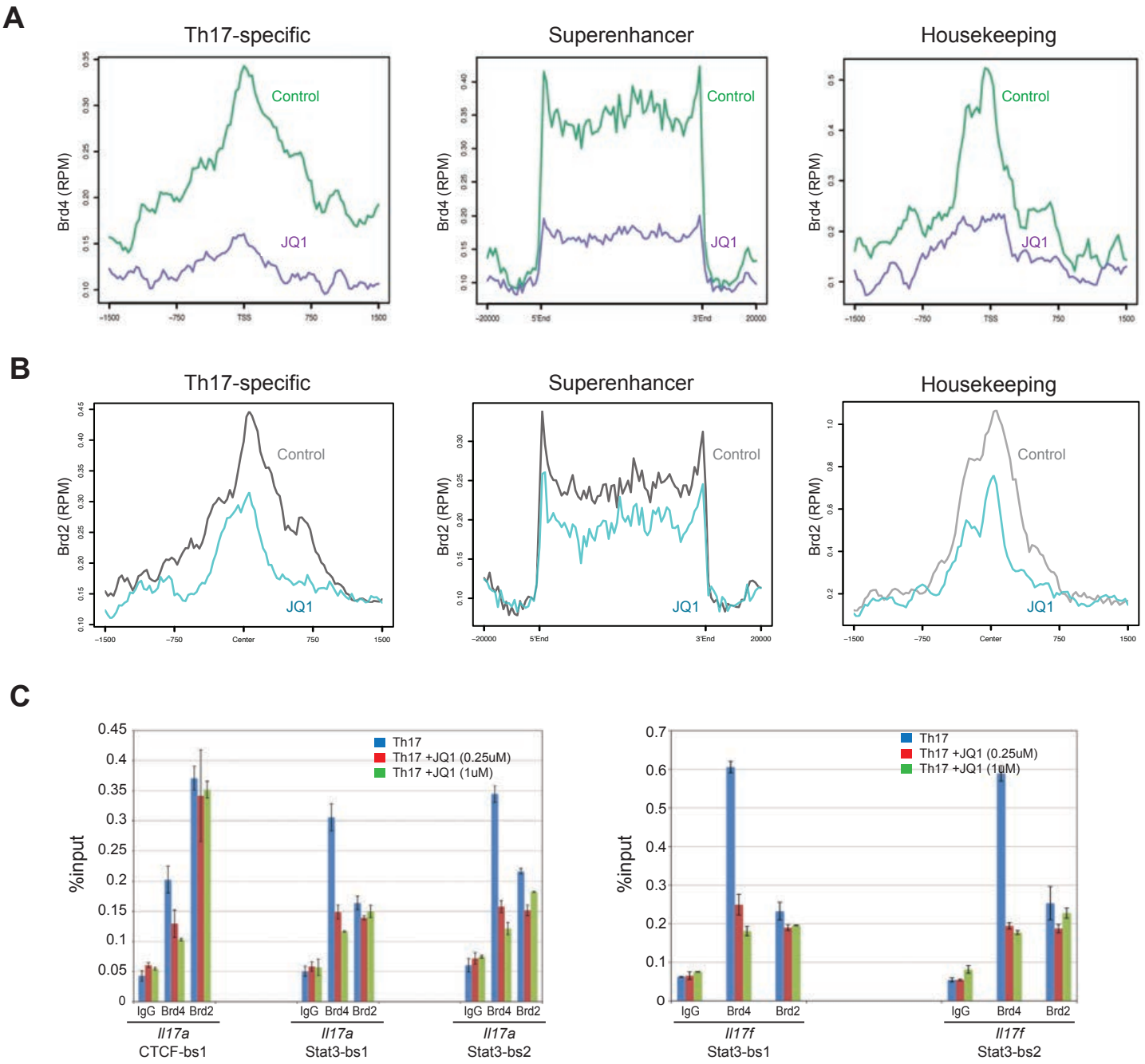

Figure S3. BET BrD inhibitor, JQ1 displaces global occupancy of Brd4, but not Brd2 on target gene loci in Th17 cells, related to Figure 3.

(A) Profiles of the ChIP-seq data showing patterns of perturbation of Brd4 occupancy across multiple gene sets of Th17 selective genes, genes with super enhancers, and housekeeping genes in Th17 cells after 2 hour-treatment of JQ1.

(B) Profiles of the ChIP-seq data showing patterns of perturbation of Brd2 occupancy across multiple gene sets of Th17 selective genes, genes with super enhancers, and housekeeping genes in Th17 cells after 2 hour-treatment of JQ1.

(C) ChIP-qPCR validation of Brd2 and Brd4 occupancy on *Il17a* and *Il17f* gene loci in Th17 cells after 2 hour-treatment of JQ1.

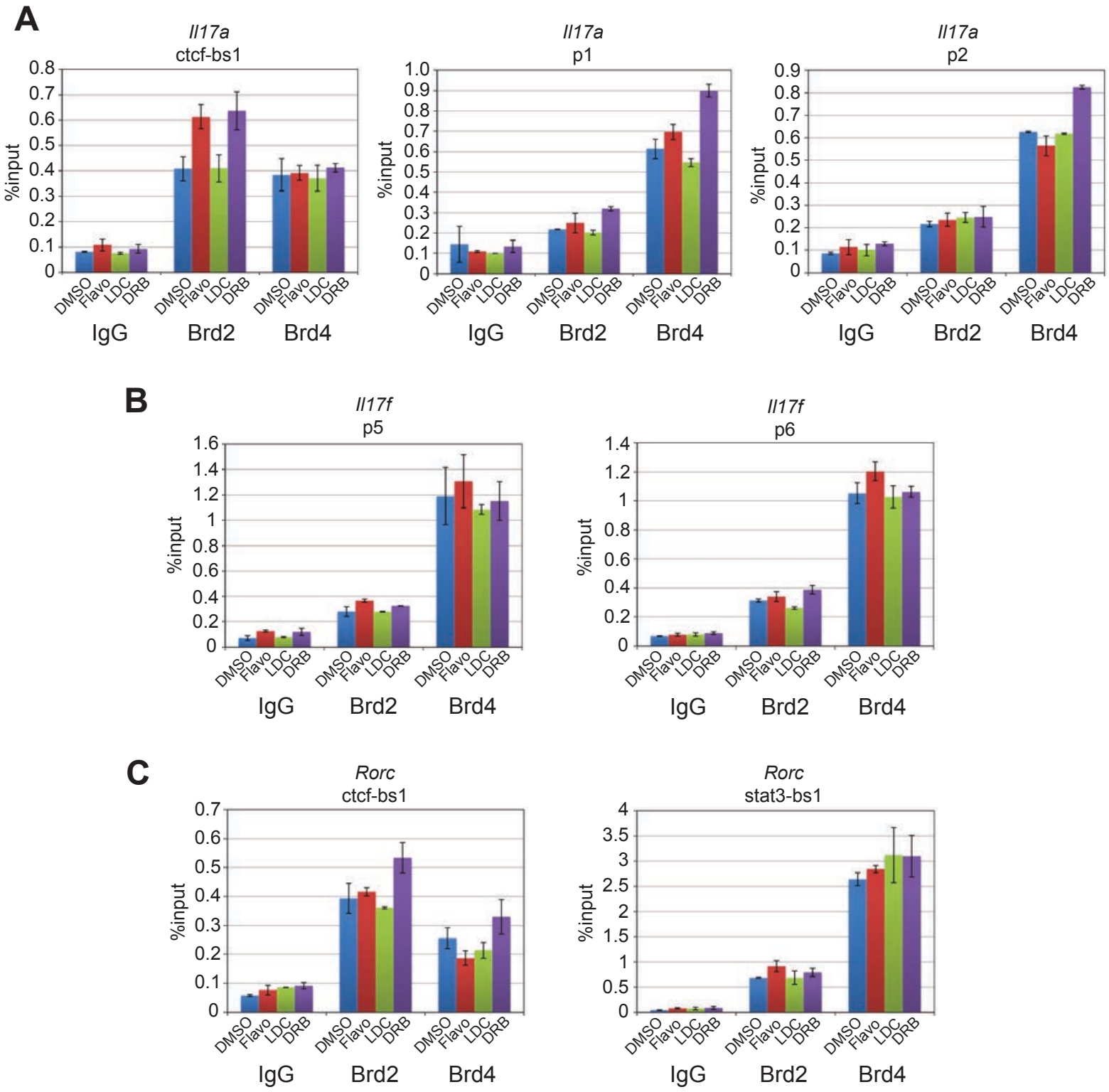

Figure S4. Effects of transcription elongation or processivity inhibition on occupancy of Brd2 and Brd4 at genomic loci of (A) *Il17a,* **(B)** *Il17f* **and (C)** *Rorc*, **as determined by ChIP-qPCR, related to Figure 4.**

Murine primary naïve CD4$^+$ T cells isolated from mouse spleen and lymph nodes, and differentiated under Th17 cell conditions for 48 hours, and then treated with CDK9 inhbitor flavopiridol (Flavo) or LDC00001 (LDC), or DRB (5,6-Dichlorobenzimidazole 1-β-D-ribofuranoside), a RNA PolII inhibitor, at 2.5 μM for 6 hours.

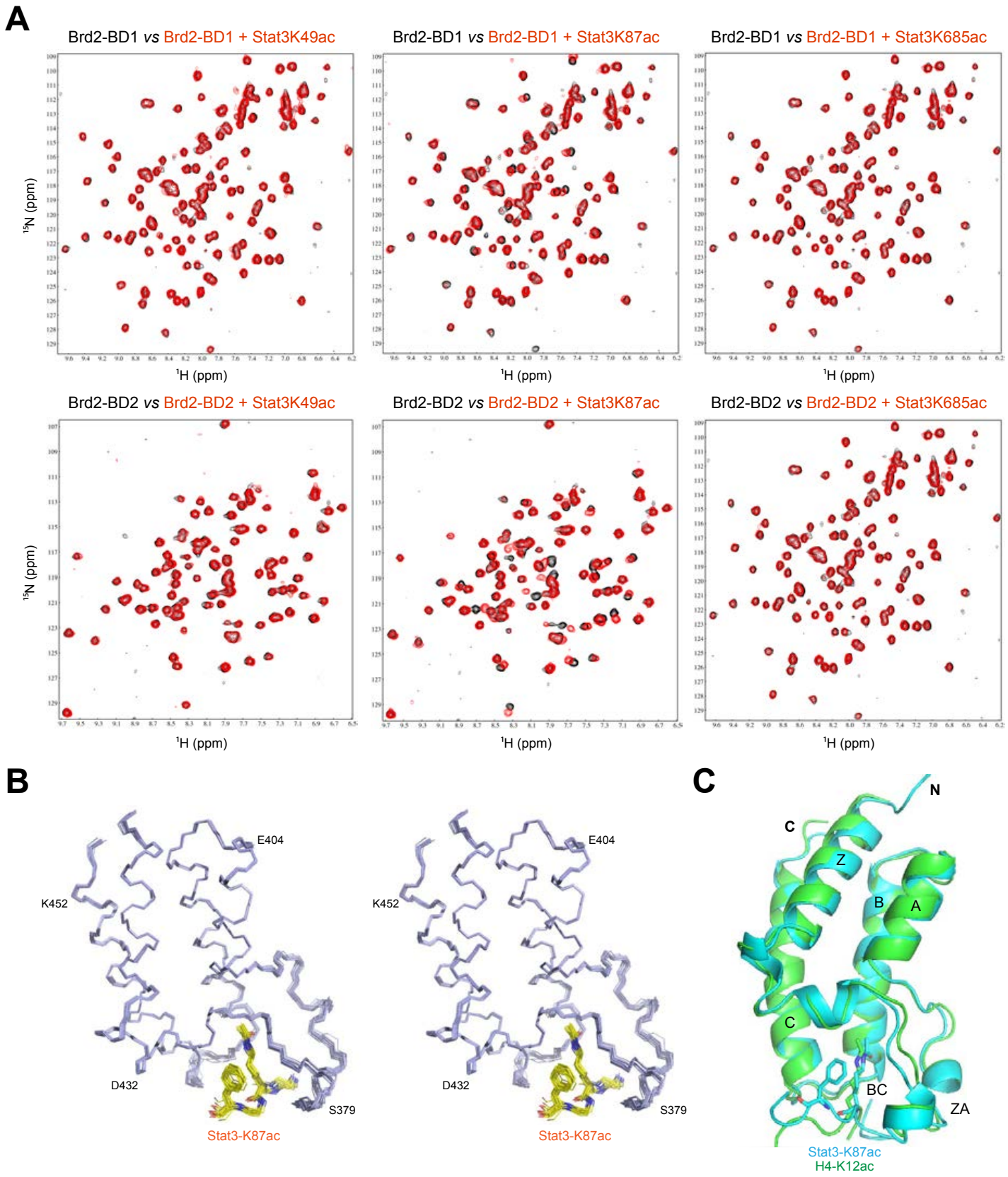

Figure S5. Assessing the molecular basis of Brd2/Stat3 interactions in Th17 cells, related to Figure 5.
(A) Comparison of 2D ^{1}H-^{15}N HSQC spectra of BD1 and BD2 of Brd2 collected in the PBS buffer of pH 7.5 at 298K in the free form (black) versus in the presence of Stat3 peptides containing K49ac (AYAAS-Kac-ESHAT, residues 44-54), K87ac (HNLL-RI-Kac-QFLQS, residues 71-82), or K685ac (PKEEAFG-Kac-YCPE, residues 678-690), respectively. The protein concentration was 0.2 mM and the molar ratio of the protein to peptide was kept at 1:5.
(B) The structure of the Brd2 BD2 in complex with a Stat3-K87ac peptide (residues 71-82) is shown as stereoview of the back-bone atoms (N, Cα and C') of 25 superimposed NMR structures of the complexes (left).
(C) Comparison of the structures of Brd2 BD2 bound to Stat3-K87ac (cyan) or histone H4-K12ac (green, PDB ID 2e3k) peptide.

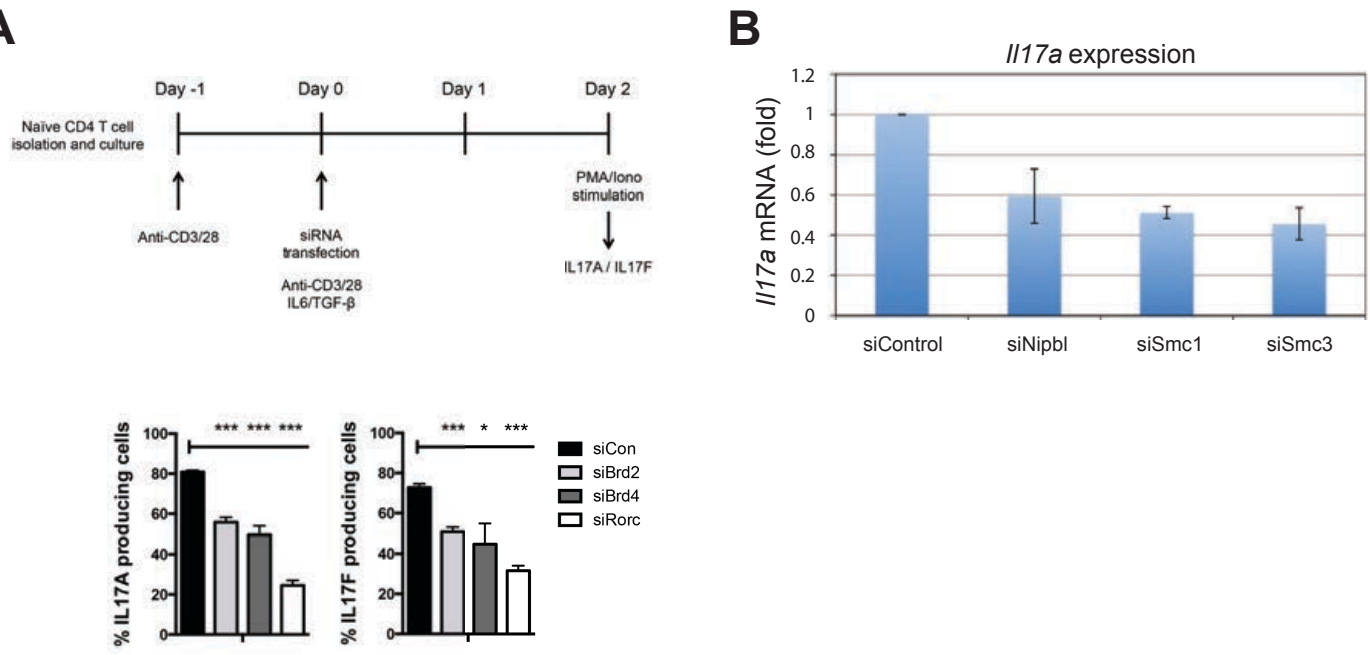

Figure S6. Analysis the roles of Brd2, Brd4, and cohesin component proteins in Il17a expression, as assessed by siRNA knockdown of *Brd2, Brd4, Rorc*, *Nipbl, Smc1* and *Smc3* individually**, related to Figure 6.**

(A) Upper right, Schematic representation of the experimental protocol. Naive $CD4^+$ T cells from wild-type mice were activated under non-polarizing (Th0: anti-CD3 and anti-CD28) condition. At 24 hours, siRNAs were transfected, and the transfected T cells were further cultured under Th0 or Th17 polarization (Th17: anti-CD3, anti-CD28, IL-6, and TGF-β) conditions for 48 hours. Cells were re-stimulated with PMA/Ionomycin for 3 hours, and cytokine production was monitored by FACS analysis. Upper left, knockdown of Brd2 and Brd4 reduced IL-17A/F production in in vitro polarized RORγ t^+ Th17 cells. Bar graphs show accumulated results from four biological replicates of two independent experiments as mean ± s.e.m., two-tailed t-test. *, $p<0.05$; ***,$p<0.001$. Lower right, representative FACS plot showing IL-17A/F production of in vitro polarized mouse Th0 and Th17 cells.

(B) qPCR analysis of the effects of *Nipbl, Smc1* or *Smc3* siRNA knockdown on Th17 cell differentiation, as assessed by the mRNA transcript level of *Il17a*.

Table S1, related to Figures 1, 2 - ChIP-seq analysis of Stat3, Brd2, Brd4 associated genes.

Table S2, related to Figures 1, 2 - ChIP-seq analysis of transcription factors associated genes.

Table S3, related to Figure 5 - Summary of statistics of the NMR structures of Brd2 BD2 in complex with the Stat3-K87ac peptide.

Table S4, related to Figures 1, 2, 6 - qPCR primers.

BET N-terminal bromodomain inhibition selectively blocks Th17 cell differentiation and ameliorates colitis in mice

Kalung Cheung[a,1], Geming Lu[b,c,1], Rajal Sharma[a], Adam Vincek[a], Ruihua Zhang[b,c], Alexander N. Plotnikov[a], Fan Zhang[a,b], Qiang Zhang[a,d], Ying Ju[d], Yuan Hu[b,c], Li Zhao[d], Xinye Han[d], Jamel Meslamani[a], Feihong Xu[b,c], Anbalagan Jaganathan[a], Tong Shen[a], Hongfa Zhu[e], Elena Rusinova[a], Lei Zeng[a,d], Jiachi Zhou[a], Jianjun Yang[b,c], Liang Peng[b,c], Michael Ohlmeyer[a], Martin J. Walsh[a,f], David Y. Zhang[e], Huabao Xiong[b,c,2], and Ming-Ming Zhou[a,2]

[a]Department of Pharmacological Sciences, Icahn School of Medicine at Mount Sinai, New York, NY 10029; [b]Department of Medicine, Icahn School of Medicine at Mount Sinai, New York, NY 10029; [c]Institute of Immunology, Icahn School of Medicine at Mount Sinai, New York, NY 10029; [d]Institute of Epigenetic Medicine, The First Hospital of Jilin University, Changchun 130061, China; [e]Department of Pathology, Icahn School of Medicine at Mount Sinai, New York, NY 10029; and [f]Department of Pediatrics, Icahn School of Medicine at Mount Sinai, New York, NY 10029

Edited by Dinshaw J. Patel, Memorial Sloan Kettering Cancer Center, New York, NY, and approved January 31, 2017 (received for review September 25, 2016)

T-helper 17 (Th17) cells have important functions in adaptor immunity and have also been implicated in inflammatory disorders. The bromodomain and extraterminal domain (BET) family proteins regulate gene transcription during lineage-specific differentiation of naïve CD4$^+$ T cells to produce mature T-helper cells. Inhibition of acetyl-lysine binding of the BET proteins by pan-BET bromodomain (BrD) inhibitors, such as JQ1, broadly affects differentiation of Th17, Th1, and Th2 cells that have distinct immune functions, thus limiting their therapeutic potential. Whether these BET proteins represent viable new epigenetic drug targets for inflammatory disorders has remained an unanswered question. In this study, we report that selective inhibition of the first bromodomain of BET proteins with our newly designed small molecule MS402 inhibits primarily Th17 cell differentiation with a little or almost no effect on Th1 or Th2 and Treg cells. MS402 preferentially renders Brd4 binding to Th17 signature gene loci over those of housekeeping genes and reduces Brd4 recruitment of p-TEFb to phosphorylate and activate RNA polymerase II for transcription elongation. We further show that MS402 prevents and ameliorates T-cell transfer-induced colitis in mice by blocking Th17 cell overdevelopment. Thus, selective pharmacological modulation of individual bromodomains likely represents a strategy for treatment of inflammatory bowel diseases.

Th17 cell differentiation | gene transcription | Brd4 | bromodomain | chemical inhibitor

CD4$^+$ T cells are important immune cells in biology and have been implicated in the pathology of autoimmune diseases and cancer (1–5). They develop in thymus to different T-helper (Th) cells to guide immune effector functions (6). The known Th effector subsets including Th1, Th2, Th17, and Treg produce signature genes and perform different immune functions (7, 8). Particularly, Th17 cells produce IL-17a and IL-17f and protect mucosa from bacterial and fungal infection (9, 10). Th17 cell development is linked to inflammatory disorders including multiple sclerosis, rheumatoid arthritis, and inflammatory bowel disease (11–13).

Lineage-specific differentiation of naïve CD4$^+$ T cells to Th17 cells is tightly controlled by gene transcription in chromatin (14–16)—a complex process that involves collective activities of key transcription factors Stat3, Batf, and Irf4, as well as Th17-specific orphan nuclear receptor RORγT (17–20). These transcription factors work with chromatin modifying enzymes and effector proteins to ensure proper timing, duration, and amplitude for ordered gene transcription in Th17 cell differentiation (15, 21). Of these are a family of bromodomain (BrD) and extraterminal domain (BET) proteins consisting of Brd2, Brd3, Brd4, and testis-specific Brdt (22, 23). BET proteins play a multifaceted role in gene transcription through their tandem bromodomains binding to lysine-acetylated histones and transcription factors during chromatin opening, transcription factor recruitment to target gene promoter and enhancer sites, and activation of paused RNA polymerase II (PolII) transcriptional machinery for productive gene activation (24, 25). Consistent with their role in T-helper-cell differentiation (26), inhibition of acetyl-lysine binding of the BET proteins by pan-BET BrD inhibitors, such as JQ1, affects differentiation of not only Th17 but also of Th1 and Th2 cells (27, 28). Because of such broad activities, unfortunately, pan-BET BrD inhibitors are thought to have limited therapeutic potential. Whether these BET proteins represent viable new epigenetic drug targets for inflammatory disorders has remained an unanswered question to this day.

Growing evidence shows that the two BrDs of BET proteins have distinct functions in gene transcription in that the second BrD (BD2) of Brd4 is dedicated to interaction with lysine-acetylated transcription factors and p-TEFb, whereas the first BrD (BD1) functions to anchor the activated Brd4/transcription protein

Significance

The bromodomain and extraterminal domain (BET) proteins regulate transcription of subset-specifying genes during lineage-specific T-helper-cell differentiation in adaptor immunity and are also implicated in inflammatory disorders. The available pan-BET bromodomain inhibitors such as JQ1 indiscriminately block the tandem bromodomains (BD1 and BD2) of the BET proteins, broadly render differentiation of different Th subsets, and have limited therapeutic potential. Here we report a small molecule, MS402, that can selectively inhibit BD1 over BD2 of the BET proteins and block Th17 maturation from mouse naive CD4$^+$ T cells, with limited or no effects on Th1, Th2, or Treg cells. MS402 effectively prevents and ameliorates T-cell transfer-induced colitis in mice by disrupting Th17 cell development, thus representing a therapeutic approach for inflammatory bowel diseases.

Author contributions: K.C., H.X., and M.-M.Z. designed research; K.C., G.L., R.S., A.V., R.Z., A.N.P., F.Z., Q.Z., Y.J., Y.H., L. Zhao, X.H., J.M., F.X., A.J., T.S., H.Z., E.R., L. Zeng, J.Z., J.Y., and L.P. performed research; D.Y.Z. contributed new reagents/analytic tools; K.C., G.L., R.S., A.V., R.Z., A.N.P., F.Z., Q.Z., Y.J., Y.H., L. Zhao, X.H., J.M., A.J., T.S., H.Z., E.R., L. Zeng, J.Z., J.Y., L.P., M.O., M.J.W., H.X., and M.-M.Z. analyzed data; and K.C., H.X., and M.-M.Z. wrote the paper.

The authors declare no conflict of interest.

This article is a PNAS Direct Submission.

Data deposition: Crystallography, atomic coordinates, and structure factors have been deposited in the Protein Data Bank, www.pdb.org (PDB ID code 5ULA). The ChIP-seq and RNA-seq data have been deposited in the Gene Expression Omnibus (GEO) database, www.ncbi.nlm.nih.gov/geo (accession nos. GSE90788 and GSE95052, respectively).

[1]K.C. and G.L. contributed equally to this work.

[2]To whom correspondence may be addressed. Email: huabao.xiong@mssm.edu or ming-ming.zhou@mssm.edu.

This article contains supporting information online at www.pnas.org/lookup/suppl/doi:10.1073/pnas.1615601114/-/DCSupplemental.

complex to target genes in chromatin through binding to lysine-acetylated histone H4 (26, 29). We sought to investigate how selective BET BrD inhibition modulates gene transcription in lineage-specific differentiation of different Th subsets. In this study, we have developed a BD1-selective BET BrD inhibitor, MS402, and showed that it can selectively render differentiation of Th17 cells over other Th cells from murine primary naïve $CD4^+$ T cells. We further demonstrated the therapeutic potential of MS402 in preventing and ameliorating adaptive T-cell transfer-induced colitis in mice through the disruption of Brd4 functions in gene transcription and Th17 cell development.

Results and Discussion

Given that the BD1 of the BET proteins is dedicated for binding to lysine-acetylated histone H4 for gene transcriptional activation (30), we reasoned that a small molecule that selectively targets the BD1 could effectively block BET functions in gene activation in chromatin. Using structure-guided design, we developed a cyclopentanone-based BrD inhibitor, MS402 (see its synthesis in Scheme S1), that displays nanomolar inhibitory activity against the BD1 (K_i of 77 nM) with a ninefold selectivity over BD2 of BRD4 (Fig. 1*A*). This selectivity is consistently seen with the BrDs of BRD2 or BRD3, albeit to a lesser extent (Fig. S1*A*). The BrD of CREB-binding protein (CBP) binds MS402 with K_i of 775 nM, 10-fold weaker than BRD4-BD1, and other representative BrDs from different subgroups of the BrD family including PCAF, SMARCA4, BPTF, and BAZ2B show very weak binding to MS402 with 50-fold or more less affinity than BRD4-BD1 (Fig. S1 *A* and *B*). MS402 is 200–300 times more potent than K5ac/K8ac-di-acetylated H4 peptide in binding to BRD4 BrDs (Fig. 1*A*).

Our 1.5-Å-resolution crystal structure of the BRD4 BD1 revealed that MS402 is bound across the ZA channel, establishing interactions with Val87, Leu92, and Leu94 on one side and Trp81, Pro82, Phe83, and Ile146 on the other (Fig. 1*B* and Table S1). The carbonyl oxygen of its cyclopentanone moiety forms two key hydrogen bonds, one with the side-chain amide of the conserved Asn140 and the other mediated by a bound water molecule to the phenoxyl group of Tyr97. In addition, this moiety makes van der Waals contacts with a gatekeeper residue Ile146. The amino group connecting cyclopentanone and chlorobenzene forms another hydrogen bond to the backbone carbonyl oxygen of Pro82 of the WPF shelf. Further, the amide nitrogen linking the two aromatic rings of MS402 forms a water-mediated hydrogen bond to the side-chain carbonyl oxygen of Gln85. The latter is unique in the BD1, corresponding to a Lys in the BD2 that is not engaged in hydrogen bond binding to MS402 as does Gln85 in BD1; point mutation of Gln85 to a Lys or Ala nearly abolished the preferred MS402 binding by BD1 over BD2 (Fig. S1 *B–D*). Further, change of Ile146 in BD1 to smaller Val439 in BD2 likely weakens van der Waals contacts between the protein and cyclopentanone, thus explaining MS402 selectivity for the BD1 over BD2 of BRD4.

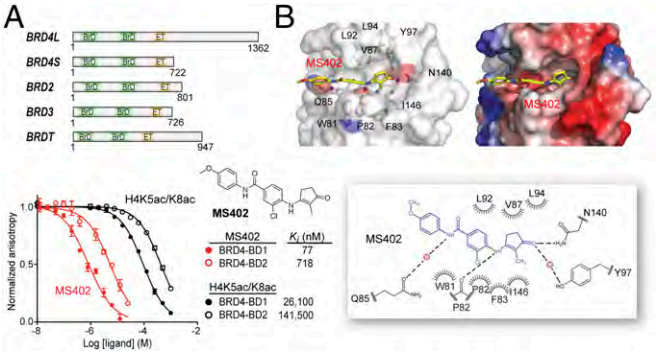

Fig. 1. Structure-guided development of MS402, a BD1-selective BET BrD inhibitor. (*A*) (*Upper*) Domain organization of mammalian BET family proteins. (*Lower*) Binding affinity of MS402 or an H4K5ac/K8ac peptide (residues 1–13) to the BrDs of BRD4 as measured in a fluorescence anisotropy binding assay using an FITC-labeled BrD inhibitor as a probe. (*B*) (*Left*) The crystal structure of MS402 (yellow) bound to the BRD4-BD1. (*Right*) Electrostatic potential surface representation of the BRD4-BD1/MS402 complex. Side chains of key residues at the ligand-binding site in the protein are shown, and bound water molecules are depicted as red spheres. (*Lower*) Schematic diagram highlights key interactions in MS402 recognition by the BRD4-BD1. Two key water molecules are shown in magenta spheres, and hydrogen bonds are drawn as dashed lines. The figure was generated using LIGPLOT (43).

To study the role of BET proteins in Th cell differentiation we isolated murine primary naïve $CD4^+$ T cells from mouse spleen and lymph nodes and treated them with IL-12, IL-4 plus α-IL-12, TGF-β plus IL-6, or TGF-β plus IL-2, respectively, to promote Th1, Th2, Th17, or Treg linage-specific differentiation over 3.5 d with or without MS402 added daily to cell culture (Fig. 2*A*). Strikingly, as shown by flow cytometry analysis, MS402, in a dose-dependent manner, inhibited IL-17 release from 18.6 to 8.0% in the Th17 polarizing condition and to a lesser extent IFN-γ production from 49.7 to 38.6% in the Th1 condition; it had little, if any, effect on IL-4 and Foxp3 expression during Th2 and Treg cell differentiation, respectively (Fig. 2*B*). MS402 did not affect T-cell proliferation as assessed in a carboxy-fluorescein succinimidyl ester dilution assay (Fig. S2*A*).

Notably, MS417, a potent pan-BET BrD inhibitor (K_i <10 nM) (26), and JQ1 (31) and I-BET762 (32) that share the diazepine scaffold, block broadly differentiation of murine primary naïve $CD4^+$ T cells to Th17, Th1, Th2, and, to a lesser extent, Treg cells under the conditions similar to those used for MS402 (Fig. 2*B* and Fig. S2 *B–D*). Our data agree with a report of suppression of Th17-mediated pathology by JQ1 (28). Further, a potent, selective CBP BrD inhibitor, CBP30 (K_d = 26 nM), was reported to suppress Th17 cell differentiation (33). Using the same condition, however, we found that CBP30 inhibits Th17 and also Th2 cell differentiation and has limited effects on Th1 or Treg cells (Fig. S2*E*). These results argue that MS402's modest activity on CBP BrD (K_i of 775 nM, 10-fold weaker than Brd4-BD1) likely does not contribute to its selective activity on Th17 cell differentiation, especially when used at submicromolar concentrations.

The selective activity of MS402 on inhibition of Th17 cell differentiation over Th1, Th2, or Treg cells is further supported by our observations that in a dose-dependent manner MS402 effectively inhibits transcriptional activation of *rorc* and *il17a* in Th17 cells, and to a lesser extent *tbx21* and *ifng* in Th1 cells, and it has only small effects on *gata3* and *il4* expression in Th2 cells, and almost no effects on *foxp3* and *il10* in Treg cells (Fig. 2*C*). These results contrast sharply to the much more broad effects of MS417 on the signature genes of Th17 and Th1 as well as Th2 cells (Fig. 2*C*). We confirmed the inhibitory effects of MS402 on additional key Th17 genes *il17f*, *il21*, *il23r*, *ahr*, *irf4*, and *il9* (Fig. S2*F*). We further observed that MS402 treatment resulted in a marked reduction of Brd4 and Cdk9 occupancy and RNA PolII Ser2 phosphorylation level at the Stat3 binding sites in *il17a/f* and *rorc* loci (Fig. S2*G*), which is required for transcription elongation (26). Notably, MS402 seems to have minimal effects on genomic occupancy of Brd2 (Fig. S2*G*). Further, MS402 inhibition is independent of IL-10 expression and does not involve IL-27 or IL-35, because it is still able to suppress Th17 and Th1 cell differentiation in $il10^{-/-}$ mice (Fig. S2*H*) and inhibit activation of *il-17a*, *il17*, *rorc*, *ifng*, and *T-bet* in $EBI3^{-/-}$ mice (Fig. S2*I*).

We next performed genomic sequencing analysis to better understand how MS402 and JQ1 affect gene transcription in Th17 cell differentiation. Specifically, we carried out chromatin immunoprecipitation sequencing (ChIP-seq) for Brd4 and RNA-seq experiments for mouse Th17 cells with and without MS402 or JQ1 treatment. Overall, MS402 and JQ1 treatments yielded a similar pattern of perturbation in gene transcription in Th17 cell differentiation (Fig. 3*A* and Fig. S3 *A–D*), albeit certain Th17 signature cytokine genes such as *il17a,f* and *il22* are perturbed slightly even more by MS402 than by JQ1 (Fig. 3*B*). Immune and cytokine ontologies seem consistently more enriched in the set of genes down-regulated by MS402 compared with JQ1 (Fig. 3*C*), whereas genes up-regulated are clustered in cell development and maturation

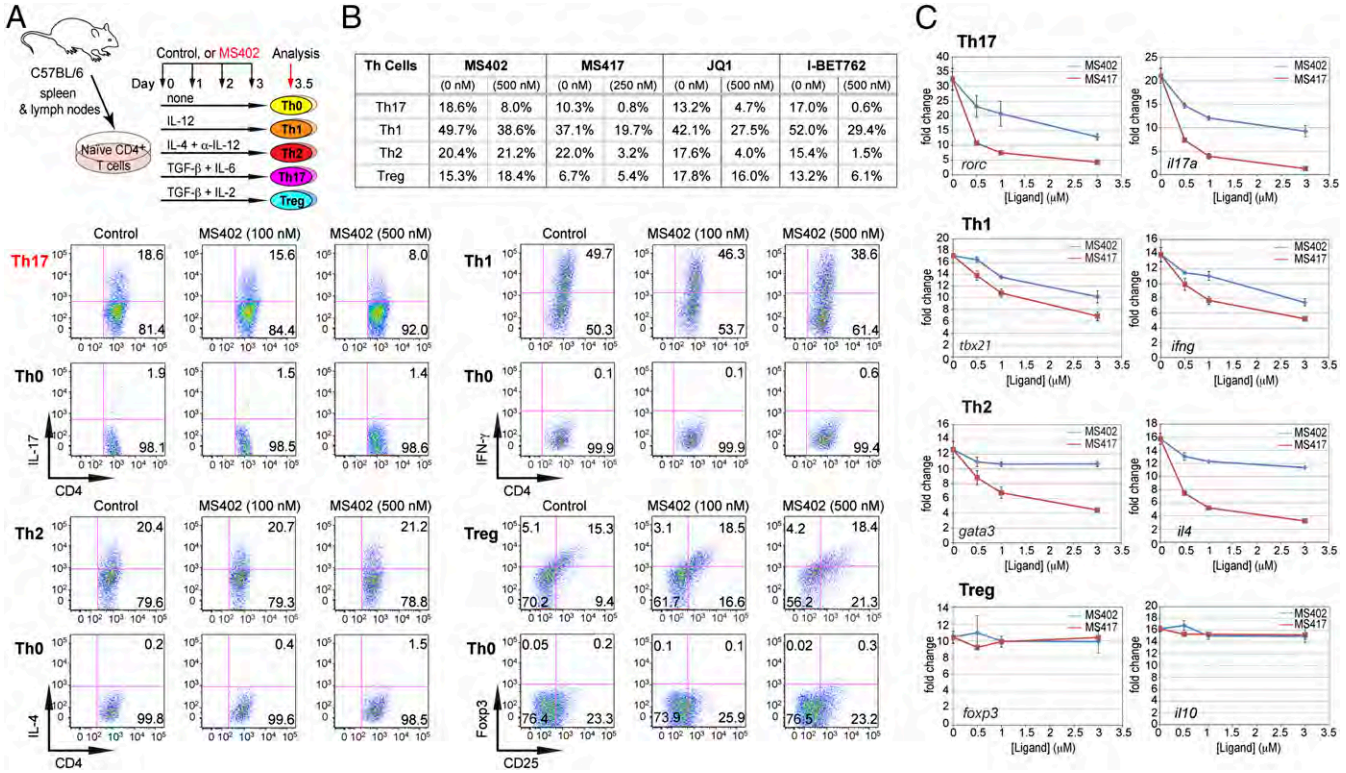

Th Cells	MS402		MS417		JQ1		I-BET762	
	(0 nM)	(500 nM)	(0 nM)	(250 nM)	(0 nM)	(500 nM)	(0 nM)	(500 nM)
Th17	18.6%	8.0%	10.3%	0.8%	13.2%	4.7%	17.0%	0.6%
Th1	49.7%	38.6%	37.1%	19.7%	42.1%	27.5%	52.0%	29.4%
Th2	20.4%	21.2%	22.0%	3.2%	17.6%	4.0%	15.4%	1.5%
Treg	15.3%	18.4%	6.7%	5.4%	17.8%	16.0%	13.2%	6.1%

Fig. 2. MS402, a bromodomain inhibitor, renders Th17 cell differentiation. (*A*) (*Upper*) A schematic illustration of the T-helper-cell differentiation study. (*Lower*) Flow cytometry analysis of mouse primary naïve CD4$^+$ T cells purified from spleens and lymph nodes of C57BL/6 mice and differentiated under Th0, Th1, Th2, Th17, and Treg polarization conditions with and without the presence of MS402 added daily at 100 nM or 500 nM. (*B*) Table summarizing the effects of MS402 or pan-BET BrD inhibitors including MS417, JQ1, and I-BET762 on T-helper-cell differentiation. (*C*) Effects of MS402 or MS417 treatment on mRNA expression levels of key Th17, Th1, Th2, or Treg subset-specific signature genes (transcription factors and cytokines) after 3-d lineage-specific cell differentiation from mouse primary naïve CD4$^+$ T cells in a dose-dependent manner.

(Fig. S3*E*). Further, Venn diagram analyses reveal that a majority of MS402-altered genes, with up or down transcriptional expression upon compound treatment, are covered by JQ1, but almost half of JQ1-affected genes are unchanged by MS402 (Fig. 3*D*). Notably, violin plot analysis of the RNA-seq data and comparison of the ChIP-seq data show that MS402 is effective similarly to JQ1 in releasing Brd4 genomic occupancy at Th17 signature genes and super enhancers but has fewer effects than JQ1 at housekeeping genes (Fig. 3*E* and Fig. S3 *F*–*H*). This apparently selective effect of MS402 over JQ1 is illustrated by representative RNA-seq tracks showing Th17 signature genes *Batf* and *Rorc* whose transcription is effectively down-regulated by MS402 or JQ1, whereas a housekeeping gene *Oxsm* is down-regulated by JQ1 but much less by MS402 (Fig. 3*F*). Given that MS402 exhibited cellular inhibitory effects on the order of its affinity for the BD1 of BET proteins, our results collectively suggest that pharmacological inhibition of the BD1 of BET proteins by MS402, likely blocking Brd4 activity required for Th17 signature gene transcriptional activation, is sufficient to render Th17 cell differentiation.

We next examined in vivo effects of MS402 in a T-cell transfer-induced colitis model in mice (Fig. 4*A*), in which Th17 cells are implicated in disease progression (11–13). After reconstitution with naïve CD4$^+$CD45RB^{hi} cells isolated from spleen and lymph nodes of C57BL/6 mice, *Rag1*$^{-/-}$ mice began losing weight after 4 wk, whereas the mice that received MS402 intraperitoneally twice a week at 10 mg/kg showed much less weight loss (Fig. 4*B*). Histology analysis revealed that 7 wk after reconstitution the colon of the T-cell transfer group mice was markedly shorter and inflamed compared with the control, whereas the colons of MS402-treated mice showed little difference in length or appearance (Fig. 4*C*). Notably, unlike the disease mice that exhibited severe inflammation at the end of the study with a disease score of 3, the MS402-treated mice displayed only mild or almost negative inflammation with a disease score of 0–1 (Fig. 4*D*). Histological study of colon sections from the disease mice confirmed more severe inflammatory cell infiltrates and significantly higher pathological scores than colons of those treated with MS402 (Fig. 4*E*). Finally, the MS402-treated mice showed a significantly lower percentage of IL-17- and IFN-γ–producing CD4$^+$ T cells in colon than the disease mice (Fig. 4*F*). Taken together, these results showed that MS402 is effective in vivo, blocking Th17 cell development required for T-cell transfer-induced colitis in mice.

We conducted another in vivo experimental colitis study to explore therapeutic potential of MS402. In this study we started MS402 treatment at week 5 when the *Rag1*$^{-/-}$ mice had developed colitis, as judged by marked weight loss, with i.p. injections twice a week at 10 mg/kg for 3 wk (Fig. 4*A*). Notably, the mice treated with MS402 exhibited a reversal of weight loss after 1 wk (Fig. 4*G*). Consistently, the MS402-treated mice showed an almost minimal degree of inflammation in the colon, as demonstrated by much improved colon length and appearance (Fig. S4*A*), a lower disease score of 0–1 (Fig. S4*B*), and markedly reduced inflammatory cell infiltrates in colon sections as compared with those of the disease-group mice (Fig. 4*H*). Further, the MS402-treated mice also had a lower population of IFN-γ–producing CD4$^+$ T cells and exhibited a much more dramatic reduction of IL-17–producing CD4$^+$ T cells in colon than the group of T-cell-transfer disease mice (Fig. 4*I*). It is worth noting that the selectivity of MS402 for Th17 over Th1 cells is more profound in this therapeutic treatment model than that in the preventive model (Fig. 4*I* vs. Fig. 4*F*). This differential effect seems to be consistent with the selectivity of MS402 on the maintenance of Th17 over Th1 cells compared with broad effects by pan-BET inhibitor JQ1 after these Th cells are differentiated ex vivo from the mouse primary naïve CD4$^+$ T cells (Fig. S4*C*). Finally, the

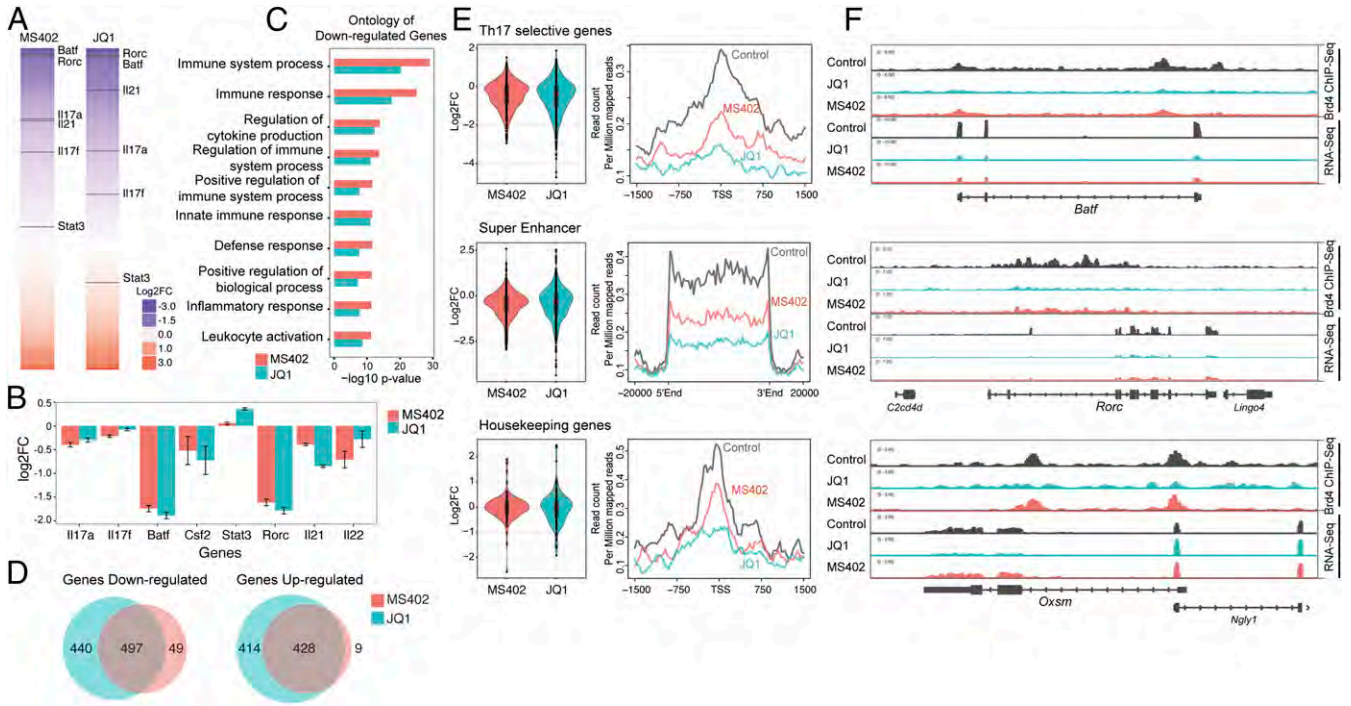

Fig. 3. Genomic analysis of BET inhibition effects on gene transcription during Th17 cell differentiation. (*A*) Effects of MS402 and JQ1 treatment on gene transcription in Th17 cell differentiation. Genes are ranked from most down-regulated to most up-regulated by compound treatment. Select Th17 signature genes whose transcriptional levels are affected by compound treatment are indicated. (*B*) MS402 and JQ1 show comparable (log2) fold change for select Th17 signature genes. (*C*) Immune and cytokine ontologies are among top-enriched down-regulated genes by MS402 or JQ1 treatment. (*D*) Venn diagram analysis of genes down- or up-regulated by MS402 and JQ1 treatment during Th17 differentiation. (*E*) Violin plots of the RNA-seq data and profiles of the ChIP-seq data showing patterns of perturbation across multiple gene sets of Th17 selective genes, genes with super enhancers, and housekeeping genes in Th17 cells upon treatment of MS402 or JQ1. (*F*) Select RNA-seq tracks illustrating changes of transcriptional expression of Brd4 target genes *Batf* and *Rorc* (Th17 selective genes) and Oxsm (housekeeping) upon the treatment of MS402 or JQ1.

MS402-treated mice had much lower mRNA expression levels of key cytokines and Th17- and Th1-specific transcription factors including *il17*, *il21*, *il22*, *il6*, *rorc*, *Tbet*, and *ifng* compared with the disease-group mice (Fig. 4*J*). Collectively, these results show that MS402 is an effective inhibitor of Th17 cell development and ameliorates adaptive T-cell transfer-induced colitis in mice.

Notably, it was recently reported that BET inhibition by JQ1 caused an increased progression of dextran sodium sulfate (DSS)-induced colitis in mice (34). Although the acute DSS colitis model is useful for study of the innate immune system in the development of intestinal inflammation, T and B cells are not required for the colitis development in this model (35). Nevertheless, these results highlight multifaceted functions of the BET proteins in adaptive and innate immunity and inflammatory pathology. Further investigation is warranted to determine the mechanistic details of the BET proteins in different functional contexts.

In summary, in this study we show that the BrDs of the BET proteins likely have distinct functions in gene transcription during differentiation of naïve $CD4^+$ T cells to different T-helper cells, and that the BD1 of Brd4 is central to Th17 cell differentiation and both BD1 and BD2 are important for Th1 and Th2 cell differentiation, whereas neither is essential for Treg cell differentiation. Notably, the BET proteins likely function differently in Th17 cells. Unlike Brd4, Brd2 genomic occupancy is minimally affected by BET inhibition, whereas as reported Brd3 has little expression in Th17 cells (28). Accordingly, our newly designed BD1-specific inhibitor MS402 is effective and sufficient to render Th17 cell differentiation likely through blocking Brd4 binding to Th17 signature gene loci whose transcriptional activation is required for Th17 cell differentiation. We further showed that selective chemical inhibition of the BD1 of Brd4 by MS402 can effectively prevent and ameliorate T-cell transfer-induced colitis in mice by blocking Th17, and to lesser extent Th1 cell development. Collectively, our study suggests a therapeutic strategy of selective targeting the BD1 of the BET proteins as a promising targeted therapy for inflammatory bowel diseases including colitis that lack a safe and effective treatment.

Materials and Methods

Methods and associated references are available in *SI Materials and Methods*.

Mice. C57BL/6 wild-type, *il10*$^{-/-}$, and *EBI3*$^{-/-}$ mice were obtained from Jackson Laboratory.

Compound. The chemical synthesis and characterization of MS402 is provided in Scheme S1 and Fig. S5.

Cell Sorting and T-Helper-Cell Differentiation. $CD4^+$ T cells were purified from mouse spleen and lymph nodes using anti-CD4 microbeads (Miltenyi Biotech). Naïve $CD4^+$ T cells were activated with plate-bound anti-CD3 (1.5 μM/mL) and anti-CD28 (1.5 μM/mL) plus cytokines IL-12 (20 ng/mL) and anti-IL4 (10 μM/mL) for Th1 conditions, IL4 (20 ng/mL), anti-IL12 (10 μM/mL), and anti–IFN-γ (10 μM/mL) for Th2 conditions, IL6 (20 ng/mL) and TGF-β (2.5 ng/mL) for Th17 conditions, and TGF-β (2.5 ng/mL) for Treg conditions. The cells were cultured for 2–3 d before harvesting for analysis. All cytokines were purchased from R&D, and neutralizing antibodies were purchased from BD Pharmigen.

Intracellular Staining and Flow Cytometry. Cells were stimulated with phorbol myristate acetate (PMA) and ionomycin for 5 h in the presence of brefeldin A before intracellular staining. Cells were fixed with IC Fixation Buffer (BD Biosciences), incubated with permeabilization buffer, and stained with PE-anti-mouse IL-17, APC-anti-IFN-γ, and PE-Cy 5.5 anti-mouse CD4 antibodies. Flow cytometry was performed on a FACSCalibur and BD LSR Fortessa (BD Biosciences).

Real-Time Quantitative PCR (qPCR). Total RNA was extracted with RNeasy Mini Kit (Qiagen) and reverse-transcribed using the SuperScript III Reverse Transcriptase (Life Technologies). All qPCR analyses were performed using Brilliant III Ultra Fast SYBR Green QPCR Master Mix (Agilent Technologies). In gene

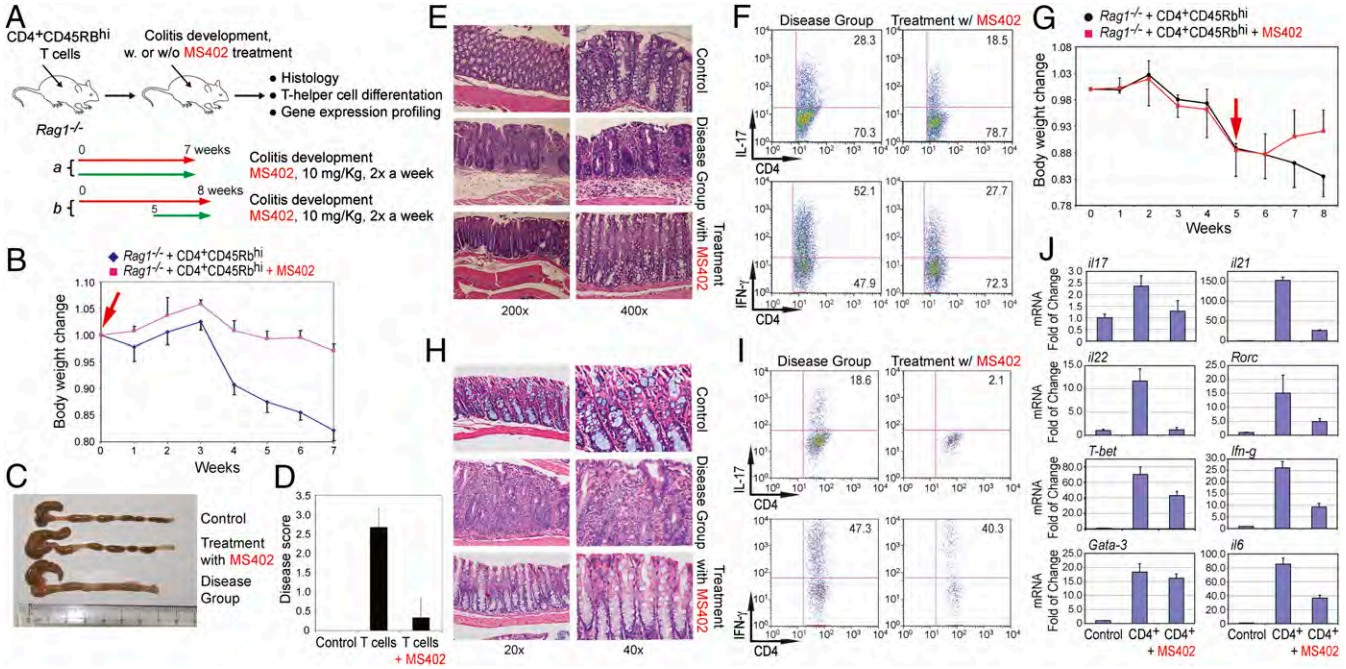

Fig. 4. MS402 ameliorates adaptive T-cell transfer-induced colitis in mice. (*A*) Scheme illustrating the experimental colitis study. $CD4^+CD45RB^{hi}$ T cells were purified from spleens and lymph nodes of wild-type or *iNOS*$^{-/-}$ mice and 5×10^5 cells were injected (i.p.) into recipient *Rag1*$^{-/-}$ mice. Mice were treated with PBS in a control group or MS402 (10 mg/kg) twice a week starting either at week 0 (*a*), or week 5 (*b*) for 7 or 3 wk, respectively. Body weight change was monitored weekly, and mice were killed at the end of experiment for histology analysis. (*B*) Changes in body weight of *Rag1*$^{-/-}$ mice ($n = 5$–6 mice per group) after i.p. transfer of wild-type $CD4^+CD45RB^{hi}$ T cells were recorded. MS402 treatment started at week 0 for 7 wk. Data are presented as the mean ± SD of the percentage of initial body weight and are representative of two similar experiments. (*C*) Changes of morphology of intestines of the *Rag1*$^{-/-}$ mice with and without MS402 treatment as in *B*. (*D*) Disease score assessing efficacy of MS402 treatment as in *B* on ameliorating inflammation of colitis in mice. The inflammation grading was graded on a scale of 0–3: negative (0), no inflammation; mild (1), mild and patchy; moderate (2), most crypts involved by inflammation; or severe (3), crypt abscess, ulceration, erosion, or submucosal involvement. The inflammation cells are most lymphocytes with some neutrophils. (*E*) Images showing H&E staining of large intestines of the *Rag1*$^{-/-}$ mice with or without MS402 treatment as in *B*. (*F*) Flow cytometry analysis of $CD4^+IL17^+$ and $CD4^+IFN\gamma^+$ T cells in large intestine from the *Rag1*$^{-/-}$ mice treated with or without MS402 treatment as in *B*. All results are statistically significant ($P < 0.05$) and are representative of more than two independent experiments. (*G*) Body weight change over time after $CD4^+$ T cells injected into recipient *Rag1*$^{-/-}$ mice with and without MS402 treatment, as indicated by a red arrow (i.e., started at week 5 until week 8). (*H*) Images showing H&E staining of large intestines of the *Rag1*$^{-/-}$ mice with or without MS402 treatment as in *G*. (*I*) Flow cytometry analysis of $CD4^+IL17^+$ and $CD4^+IFN\gamma^+$ T cells in large intestine from the *Rag1*$^{-/-}$ mice treated with or without MS402 starting at week 5 as in *G*. All results are statistically significant ($P < 0.05$) and are representative of more than two independent experiments. (*J*) mRNA levels of Th17 and Th1-specific genes measured in the *Rag1*$^{-/-}$ mice treated with or without MS402 starting at week 5 as in *G*.

expression analysis all data were normalized with Actin/Gapdh and represented relative to the control sample (fold change). For ChIP-qPCR relative occupancies were calculated as ratio of the amount of immunopreciptated DNA to that of the input sample (percent input). Measurements were performed in duplicate, and error bars denote experimental SDs. Results are representative of more than two independent experiments. Primer sequences are available in Table S2.

ELISA. All ELISA kits were purchased from eBioscience and experiments were performed according to protocols provided by the manufacturer. Briefly, supernatants of samples were incubated in plates coated with capture antibody. Detection antibody was added after a total of five washes. Avidin-HRP was then added after a total of five washes. Plates were read at 450 nm after addition of substrate solution and stop solution. Concentration of the cytokines in samples was calculated with reference to the absorbance value obtained from the standard curve.

ChIP. Cells were chemically cross-linked with 1% formaldehyde solution for 10 min at room temperature followed by the addition of 2.5 M glycine (to a final concentration of 125 mM) for 5 min. Cells were rinsed twice with cold 1× PBS and then lysed in Szak's RIPA buffer [150 mM NaCl, 1% Nonidet P-40, 0.5% deoxycholate, 0.1% SDS, 50 mM Tris·HCl, pH 8, 5 mM EDTA, Protease Inhibitor mixture (Roche), and 10 mM PMSF]. Cells were then sonicated using sonicator (QSonica) for 10 pulses of 15 s at a voltage of 70 V, followed by a 1-min rest on ice. Sonicated chromatin was cleared by centrifugation. The resulting chromatin extract was incubated overnight at 4 °C with appropriate primary antibody (anti-Brd4 or IHC-00396) and 25 μL of Protein G and 25 μL of Protein A magnetic beads (Dynabeads; Life Technologies). Beads were washed two times with incomplete Szak's RIPA buffer (without PMSF and Protease Inhibitor mixture), four times with Szak's IP Wash Buffer (100 mM Tris·HCl, pH 8.5, 500 mM LiCl, 1% Nonidet P-40, and 1% deoxycholate), then twice again with incomplete RIPA buffer and twice with cold 1× Tris-EDTA. Complexes were eluted from beads in Talianidis Elution Buffer by heating at 65 °C for 10 min and then by adding NaCl to a final concentration of 200 mM and reverse cross-linking was performed overnight at 65 °C. Input DNA was concurrently treated for cross-link reversal. Samples were then treated with RNaseA and proteinase K for an hour, extracted with phenol/chloroform, and ethanol-precipitated. The pellet was resuspended in water and used for subsequent ChIP-seq library preparation or analyzed by qPCR as described above.

T-Cell-Transfer Colitis Studies and Histopathology. T-cell-transfer colitis was performed as previously described (36, 37). Briefly, purified $CD4^+CD45RB^{hi}$ T cells from C57/B6 mice were injected i.p. into *Rag1*$^{-/-}$ recipients (5×10^5 cells per mouse in 200 μL sterile PBS per injection). Mice were weighed every week throughout the course of experiments. After 5–7 wk, mice were killed and colon tissues were excised. Tissues were fixed in 10% (vol/vol) buffered formalin and paraffin-embedded. The sections (5 μm) of tissue samples were stained with H&E. All of the slides were read and scored by an experienced pathologist without previous knowledge of the type of treatment. The degree of inflammation in the epithelium, submucosa, and muscularis propria was scored separately.

Sequencing Library Preparation and Sequencing. ChIPed-DNA was end-repaired with T4 DNA polymerase and polynucleotide kinase. An A-base was added to the end-repaired DNA fragments. Solexa adaptors were ligated to the DNA fragments and 200- to 300-bp size fractions were obtained using E-gel (Life Technologies). Adaptor-modified fragments were enriched by 18 cycles of PCR amplification. The DNA library prep was validated in Bioanalyzer for quantity and size. The input- and ChIPed-DNA libraries were sequenced on the Illumina

HiSeq2000 platform with 50-bp read length in a single end mode. RNA-seq libraries were prepared from TRIzol-extracted RNA samples from which rRNA was removed using Ribo-ZeroTM and following the TruSeq Stranded Total RNA Sample Prep kit protocol (Illumina). The input- and ChIP-DNA libraries were sequenced on the Illumina HiSEq. 2000 platform with 50-bp read length in a single end mode. Sequencing of RNA libraries was performed on the Illumina HiSEq. 2000 platform with 100-bp read length in a paired end mode. All ChIP-seq and RNA-seq data in this study are deposited in the Gene Expression Omnibus under the accession nos. GSE90788 and GSE95052, respectively.

Bioinformatics Analysis. For ChIP-seq analysis the input and ChIP samples were sequenced by Illumina HiSeq200. After QC filtering by FASTAX (hannonlab.cshl.edu/fastx_toolkit/), only the reads with a quality score Q20 in at least 90% bases were included for analysis. The reads from both input and ChIP samples were filtered and trimmed using Trimmomatic (38) and then aligned to mm9 reference genome using Bowtie. The peaks in the ChIP sample in reference to the input sample were called from read alignments by MACS algorithm (v1.4) and then the distance to the closest transcription start site (TSS) was annotated from genome mapping information of RefSeq transcripts. Genes associated with peaks were annotated (amp.pharm.mssm.edu/Enrichr/). Peaks were chosen with the criteria false discovery rate (FDR) <0.01 and P value <0.005. ChIP-seq from published work was taken from GSE60482 (Th17 p300) (15, 39). This was treated the same as in-house-generated ChIP-Seq. Finally, the alignment and coverage of ChIPseq data were visualized by Integrative Genomics Viewer (software.broadinstitute.org/software/igv/). Gene annotation and pathway analysis of the identified genes was performed using the Database for Annotation, Visualization and Integrated Discovery (https://david.ncifcrf.gov/). For RNA-Seq analysis the reads were filtered and trimmed using Trimmomatic (38) and aligned to the mm9 mouse reference genome and indexes based on UCSC annotations using TopHat (40). HTSeq (41) was used to find the read counts across the UCSC reference genome. Differentially expressed genes were identified by the R package DESeq2 (42) using an FDR <0.1 and fold change >1.5. RNA-Seq from Th1 and Th2 cells was taken from GSE40463. These data were analyzed in the same way as in-house-generated data. Heat maps were derived by sorting all genes with counts ≥5 by log-fold change for each compound treatment.

Statistical Analysis. Statistical analysis was performed using Student's t test. P values <0.05 were considered statistically significant.

Data Deposition. Structure factors and coordinates for the BRD4-BD1/MS402 complex have been deposited in the Protein Data Bank (PDB ID code 5ULA).

Study Approval. Mouse experiments were approved by the Institutional Animal Care and Use Committees of the Icahn School of Medicine at Mount Sinai.

ACKNOWLEDGMENTS. We thank Dr. J. Jakoncic and the staff at the X6A beamline of the National Synchrotron Light Sources at the Brookhaven National Laboratory for assisting with X-ray data collection. This work was supported in part by the research fund from the First Hospital of Jilin University, and the research grants from the National Natural Science Foundation of China (81601409) (to L. Zhao) and the US National Institutes of Health (to L. Zeng, M.J.W., H.X., and M.-M.Z.).

1. Iwasaki A, Medzhitov R (2015) Control of adaptive immunity by the innate immune system. *Nat Immunol* 16(4):343–353.
2. Tabas I, Glass CK (2013) Anti-inflammatory therapy in chronic disease: Challenges and opportunities. *Science* 339(6116):166–172.
3. Abraham C, Medzhitov R (2011) Interactions between the host innate immune system and microbes in inflammatory bowel disease. *Gastroenterology* 140(6):1729–1737.
4. Rubin DC, Shaker A, Levin MS (2012) Chronic intestinal inflammation: Inflammatory bowel disease and colitis-associated colon cancer. *Front Immunol* 3:107.
5. Saleh M, Trinchieri G (2011) Innate immune mechanisms of colitis and colitis-associated colorectal cancer. *Nat Rev Immunol* 11(1):9–20.
6. Takahama Y (2006) Journey through the thymus: Stromal guides for T-cell development and selection. *Nat Rev Immunol* 6(2):127–135.
7. Park H, et al. (2005) A distinct lineage of CD4 T cells regulates tissue inflammation by producing interleukin 17. *Nat Immunol* 6(11):1133–1141.
8. Harrington LE, et al. (2005) Interleukin 17-producing CD4+ effector T cells develop via a lineage distinct from the T helper type 1 and 2 lineages. *Nat Immunol* 6(11):1123–1132.
9. Murphy KM, Reiner SL (2002) The lineage decisions of helper T cells. *Nat Rev Immunol* 2(12):933–944.
10. Wilson CB, Rowell E, Sekimata M (2009) Epigenetic control of T-helper-cell differentiation. *Nat Rev Immunol* 9(2):91–105.
11. Miossec P, Kolls JK (2012) Targeting IL-17 and TH17 cells in chronic inflammation. *Nat Rev Drug Discov* 11(10):763–776.
12. Dong C (2008) TH17 cells in development: An updated view of their molecular identity and genetic programming. *Nat Rev Immunol* 8(5):337–348.
13. Littman DR, Rudensky AY (2010) Th17 and regulatory T cells in mediating and restraining inflammation. *Cell* 140(6):845–858.
14. Medzhitov R, Horng T (2009) Transcriptional control of the inflammatory response. *Nat Rev Immunol* 9(10):692–703.
15. Ciofani M, et al. (2012) A validated regulatory network for Th17 cell specification. *Cell* 151(2):289–303.
16. Kanno Y, Vahedi G, Hirahara K, Singleton K, O'Shea JJ (2012) Transcriptional and epigenetic control of T helper cell specification: Molecular mechanisms underlying commitment and plasticity. *Annu Rev Immunol* 30:707–731.
17. Yang XO, et al. (2007) STAT3 regulates cytokine-mediated generation of inflammatory helper T cells. *J Biol Chem* 282(13):9358–9363.
18. Schraml BU, et al. (2009) The AP-1 transcription factor Batf controls T(H)17 differentiation. *Nature* 460(7253):405–409.
19. Brüstle A, et al. (2007) The development of inflammatory T(H)-17 cells requires interferon-regulatory factor 4. *Nat Immunol* 8(9):958–966.
20. Okamoto K, et al. (2010) IkappaBzeta regulates T(H)17 development by cooperating with ROR nuclear receptors. *Nature* 464(7293):1381–1385.
21. Yosef N, et al. (2013) Dynamic regulatory network controlling TH17 cell differentiation. *Nature* 496(7446):461–468.
22. Dhalluin C, et al. (1999) Structure and ligand of a histone acetyltransferase bromodomain. *Nature* 399(6735):491–496.
23. Smith SG, Zhou MM (2016) The bromodomain: A new target in emerging epigenetic medicine. *ACS Chem Biol* 11(3):598–608.
24. Hargreaves DC, Horng T, Medzhitov R (2009) Control of inducible gene expression by signal-dependent transcriptional elongation. *Cell* 138(1):129–145.
25. Hnisz D, et al. (2013) Super-enhancers in the control of cell identity and disease. *Cell* 155(4):934–947.
26. Zhang W, et al. (2012) Bromodomain-containing protein 4 (BRD4) regulates RNA polymerase II serine 2 phosphorylation in human CD4+ T cells. *J Biol Chem* 287(51):43137–43155.
27. Bandukwala HS, et al. (2012) Selective inhibition of CD4+ T-cell cytokine production and autoimmunity by BET protein and c-Myc inhibitors. *Proc Natl Acad Sci USA* 109(36):14532–14537.
28. Mele DA, et al. (2013) BET bromodomain inhibition suppresses TH17-mediated pathology. *J Exp Med* 210(11):2181–2190.
29. Schröder S, et al. (2012) Two-pronged binding with bromodomain-containing protein 4 liberates positive transcription elongation factor b from inactive ribonucleoprotein complexes. *J Biol Chem* 287(2):1090–1099.
30. Sanchez R, Zhou MM (2009) The role of human bromodomains in chromatin biology and gene transcription. *Curr Opin Drug Discov Devel* 12(5):659–665.
31. Filippakopoulos P, et al. (2010) Selective inhibition of BET bromodomains. *Nature* 468(7327):1067–1073.
32. Nicodeme E, et al. (2010) Suppression of inflammation by a synthetic histone mimic. *Nature* 468(7327):1119–1123.
33. Hammitzsch A, et al. (2015) CBP30, a selective CBP/p300 bromodomain inhibitor, suppresses human Th17 responses. *Proc Natl Acad Sci USA* 112(34):10768–10773.
34. Wienerroither S, et al. (2014) Regulation of NO synthesis, local inflammation, and innate immunity to pathogens by BET family proteins. *Mol Cell Biol* 34(3):415–427.
35. Chassaing B, Aitken JD, Malleshappa M, Vijay-Kumar M (2014) Dextran sulfate sodium (DSS)-induced colitis in mice. *Curr Protoc Immunol* 104(Unit 15):25.
36. Totsuka T, et al. (2007) IL-7 Is essential for the development and the persistence of chronic colitis. *J Immunol* 178(8):4737–4748.
37. Powrie F, Leach MW, Mauze S, Caddle LB, Coffman RL (1993) Phenotypically distinct subsets of CD4+ T cells induce or protect from chronic intestinal inflammation in C. B-17 scid mice. *Int Immunol* 5(11):1461–1471.
38. Bolger AM, Lohse M, Usadel B (2014) Trimmomatic: A flexible trimmer for Illumina sequence data. *Bioinformatics* 30(15):2114–2120.
39. Wei L, et al. (2010) Discrete roles of STAT4 and STAT6 transcription factors in tuning epigenetic modifications and transcription during T helper cell differentiation. *Immunity* 32(6):840–851.
40. Trapnell C, Pachter L, Salzberg SL (2009) TopHat: Discovering splice junctions with RNA-Seq. *Bioinformatics* 25(9):1105–1111.
41. Anders S, Pyl PT, Huber W (2015) HTSeq–a Python framework to work with high-throughput sequencing data. *Bioinformatics* 31(2):166–169.
42. Love MI, Huber W, Anders S (2014) Moderated estimation of fold change and dispersion for RNA-seq data with DESeq2. *Genome Biol* 15(12):550.
43. Wallace AC, Laskowski RA, Thornton JM (1995) LIGPLOT: A program to generate schematic diagrams of protein-ligand interactions. *Protein Eng* 8(2):127–134.
44. Zeng L, Zhang Q, Gerona-Navarro G, Moshkina N, Zhou MM (2008) Structural basis of site-specific histone recognition by the bromodomains of human coactivators PCAF and CBP/p300. *Structure* 16(4):643–652.
45. Zhang G, et al. (2012) Down-regulation of NF-κB transcriptional activity in HIV-associated kidney disease by BRD4 inhibition. *J Biol Chem* 287(34):28840–28851.
46. Nikolovska-Coleska Z, et al. (2004) Development and optimization of a binding assay for the XIAP BIR3 domain using fluorescence polarization. *Anal Biochem* 332(2):261–273.
47. Huynh K, Partch CL (2015) Analysis of protein stability and ligand interactions by thermal shift assay. *Curr Protoc Protein Sci* 79:28.9.1–14.
48. Otwinowski Z, Minor W (1997) [20] Processing of X-ray diffraction data collected in oscillation mode. *Methods Enzymol* 276:307–326.
49. Vagin A, Teplyakov A (1997) MOLREP: An automated program for molecular replacement. *J Appl Cryst* 30(6):1022–1025.
50. Murshudov GN, Vagin AA, Dodson EJ (1997) Refinement of macromolecular structures by the maximum-likelihood method. *Acta Crystallogr D Biol Crystallogr* 53(Pt 3):240–255.
51. Emsley P, Cowtan K (2004) Coot: Model-building tools for molecular graphics. *Acta Crystallogr D Biol Crystallogr* 60(Pt 12 Pt 1):2126–2132.

Supporting Information

Cheung et al. 10.1073/pnas.1615601114

SI Materials and Methods

Protein Preparation. Expression and purification of the recombinant human bromodomains of BAZ2B, BPTF, BRD4, BRD7, PCAF, and SMARCA4 in poly-His-tag form were carried out using a previously described procedure (44, 45). Isotope-labeled protein samples of the BrDs were prepared from HeLa cells grown in a minimal medium containing $^{15}NH_4Cl$ with or without $^{13}C_6$-glucose in either H_2O or 75% ^2H_2O. The protein was purified by affinity chromatography on a nickel-IDA column (Life Technolgies), followed by the removal of poly-His tag by thrombin cleavage.

Fluorescence Anisotropy Binding Assay. Binding affinity of MS402 for various human BrDs was assessed in a fluorescence anisotropy competition assay using an FITC-labeled MS417 as an assay probe as described previously (45). Competition experiments were performed with a BrD protein (0.25–1 μM) and the fluorescent probe (80 nM) and increasing concentration of unlabeled competing ligand in a PBS buffer (pH 7.4) in total volume of 80 μL. Measurements were obtained after a 1-h incubation of the fluorescent ligand and the protein at 25 °C with a Safire 2 microplate reader (Tecan). In a competition-binding assay, fluorescent ligand concentration was $\leq 2\ K_d$, and protein concentration was set at which 50–80% of fluorescent ligand is bound. The dissociation constant of a competing ligand was calculated with the correction to the Cheng–Prussoff equation introduced by Nicolovska-Coleska et al. (46). Assuming one-site competitive binding model, the equation used to calculate K_i's from IC_{50} values recovered from fitting data using Prism is

$$K_i = \frac{[I_{50}]}{\left(\frac{[L_{50}]}{K_d} + \frac{[P_0]}{K_d} + 1\right)},$$

where $[I_{50}]$ is the concentration of free inhibitor at 50% inhibition, $[L_{50}]$ is the concentration of free labeled ligand at 50% inhibition, and $[P_0]$ is the concentration of free protein at 0% inhibition. Note that K_d for each protein–probe pair is the limit of resolvable K_i in a competition assay.

Thermal Shift Assay Assessing Protein/Ligand Binding. Thermal melting experiments were carried out using a reported procedure (47) in an Mx3005p Realtime PCR machine (Agilent). The protein sample (10 μM) was mixed with MS402 (10 μM) in 20 μL of Hepes buffer (10 mM) of pH 7.5 containing 500 μM NaCl, and the assay was carried out in a 96-well plate. SYPRO Orange (Sigma Aldrich) was added as fluorescence probe at a dilution of 1:1,000. Excitation and emission filters for SYPRO Orange dye were set to 465 nM and 590 nM, respectively. The temperature was raised with a step of 3 °C/min from 25 °C to 95 °C and a fluorescence reading was taken at each interval. The fluorescent data were fitted to a Boltzmann sigmoidal equation (47) using Prism: y = bottom + (top − bottom)/[1 + exp($T_m - x$/slope)], where y is fluorescence emission in arbitrary units, x is temperature, bottom is baseline fluorescence at low temperature, top is maximal fluorescence at the top of the dataset, slope describes the steepness of the curve, and T_m is the melting temperature of the protein. The observed temperature shifts, ΔT_m, were recorded as T_m difference without or with MS402 in the protein sample.

Protein Crystallization and X-Ray Diffraction Data Collection. Purified BRD4-BD1 (16 mg/mL) was mixed with MS402 at 1:5 molar ratio of protein:ligand. The complex was crystallized using the sitting drop vapor diffusion method at 20 °C by mixing 1 μL of protein solution with 1 μL of the reservoir solution that contains 4.3 M of sodium chloride and Hepes-NaOH, pH 7.5. Crystals were soaked in the corresponding mother liquor supplemented with 20% ethylene glycerol as cryoprotectant before freezing in liquid nitrogen. X-ray diffraction data were collected at 100 K at beamline X6A of the National Synchrotron Light Source at Brookhaven National Laboratory. Data were processed using the HKL-2000 suite (48). The BRD4-BD1 structure was solved by molecular replacement using the program MOLREP (49), and the structure refinement was done using the program Refmac (50). The graphics program Coot (51) was used for model building and visualization. Crystal diffraction data and refinement statistics for the structure are displayed in Table S1.

Chemical Synthesis. All reactions were carried out in oven-dried glassware under an atmosphere of argon. Liquid chromatography mass spectra (LCMS) analysis was conducted from a computer running Agilent Technologies MassHunter A02.02 software interfaced to a 1200 HPLC system and G1969A high-resolution atmospheric pressure interface time-of-flight mass spectrometer. HPLC conditions are as follows: Zorbax 300SB-C18 narrow-bore column (2.1 × 150 mm, 5 μm), held constant at 45 °C; flow rate = 0.4 mL/min; solvent (A) = H_2O:acetonitrile (9:1) containing formic acid (0.1%); solvent (B) = H_2O:acetonitrile (1:9) containing formic acid (0.1%); solvent B % (time) = 1% (0–1 min), 1–99% (1–4 min), 99% (4–8 min). Sample ionization: Electrospray ionization, positive mode; gas temperature = 350 °C; drying gas = 11.0 L/min; nebulizer = 45 psig; capillary = 4.0 kV. Mass spectra data processing was conducted using Analyst QS 1.1 software. Theoretical mass to charge ratios were calculated using ChemDraw software. In relevant cases identifiable, radical cation of mass plus hydrogen, $[M+H]^+$; mass plus sodium, $[M+Na]^+$; two masses plus hydrogen, $[2M+H]^+$; and two masses plus sodium, $[2M+Na]^+$ data were recorded. Proton (^1H) and carbon (^{13}C) NMR spectra were acquired on a Bruker DRX-600 spectrometer at 600 and 125 MHz, respectively. Chemical shifts were expressed in parts per million downfield from tetramethylsilane (TMS 0.03%, ^1H = 0 ppm), or the solvent resonance as an internal standard D6-DMSO (^{13}C = 39.5 ppm). Signals were reported as chemical shift [multiplicity (s, singlet; d, doublet; m, multiplet; and br, broad), coupling constant, integration]. The high-resolution mass spectrometer (HRMS) result was obtained from the Mass Spectrometer Core Facility at Columbia University using a HX-110 double-focusing high-resolution mass spectrometer (JEOL Ltd.) with 10-kV acceleration voltage, fast atom bombardment ionization Xe, and 3-kV collision energy.

The synthesis of **5** (MS402) [3-chloro-*N*-(4-methoxyphenyl)-4-((2-methyl-3-oxocyclopent-1-en-1-yl)amino)benzamide] was carried out by following the reaction steps outlined in Scheme S1.

Synthesis of 3-Chloro-4-Formamidobenzoic Acid (2). Formic acid (18.1 mL, 40 eq) and acetic anhydride (11.3 mL, 10 eq) were mixed and heated to 50 °C for 1 h. Then 4-amino-3-chlorobenzoic acid (**1**, 2.06 g, 12.0 mmol, 1 eq) was added and the whole was heated to 65 °C for 2 h. The reaction mixture was allowed to cool to room temperature and then poured into ice-cold H_2O. The precipitate was collected by filtration, washed with H_2O, and dried on the frit. This method yielded 2.2 g (92% yield) of white microcrystals from precipitate.

Melting point (m.p.): 227–229 °C; ^1H-NMR (600 MHz, d_6-DMSO) δ 13.19 ppm (s, 1H), 10.15 (d, J = 2.1 Hz, 1H), 8.43 (d, J = 0.6 Hz,

1H), 8.38 (d, J = 8.6 Hz, 1H), 7.96–7.97 (m, 1H), 7.90 (dd, J = 8.5, 1.4 Hz, 1H); ^{13}C-NMR (125 MHz, d_6-DMSO) δ 166.2, 161.3, 138.6, 130.7, 129.4, 127.5, 122.8, 122.0; LCMS t = 3.0 min, (m/z): $[M+H]^+$ calculated for $C_8H_7ClNO_3$, 200.0114; found, 200.0115; $[2M+H]^+$ calculated for $C_{16}H_{13}Cl_2N_2O_6$, 399.0151; found, 399.0149; $[2M+Na]^+$ calculated for $C_{16}H_{12}Cl_2N_2NaO_6$, 420.9970; found, 420.9963.

Synthesis of 3-Chloro-4-Formamido-*N*-(4-Methoxyphenyl)Benzamide (3). *N*-methylmorpholine (0.95 mL, 1.2 eq) and isobutylchloroformate (1.12 mL, 1.2 eq) were added to **2** (1.44 g, 7.2 mmol) stirring in CH_2Cl_2 (30 mL), in a screw-capped vial. After stirring for 30 min, *p*-anisidine (1.06 g, 1.2 eq) and a second aliquot of *N*-methylmorpholine (0.95 mL) were added. The vial was sealed and stirred at room temperature for 18 h. The precipitate was filtered and rinsed with CH_2Cl_2, H_2O and diethyl ether. The method yielded 1.75 g (80% yield) of white microcrystals from precipitate.

m.p.: 238–240 °C; ^{1}H-NMR (600 MHz, d_6-DMSO) δ 10.16 ppm (s, 1H), 10.11 (s, 1H), 8.43 (s, 1H), 8.34 (d, J = 8.4 Hz, 1H), 8.11 (s, 1H), 7.93 (d, J = 8.4 Hz, 1H), 7.66 (d, J = 8.7 Hz, 2H), 6.93 (d, J = 8.8 Hz, 2H), 3.75 (s, 3H); ^{13}C-NMR (125 MHz, d_6-DMSO) δ 163.5, 161.2, 156.0.5, 137.4, 132.4, 131.6, 129.1, 127.7, 123.0, 122.5 (2C), 122.1, 114.2 (2C), 55.6; LCMS t = 4.0 min, (m/z): $[M+H]^+$ calculated for $C_{15}H_{14}ClN_2O_3$, 305.0693; found, 305.0690; $[M+Na]^+$ calculated for $C_{15}H_{13}ClN_2NaO_3$, 327.0512; found 327.0498; $[2M+H]^+$ calculated for $C_{30}H_{27}Cl_2N_4O_6$, 609.1308; found, 609.1304; $[2M+Na]^+$ calculated for $C_{30}H_{26}Cl_2N_4NaO_6$, 631.1127; found, 631.1133.

Synthesis of 4-Amino-3-Chloro-*N*-(4-Methoxyphenyl)Benzamide (4). Acetyl chloride (10.9 mL, 14 eq) was added to a CH_2Cl_2:MeOH (50 mL, 1:1) mixture at 0 °C, followed by **3** (3.35 g, 11.0 mmol). After warming to room temperature, the hydrochloride salt was collected by filtration and dried on the frit. Method yielded 2.77 g of white microcrystals (80% yield) from precipitate. The salt was added to saturated aq Na_2CO_3 (50 mL) and the free base was extracted with CH_2Cl_2 (3 × 30 mL) and EtOAc (30 mL). The organic layers were combined, dried over sodium sulfate, filtered, and concentrated on the rotovap.

m.p.: 144–146 °C; ^{1}H-NMR (600 MHz, d_6-DMSO) δ 9.81 ppm (s, 1H), 7.90 (d J = 2.0 Hz, 1H), 7.70 (dd, J = 8.5, 2.0 Hz, 1H), 7.64 (m, 2H), 6.91 (m, 2H), 6.83 (d, J = 8.5 Hz, 1H), 6.0 (s, 2H), 3.74 (s, 3H); ^{13}C-NMR (125 MHz, d_6-DMSO) δ 164.1, 155.7, 148.1, 132.9, 129.2, 128.2, 122.9, 122.2 (2C), 116.5, 114.5, 114.1 (2C), 55.6; LCMS t = 4.1 min, (m/z): $[M+H]^+$ calculated for $C_{14}H_{14}ClN_2O_2$, 277.0744; found, 277.0744; $[M+Na]^+$ calculated for $C_{14}H_{13}ClN_2NaO_2$, 299.0563; found 299.0552; $[2M+H]^+$ calculated for $C_{28}H_{27}Cl_2N_4O_4$, 553.1409; found, 553.1411; $[2M+Na]^+$ calculated for $C_{28}H_{26}Cl_2N_4NaO_4$, 575.1229; found, 575.1228.

Synthesis of 3-Chloro-*N*-(4-Methoxyphenyl)-4-((2-Methyl-3-Oxocyclopent-1-en-1-yl)Amino)Benzamide (5, MS402). The 2-methyl-1,3-cyclopentandione (1.17 g, 10.4 mmol) and **4** (3.26 g, 10.4 mmol) were heated to reflux in toluene (200 mL). Upon reflux the solution was removed from heating, and p-toluene sulfonic acid (p-TSA) as an acid catalyst was added. The apparatus was equipped with a Dean-Stark condenser and returned to reflux for 18 h. The solvent was removed on the rotovap and the subsequent crude material was recrystallized from the indicated solvent. The method yielded 2.7 g (70% yield), after recrystallization from AcOH, followed by recrystallization from MeOH.

m.p.: 225–226 °C; ^{1}H-NMR (600 MHz, d_6-DMSO) δ 10.21 ppm (s, 1H), 8.96, (s, 1H), 8.12 (d, J = 1.4 Hz, 1H), 7.92–7.94 (m, 1H), 7.66 (d, J = 8.9 Hz, 2H), 7.48 (d, J = 8.3 Hz, 1H), 6.94 (d, J = 8.9 Hz, 2H), 3.75 (s, 3H), 2.49–2.51 (m, 2H), 2.22–2.46 (m, 2H), 1.48 (s, 3H); ^{13}C-NMR (125 MHz, d_6-DMSO) δ 202.7, 168.8, 163.1, 155.7, 139.3, 133.0, 131.9, 128.9, 128.8, 127.2, 127.1, 122.0 (2C), 113.8 (2C), 110.7, 55.2, 32.7, 25.7, 7.6; LCMS t = 4.2 min, (m/z): $[M+H]^+$ calculated for $C_{20}H_{20}ClN_2O_3$, 371.1162; found, 371.1166; $[M+Na]^+$ calculated for $C_{20}H_{19}ClN_2NaO_3$, 393.0982; found 393.0978; $[2M+H]^+$ calculated for $C_{40}H_{39}Cl_2N_4O_6$, 741.2247; found, 741.2252; $[2M+Na]^+$ calculated for $C_{40}H_{38}Cl_2N_4NaO_6$, 763.2066; found, 763.2054; HRMS (m/z): $[M+H]^+$ calculated for $C_{20}H_{20}ClN_2O_3$, 371.1162; found 371.1158.

The ^{1}H and ^{13}C NMR spectra of compound **5** (MS402) are shown in Fig. S5.

A

BrDs	MS402	MS417	JQ1	I-BET762
	Ki (nM)			
BRD4-BD1	77	< 7.6	19.7	29.6
BRD4-BD2	718	< 10.4	22.7	13.5
BRD3-BD1	110	< 2.5	9.4	12.1
BRD3-BD2	200	< 10.4	23.2	12.5
BRD2-BD1	83	<12.4	48.2	68.4
BRD2-BD2	240	< 6.8	21.8	20.1
CBP	775	1,035	1,231	1,256
PCAF	4,120	N/D	N/D	N/D
SMARCA4	6,560	N/D	N/D	N/D
BPTF	5,430	N/D	N/D	N/D
BAZ2B	8,690	N/D	N/D	N/D

Note: N/D stands for no binding data.

B

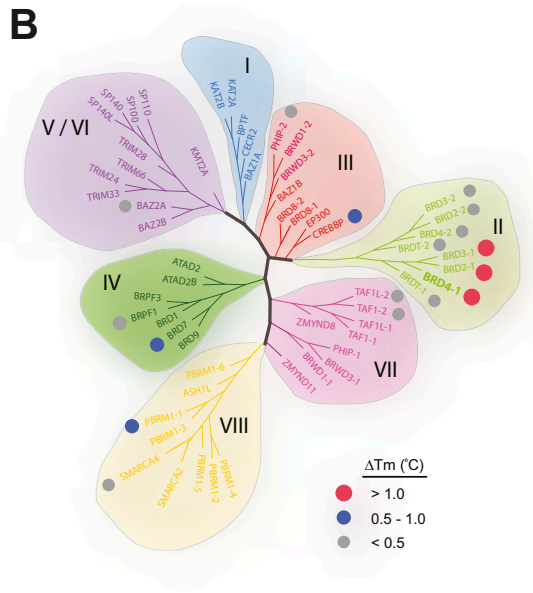

	ΔTm (°C)
BRD4-BD1	1.30
BRD4-BD1-Q85K	0.75
BRD4-BD1-Q85A	0.27
BRD4-BD2	0.31
BRD2-BD1	1.21
BRD3-BD1	1.26
BRDT-BD1	0.06
BRD2-BD2	0.33
BRD3-BD2	0.40
BRDT-BD2	0.10
BAZ2A	0.02
CBP	0.83
PHIP-BD2	0.04
BRD7	0.60
BRPF1	0.37
PBRM1-BD1	0.59
SMARCA4	0.23
TAF1-BD2	0.19
TAF1L-BD2	0.04

C

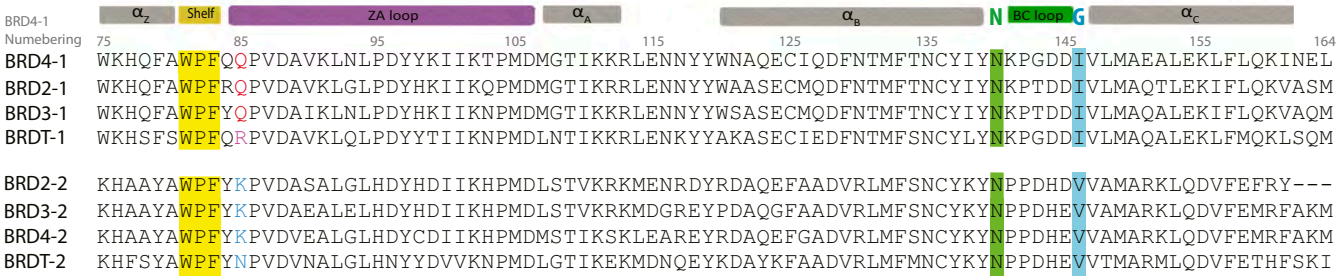

D

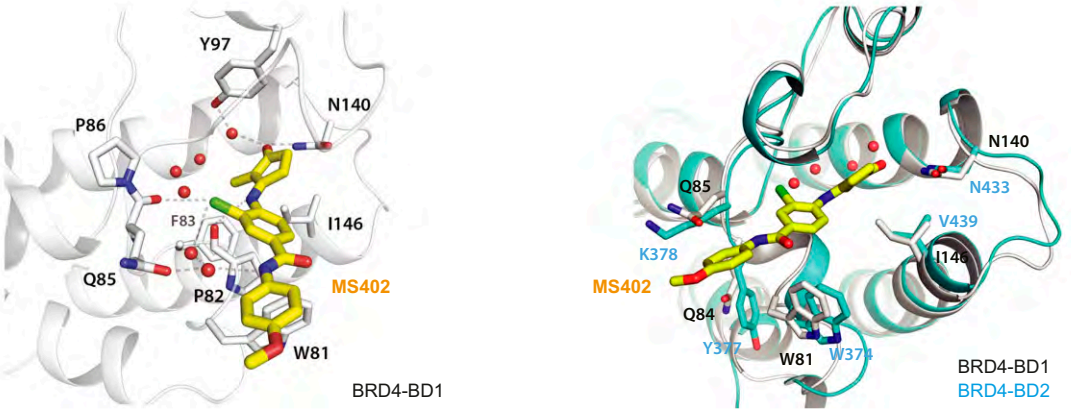

Fig. S1. MS402, a BD1-selective BET bromodomain inhibitor. (*A*) Binding affinity of MS402 to BrDs that represent different subgroups of the human BrD family, as determined in a fluorescence anisotropy assay. See experimental details in *SI Materials and Methods*. (*B*) Characterization of MS402 binding to representative human BrDs, as assessed by measuring protein thermal stability with and without the presence of the chemical ligand. The results are depicted in the phylogenetic tree of the human BrD family with dots that are color-coded for high affinity (red), modest affinity (blue), or low or no binding (gray). PCAF is also known as histone acetyltransferase KAT2B. (*C*) Sequence alignment of BET-BD1 and BD2 using the UniProt database and the PROMALS3D server. The conserved Asn and the gatekeeper residue in αC are highlighted with green and blue background, respectively. The WPF shelf residues are highlighted in yellow and the key residue Gln85 is colored in red for BRD4-BD1 and its counterpart Lys in BRD4-BD2 is in blue. (*D*) (*Left*) A detailed view of the polar interactions engaged by MS402 with binding site residues of BRD4-BD1. Hydrogen bonds are shown by dashed lines. (*Right*) Superimposition of MS402 bound to BRD4-BD1 (5E87, colored in white) with BRD4-BD2 (2YEM, colored in cyan).

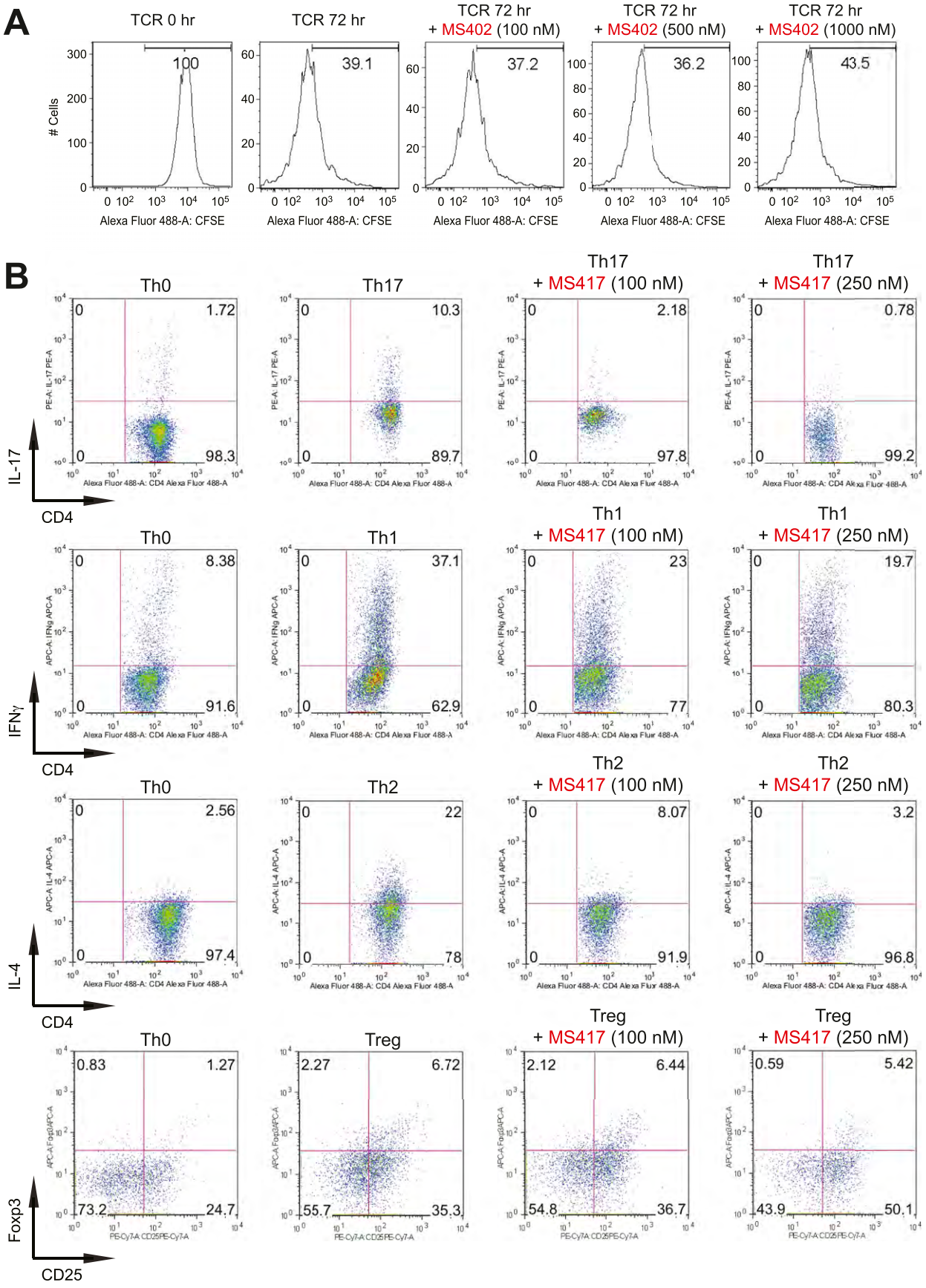

Fig. S2. (Continued)

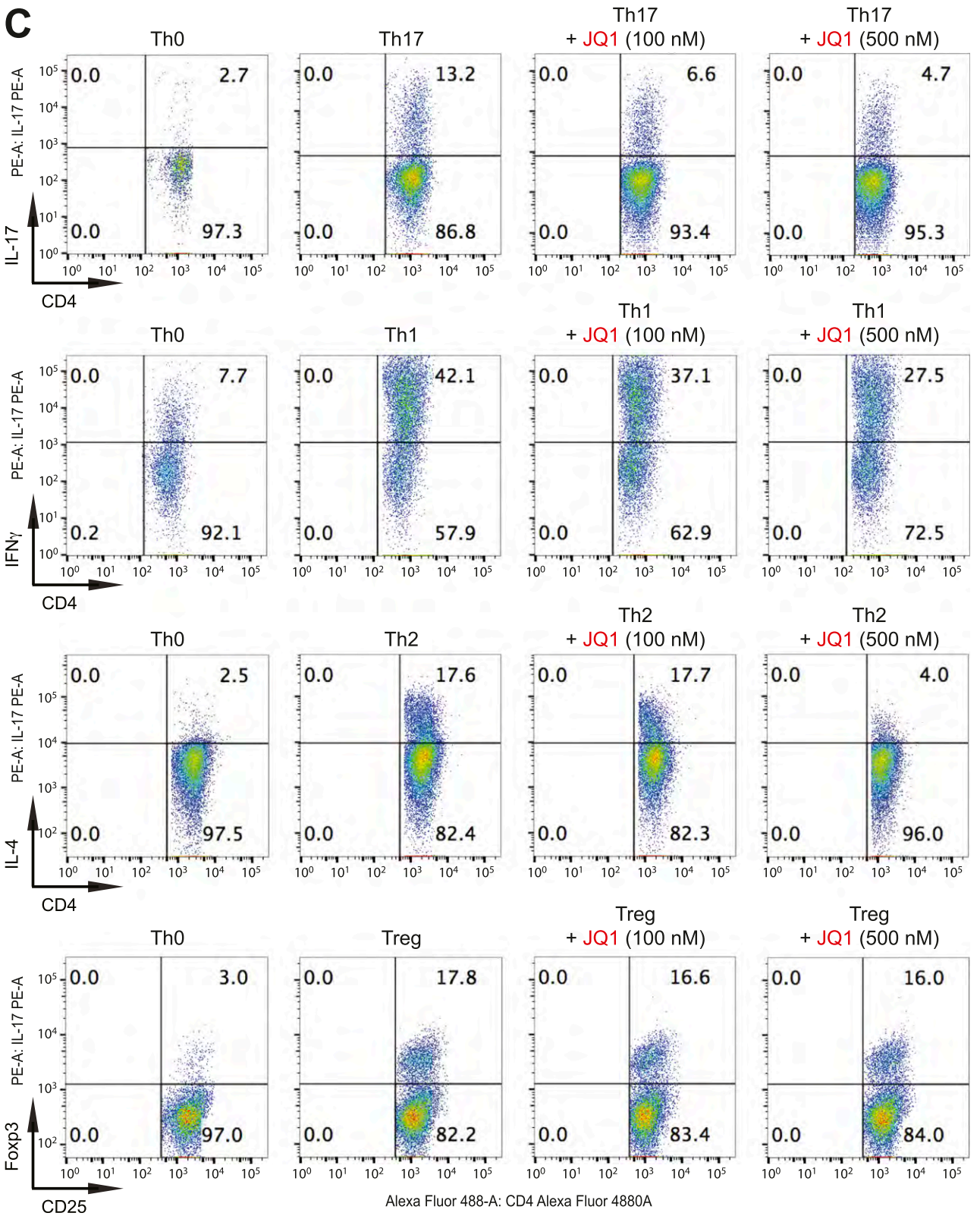

Fig. S2. (Continued)

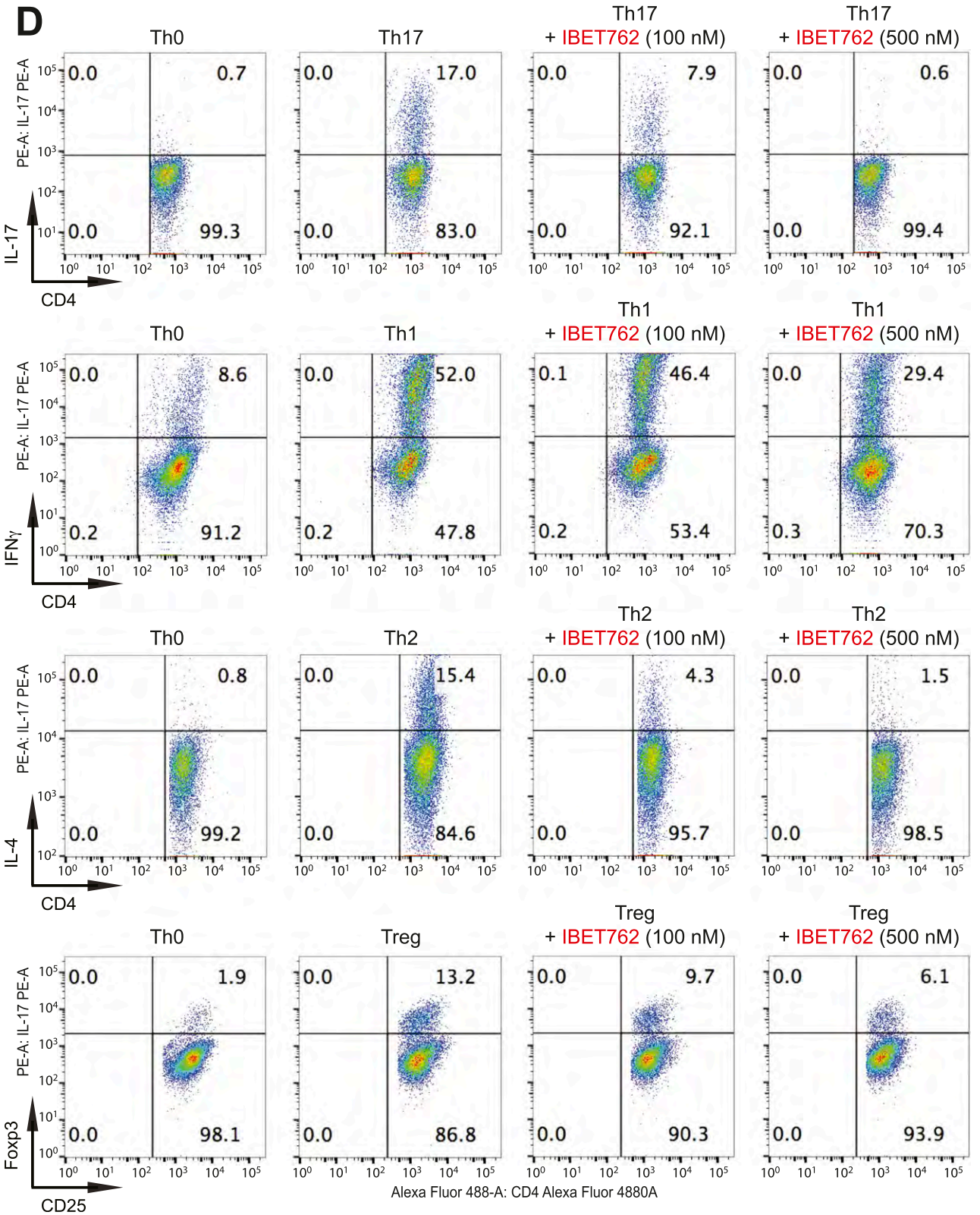

Fig. S2. (Continued)

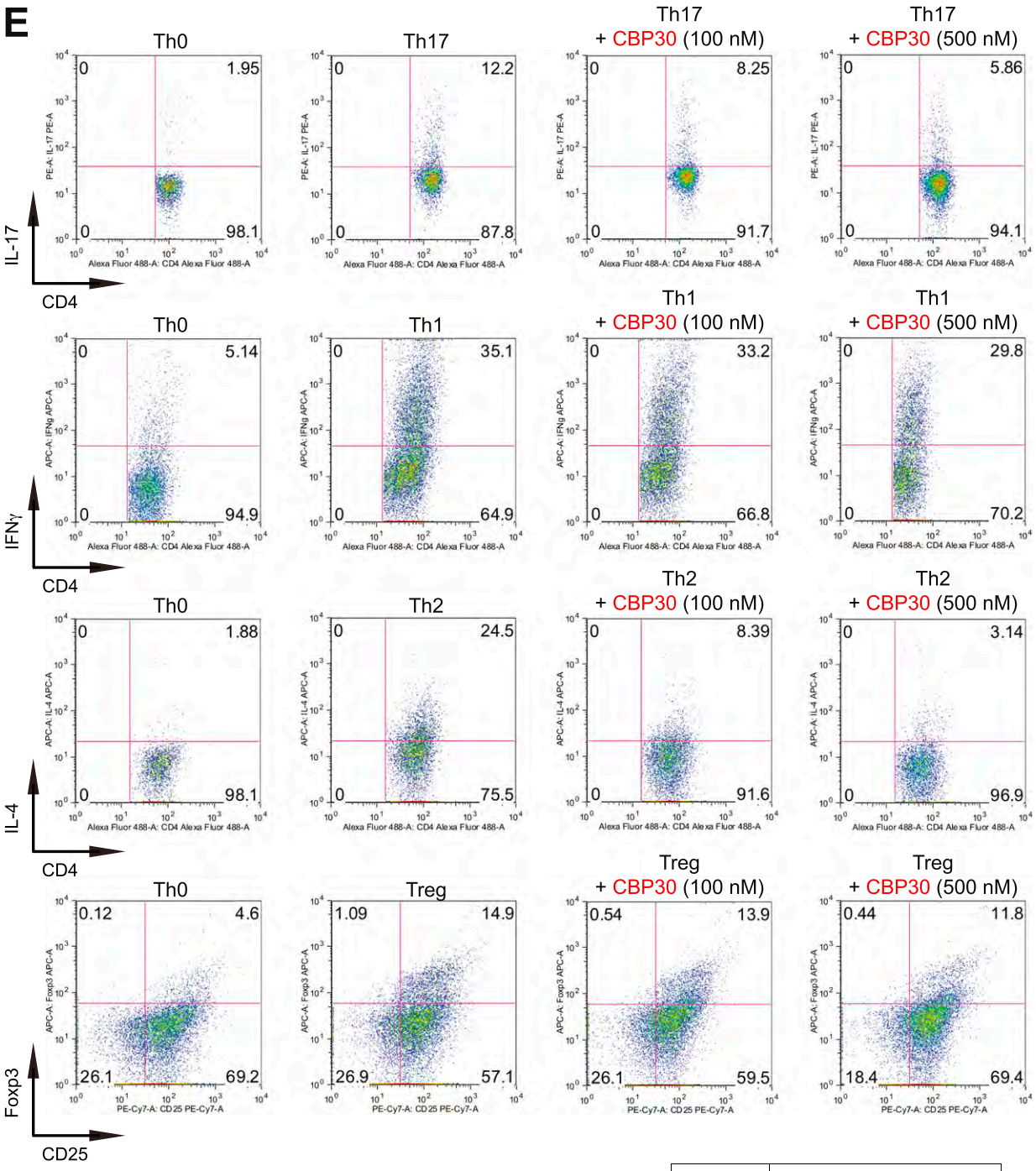

Th Cells	CBP30		
	(0 nM)	(100 nM)	(500 nM)
Th17	12.0%	8.3%	5.9%
Th1	35.1%	33.2%	29.8%
Th2	24.5%	8.4%	3.1%
Treg	14.9%	13.9%	11.8%

Fig. S2. (Continued)

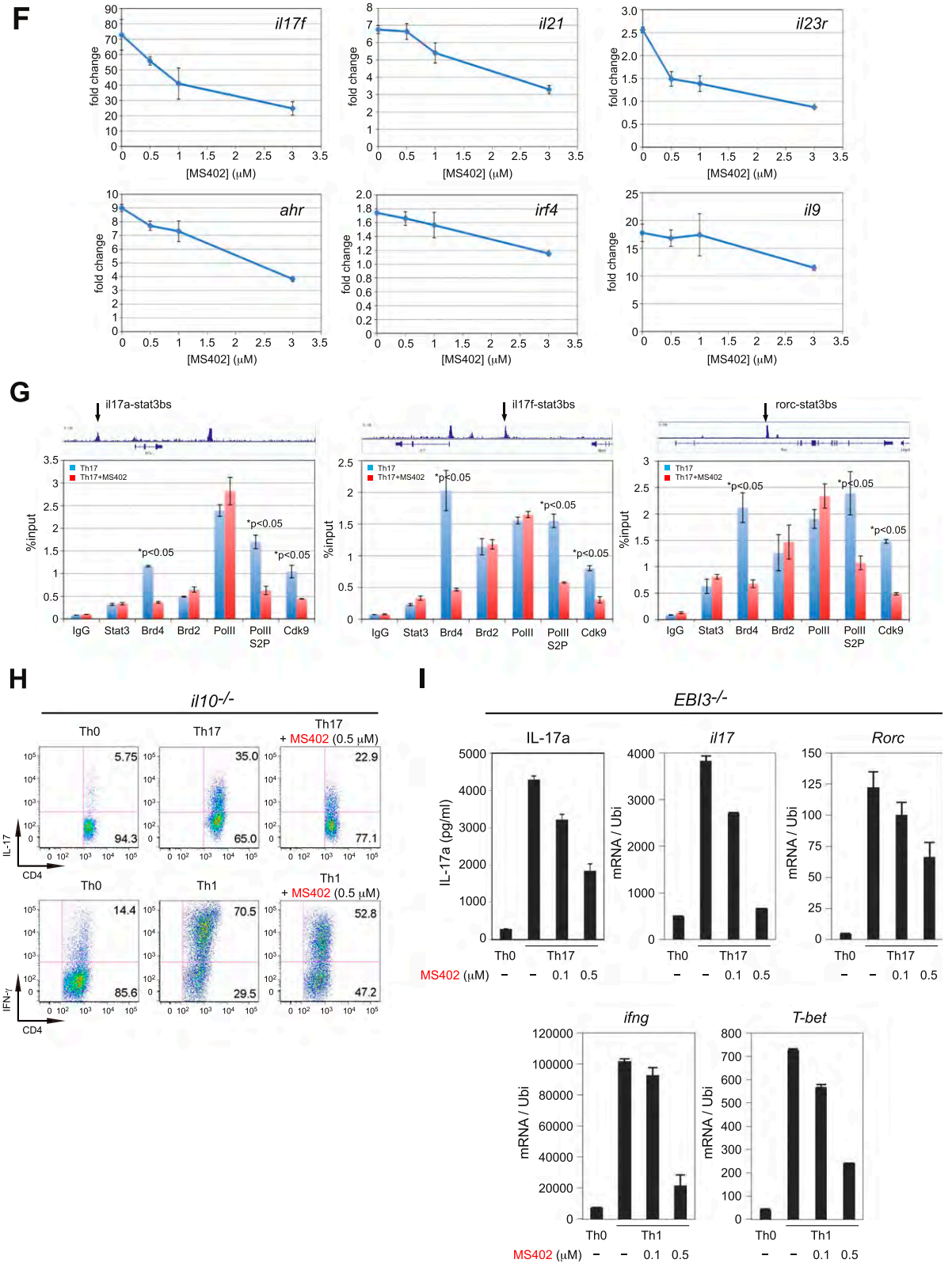

Fig. S2. BET proteins control gene transcriptional programs in cell differentiation of T-helper cells. (*A*) Naive CD4$^+$ T cells isolated from spleen and lymph nodes and stimulated to proliferate with plant-bound anti-CD3 plus anti-CD28 for 72 h under different concentrations of MS402. (*B*) Flow cytometry analysis of mouse primary naïve CD4$^+$ T cells purified from spleens and lymph nodes of C57BL/6 mice and differentiated under Th0, Th1, and Th17 polarization conditions after 3 d with and without MS417 added daily at 100 nM or 250 nM. (*C*) Flow cytometry analysis of mouse primary naïve CD4$^+$ T cells purified from spleens and lymph nodes of C57BL/6 mice and differentiated under Th0, Th1, and Th17 polarization conditions after 3 d with and without JQ1 added daily at 100 nM or 500 nM. (*D*) Flow cytometry analysis of mouse primary naïve CD4$^+$ T cells purified from spleens and lymph nodes of C57BL/6 mice and differentiated under Th0, Th1,

Legend continued on following page

and Th17 polarization conditions after 3 d with and without IBET762 added daily at 100 nM or 500 nM. (*E*) Flow cytometry analysis of mouse primary naïve $CD4^+$ T cells purified from spleens and lymph nodes of C57BL/6 mice and differentiated under Th0, Th1 and Th17 polarization conditions after 3 d with and without a selective CBP BrD inhibitor, SGC-CBP30 added daily at 100 nM or 500 nM. (*F*) Effects of MS402 treatment on mRNA expression levels of additional Th17-specifying transcription factors and cytokines after 3-d Th17-specific cell differentiation from mouse primary naïve $CD4^+$ T cells in a dose-dependent manner. (*G*) ChIP-seq tracks of Stat3 on *il17a-f* and *rorc* gene loci in Th17 cells (*Upper*) and ChIP-qPCR analysis of Stat3, Brd4, Brd2, PolII, PolIIS2P, and Cdk9 in Th17 cells treated with and without MS402 (3 μM) (*Lower*). Statistically significant ($*P < 0.05$) results are annotated. All results are representative of more than two independent experiments. (*H*) (*Upper*) Naïve $CD4^+$ T cells of *il10*$^{-/-}$ mice were differentiated under Th0 and Th17 polarizing conditions. Th17 cells were treated with or without MS402 (500 nM). After in vitro culturing for 3 d the cells were restimulated with PMA/ionomycine for 6 h, stained for intracellular IL-17 for flow cytometry analysis. (*Lower*) A similar experiment was performed under Th1 polarizing conditions to assess MS402's effect on IFN-γ–producing $CD4^+$ cells. (*I*) Naive $CD4^+$ T cells isolated from *EBI3*$^{-/-}$ mice were differentiated under Th1 or Th17 polarizing conditions. Th17 cells were treated with or without MS402 added daily at concentration of 100 or 500 nM. After in vitro culturing for 3 d the cells were restimulated with PMA/ionomycine for 6 h, and real-time PCR was performed for detection of mRNA expression of Th17 and Th1 cytokines and transcription factors. In addition, supernatants were harvested and IL-17 production was analyzed by ELISA.

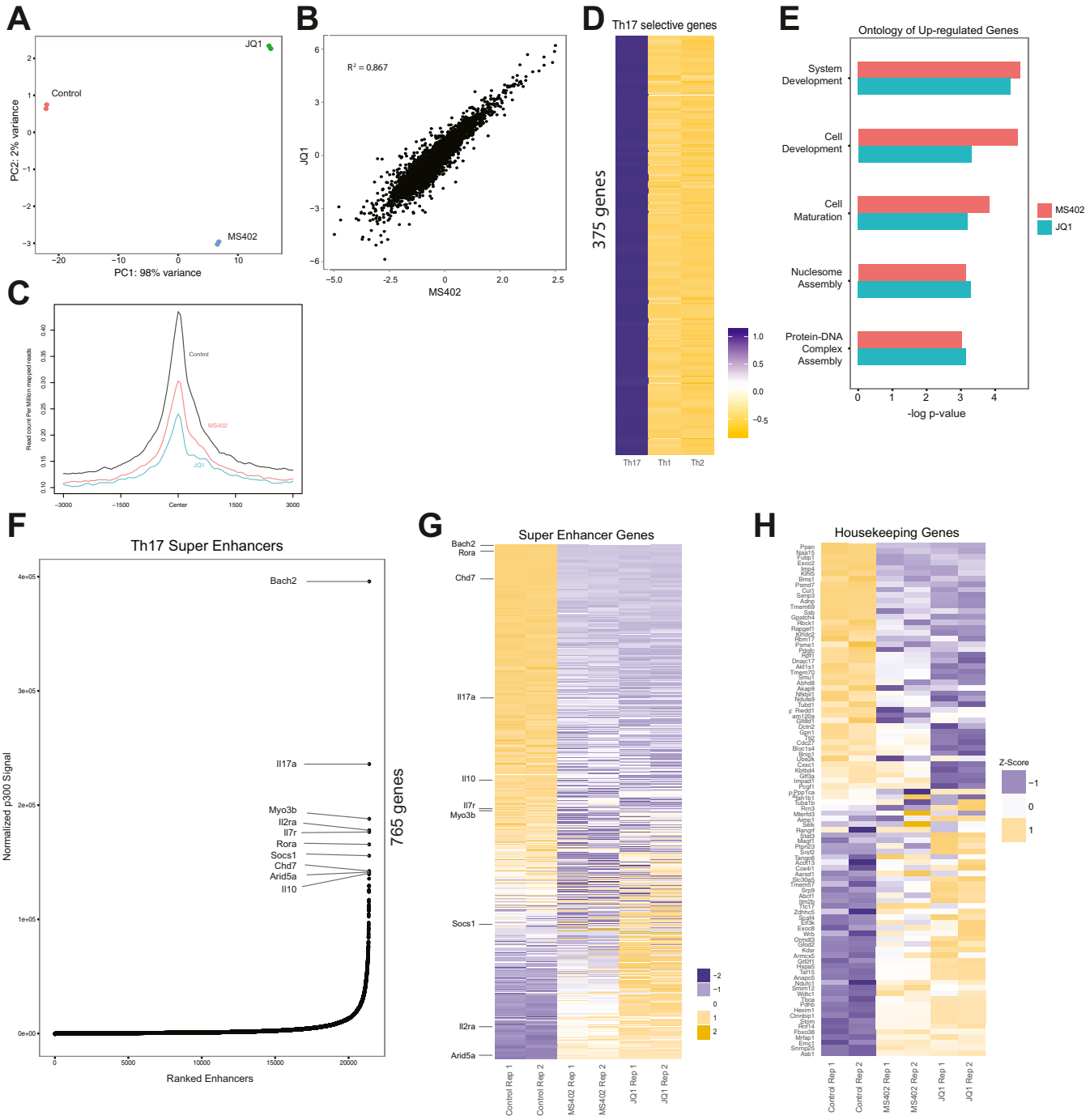

Fig. S3. Genomic analysis of BET inhibition effects on gene transcription in Th17 cell differentiation. (*A*) Principal component analysis plot showing the reproducibility of each RNA-seq experiment. JQ1 and MS402 samples also cluster together along the PC1 axis. (*B*) Scatter plot of log-fold change of genes altered by JQ1 and MS402 treatment illustrating a similar pattern of change for all affected genes. (*C*) TSS profiles of Brd4 occupancy at all genes before and after JQ1 and MS402 treatment showing Brd4 displacement by the compounds. (*D*) A group of 375 genes is up-regulated twofold in Th17 cells compared with Th1 and Th2 cells. This set is used in Fig. 3*B*. (*E*) Genes, up-regulated by MS402 and JQ1 treatment, are enriched for similar ontologies, including developmental genes as well as genes involved in chromatin maintenance. (*F*) Super enhancers discovered using a ROSE-type algorithm on p300 peaks in Th17 cells. Over 750 genes in proximity to super enhancers were discovered, with the top 10 labeled. (*G*) Treatment by JQ1 and MS402 demonstrates a similar pattern in down-regulation of the majority of super-enhancer genes, as identified in *C*. (*H*) Treatment by JQ1 alters a representative set of 100 housekeeping genes in greater fashion compared with MS402. Both compounds, however, demonstrate similar trends in up-regulation and down-regulation of these housekeeping genes. This set was used for analysis in Fig. 3*B*.

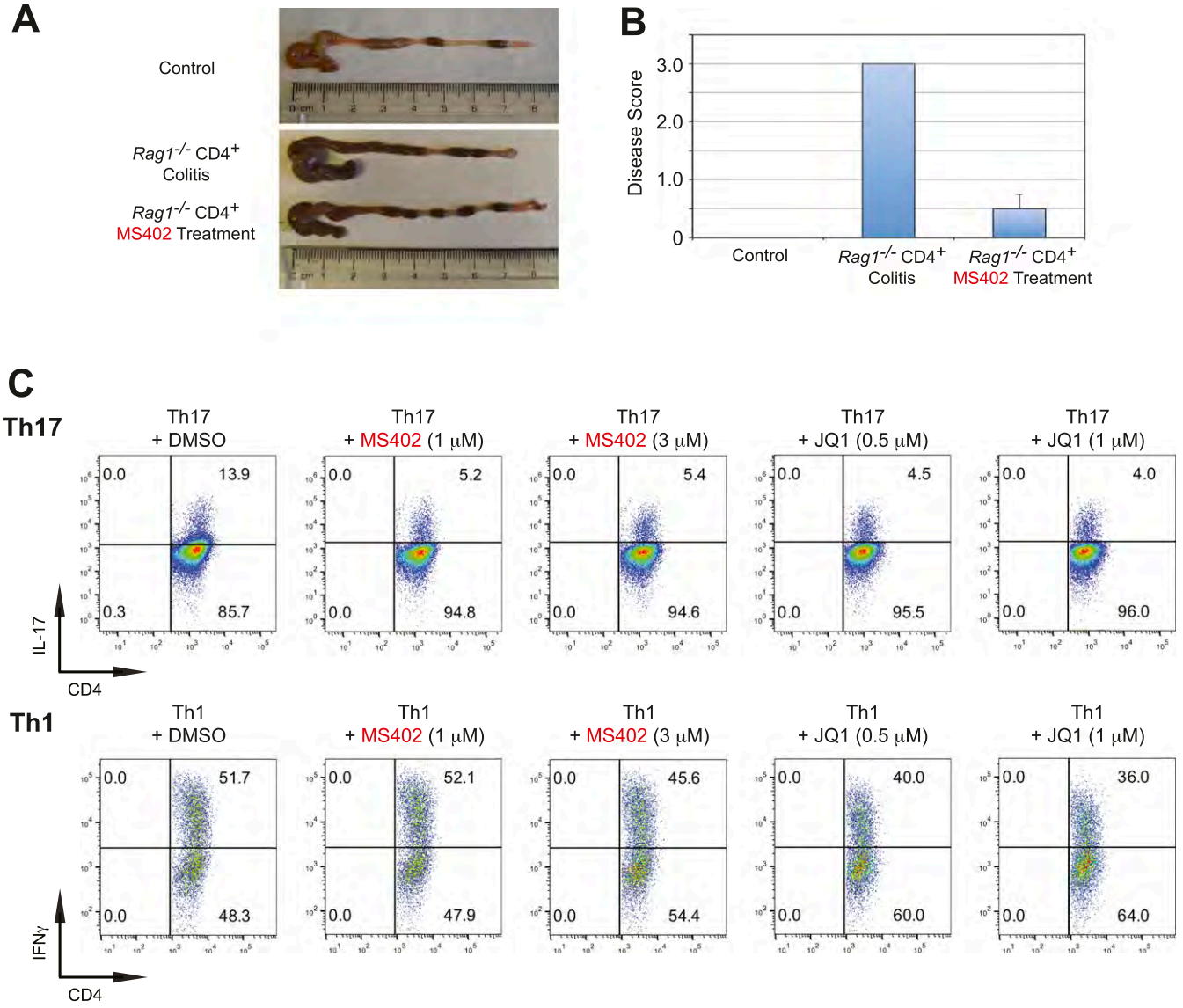

Th Cells	Control	MS402		JQ1	
	DMSO	(1 μM)	(3 μM)	(0.5 μM)	(1 μM)
Th17	13.9%	5.2%	5.4%	4.5%	4.0%
Th1	51.7%	52.1%	45.6%	40.0%	36.0%

Fig. S4. MS402 ameliorates adoptive T-cell transfer-induced colitis in mice. (*A*) Changes of morphology of intestines of the *Rag1*$^{-/-}$ mice with and without MS402 treatment started at week 5 until week 8, as indicated in Fig. 4*A*. (*B*) Disease score assessing efficacy of MS402 treatment as in *A* on ameliorating inflammation of colitis in mice. The inflammation grading was graded on a scale of 0–3: negative (0), no inflammation; mild (1), mild and patchy; moderate (2), most crypts involved by inflammation; or severe (3), crypt abscess, ulceration, erosion, or submucosal involvement. The inflammation cells are most lymphocytes with some neutrophils. (*C*) Flow cytometry analysis assessing the effects of MS402 or JQ1 treatment (24 h at the indicated concentrations) on the maintenance of Th17 and Th1 cells after being differentiated from mouse primary naïve CD4^{+} T cells purified from spleens and lymph nodes of C57BL/6 mice under Th17 and Th1 polarization conditions after 3 d. These results are statistically significant ($P < 0.05$) and are representative of more than two independent experiments.

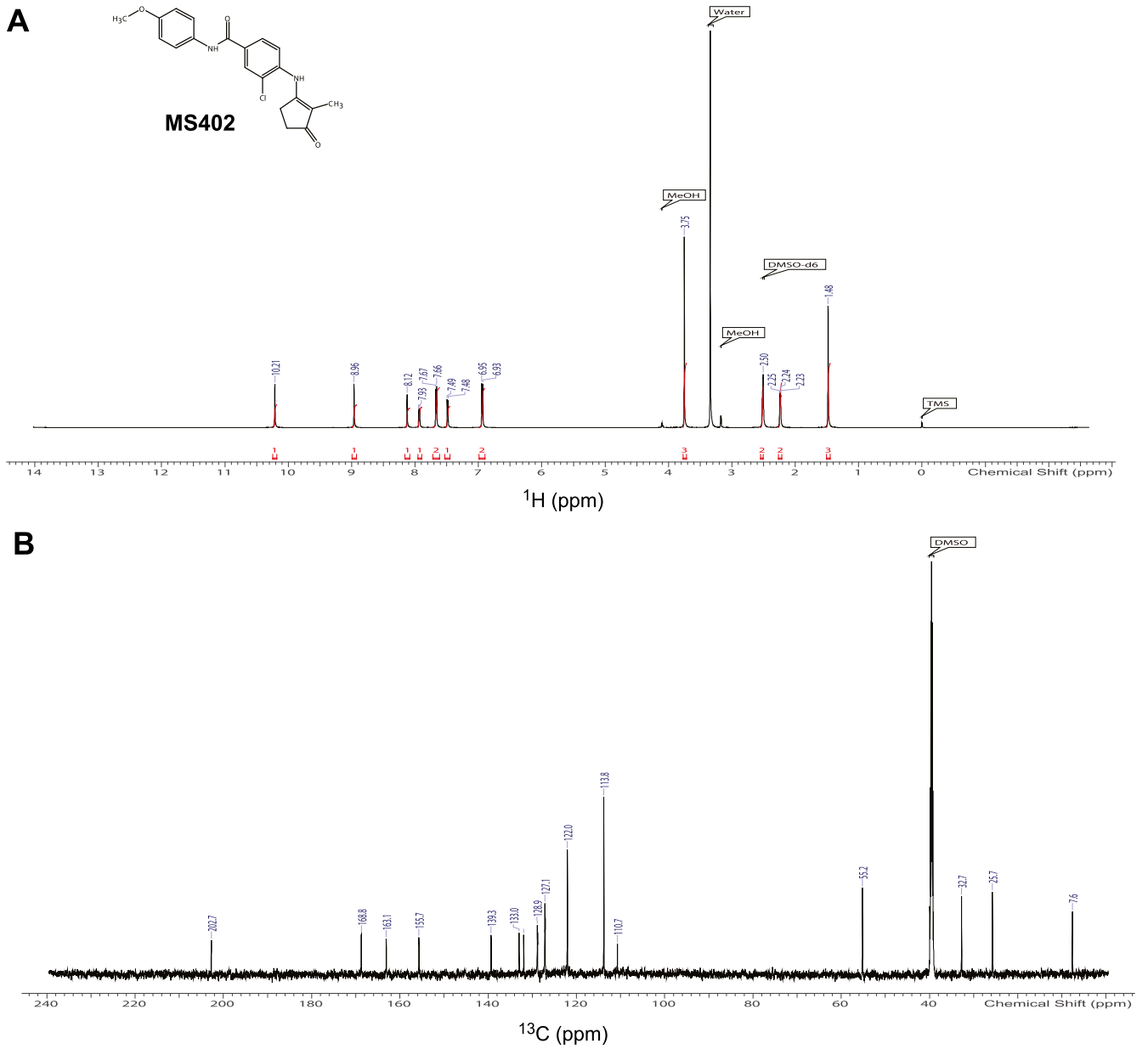

Fig. S5. NMR spectra of compound 5, MS402. (*A*) The ^{1}H and (*B*) ^{13}C NMR spectra of MS402 in d6-DMSO, collected on a 600-MHz Bruker NMR spectrometer at room temperature.

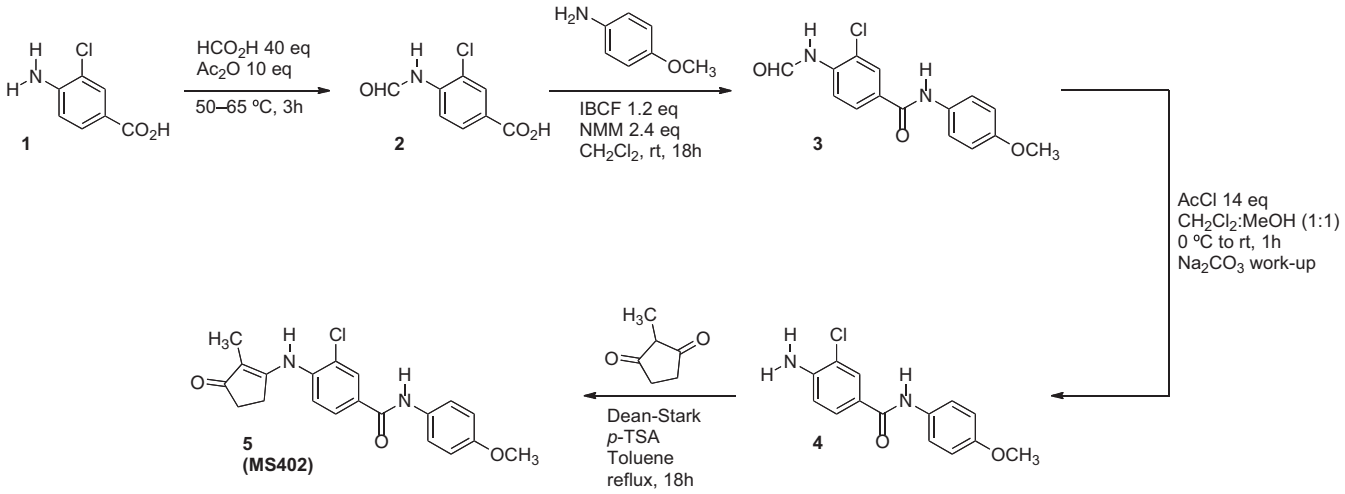

Scheme S1. Synthetic scheme of MS402.

Table S1. Crystallography data and refinement statistics of the BRD4-BD1/MS402 complex structure

Parameters	BRD4-BD1/MS402
Data collection	
Space group	P32
Cell dimensions	
a, *b*, *c*, Å	47.66, 47.66, 124.21
α, β, γ , °	90, 90, 120
Resolution, Å (highest-resolution shell)	23.8–1.5 (1.54–1.5)
Measured reflections	276,330
Unique reflections	48,479
R_{merge}	6.0 (43.9)
I/σ	40.1 (3.1)
Completeness, %	96.3 (90.9)
Redundancy	5.7 (5.6)
Refinement	
Resolution, Å	23.8–1.5
No. of reflections	45,565
R_{work}/ R_{free}, %	14.1/18.1
No. of atoms	
Protein	1,043
Compound	26
Water	217
B-factors, Å^2	
Protein	20.2
Compound	17.6
Water	40.6
Rmsd	
Bond lengths, Å	0.021
Bond angles, °	1.97
Ramachandran plot, % residues	
Favored	99.2
Additional allowed	0.8
Generously allowed	0
Disallowed	0

Table S2. Primers used for RT-qPCR analysis

Primers	Forward	Reverse
RT-PCR primers		
GAPDH	AACTTTGGCATTGTGGAAGG	GGATGCAGGGATGATGTTCT
Brd2	Qiagen Mm_brd2_1_SG	
Brd3	Qiagen Mm_brd3_1_SG	
Brd4	Qiagen Mm_brd4_var1_SG	
IL17a	CTTCATCTGTGTCTCTGATGCTGTT	TCGCTGCTGCCTTCACTGT
IL17f	CAAAACCAGGGCATTTCTGT	ATGGTGCTGTCTTCCTGACC
IL21	CGCCTCCTGATTAGACTTCG	GCCCCTTTACATCTTGTGGA
Rorc	TGCAAGACTCATCGACAAGG	AGGGGATTCAACATCAGTGC
IFNg	CAACAGCAAGGCGAAAAAGG	GGACCACTCGGATGAGCTCA
Tbx21	CAACAACCCCTTTGCCAAAG	TCCCCCAAGCAGTTGACAGT
IL4	GGCATTTTGAACGAGGTCACA	AGGACGTTTGGCACATCCA
ChIP-qCPR primers		
IL17-p1	CAGGTATTATTCTCAGGGCTTTGG	TGGCAATGGTGTCTTTTCTTTG
IL17-p2	CACCTCACACGAGGCACAAG	ATGTTTGCGCGTCCTGATC
IL17-p3	GGATTAAGGGCACACGTGTTG	TTTCCCCACTCTGTCTTTCCA
IL17-p4	TCATCGGCTCCCACACAGA	GGCAGTACCGAAGCTGTTTCA
IL17-p5	CCCACAAAGCAACACTCTTGTC	ACTGCATGACCCGAAAGCA
IL17-p6	GCATCGCATCTTTCAAACCA	TTAGGATAAGCGCCCAGTGAAT
rorc-p4	CCCTGGGAGGAAAGCGAGTCAGAATGA	AGCTTGGGAATTGGACATTGGATGGATGAG
rorc-bs1	AGCTTTGCTGTGGAAGATGTTTC	GAAGGGCTGGTAGGGAAGTCA
rorc-nonstat	GCCAACAGGACTTTTGCCCAGC	TGGAGGGTGAGGCTCTGCTAACT
tbx21-p1	CACCATCTCGCTTTCCGCT	TCCCCCTGGCTGACTTTTC
tbx21-p2	CCCCGGGGTCTGGGATATAGTTCA	GGGGGTGGAACCAGAAGCGT
tbx21-p3	CACCCAAAGCAGCCCACGG	CGCTAGCTGTTACGCTGCCAC
tbx21-p4	CCGCCCCCTCGTGGCTAATAC	GGGTCGGGGCTTCAGTCCTC
tbx21-p5	AGCGCGACTCTCAGCTTCCC	CGCGCGAGGACTACGCATTG
tbx21-p6	TGACCTCAGGCCACAGCGAG	TTCCGGCCCATGCGAACTCT
ifng-p1	GGGCTTCCTCACCACATTGGCT	TGCAATGGGGGAAGCCTTTTCAAAC
ifng-p2	AAGGCTCCCTGTGCTGTGC	GTCTCCCCCTTTTTGCCCT
ifng-p3	ACCCCAAATGGTGTGAAGTAAAA	CCCACCTGTGCCATTCTTGT
ifng-p4	TCCTCCTGCGGCCTAGCTCT	AGCCAAGATGCAGTGTGTAGCGT
ifng-p5	TGCCTCCCGTATGTGTTTGGAGC	CTGCCCCCTTATGGTCCAGGC
ifng-p6	CCTTCTTCAGCAACAGCAAGGCG	GCCGTCTCACCTCAAACTTGGC
ifng-p7	ACAGGTCCAGCGCCAAGCAT	CAGCTGGTGGACCACTCGGA

nature COMMUNICATIONS

ARTICLE

Received 10 Mar 2016 | Accepted 30 Nov 2016 | Published 15 Feb 2017

DOI: 10.1038/ncomms14228 OPEN

Dub3 inhibition suppresses breast cancer invasion and metastasis by promoting Snail1 degradation

Yadi Wu[1,2], Yu Wang[1,2], Yiwei Lin[2,3], Yajuan Liu[2,3], Yifan Wang[2,3], Jianhang Jia[2,3], Puja Singh[4], Young-In Chi[4], Chi Wang[2,5], Chenfang Dong[6], Wei Li[7], Min Tao[7], Dana Napier[2,8], Qiuying Shi[2,8], Jiong Deng[9], B. Mark Evers[2,10] & Binhua P. Zhou[2,3,11]

Snail1, a key transcription factor of epithelial–mesenchymal transition (EMT), is subjected to ubiquitination and degradation, but the mechanism by which Snail1 is stabilized in tumours remains unclear. We identify Dub3 as a bona fide Snail1 deubiquitinase, which interacts with and stabilizes Snail1. Dub3 is overexpressed in breast cancer; knockdown of Dub3 resulted in Snail1 destabilization, suppressed EMT and decreased tumour cell migration, invasion, and metastasis. These effects are rescued by ectopic Snail1 expression. IL-6 also stabilizes Snail1 by inducing Dub3 expression, the specific inhibitor WP1130 binds to Dub3 and inhibits the Dub3-mediating Snail1 stabilization *in vitro* and *in vivo*. Our study reveals a critical Dub3–Snail1 signalling axis in EMT and metastasis, and provides an effective therapeutic approach against breast cancer.

[1] Department of Pharmacology & Nutritional Sciences, The University of Kentucky, College of Medicine, Lexington, Kentucky 40506, USA. [2] Markey Cancer Center, The University of Kentucky, College of Medicine, Lexington, Kentucky 40506, USA. [3] Department of Molecular and Cellular Biochemistry, The University of Kentucky, College of Medicine, Lexington, Kentucky 40506, USA. [4] The Hormel Institute, University of Minnesota, Austin, Minnesota 55912, USA. [5] Department of Biostatistics, The University of Kentucky, College of Medicine, Lexington, Kentucky 40506, USA. [6] Department of Pathology and Pathophysiology, Zhejiang University School of Medicine, Zhejiang 310058, China. [7] Department of Oncology, The First Affiliated Hospital of Soochow University, PREMED Key Laboratory for Precision Medicine, Soochow University, Suzhou 215006, China. [8] Department of Pathology, The University of Kentucky, College of Medicine, Lexington, Kentucky 40506, USA. [9] Key Laboratory of Cell Differentiation and Apoptosis of Chinese Minister of Education, Shanghai Jiao Tong University School of Medicine, Shanghai 200025, China. [10] Department of Surgery, the University of Kentucky, College of Medicine, Lexington, Kentucky 40506, USA. [11] State Key Laboratory of Oncology in South China, Sun Yat-sen University Cancer Center, Collaborative Innovation Center for Cancer Medicine, Guangzhou 510060, China. Correspondence and requests for materials should be addressed to Y.W. (email: yadi.wu@uky.edu) or to B.P.Z. (email: ZhouBh@sysucc.org.cn or peter.zhou@uky.edu).

Approximately 90% of cancer death are caused by metastasis[1], which is an exceedingly complex process involving tumour cell motility, intravasation, circulation in the blood or lymph system, extravasation and growth in new tissues and organs. The increased motility and invasive properties of metastatic tumour cells are reminiscent of events that occur during epithelial–mesenchymal transition (EMT), which is a distinctive morphogenic process that occurs during embryonic development, chronic degeneration and fibrosis of organs, and tumour invasion and metastasis[2,3]. During EMT, epithelial cells acquire fibroblast-like properties, exhibit reduced intercellular adhesion and show increased motility. Several transcription factors are associated with EMT, including the Snail1/Slug family[4], Twist[5], δEF1/ZEB1 and SIP1/ZEB2 (refs 6,7).

Snail1, a zinc-finger containing transcription factor, was identified in *Drosophila* as a suppressor of *shotgun* (an E-cadherin homologue) transcription, which controls large-scale cell movement during mesoderm formation and neural crest delamination[4]. Snail1 expression is tightly regulated during development; this regulation is often disrupted in metastatic breast cancer. Overexpression of Snail1 was found in both epithelial and endothelial cells of invasive breast cancer[8]. Snail1 expression correlates with the tumour grade and nodal metastasis for invasive ductal carcinoma[9–11] and predicts a poor outcome in patients with breast cancer[12]. Snail1 overexpression also induces resistance to apoptosis, confers tumour recurrence and generates breast cancer stem cell (CSC)-like properties[13,14]. We recently found that Snail1 induces aerobic glycolysis by repressing fructose-1,6-biphosphatase (FBP1) expression, and thus provides metabolic growth advantages to breast cancer[15].

Although several signalling pathways, such as EGF, FGF, HGF, TGFβ and Notch, can induce Snail1 transcription under different cellular contexts[16], Snail1 is a labile protein and is under constant protein ubiquitination and degradation mediated by FBXL14, β-TRCP1 or FBXO11 (refs 11,17,18). For example, phosphorylation of Snail1 by glycogen synthase kinase-3β (GSK-3β) promotes Snail1 export from the nucleus. In the cytoplasm, Snail1 undergoes a second phosphorylation by GSK-3β, which targets the protein for β-TRCP1-mediated cytoplasmic degradation. In addition, PDK1 phosphorylates Snail1 to form a Snail1–FBXO11 complex in the nucleus[17]. On the other hand, we reported that Snail1 stabilization is induced by the inflammatory cytokine TNFα through the NF-κB pathway to block Snail1 ubiquitination[19]. However, a comprehensive account of the mechanisms by which Snail1 escapes ubiquitination and degradation in breast cancer remains unknown.

Ubiquitination is a reversible process and ubiquitin moieties are removed from polypeptides by Deubiquitinases (DUBs). DUBs are classified into ubiquitin C-terminal hydrolase (UCH), ubiquitin-specific processing proteases (USP), Jab1/Pad1/MPN-domain containing metallo-enzymes (JAMM), Otu domain ubiquitin-aldehyde binding proteins (OTU) and Ataxin-3/Josephin-domain containing proteins (Ataxin-3/Josephin). Growing evidence shows that DUBs are essential for the regulation of many cellular functions including transcription, DNA repair and cell cycle progression[20]. Dub3 belongs to the USP group, and is an immediate early gene that belongs to a subfamily of cytokine-inducible DUBs[20]. Specifically, Dub3 is rapidly induced by IL-4 and IL-6 (refs 21,22). Cdc25A is a known substrate of Dub3 that promotes oncogenic transformation[23]. In agreement with this report, high Dub3 expression in mouse embryonic stem cells couples the G1/S checkpoint to pluripotency through regulation of Cdc25A (ref. 24), and depletion of Dub3 from breast cancer cells reduces proliferative potential *in vivo*. In addition to the role in breast cancer, Dub3 expression correlates with tumour progression and poor prognosis in human epithelial ovarian cancer[25]. However, these observations do not specifically explain the role of Dub3 in mediating tumour cell invasion and metastasis.

In the current study we utilize unbiased approaches to identify the specific DUB responsible for Snail1 stabilization, and identify Dub3 as a bona fide DUB of Snail1. The Dub3–Snail1 signalling axis forms a 'sensor and effector' circuitry by overlaying inflammatory stimulation to EMT and metastasis.

Results

Dub3 is a deubiquitinase of Snail1. To understand the regulation of Snail1, we purified the Snail1 complexes from nuclear extracts of 201 HeLa S3 cells expressing Flag-Snail1 (ref. 26). The immunocomplex was separated on SDS–PAGE and subjected to top-down mass spectrometry analysis. We determined that several histone methyltransferases/demethylases, such as LSD1 (ref. 26), Suv39H1 (ref. 27) and G9a (ref. 28) as well as Dub3, were associated with Snail1 (Supplementary Fig. 1a). In a parallel experiment, we performed a small interfering RNA (siRNA) library screening, which consisted of four non-overlapping siRNA targeting the 99 known or putative DUBs. This initial screen identified 11 genes that may directly or indirectly control Snail1 stability (Supplementary Fig. 1b). When these DUBs were co-expressed with Snail1 in HEK293 cells, we found that USP12, Dub3 and USP28 significantly increased Snail1 levels, similar to results obtained when cells were treated with the proteasome inhibitor MG132 (Supplementary Fig. 1b). However, only Dub3 interacted with Snail1 in the co-immunoprecipitation (IP) assay (Supplementary Fig. 1c). These two independent and unbiased analyses point to the critical role of Dub3 in the regulation of Snail1.

To further investigate the relationship of these two proteins, we co-expressed Snail1 with Dub3 in HEK293 cells. Expression of wild-type (WT) Dub3 stabilized Snail1. A Dub3 mutant, in which the catalytic cysteine had been replaced with serine (C89S, CS), showed no such effect, indicating that the enzymatic activity of Dub3 is required for Snail1 stabilization (Fig. 1a). A steady-state level of Snail1 was enhanced by increasing Dub3 expression in a dose-dependent manner (Fig. 1b). When Dub3 was co-expressed with GFP-Snail1 in HEK293 cells, we found that Dub3 stabilized and co-localized with GFP-Snail1 in nuclei (Fig. 1c). Although we did not find any correlation between Dub3 and Snail1 mRNA levels, expressions of Dub3 and Snail1 in multiple cancer cell lines, ranging from colon, prostate and breast tumours, were highly correlated (Fig. 1d). Dub3 was highly expressed in basal-like breast cancer (BLBC) cells that contain high levels of Snail1. In addition, Dub3 expression correlated with Snail1 in colon and prostate cancer cell lines, suggesting that this Dub3–Snail1 correlation is not tissue-specific. Dub3 expression also correlated with Snail1 levels in 12 cases of fresh breast tumours (Fig. 1e). These data suggest that Dub3 controls the level of Snail1 through deubiquitination to prevent degradation. Consistent with this idea, knockdown of endogenous Dub3 resulted in a rapid loss of endogenous Snail1 protein, but had no effect on mRNA levels, in MDA-MB231 and MDA-MB157 cells (Fig. 1f). The down-regulation of Snail1 in Dub3-knockown MDA-MB157 cells was restored by MG132 treatment (Fig. 1g), indicating that Dub3-knockdown facilitates the ubiquitination and degradation of Snail1.

Dub3 is evolutionarily conserved from *Drosophila* to humans[29]. Strikingly, knocked-out Dub3 expression using UAS-RNAi lines that target Dub3 in *Drosophila*, show no invagination/gastrulation, which require both EMT and stem

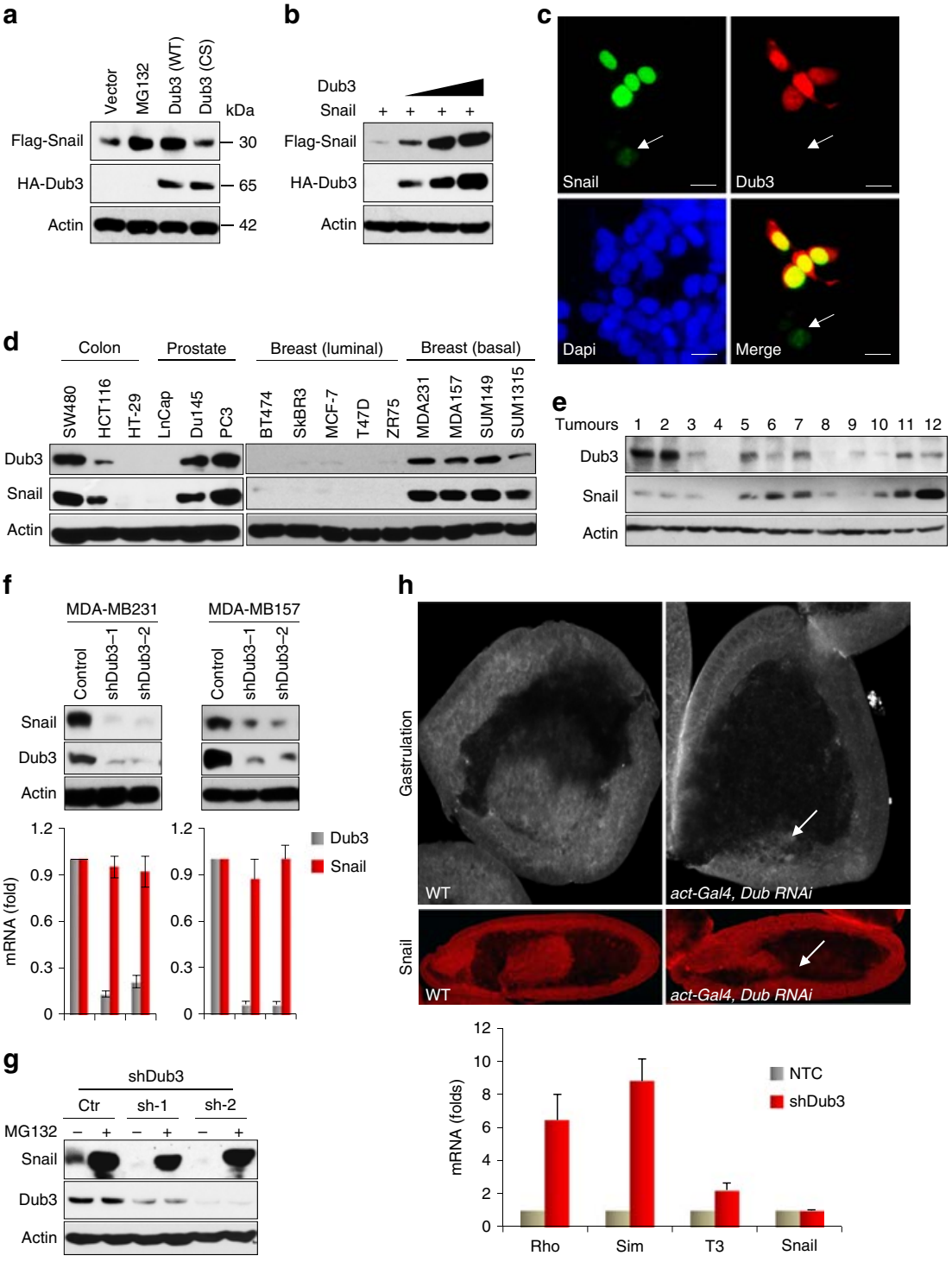

Figure 1 | Dub3 stabilizes Snail1. (**a**) Flag-Snail1 was co-expressed with HA-tagged Dub3 (either wild-type, WT, or catalytic inactive C89S mutant, CS) in HEK293 cells or cells were treated with MG132 for 6 h. Expression of Snail1 and Dub3 were assessed by western blot. (**b**) Flag-Snail1 was co-expressed with increasing amounts of HA-Dub3 in HEK293 cells. Lysates were subjected to analysis by western blot. (**c**) GFP-Snail1 was co-expressed with HA-Dub3 in HEK293 cells. After fixation, the cellular location of Snail1 (green) and Dub3 (red) was examined by immunofluorescent (IF) staining using anti-HA antibody and visualized by fluorescence microscopy (nuclei were stained with Dapi; blue). Arrowhead identifies a cell expressing only GFP-Snail1 but not Dub3. Scale bars, 25 μm. (**d**) The protein expression of Dub3 and Snail1 in various cancer cell lines was analysed by western blot. (**e**) Expression of Dub3 and Snail1 from 12 human breast tumours (fresh frozen) was analysed by western blot. (**f**) The protein expression of Dub3 and Snail1 from MDA-MB157 and MDA-MB231 cells stably transfected with control or two individual Dub3 shRNAs was analysed by western blot and the mRNA was detected by real-time PCR (mean ± s.e.m. in three separate experiments). (**g**) The protein expression of Dub3 and Snail1 from MDA-MB157 cells stably transfected with control or two individual Dub3 shRNAs and treated with or without 10 μM MG132 for 6 h was analysed by western blot. (**h**) Gastrulation and Snail1 expression were detected in *Drosophila* embryos and the mRNA was detected by real-time PCR using stage 11 cells (mean ± s.e.m. in three separate experiments).

cell renewal (up panel, Fig. 1h). This observation was very similar to that seen with a mutant Snail1 in *Drosophila* embryos, in which Snail1 is absolutely required for the dissociation and invagination of cells from epiblast[30]. Consistent with this observation, we noticed a drastic reduction of Snail1 in stage 11 cells. In addition, expression of several genes that are known to be repressed by Snail1 in this event, such as *Rho, Sim* and *T3*, were restored in embryos isolated from these RNAi lines (bottom panel, Fig. 1h). Together, these data indicated that Dub3 is specific for the control of Snail1 *in vivo*.

Dub3 interacts with Snail1. To further investigate the interaction of Dub3 with Snail1, we co-expressed Flag-Dub3 and HA-Snail1 in HEK293 cells and performed a co-IP experiment. After IP of Snail1, we detected an associated Dub3, and vice versa (Fig. 2a). IP of endogenous Snail1 and Dub3 from MDA-MB157 and MDA-MB231 cells also demonstrated the presence of endogenous Dub3 and Snail1, respectively (Fig. 2b). To identify the region in Snail1 that associates with Dub3, we generated two deletion mutants of Snail1 (refs 28,31): the N-terminal Snail1 (amino acids 1–153), which contains the SNAG domain of Snail1; and the C-terminal Snail1 (amino acids 153–264), which includes the conserved zinc finger motif (Fig. 2c). When these two deletion mutants of Snail1 were co-expressed with Dub3 in HEK293 cells, we found that the N-terminal region of Snail1 was responsible for its interaction with Dub3 (Fig. 2c). In addition, when GST-Dub3 was incubated with full-length or deletion mutants of Snail1, only the full-length and N-terminal domain of Snail1 were pulled down by GST-Dub3 (Fig. 2d).

Dub3 contains two functional domains; the N-terminal catalytic (UCH) domain and two hyaluronan binding motifs at its C terminus. To identify the region of Dub3 responsible for the interaction with Snail1, we generated a Myc-tagged full-length, N-terminal deletion, and C-terminal deletion of Dub3 (Fig. 2e) and co-expressed them with Snail1 in HEK293 cells. We found that the N-terminal catalytic domain retained the ability to interact with Snail1. However, when the C-terminal mutant was utilized, Dub3 was unable to interact with Snail1. When GST-Snail1 was pulled down, we found the presence of full-length and N-terminal Dub3 (Fig. 2f). Consistent with this, Dub3 only stabilized the N-terminal but not the C-terminal fragments of Snail1 (Fig. 2g). The interaction between Dub3 and Snail1 was further confirmed by immunofluorescence (IF) analysis showing that endogenous Dub3 co-localized with Snail1 in the nucleus of MDA-MB231 cells (Fig. 2h). Taken together, our results indicate that Dub3 interacts with Snail1 and that this interaction is mediated through the N-terminal regions of Dub3 and N-terminal region of Snail1.

Dub3 stabilizes Snail1 through deubiquitination. The interaction of Dub3 with Snail1 suggests that Dub3 regulates the protein stability of Snail1. To test this idea, we co-expressed Snail1 with Dub3 or vector control in HEK293 cells and examined Snail1 degradation. After treatment with cycloheximide to block newly protein synthesis, Snail1 degraded rapidly in cells transfected with a control vector (Fig. 3a). However, Snail1 levels were stabilized in the presence of Dub3 and this effect continued for up 4 h in the presence of cycloheximide. To test whether endogenous Snail1 is also subjected to similar regulation by Dub3, we knocked down endogenous Dub3 in MDA-MB231 cells, and found that endogenous Snail1 became unstable and degraded rapidly (Fig. 3b). To extend these findings and determine whether this Dub3 effect is mediated through a de-ubiquitination of Snail1, we co-expressed Flag-Snail1 with either WT- or CS-Dub3 in HEK293 cells. After immunoprecipitating Snail1 from cells treated with MG132, we found that Snail1 was heavily ubiquitinated (lane 1, Fig. 3c). However, co-expression of WT-Dub3 almost completely abolished Snail1 ubiquitination while the CS-Dub3 did not have this effect (lanes 2 versus 3, Fig. 3c). Conversely, Snail1 ubiquitination significantly increased in Dub3-knockdown MDA-MB157 and MDA-MB231 cells after MG132 treatment (Fig. 3d). In an *in vitro* deubiquitination assay as described by Dupont *et al.*[32], we incubated poly-ubiquitinated Snail1 with purified WT-Dub3 or CS-Dub3. We found that WT-Dub3, but not CS-Dub3, specifically removed Snail1 ubiquitin moieties *in vitro* (Fig. 3e), indicating that Dub3 stabilizes Snail1 by removing its ubiquitination directly.

Previous studies showed that β-TRCP1 and FBXL14 are specific E3 ligases mediating the ubiquitination and degradation of Snail1 (refs 11,18,33). We investigated whether Dub3 stabilized Snail1 by impeding the activity of β-TRCP1 and FBXL14. Consistent with prior results, expression of β-TRCP1 and FBXL14 increased Snail1 protein degradation (lanes 4 and 7 versus lane 1, Fig. 3f). Expression of the WT-Dub3, but not CS-Dub3, blocked Snail1 degradation mediated by these two ligases. Conversely, knockdown β-TRCP1 or FBXL14 increased Snail1 stability (lanes 2 and 3, Fig. 3g). However, knockdown of Dub3 blocked the Snail1 stabilization effect mediated by the knockdown of either β-TRCP1 or FBXL14 (lanes 4 and 5, Fig. 3g), indicating that Dub3 is a critical factor controlling Snail1 stability. In agreement with this observation, expression of β-TRCP1 and FBXL14 increased Snail1 polyubiquitination (Fig. 3h), which was attenuated by expression of WT-Dub3 (lanes 3 versus 2, lanes 6 versus 5, Fig. 3h). Knockdown of β-TRCP1 or FBXL14 reduced Snail1 polyubiquitination, which was hampered by simultaneous knockdown Dub3 (Supplementary Fig. 2a). Both β-TRCP1 and FBXL14 share the same lysine pattern and target Snail1 degradation through ubiquitin modification of lysine 98, 137 and 146 (ref. 18). Consistent with previous reports, the Snail1 triple mutant (K3R) is more stable than WT-Snail1 (Supplementary Fig. 2b). However, ectopic expression of Dub3 still increased K3R accumulation, indicating that other lysines could be involved in Snail1 stability. Together, these data demonstrated that Dub3 counteracts β-TRCP1- and FBXL14-mediated Snail1 ubiquitination through deubiquitination.

Dub3 expression induces EMT. To study the functional effects of Dub3, we expressed Dub3 in two luminal breast tumour cell lines, MCF7 and T47D, which contain little endogenous Dub3 and Snail1 (Fig. 4a). Dub3 expression induced Snail1 stabilization as well as downregulation of E-cadherin and oestrogen receptor alpha (ERα) in these cells (Fig. 4a,b). Consistently, Dub3 expression induced a morphologic change indicative of EMT (Fig. 4b), including downregulation of epithelial markers (E-cadherin, Claudin-7 and Occludin) and the upregulation of mesenchymal molecules (N-cadherin and Vimentin) (Fig. 4c, Supplementary Fig. 3a). In addition, Dub3 expression converted these luminal cells into a basal-like phenotype; these cells lost luminal markers, such as ERα, FOXA1, CK18 and AGR2, and gained expression of basal molecules such as CK5, CD44 and EGFR (Fig. 4d, Supplementary Fig. 3a). We then tested the migration and invasiveness of these cells. Dub3 expression markedly increased the cell migration and invasive capacity (Fig. 4e,f, Supplementary Fig. 3b,c).

The catalytic activity of Dub3 is required for these functions, because CS-Dub3 could not induce Snail1 upregulation, or the morphological changes associated with EMT, or increased cell migration and invasion in these cells (Fig. 4a–f, Supplementary

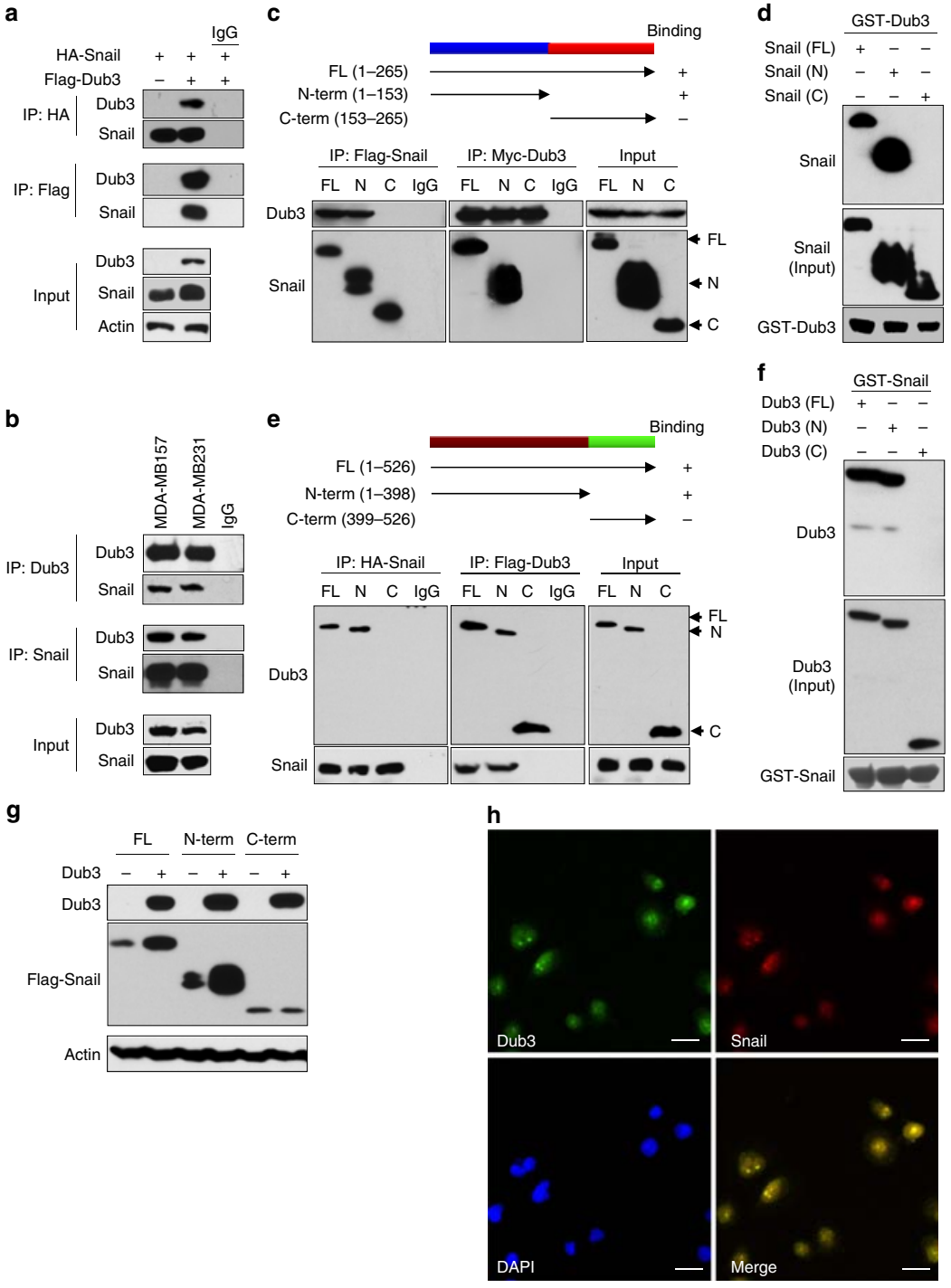

Figure 2 | Dub3 interacts with Snail1. (**a**) HA-Snail1 was co-expressed with vector or Flag-Dub3 in HEK293 cells. Snail1 and Dub3 were immunoprecipitated (IP) with HA or Flag antibody, respectively, and the associated Dub3 and Snail1 were analysed by western blot using either Flag or HA antibody. One-fortieth of the lysate from each sample was subjected to western blot to examine the expression of Snail1 and Dub3 (input lysate). (**b**) Endogenous Snail1 and Dub3 were captured by IP from MDA-MB231 and MDA-MB157 cells, and the bound endogenous Dub3 and Snail1 were examined by western blot. (**c**) Schematic diagram showing the structure of Snail1 and deletion constructs used (top panel). Flag-tagged full-length (FL) or deletion mutants of Snail1 were co-expressed with Myc-Dub3 in HEK293 cells. Extracts were subjected to IP with Flag or Myc antibody, and bound Dub3 or Snail1 was analysed by Western blot using either Myc or Flag antibody. (**d**) Lysates from HEK293 cells expressing WT or different deletion mutants of Flag-Snail1 were mixed with GST-Dub3. After pull-down by glutathione-agarose, the associated proteins were analysed by western blot. (**e**) Schematic diagram showing the structure of Dub3 and deletion constructs used (top panel). Myc-tagged full-length or deletion mutants of Dub3 were co-expressed HA-Snail1 in HEK293 cells. Extracts were subjected to IP with Myc or HA antibody, and the bound Snail1 or Dub3 was analysed by western blot using either HA or Myc antibody. (**f**) Lysates from HEK293 cells expressing WT or different deletion mutants of Myc-Dub3 were mixed with GST-Snail1. After pull-down by glutathione-agarose, the associated proteins were analysed by western blot. (**g**) Myc-Dub3 was co-expressed with Flag-tagged full-length or deletion mutants of Snail1 in HEK293 cells. The protein expressions of Dub3 and Snail1 were analysed by western blot. (**h**) Endogenous Dub3 and Snail1 in MDA-MB231 cells was detected by IF staining. Scale bars, 20 μm.

Fig. 3a–c). In addition, these functional activities promoted by Dub3 required Snail1 upregulation, because knockdown of Snail1 greatly inhibited these changes (Fig. 4a–f, Supplementary Fig. 3a–c). Together, these data indicate that Dub3 can induce EMT (luminal to basal-like phenotype conversion) by stabilizing Snail1 in breast cancer cells.

Knockdown of Dub3 suppresses Snail1's function. To further assess the function of Dub3 in breast cancer, we established stable clones with Dub3 knockdown in MDA-MB231 and MDA-MB157 cells. We achieved 80–90% knockdown efficiency of endogenous Dub3 using two independent shRNAs (Fig. 5a). For both clones, Dub3-knockdown increased E-cadherin and Claudin-7 levels, downregulated expression of Vimentin and N-Cadherin, with concomitant changes of other EMT markers (Fig. 5a, Supplementary Fig. 4a). IF analysis also suggested a downregulation of E-cadherin and upregulation of Vimentin and N-cadherin (Fig. 5b). Dub3 knockdown greatly inhibited the migration and invasive capabilities of these cells (Fig. 5c,d, Supplementary Fig. 4b,c). Individual cell tracking also revealed Dub3 knockdown reduced the velocity and directionality of cell migration, and strongly inhibited the net distance of cell migration in MDA-MB231 and MDA-MB157 cells

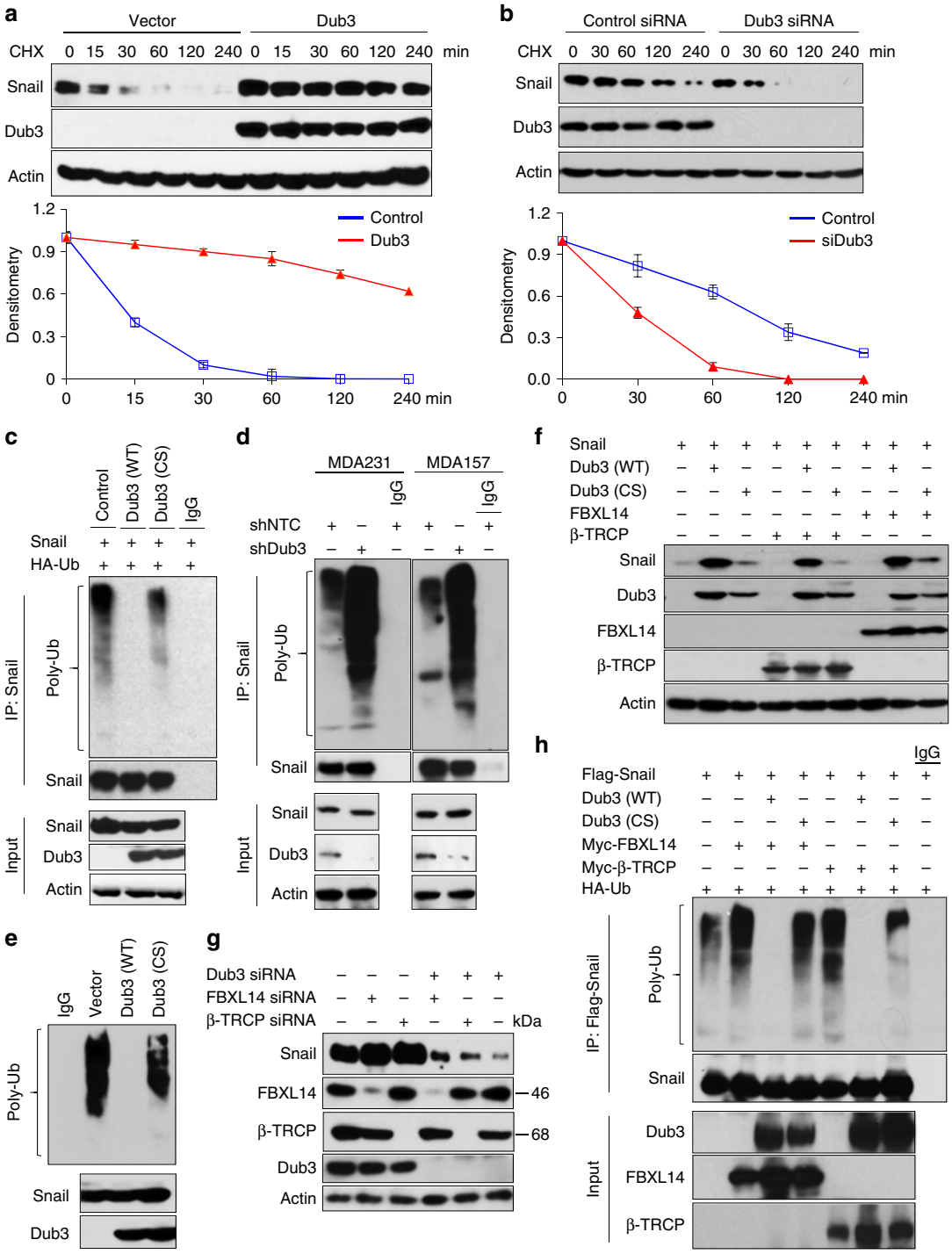

(Fig. 5e, Supplementary Fig. 4d). Importantly, Snail1-rescued expression partially inhibited E-cadherin and claudin-7 upregulation and increased Vimentin and N-cadherin expression in Dub3-knockdown MDA-MB231 and MDA-MB157 cells (Fig. 5a,b). Functionally, Snail1-rescued expression also restored migration and invasion in these Dub3-knockdown cell lines (Fig. 5c–e, Supplementary Fig. 4b–d).

MDA-MB231 and MDA-MB157 cells appear with stellate projections in 3D culture. Cells with Dub3 knockdown exhibited a marked change in morphology, with rounded/polygonal shape (Supplementary Fig. 4e). To extend assessment of the critical role of Dub3 in regulating CSC-like properties in human breast cancer, we examined tumorsphere formation in Dub3-knockdown clones. We found that Dub3 knockdown greatly reduced the number and size of primary and secondary tumorspheres in MDA-MB231 and MDA-MB157 cells (Fig. 5f, Supplementary Fig. 5a). This function of Dub3 is likely mediated through the regulation of Snail1, as Snail1 rescued expression (expressing Snail1-IRES-GFP) greatly restored the number and size of tumorspheres in these two cell lines. As human breast CSCs are enriched in a $CD44^{high}/CD24^{low}$ population[14,34–38], we measured this population in MDA-MB157 and MDA-MB231 cells with Dub3 knockdown using fluorescence-activated cell sorting (FACS). We found that Dub3 knockdown reduced the $CD44^{high}/CD24^{low}$ population in both cell lines (Fig. 5g, Supplementary Fig. 5b). To corroborate these findings, we also used a second set of breast CSC markers ($CD49f^{high}/CD24^{low}$)[39–42]. Similar to the results presented above, Dub3 knockdown reduced the population of $CD49f^{high}/CD24^{low}$ cells in MDA-MB231 and MDA-MB157 cells (lower panel in Fig. 5g, Supplementary Fig. 5c). Again, the reduction of a CSC population in Dub3-knockdown clones appears to be mediated by the downregulation of Snail1, as rescued Snail1 expression in Dub3-knockdown clones largely recovered the CSC phenotype. Taken together, these results clearly support our assessment that Dub3 is the crucial factor controlling Snail1 stability, EMT, migration and invasion, as well as CSC characteristics.

Knockdown of Dub3 blocks breast cancer metastasis. To directly assess whether Dub3 promotes metastasis *in vivo*, we intravenously injected Dub3-knockdown MDA-MB231 cells into female SCID mice and subjected these mice to bioluminescent imaging (BLI). Dub3-knockdown cells exhibited a reduced number of lung nodules at early time points (Fig. 6a,b), implying that Dub3 is critical for the extravasation and/or colonization of breast tumour cells in lung. At 35 days post-injection, all control mice were moribund due to massive lung metastases with an average of 150 visible metastatic nodules per mouse (Fig. 6c,d). In contrast, mice injected with Dub3-knockdown cells were viable and free of detectable metastases. Histologic analyses supported the macroscopic observations and disclosed a high number of metastatic lesions produced by control cells whereas Dub3-knockdown cells lacked metastatic colonies (Fig. 6c,d). Consistent with the function of Snail1 *in vitro*, expression of exogenous Snail1 in Dub3-knockdown cells largely rescued the formation of lung metastases (Fig. 6a,d).

Snail1 is a key transcription factor of EMT[4,43]. To rule out the possibility of cellular adaptation effect associated with stable gene downregulation and to examine the temporal regulation of Snail1 *in vivo*, we generated a doxycycline (DOX)-inducible expression of Dub3 shRNA or control shRNA (TRIPZ lentiviral inducible shRNAmir system from Thermo Fisher Scientific) in MDA-MB231 cells. Treatment with DOX for 6 days achieved almost complete Dub3-knockdown and resulted in a remarkable downregulation of Snail1 (Fig. 6e). In an experimental metastasis model, we intravenously injected these cells into female SCID mice (left panel, Fig. 6f). Mice received DOX or no DOX in the drinking water 24 h after tumour cell inoculation. Dub3 knockdown after DOX treatment significantly decreased lung metastasis and lung weight, but these parameters showed no difference in control mice with or without DOX treatment (middle and right panels, Fig. 6f).

To further examine the therapeutic efficacy of systemic inhibition of Dub3 in preventing tumour recurrence and metastasis, we performed a spontaneous metastasis model analysis, in which control and DOX-inducible Dub3 shRNA MDA-MB231 cells were implanted into mammary fat pads of 6-week-old female SCID mice. When tumours reached a volume of 1 cm^3, the tumours was surgically removed. Mice then received DOX or no DOX in drinking water (left panel, Fig. 6g). Strikingly, the recurrent tumour was significantly inhibited in mice with the Dub3 shRNA expression (middle panel, Fig. 6g). In parallel, depletion of Dub3 also dampened spontaneous lung metastasis (right panel, Fig. 6g). Collectively, these data indicate that Dub3 facilitates breast cancer metastasis through, in large part, Snail1 stabilization.

Dub3 is critical for IL-6-induced Snail1 stabilization. We showed previously that IL-6 and TNFα can stabilize Snail1 by

Figure 3 | Dub3 deubiquitinates Snail1 and antagonizes the function of Snail1's E3 ligase. (**a**) Flag-Snail1 was co-expressed with vector or Myc-Dub3 in HEK293 cells. After treatment with cycloheximide (CHX) for the indicated time intervals, expression of Snail1 and Dub3 was analysed by western blot (top panel) using Flag and Myc antibodies, respectively. The intensity of Snail1 expression for each time point was quantified by densitometry and plotted (bottom panel). Experiment was repeated three times and a representative experiment is presented (mean ± s.e.m. in three separate experiments). (**b**) MDA-MB231 cells were transfected with control or Dub3 siRNA. After treatment with CHX as indicated above, expression of endogenous Snail1 and Dub3 was analysed by western blot (top panel); the intensity of Snail1 expression for each time point was quantified by densitometry and plotted (bottom panel) (mean ± s.e.m. in three separate experiments). Experiment was repeated three times and a representative experiment is presented. (**c**) Flag-Snail1 and HA-ubiquitin were co-expressed with WT or CS mutant Dub3 in HEK293 cells. After treatment with 10 μM MG132 for 6 hr, Snail1 was subjected to IP and the poly-ubiquitination of Snail1 assessed by western blot using HA antibody. IP Snail1 was blotted using Flag antibody. Input protein levels of Snail1 and Dub3 were examined using Flag and Myc antibodies, respectively. (**d**) MDA-MB231 and MDA-MB157 cells stably transfected with control, or Dub3 shRNA were treated with MG132 for 6 hr. Extracts were subjected to IP with Snail1 antibody and the poly-ubiquitination of Snail1 assessed by western blot using ubiquitin antibody. Input of Snail1 and Dub3 were analysed by western blot. (**e**) Ubiquitinated Snail1 was purified from MG132-treated HEK293 cells expressing Flag-Snail1, and then incubated with purified Myc-tagged WT-Dub3 or CS-Dub3 in a deubiquitination assay as described in Experimental Procedures. The poly-ubiquitinated state of Snail1 was assessed by western blot using HA antibody. The immuno-purified Snail1 and Dub3 used in this assay were analysed using Flag and Myc antibodies, respectively. (**f**) Flag-Snail1 was co-expressed with the indicated expression plasmids, and the expression of Snail1, Dub3, FBXL14, and β-TRCP1 were analysed by western blot. (**g**) MDA-MB231 cells were transfected with indicated siRNA and cell lysates were analysed by western blot. (**h**) Flag-Snail1 and HA-ubiquitin were co-expressed with indicated expression plasmids in HEK293 cells. After treatment with 10 μM MG132 for 6 h, Snail1 was obtained by IP and the poly-ubiquitination of Snail1 assessed detected by western blot using HA antibody. IP Snail1 was blotted using Flag antibody. Input protein levels for Dub3, FBXL14 and β-TRCP1 were assessed by western blot.

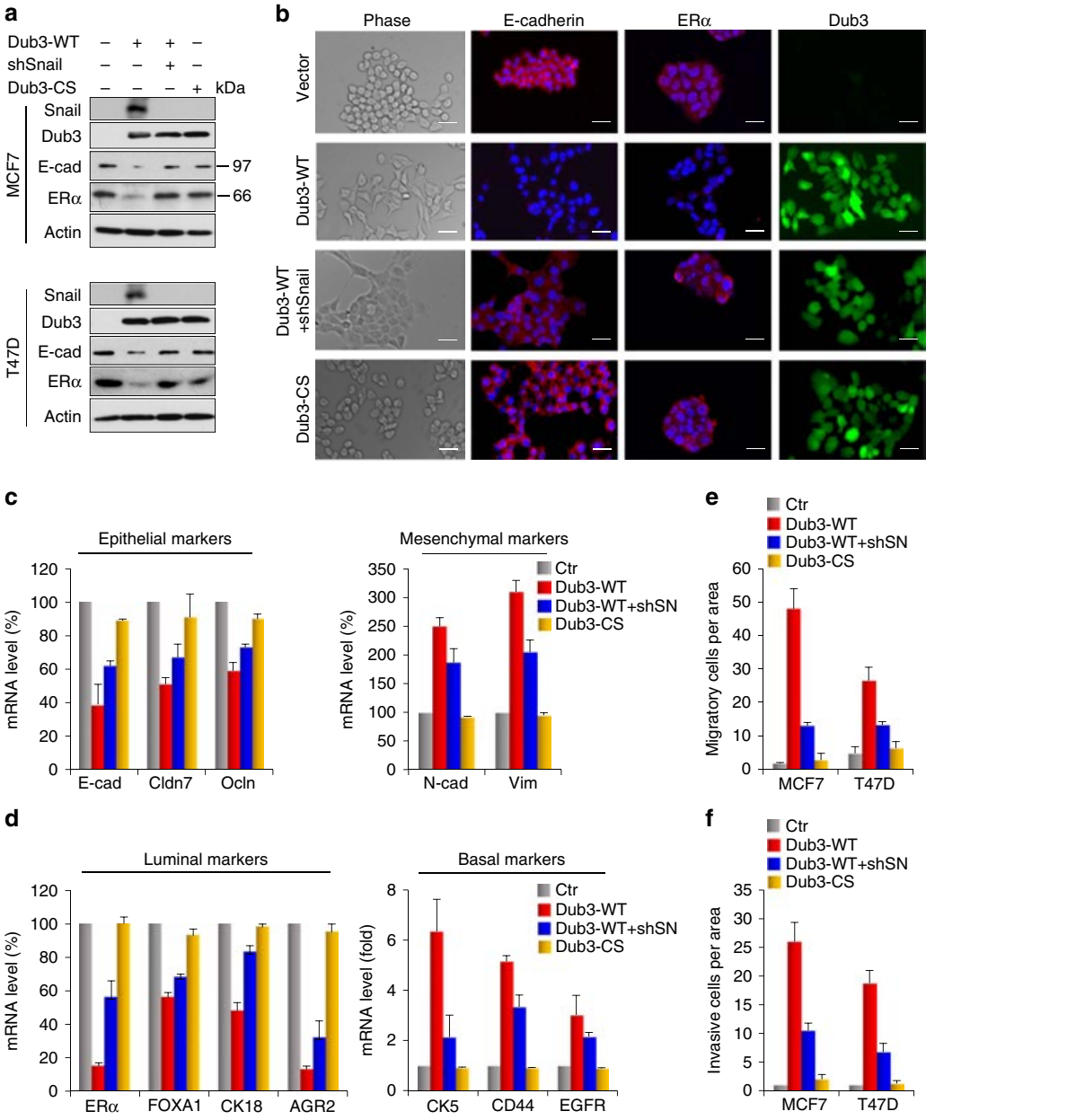

Figure 4 | Overexpression of Dub3 induces EMT. (**a**) WT- or CS-Dub3 was expressed in MCF7 and T47D cells. A rescue experiment with knockdown of Snail1 expression in WT-Dub3 expressing cells was also performed. The level of Snail1, Dub3, E-cadherin and ERα was analysed by western blot. (**b**) WT- or CS-Dub3 was expressed in MCF7 cells. A rescue experiment with knockdown of Snail1 expression in WT-Dub3 expressing cells was also performed. Morphologic changes indicative of EMT are shown in the phase contrast images; expression of E-cadherin, ERα and Dub3 was assessed by IF staining. Nuclei were visualized with DAPI (blue). Scale bars, 20 μm. (**c**,**d**) WT- or CS-Dub3 was expressed in MCF7 cells. A rescue experiment with knockdown of Snail1 expression in WT-Dub3 expressing cells was also performed. The mRNA levels of epithelial, mesenchymal (**c**), luminal, and basal (**d**) markers were quantitated by real-time PCR. Data are shown as mean ± s.d. of two separate experiments in triplicates. (**e**) Boyden chamber migration assay of modified MCF7 and T47D cells, as described in **a**. Data are presented as mean ± s.e.m. (**f**) Boyden chamber invasion assay of modified MCF7 and T47D cells, as described in **a**. Data are presented as mean ± s.e.m.

inhibiting the ubiquitination of Snail1, leading to EMT[19]. Interestingly, Dub3 was initially identified as an early response gene after stimulation by IL-6 and other cytokines[21,22]. These observations prompted us to investigate whether IL-6 induces Snail1 stabilization through Dub3 expression. We treated MDA-MB231 and MDA-MB157 cells with IL-6 (50 ng ml^{-1}) for different time intervals. Consistent with previous findings[22], Dub3 was rapidly induced in these two cell lines after 1 h of IL-6 stimulation (Fig. 7a). Snail1 was also robustly increased after 1 h of IL-6 stimulation and levels reached a maximum at 2 h. However, Snail1 mRNA levels showed no significant increase by 4 h of IL-6 treatment in these two cell lines (Supplementary Fig. 6a). In contrast, Dub3 knockdown in MDA-MB231 and MDA-MB157 cells not only reduced the endogenous level of Snail1 but also blocked IL-6-induced Snail1 stabilization (Fig. 7b).

The enzymatic activity of Dub3 is dependent on the ubiquitin carboxyl-terminal hydrolase (UCH) domain, which shares ~50% sequence similarity (including strictly conserved catalytic

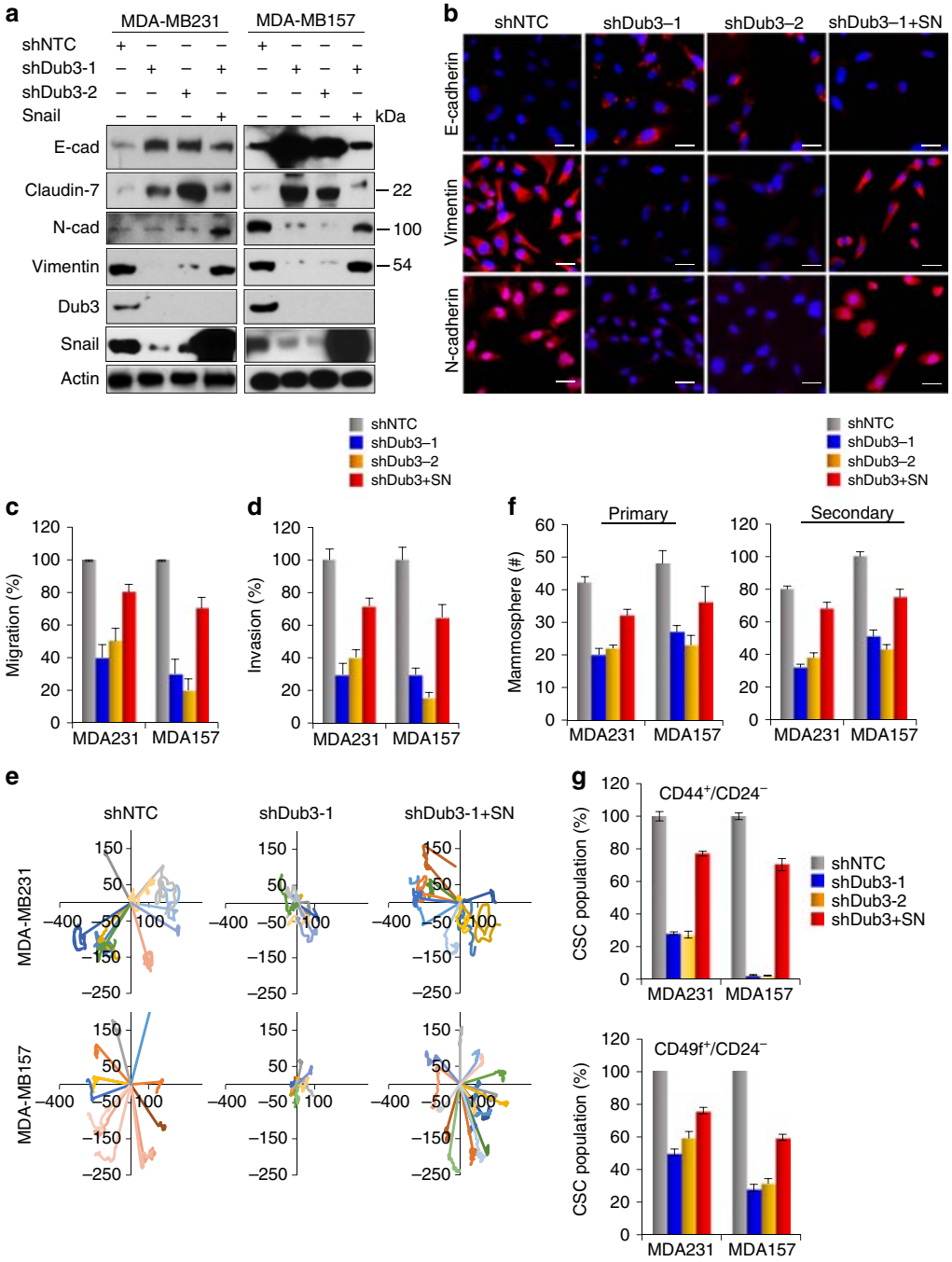

Figure 5 | Knockdown of Dub3 inhibits migration, invasion and CSC-like characteristics in BLBC cells by downregulation of Snail1. (**a**) Dub3 was knocked down by two different shRNA in MDA-MB231 and MDA-MB157 cells. Rescued Snail1 expression in these Dub3-knockdown clones were also performed. The expression of E-cadherin, Claudin-7, N-Cadherin, Vimentin, Dub3, and Snail1 was analysed by western blot. (**b**) IF images of EMT markers in MDA-MB231 cell lines described in (**a**). Scale bars, 20 μm. (**c**) Graphic representation of cell motility described in **a** analysed by a wound healing assay. Data are the percentage of migrating cells as the mean ± s.e.m. of three separate experiments. (**d**) Graphic representation of cell invasion described in **a**. Data are the percentage of vector control values (mean ± s.e.m. in three separate experiments in duplicates). (**e**) Cell trajectories of randomly selected cells described in **a**; each line indicates an individual cell's migration. (**f**) Graphic representation of primary and secondary tumorsphere-formation from cells described in **a** and are the mean ± s.d. from three independent experiments (left panel). (**g**) Graphic representation of the $CD44^{high}/CD24^{low}$ (top) and $CD49f^{high}/CD24^{low}$ population from cells described in **a** was examined by FACS analysis and are the mean ± s.e.m. from three independent experiments.

residues) with the UCH domain of USP2 (ref. 44), for which a structure has recently been reported (PDB access code 2HD5; please see 'Methods' for detail)[45]. We performed a docking analysis with several known DUB inhibitors and found that WP1130 could bind to the catalytic entry site of the UCH domain (left and middle panels, Fig. 7c)[46–48]. The physical interaction between recombinant Dub3 protein and WP1130 was further confirmed by an *in vitro* thermal shift binding assay[49]. As shown in Fig. 7c (right panel), WP1130 binding to Dub3 significantly shifted the melting temperature (Tm) of

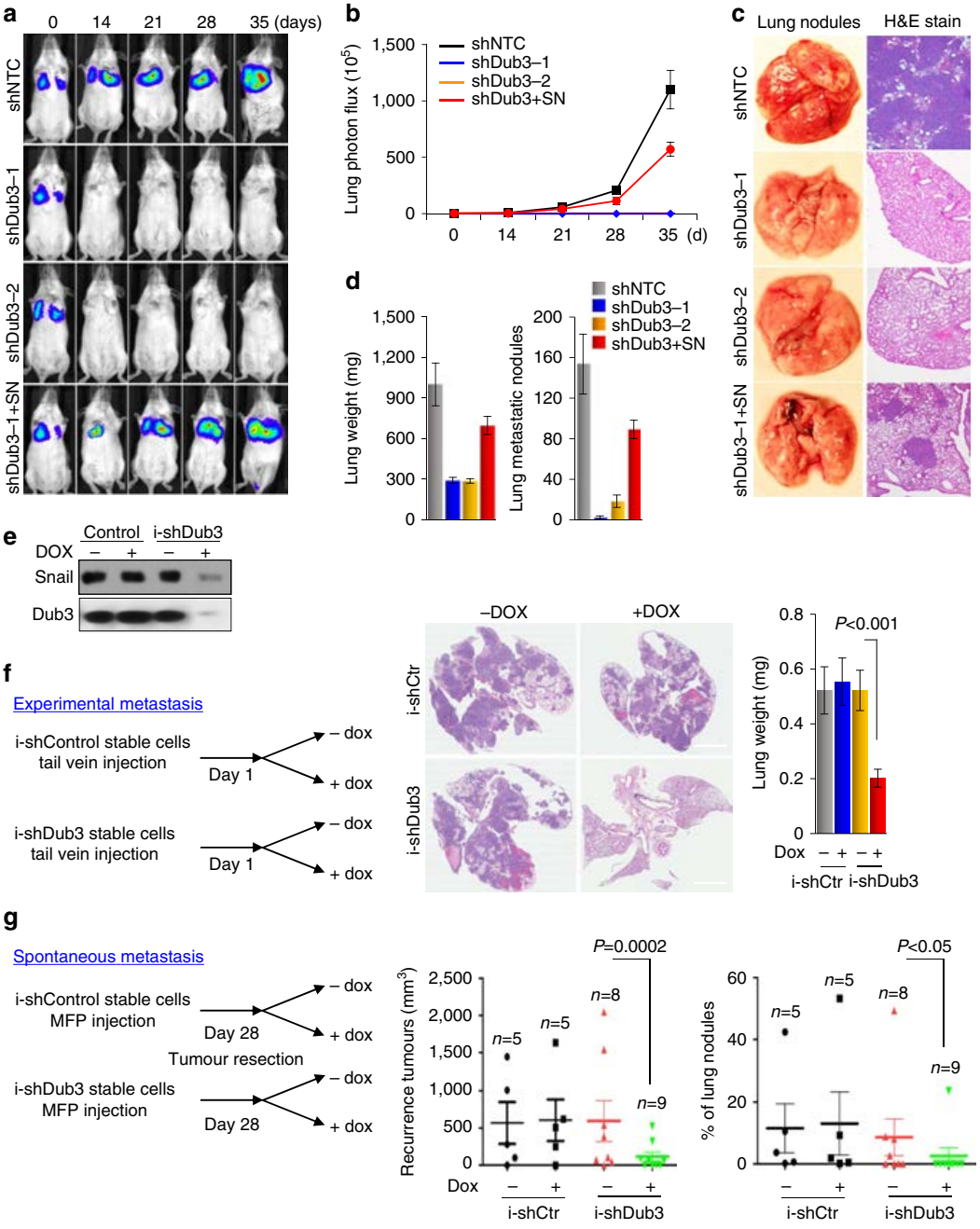

Figure 6 | Knockdown of Dub3 inhibits tumour metastasis and recurrence of breast cancer *in vivo*. (**a**) MDA-MB231-luc cells stably transfected with control, Dub3 shRNAs or Dub3-knockdown cells with Snail1 rescued expression were injected through tail vein into female SCID mice. Lung metastasis was assessed every week by bioluminescence imaging. Presented images are representative of each experimental group. (**b**) Normalized bioluminescence signals from lung metastasis in mice ($n=6$) as experiment outlined above. Data are presented as mean ± s.e.m. (**c**) Representative images of lung lesions from experimental groups in **a**. (**d**) Graphic representation of lung weight and number of metastatic nodules from mice in experimental groups described in **a**. Data are presented as mean ± s.e.m. (**e**) MDA-MB231 cells stably transduced with Dub3-inducible shRNA were treated with or without DOX. Expression of Snail1 and Dub3 were analysed by western blot. (**f**) Schematic diagram outlining the experimental metastasis model (left panel). Images are the representative H&E stained lung sections (middle panel) and quantification of lung weight (right panel) from these mice. (**g**) Schematic diagram outlining the spontaneous metastasis model (left panel). Graphic representation of recurrent tumour size (middle panel) and metastatic lung nodules from these mice (right panel). For (**f**,**g**) *P* values were determined by Student's *t*-test. Data are presented as mean ± s.e.m.

Dub3 while the furan compound (negative control) had no effect under the same conditions. Negative Tm shifts (ΔTm) can be attributed to the compound destabilizing the protein or to the compound aggregating and causing early destabilization[50]. These types of negative shifts were observed for the compounds which contain heavy metal atoms, such as bromine (Br) in WP1130, and generate energetically unfavourable strains when interacting with the proteins[51,52]. In addition, the direct binding between Dub3-UCH and WP1130 was demonstrated by the shifts during a native gel analysis in which similar dose-dependency and potential protein destabilization was observed (Supplementary Fig. 6b). These data clearly indicate that WP1130 physically interacts with Dub3 and can potentially alter its enzymatic activity. We thus

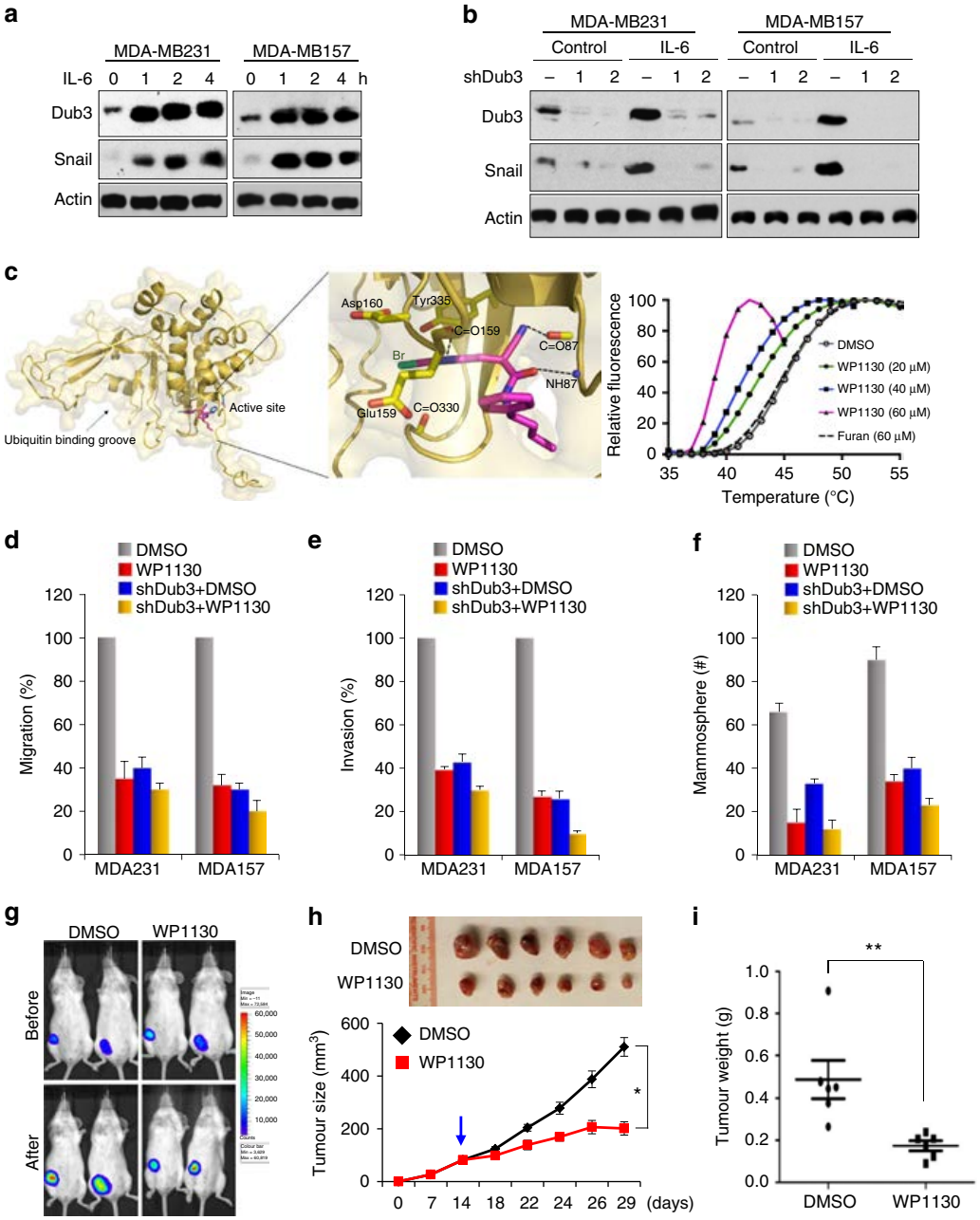

Figure 7 | Dub3 is critical for IL-6 induced Snail1 stabilization. (**a**) MDA-MB157 and MDA-MB231 cells were serum starved for 24 h, then treated with IL-6 for different time intervals. Expression of endogenous Snail1 and Dub3 were assessed by western blot. (**b**) MDA-MB231 and MDA-MB157 cells with Dub3-knockdown by two individual shRNAs or vector control were serum starved for 24 h followed by IL-6 treatment for 4 h. Expression of endogenous Snail1 and Dub3 were assessed by western blot. (**c**) A predicted model structure of Dub3 and WP1130 complex. The Dub3-UCH domain structure (yellow) is shown as ribbons while WP1130 (magenta) and the catalytic triad residues (sky blue: Cys89, His334, and Asp350) are shown as sticks. The inhibitor molecule binds to the opening surface of the active site where the ubiquitin cleavage site is presented. A zoom-up view of the interaction network is shown in the inset where the interacting residues are represented by sticks. These interactions include hydrogen bonds with backbone atoms (dotted lines) and potential halogen (Br) bonding interactions with the neighbouring electronegative atoms. Normalized melting curves (Right panel) depicting dose-dependent shifted thermal stability of Dub3 by WP1130 (coloured lines) from that of the apo protein (grey line), but not by a furan compound (dotted line; negative control). Tm for apo protein and ΔTm values for compound-bound proteins are indicated. (**d**) MDA-MB231 and MDA-MB157 cells stably expressing control vector or Dub3 shRNA were treated with 0.5 μM WP1130 for 24 h and analysed for cell migration using a wound healing assay. Graphic representation is the percentage of migration (mean ± s.e.m. in three separate experiments). (**e**) MDA-MB231 and MDA-MB157 cells stably expressing control vector or Dub3 shRNA were treated with 0.5 μM WP1130 for 4 h and analysed for cell invasion. Graphic representation is the percentage of invasive cells (mean ± s.e.m. in three separate experiments in duplicates). (**f**) MDA-MB231 and MDA-MB157 cells stably expressing control vector or Dub3 shRNA were treated with 0.5 μM WP1130 and analysed for tumorsphere-formation. Graphic representation is the number of tumorspheres (mean ± s.e.m. in three separate experiments). (**g**,**i**) MDA-MB231-luc cells were injected into the mammary fat pad of SCID mice. When tumours reached 100 mm^3, mice were divided into two groups and treated with WP1130 (50 $mg\,kg^{-1}$) or solvent, respectively. Tumour size was recorded by bioluminescence imaging before or after 2-week of treatment (**g**). Tumour growth (**h**) and weights (**i**) were measured. Presented data are the mean ± s.d. from six mice. *$P \leq 0.05$, **$P \leq 0.01$; Student's *t*-test.

Table 1 | Expression of Snail1 in different subtypes of breast tumour specimens.

	Snail1			Total	
	Negative	Low	High		
Non-TNBC					
*Luminal (ER^+)	42	38	30	110	169
†$HER2^+$	15	26	18	59	
‡TNBC (ER^-, PR^-, $HER2^-$)	21	33	111		165
Total	78	97	159		334

*$P = 0.210$, $R = -0.097$.
†$P = 0.210$, $R = 0.097$.
‡$P = 0.010$, $R = 0.488$.

Table 2 | Expression of Dub3 in different subtypes of breast tumour specimens.

	Dub3			Total	
	Negative	Low	High		
Non-TNBC					
*Luminal (ER^+)	36	45	29	110	169
†$HER2^+$	14	23	22	59	
‡TNBC (ER^-, PR^-, $HER2^-$)	32	31	102		165
Total	82	99	153		334

*$P = 0.112$, $R = -0.123$.
†$P = 0.112$, $R = 0.123$.
‡$P = 0.010$, $R = 0.379$.

Table 3 | Co-expression of Dub3 and Snail1 in different subtypes of breast cancer specimens.

Dub3	Snail1			Total		
	Negative	Low	High			
Non-TNBC						
*Luminal (ER^+)						
Negative	17	12	7	36	110	169
Low	16	13	16	45		
High	9	13	7	29		
†$HER2^+$						
Negative	3	8	3	14	59	
Low	6	12	5	23		
High	6	6	10	22		
‡TNBC (ER^-, PR^-, $HER2^-$)						
Negative	17	8	7	32		165
Low	2	15	14	31		
High	2	10	90	102		
Total	78	97	159		334	

*$P = 0.265$, $R = 0.107$.
†$P = 0.424$, $R = 0.106$.
‡$P = 0.001$, $R = 0.643$.

treated MDA-MB231 cells with WP1130 and PR619, a non-selective inhibitor of the deubiquitinating enzymes[53]. Treatment of 0.5 μM WP1130 dramatically inhibited the intrinsic and IL-6-induced Snail1 stabilization while PR619 was less effective (Supplementary Fig. 6c). These results provide proof-of-concept that a Dub3 inhibitor will suppress the function of Snail1 by promoting its degradation; the findings also provide insight into an effective treatment modality for patients with BLBC. To further assess whether WP1130 treatment can inhibit Snail1 function, we first assessed the cytotoxicity of this compound in normal human breast epithelial (MCF10A) and in tumour (MDA-MB231) cell lines. Treatment with 1 μM WP1130 for up to 48 h, did not elicit any cytotoxicity in these cells (Supplementary Fig. 6d). We then treated the cells with 0.5 μM WP1130 and performed functional assays. We found that WP130 not only reduced tumour cell migration and invasion but also inhibited tumour mammosphere formation (Fig. 7d–f, Supplementary Fig. 7a–c). The suppressive effects of WP1130 are mainly mediated through Dub3 inhibition, because Dub3 knockdown greatly reduced the suppressive effects mediated by WP1130.

In vivo studies were performed by injecting MDA-MB231 cells into the mammary fat pads of NOD-SCID mice. When tumours were $\sim 100\,mm^3$, mice were divided into two groups to receive treatments of WP1130 or solvent control for two weeks. We found that WP1130 treatments significantly inhibited tumour growth (Fig. 7g–i). Taken together, these data indicate that the Dub3–Snail1 axis is the critical 'sensor-executor module' controlling EMT in response to microenvironmental signals.

Dub3 and Snail1 are coordinately overexpressed in tumours. To further examine the Dub3–Snail1 relationship in human breast cancer, we performed immunohistochemical (IHC) analysis to examine Dub3 and Snail1 expression in a breast TMA generated by the Bio-specimen Repository in our Cancer Center at the University of Kentucky College of Medicine. The TMA contains 334 cases of breast tumour specimens, including 110 luminal, 59 HER2-overexpressing and 165 triple-negative breast cancer (TNBC) (Tables 1–3). Consistent with our observations in tumour cell lines, the intensity and distribution of Dub3 positively correlated with Snail1 in TNBC (Tables 1–3, Fig. 8a). We also found that Dub3 was upregulated in invasive tumour tissue compared with normal breast tissue from two gene expression datasets in Oncomine (Supplementary Fig. 8).

Because Snail1 expression predicts decreased relapse-free survival in women with breast cancer[54], we reasoned that women with primary breast cancers expressing high level of Dub3 relapsed at a faster rate than women whose breast cancers express low level of Dub3 in a pattern similar to that of Snail1. Therefore, we analysed two microarray expression datasets derived from primary human breast cancers in which both Dub3 expression level and clinical outcome were available. Intriguingly, individuals with high Dub3 expression had a significantly higher probability of developing distant metastasis and a reduced interval of disease-free survival (Fig. 8b). These results suggest that Dub3 expression may represent an important prognostic indicator for breast cancer in the clinical setting.

Discussion

Snail1 is a crucial transcription factor that plays an essential role in EMT, metastasis, CSC-like properties, metabolism and tumour recurrence. In this study, we found that Dub3 is a bona fide DUB for Snail1. The function of Dub3 is likely conserved from *Drosophila* to mammals, and knockdown of Dub3 increases, whereas Dub3 expression decreases, the ubiquitination and degradation of Snail1. The loss of Dub3 can be rescued by expressing exogenous Snail1. Most critically, a tight correlation between Dub3 and Snail1 on multiple cancer cell lines and human breast tumour specimens confirms their potential regulation. Our study provides several new insights into the involvement of ubiquitination in breast cancer metastasis. First, our study suggests that the Dub3–Snail1 signalling axis represents an important 'sensor-executor' module in breast cancer. It has

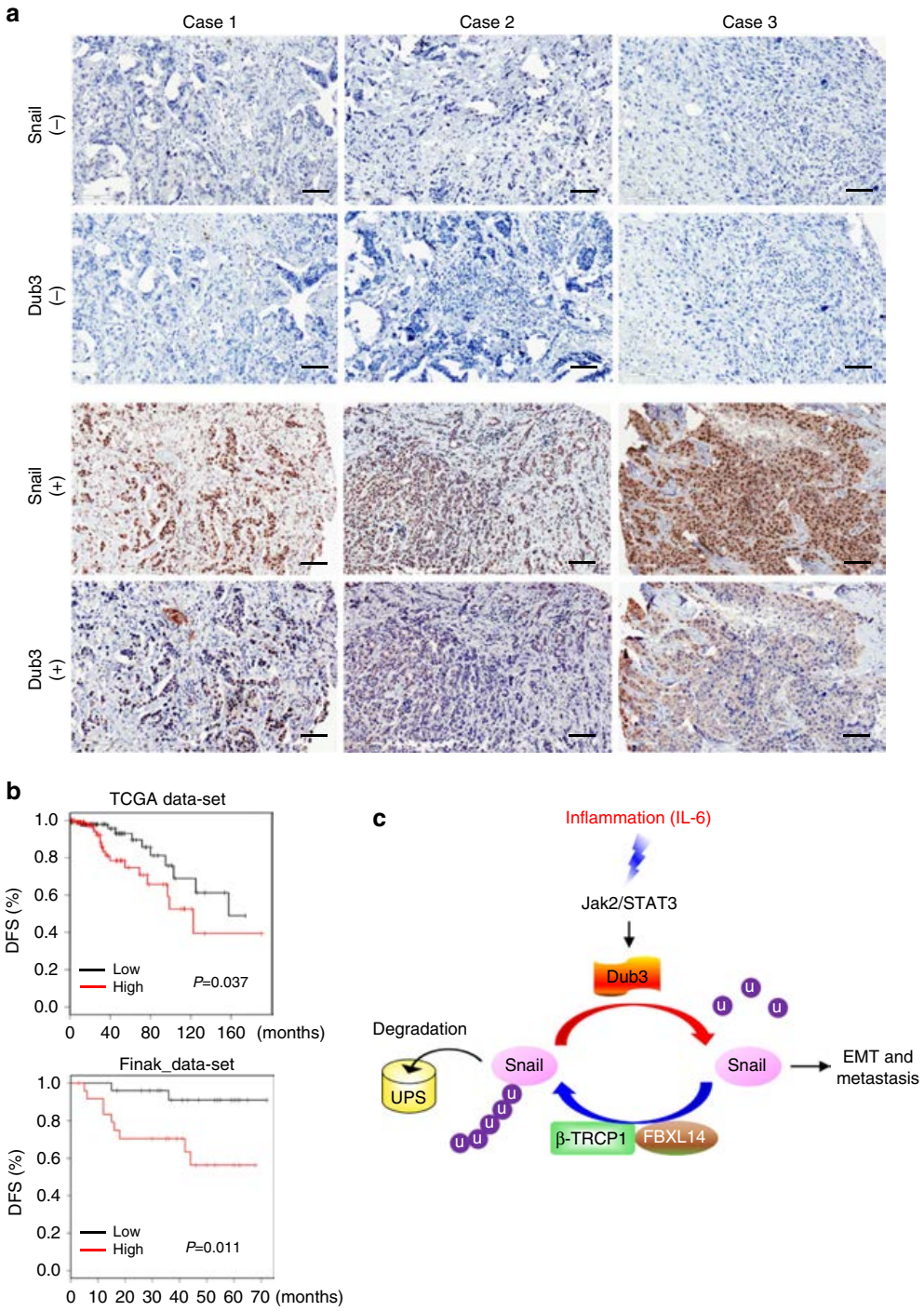

Figure 8 | Expression of Dub3 and Snail1 are positively correlated in breast cancer patients. (**a**) The 334 surgical specimens of breast cancer were immunostained using antibodies against Dub3, Snail1, and the control serum (data not shown). Images with consecutive IHC staining of both Dub3 and Snail1 in six cases of breast tumours (top panel: three cases of negative staining; bottom panel: three cases of positive) are shown (Scale bars, 50 μm). Statistical analysis is shown Tables 1-3. (**b**) Kaplan–Meier plots of distant metastasis-free survival of patients, stratified by expression of Dub3. Data obtained from the TCGA and Finak database. *P*-values represent log-rank testing of the difference in cumulative survival. (**c**) A proposed model to illustrate Dub3 induces Snail1 stabilization through a deubiquitination event. IL-6 induces the expression of Dub3, which antagonizes the function Snail1's ubiquitin E3 ligase (such as FBXL14 and β-TRCP1), leading to Snail1 stabilization and the acquisition of EMT and metastasis.

been noted that the migration and invasive capabilities of tumour cells at the invasive front are initiated and propelled by an inflammatory microenvironment through the induction of EMT. IL-6, a major cytokine present in the tumour microenvironment, can induce EMT and promote metastasis through the STAT3 signalling pathway in breast cancer, head and neck cancer and pancreatic cancer[55]. Elevated IL-6 level predicts tumour recurrence, poor response to chemotherapy, poor survival and tumour metastasis[56]. IL-6 is also identified as a major cytokine secreted by BLBC cells and is essential for the CSC-like characteristic of BLBC[57]. Therefore, it is likely that BLBC cells and infiltrated TAMs secrete IL-6 and provide

autocrine and paracrine feed-forward mechanisms, respectively, to sustain EMT and maintain CSC-like traits. Intriguingly, BLBC cells contain high levels of Dub3 and Snail1 and possess invasiveness and CSC-like characteristics. In contrary, the ERα-positive luminal subtype breast tumour cells (such as MCF7 and T47D), do not express IL-6 (ref. 55) and contain little Snail1. Interestingly, Dub3 is an early response gene of IL-6, and our study indicates that Dub3 is a critical deubiquitinase of Snail1. Therefore, Dub3 is one of the 'long-sought' missing molecule that senses extracellular inflammatory signals and converts them to Snail1 stabilization, which leads to the acquisition of CSC-like traits, invasion and therapeutic resistance in BLBC (Fig. 8c).

Second, our study indicates that Dub3 can block the activity of β-TRCP1 and FBXL14 to stabilize Snail1. Three E3 ligases have been identified that mediate Snail1 degradation. We previously demonstrated that GSK-3β phosphorylates Snail1 and promotes its nuclear export and interaction with β-TRCP1 (ref. 11). FBXL14, the human homologue of the Partner of Paired (Ppa) gene product which degrades Snail1 in *Xenopus laevis*, also degrades Snail1 in a phosphorylation-independent manner[18]. Recently, it has been shown that Snail1 can also be degraded by FBXO11 in a PDK1 phosphorylation-dependent manner in the nucleus[17,58]. It is likely that these different F-box containing E3 ligases function differently under diverse cellular contexts. We found that Dub3 can counteract the function of β-TRCP1 and FBXL14 by stabilizing Snail1. Intriguingly, both β-TRCP1 and FBXL14 can also modulate the degradation of other EMT-TFs, such Slug and Twist[18,59,60]. Whether Dub3 can also counteract the function of β-TRCP1 and FBXL14 in stabilizing Slug and Twist is a question that requires further investigation.

Third, our study indicates that Dub3 is an excellent therapeutic target for the inhibition of breast cancer metastasis and recurrence. Snail1 becomes stabilized and elevated in BLBC, but there is no clear ligand-binding domain for targeting Snail1, which creates a formidable obstacle for the development of small molecules to inhibit Snail1's functions. Our results indicate that Dub3 is a crucial molecule controlling inflammation-mediated Snail1 stabilization. Indeed, WP1130, which can bind to the catalytic entry site of the Dub3 UCH domain, blocked tumour cell migration, invasion and suppressed CSC-like properties. These data provide a proof-of-concept for therapeutic development of small molecules to inhibit the activity of Dub3 in metastatic breast cancer. Consistent with our findings, DUBs have emerged as a potential therapeutic target, given their role in several human diseases including cancer[61]. For example, the efficacy of a small molecule inhibitor of USP7 in multiple myeloma disease models provide the rationale for the development of next-generation USP-based therapies, and specifically demonstrates the promise of therapeutics targeting DUB to improve patient outcome[62]. Previously, Dub3 has been demonstrated to regulate both cell proliferation and G1/S cell-cycle progression and is increased in tumours. The current data strengthens the view that Dub3 is an ideal candidate for the development of potential inhibitors for cancer treatment based on the dual role of Dub3 in regulating cell growth and metastasis.

Methods

Plasmids and reagents. Plasmids of wild-type and deletion mutants for Snail1 were generated as described[26]. The WT-Dub3 was from addgene. Dub3 (C89S) was generated using the QuikChange Mutagenesis kit (Stratagene, La Jolla, CA) as described previously[31]. All sequences were verified by DNA sequencing. Deletion mutants of Dub3 were constructed as described previously[31]. Antibodies used include: anti-Flag (F3165, 1:4,000, anti-Actin (A2228, 1:10,000), anti-Myc (9E10, 1:3,000) from Sigma-Aldrich (St. Louis, MO), Anti-Dub3 (Abcam, ab12991, 1:1,000); anti-Ub (Millipore, MAB1510, 1:500), N-cadherin (Upstate, 05-915, 1:1,000), anti-Snail1 (Cell Signaling, 4719, 1:1,000), Vimentin (Ab-2, 1:2,000) and ERα (Ab-15, 1:1,000) from Neomarkers, anti-HA (Roche, 3F10, 1:10,000), and anti-E-cadherin (610181, 1:10,000, BD Bioscience) and Claudin-7 (Abcam, ab27487, 1:1,000). Dub3 shRNA expression plasmids were purchased from MISSION shRNA at Sigma-Aldrich (St. Louis, MO). WP1130 and PR619 were from Selleck. Smartpool siRNA against human Dub3 was from Dharmacon (Chicago, IL).

Cell culture. The human embryonic kidney HEK293, breast cancer MDA-MB231, MDA-MB157, MCF7, SKBR3, and colon cancer HCT116, HT-29 cell lines were purchased from the American Type Culture Collection (Manassas, VA) and grown in Dulbecco's modified Eagle's/F12 medium plus 10% fetal bovine serum as described previously[26]. Breast cancer cell lines (T47D, ZR75, BT474) and prostate cancer cell lines (LNCaP, Du145, PC3) were grown in RPMI1640 plus 10% FBS. The culture medium for SUM159 and SUM149 is Ham's F-12 (Invitrogen) supplemented with 5% FBS, 5 μg ml^{-1} insulin, and 1 μg ml^{-1} hydrocortisone (Sigma, St. Louis, MO). All the cells lines are routinely checked for morphological and growth changes to probe for cross-contaminated, or genetically drifted cells. If any of these features occur, we use the short tandem repeat (STR) profiling service by ATCC to re-authenticate the cell lines.

Small interfering RNA library screening. The human deubiquitinating enzyme siGENOME RTF Library was purchased from Dharmacon (Chicago, IL). The screen was performed according to manufacturer's instructions. In brief, the cells were added to the rehydrated Dharmacon RTF siRNA library plates. Two days later, the cell lysates were extracted and the expression of Snail1 was detected with western blot.

Invasion assay. Invasion assays were performed in Boyden chambers coated with Matrigel as instructed by the manufacturer (BD Biosciences, San Jose, CA). Various cancer cell lines were seeded on the top of the Matrigel in the upper chamber while the bottom chambers were filled with non-serum culture medium plus 100 nM LPA. The invasive cancer cells were stained with crystal violent. All experiments were performed in triplicate.

Single-cell migration assay. Cells were seeded on glass-bottomed dishes (MatTek, Ashland, MA, USA) that had been coated with 5 μg ml^{-1} fibronectin. Real-time images were taken under Nikon Biostation IMQ Cell every 10 min for 6 h. The movement of individual cells was analysed using NIS-Element AR Software (Nikon), and the distance that was travelled during time was measured as indicated.

GST pull-down assay. Glutathione-*S*-transferase proteins were expressed as described previously[31]. Cells were subjected to lysis in GST pull-down buffer (20 mM Tris, 150 mM NaCl and 1% Nonidet P-40 with protease cocktail) and rotated with glutathione–Sepharose-bound GST-Snail1 or GST-Dub3. The binding complexes were eluted with SDS–PAGE sample buffer. About one-tenth of these eluents were analysed by western blot and the rest were examined for the presence of purified GST protein by Coomassie Blue staining.

Immunoprecipitation and western blotting. For protein extraction, 5×10^5 cells per well were plated onto six-well plates and transiently transfected with indicated expression plasmids. At 48 h after transfection, cells were incubated with or without the proteasome inhibitor MG132 (10 μM) for an additional 6 h before protein extraction and western blot analysis. Primary antibodies against Flag (M2, 1:1,000) and HA (3F10, 1:4,000) were used for protein detection. For IP, HEK293 cells transfected with the indicated expression plasmids were lysed in buffer (50 mM Tris (pH 7.5), 150 mM NaCl, 5 μg ml^{-1} aprotinin, 1 μg ml^{-1} pepstatin, 1% Nonidet P-40, 1 mM EDTA and 0.25% deoxycholate). Total cell lysates (1,000 μl) were incubated overnight with 1 μg of anti-HA or anti-Flag antibody conjugated to agarose beads (Roche Molecular Biochemicals) at 4 °C. The beads were then washed with lysis buffer, and the immunoprecipitated protein complexes were resolved by 10% SDS–PAGE. Some important original immunoblotting results are shown in Supplementary Fig. 9.

Immunofluorescence staining. For IF microscopy, cells were grown on cover slips, fixed with 4% paraformaldehyde and incubated overnight with anti-Dub3 and anti-Snail1 antibodies. Proteins were visualized by incubation with goat anti-mouse conjugated with Alexa fluor 568 and goat-anti-rabbit conjugated with Alexa fluor 488, respectively (Invitrogen, Carlsbad, CA). Finally, cover slips were incubated with 4′,6′-diamidino-2-phenylindole (Sigma-Aldrich) for 20 min and visualized under a fluorescent microscope.

Immunohistochemical staining. Breast cancer tissue microarray (TMA) of 334 cases of invasive ductal carcinomas is obtained from the tissue bank at the Markey Cancer Center's tissue repository at our institute. Tissue samples were

stained with anti-Dub3 (Abcam, ab12991, 1:100 dilution) and anti-Snail1 (Abcam, ab53519, 1:250 dilution) antibodies, and each sample was scored by an *H*-score method that combines the values of immunoreaction intensity and the percentage of tumour cell staining as described previously[19]. Chi-square analysis was used to analyse the relationship between Dub3 and Snail1 expression; statistical significance was defined as $P<0.05$.

Quantitative real-time PCR. Total RNA was isolated using RNeasy Mini kit (Qiagen) according to the manufacturer's instructions. Specific quantitative real-time PCR experiments were performed using SYBR Green Power Master Mix following manufacturer's protocol (Applied Biosystems).

Fluorescence-activated cell sorting. Cells were detached from plates and incubated with anti-human CD44 and anti-human CD24 (PE-conjugated, ebioscience) or anti-human CD49f (PE/Cy7 CD49f, e-Bioscience), finally analysed using a FACSCalibur flow cytometer.

Tumorsphere formation assay. Tumorsphere cultures were performed as described in Dontu *et al.*[63]. In brief, Cell monolayers were plated as single-cell suspensions on ultra-low attachment plates (Corning) in DMEM/F12 medium supplemented with 20 ng ml^{-1} EGF, 10 µg ml^{-1} insulin, 0.5 µg ml^{-1} hydrocortisone and B27. Tumorspheres were counted via visual inspection after 5–10 days.

***In vivo* ubiquitination assay.** HEK293 cells were transfected with HA-ubiquitin, Flag-Snail1 and Myc-Dub3 plasmids as indicated. The cells were treated for 6 h with 10 µM MG132 at 48 h post transfection, and then lysed. The samples were immunoprecipitated using anti-Flag agarose (Sigma).

***In vitro* deubiquitination assay.** The *in vitro* deubiquitination was performed as described[32]. Briefly, HA-ubiquitin and Flag-Snail1 were co-expressed in HEK293 cells. After cells were treated with 10 µM MG132 for 6 h, ubiquitinated Snail1 was isolated by IP with Flag antibody. In a parallel experiment, Myc-Dub3 (WT or CS) or vector was expressed in HEK293 cells, and purified by IP with anti-Myc Affinity Matrix (Roche, USA). The purified Dub3 was eluded with Myc peptide, dialyzed and subsequently incubated with ubiquitinated Snail1 in a deubiquitination reaction buffer (50 mM HEPES, pH 7.5, 100 mM NaCl, 5% glycerol, 5 mM $MgCl_2$, 1 mM ATP and 1 mM DTT) at 30 °C. The ubiquitinated status of Snail1 was analysed by western blot with HA antibody.

Complex model structure of Dub3 and WP1130. For protein–ligand docking studies, the three-dimensional (3D) structure of Dub3-UHC was built by comparative protein structure modelling from the homologous USP2 crystal structure (PDB access code 2HD5) as a template using the programme MODELLER[64]. The WP1130 atomic coordinates were generated using the stereochemistry information stored in PubChem. The complex structure was modelled using the SwissDock protein-small molecule docking simulation software[65]. This software adopts the CHARMM simulation programme[66], which preforms numerous conformational and path sampling methods, free energy estimates, molecular minimization, dynamics and analysis techniques. This programme has been known to be highly successful for small and relatively rigid ligands with <10 flexible rotatable bonds.

Fluorescence based thermal shift assay. Purified recombinant Dub3 protein was used to screen small molecule compounds in a fluorescence based thermal shift assay[49]. Dub3 protein was dispersed in a buffer containing 20 mM HEPES, pH 7.0 and 150 mM NaCl. The final protein concentration in a 20 µl reaction volume was 10 µM. Ligands to be tested were added at 2×, 4×, or 6× concentration such that the DMSO concentration never exceeded 2%. SYPRO Orange dye (Invitrogen) was added last at a 5× concentration. The PCR tubes were then sealed, centrifuged and heated from 25 to 95° at a rate of 1° per min on 7500 Real-Time PCR machine (Applied Biosystems). Raw data analysis and curve fitting to calculate Tm values was performed as described.

***In vivo* tumorigenesis assay.** Female SCID mice (6–8 week old) were purchased from Taconic (Germantown, NY) and maintained and treated under specific pathogen-free conditions. All procedures were approved by the Institutional Animal Care and Use Committee at the University of Kentucky College of Medicine and conform to the legal mandates and federal guidelines for the care and maintenance of laboratory animals. Mice were injected with the breast cancer MDA-MB231-luc cells and corresponding stable clones with knockdown of Dub3 or Snail1 expression (5×10^5 cells per mouse, 6 mice per group) via tail vein injection. Lung metastasis was monitored by the IVIS bioluminescence imaging system.

For the spontaneous metastatic model, mice were injected with the breast cancer MDA-MB231-luc cells and corresponding inducible stable cells via mammary gland fat pad. The growth of the primary tumour was monitored by external caliper measurement once a week. When tumours were ~1 cm^3, the primary tumour was surgically removed and the incision was closed with wound clips. The mice were randomly separated into two groups and treated with or without doxycycline in the drinking water. Animals were euthanized 5 weeks after primary tumour removal to investigate the development of pulmonary metastasis.

For animals subjected to drug treatment, MDA-MB231-luc cells were injected into the mammary gland fat pad of 8-week-old female SCID mice. Tumour growth was monitored with caliper measurements. When tumours were ~100 mm^3 in size, WP1130 was administered every other day for 2 weeks. Data were analysed using the Student's *t*-test; a *P* value <0.05 was considered significant.

Patient samples. The frozen fresh tumour samples were collected from resected breast tumours from patients at our institute with the approval of the Institutional Review Board. These frozen samples were 'snap-frozen' in liquid nitrogen and stored at −80 °C. Each sample was examined histologically with hematoxylin and eosin (H&E) stained sections. Regions from tumour samples were microdissected and examined. Only samples with a consistent tumour cell content of more than 75% in tissues were used for analysis. Samples were then homogenized using 20 strokes of a Dounce homogenizer in 1 ml of homogenizing buffer. Following centrifugation, pellets were re-suspended in lysis buffer and processed for western blot.

Data availability. The data that support the findings of this study are available from the corresponding authors upon reasonable request.

References

1. Van't Veer, L. J. & Weigelt, B. Road map to metastasis. *Nat. Med.* **9,** 999–1000 (2003).
2. Thiery, J. P. Epithelial-mesenchymal transitions in tumour progression. *Nat. Rev. Cancer* **2,** 442–454 (2002).
3. Thiery, J. P., Acloque, H., Huang, R. Y. & Nieto, M. A. Epithelial-mesenchymal transitions in development and disease. *Cell* **139,** 871–890 (2009).
4. Nieto, M. A. The snail superfamily of zinc-finger transcription factors. *Nat. Rev. Mol. Cell Biol.* **3,** 155–166 (2002).
5. Yang, J. *et al.* Twist, a master regulator of morphogenesis, plays an essential role in tumor metastasis. *Cell* **117,** 927–939 (2004).
6. Thiery, J. P. & Sleeman, J. P. Complex networks orchestrate epithelial-mesenchymal transitions. *Nat. Rev. Mol. Cell Biol.* **7,** 131–142 (2006).
7. Zheng, H. & Kang, Y. Multilayer control of the EMT master regulators. *Oncogene* **33,** 1755–1763 (2014).
8. Parker, B. S. *et al.* Alterations in vascular gene expression in invasive breast carcinoma. *Cancer Res.* **64,** 7857–7866 (2004); erratum **64,** 8794 (2004).
9. Blanco, M. J. *et al.* Correlation of Snail expression with histological grade and lymph node status in breast carcinomas. *Oncogene* **21,** 3241–3246 (2002).
10. Cheng, C. W. *et al.* Mechanisms of inactivation of E-cadherin in breast carcinoma: modification of the two-hit hypothesis of tumor suppressor gene. *Oncogene* **20,** 3814–3823 (2001).
11. Zhou, B. P. *et al.* Dual regulation of Snail by GSK-3beta-mediated phosphorylation in control of epithelial-mesenchymal transition. *Nat. Cell Biol.* **6,** 931–940 (2004).
12. Elloul, S. *et al.* Snail, Slug, and Smad-interacting protein 1 as novel parameters of disease aggressiveness in metastatic ovarian and breast carcinoma. *Cancer* **103,** 1631–1643 (2005).
13. Kajita, M., McClinic, K. N. & Wade, P. A. Aberrant expression of the transcription factors Snail and Slug alters the response to genotoxic stress. *Mol. Cell. Biol.* **24,** 7559–7566 (2004).
14. Mani, S. A. *et al.* The epithelial-mesenchymal transition generates cells with properties of stem cells. *Cell* **133,** 704–715 (2008).
15. Dong, C. *et al.* Loss of FBP1 by Snail-mediated repression provides metabolic advantages in basal-like breast cancer. *Cancer Cell* **23,** 316–331 (2013).
16. Barrallo-Gimeno, A. & Nieto, M. A. The Snail genes as inducers of cell movement and survival: implications in development and cancer. *Development* **132,** 3151–3161 (2005).
17. Zheng, H. *et al.* PKD1 phosphorylation-dependent degradation of SNAIL by SCF-FBXO11 regulates epithelial-mesenchymal transition and metastasis. *Cancer Cell* **26,** 358–373 (2014).
18. Vinas-Castells, R. *et al.* The hypoxia-controlled FBXL14 ubiquitin ligase targets SNAIL1 for proteasome degradation. *J. Biol. Chem.* **285,** 3794–3805 (2010).
19. Wu, Y. *et al.* Stabilization of snail by NF-kappaB is required for inflammation-induced cell migration and invasion. *Cancer Cell* **15,** 416–428 (2009).
20. Reyes-Turcu, F. E., Ventii, K. H. & Wilkinson, K. D. Regulation and cellular roles of ubiquitin-specific deubiquitinating enzymes. *Annu. Rev. Biochem.* **78,** 363–397 (2009).
21. Baek, K. H. Cytokine-regulated protein degradation by the ubiquitination system. *Curr. Protein Pept. Sci.* **7,** 171–177 (2006).
22. Burrows, J. F. *et al.* DUB-3, a cytokine-inducible deubiquitinating enzyme that blocks proliferation. *J. Biol. Chem.* **279,** 13993–14000 (2004).
23. Pereg, Y. *et al.* Ubiquitin hydrolase Dub3 promotes oncogenic transformation by stabilizing Cdc25A. *Nat. Cell Biol.* **12,** 400–406 (2010).

24. van der Laan, S., Tsanov, N., Crozet, C. & Maiorano, D. High Dub3 expression in mouse ESCs couples the G1/S checkpoint to pluripotency. *Mol. Cell* **52,** 366–379 (2013).
25. Zhou, B., Shu, B., Xi, T., Su, N. & Liu, J. Dub3 expression correlates with tumor progression and poor prognosis in human epithelial ovarian cancer. *Biomed. Pharmacother.* **70,** 84–89 (2015).
26. Lin, Y. *et al.* The SNAG domain of Snail1 functions as a molecular hook for recruiting lysine-specific demethylase 1. *EMBO J.* **29,** 1803–1816 (2010).
27. Dong, C. *et al.* Interaction with Suv39H1 is critical for Snail-mediated E-cadherin repression in breast cancer. *Oncogene* **32,** 1351–1362 (2012).
28. Dong, C. *et al.* G9a interacts with Snail and is critical for Snail-mediated E-cadherin repression in human breast cancer. *J. Clin. Invest.* **122,** 1469–1486 (2012).
29. Gondo, Y. *et al.* Human megasatellite DNA RS447: copy-number polymorphisms and interspecies conservation. *Genomics* **54,** 39–49 (1998).
30. Leptin, M. & Grunewald, B. Cell shape changes during gastrulation in *Drosophila*. *Development* **110,** 73–84 (1990).
31. Wu, Y., Evers, B. M. & Zhou, B. P. Small C-terminal domain phosphatase enhances snail activity through dephosphorylation. *J. Biol. Chem.* **284,** 640–648 (2009).
32. Dupont, S. *et al.* FAM/USP9x, a deubiquitinating enzyme essential for TGFbeta signaling, controls Smad4 monoubiquitination. *Cell* **136,** 123–135 (2009).
33. Yook, J. I., Li, X. Y., Ota, I., Fearon, E. R. & Weiss, S. J. Wnt-dependent regulation of the E-cadherin repressor Snail. *J. Biol. Chem.* **280,** 11740–11748 (2005).
34. Al-Hajj, M., Wicha, M. S., Benito-Hernandez, A., Morrison, S. J. & Clarke, M. F. Prospective identification of tumorigenic breast cancer cells. *Proc. Natl Acad. Sci. USA* **100,** 3983–3988 (2003).
35. Cordenonsi, M. *et al.* The Hippo transducer TAZ confers cancer stem cell-related traits on breast cancer cells. *Cell* **147,** 759–772 (2011).
36. Marotta, L. L. *et al.* The JAK2/STAT3 signaling pathway is required for growth of CD44CD24 stem cell-like breast cancer cells in human tumors. *J. Clin. Invest.* **121,** 2723–2735 (2011).
37. Pattabiraman, D. R. *et al.* Activation of PKA leads to mesenchymal-to-epithelial transition and loss of tumor-initiating ability. *Science* **351,** aad3680 (2016).
38. Su, Y. *et al.* Somatic cell fusions reveal extensive heterogeneity in basal-like breast cancer. *Cell Rep.* **11,** 1549–1563 (2015).
39. Lo, P. K. *et al.* CD49f and CD61 identify Her2/neu-induced mammary tumor-initiating cells that are potentially derived from luminal progenitors and maintained by the integrin-TGFbeta signaling. *Oncogene* **31,** 2614–2626 (2012).
40. Meyer, M. J. *et al.* $CD44^{pos}CD49f^{hi}CD133/2^{hi}$ defines xenograft-initiating cells in estrogen receptor-negative breast cancer. *Cancer Res.* **70,** 4624–4633 (2010).
41. To, K. *et al.* Y-box binding protein-1 induces the expression of CD44 and CD49f leading to enhanced self-renewal, mammosphere growth, and drug resistance. *Cancer Res.* **70,** 2840–2851 (2010).
42. Yin, Y. *et al.* CD151 represses mammary gland development by maintaining the niches of progenitor cells. *Cell Cycle* **13,** 2707–2722 (2014).
43. Nieto, M. A. Epithelial plasticity: a common theme in embryonic and cancer cells. *Science* **342,** 1234850 (2013).
44. Zhang, W. *et al.* Contribution of active site residues to substrate hydrolysis by USP2: insights into catalysis by ubiquitin specific proteases. *Biochemistry* **50,** 4775–4785 (2011).
45. Samara, N. L., Ringel, A. E. & Wolberger, C. A role for intersubunit interactions in maintaining SAGA deubiquitinating module structure and activity. *Structure* **20,** 1414–1424 (2012).
46. Thrane, S. *et al.* A kinase inhibitor screen identifies Mcl-1 and Aurora kinase A as novel treatment targets in antiestrogen-resistant breast cancer cells. *Oncogene* **34,** 4199–4210 (2015).
47. Juliana, C. *et al.* Non-transcriptional priming and deubiquitination regulate NLRP3 inflammasome activation. *J. Biol. Chem.* **287,** 36617–36622 (2012).
48. Qiu, M. *et al.* Pyrrolidine dithiocarbamate inhibits herpes simplex virus 1 and 2 replication, and its activity may be mediated through dysregulation of the ubiquitin-proteasome system. *J. Virol.* **87,** 8675–8686 (2013).
49. Niesen, F. H., Berglund, H. & Vedadi, M. The use of differential scanning fluorimetry to detect ligand interactions that promote protein stability. *Nat. Protoc.* **2,** 2212–2221 (2007).
50. Cummings, M. D., Farnum, M. A. & Nelen, M. I. Universal screening methods and applications of ThermoFluor. *J. Biomol. Screen.* **11,** 854–863 (2006).
51. McDonnell, P. A. *et al.* Assessing compound binding to the Eg5 motor domain using a thermal shift assay. *Anal. Biochem.* **392,** 59–69 (2009).
52. Silvestre, H. L., Blundell, T. L., Abell, C. & Ciulli, A. Integrated biophysical approach to fragment screening and validation for fragment-based lead discovery. *Proc. Natl Acad. Sci. USA* **110,** 12984–12989 (2013).
53. Altun, M. *et al.* Activity-based chemical proteomics accelerates inhibitor development for deubiquitylating enzymes. *Chem. Biol.* **18,** 1401–1412 (2011).
54. Moody, S. E. *et al.* The transcriptional repressor Snail promotes mammary tumor recurrence. *Cancer Cell* **8,** 197–209 (2005).
55. Sullivan, N. J. *et al.* Interleukin-6 induces an epithelial-mesenchymal transition phenotype in human breast cancer cells. *Oncogene* **28,** 2940–2947 (2009).
56. Berishaj, M. *et al.* Stat3 is tyrosine-phosphorylated through the interleukin-6/glycoprotein 130/Janus kinase pathway in breast cancer. *Breast Cancer Res.* **9,** R32 (2007).
57. Marotta, L. L. *et al.* The JAK2/STAT3 signaling pathway is required for growth of $CD44^{+}CD24^{-}$ stem cell-like breast cancer cells in human tumors. *J. Clin. Invest.* **121,** 2723–2735 (2011).
58. Jin, Y. *et al.* FBXO11 promotes ubiquitination of the Snail family of transcription factors in cancer progression and epidermal development. *Cancer Lett.* **362,** 70–82 (2015).
59. Frescas, D. & Pagano, M. Deregulated proteolysis by the F-box proteins SKP2 and beta-TrCP: tipping the scales of cancer. *Nat. Rev. Cancer* **8,** 438–449 (2008).
60. Zhong, J., Ogura, K., Wang, Z. & Inuzuka, H. Degradation of the transcription factor Twist, an oncoprotein that promotes cancer metastasis. *Discov. Med.* **15,** 7–15 (2013).
61. Nicholson, B., Marblestone, J. G., Butt, T. R. & Mattern, M. R. Deubiquitinating enzymes as novel anticancer targets. *Future Oncol.* **3,** 191–199 (2007).
62. Chauhan, D. *et al.* A small molecule inhibitor of ubiquitin-specific protease-7 induces apoptosis in multiple myeloma cells and overcomes bortezomib resistance. *Cancer Cell* **22,** 345–358 (2012).
63. Dontu, G. *et al. In vitro* propagation and transcriptional profiling of human mammary stem/progenitor cells. *Genes Dev.* **17,** 1253–1270 (2003).
64. Webb, B. & Sali, A. Comparative protein structure modeling using MODELLER. *Curr. Protoc. Bioinform.* **47,** 5.6.1–5.6.32 (2014).
65. Grosdidier, A., Zoete, V. & Michielin, O. SwissDock, a protein-small molecule docking web service based on EADock DSS. *Nucleic Acids Res.* **39,** W270–W277 (2011).
66. Brooks, B. R. *et al.* CHARMM: the biomolecular simulation program. *J. Comput. Chem.* **30,** 1545–1614 (2009).

Acknowledgements

We thank Dr Cathy Anthony for critical reading and editing of this manuscript. We also thank Drs Diaz VM and de Herreros AG for providing Snail1 K3R and FBXL14 plasmids. This research was supported by the Shared Resources of the University of Kentucky Markey Cancer Center (P30CA177558 to B.M.E.). This work was also supported by grants from NIH (CA125454 and CA188118), DoD (BC140733P1), Mary Kay Ash Foundation and the Frankfort Country Club's Ladies Golf Association (to B.P. Zhou), and American Cancer Society Research Scholar Award (RSG13187) (to Y.Wu).

Author contributions

Y.Wu and B.P.Z. conceived and designed the study. Y.Wu, Y.Wang, Y.Lin, Y.Wang and C.D. performed most of the study. Y.Liu and J.J. performed the study on *Drosophila* analyses. D.N. and Q.S. help on the IHC and tumour sample analyses. P.S. and Y.-I.C. performed Dub3 protein purification and binding analyses. C.W. performed bio-informatic and statistical analyses. J.D., W.L. and M.T. and B.M.E. discussed the results, conceived some experiments, and provided critical reagents and comments. Y.Wu and B.P.Z. wrote the manuscript.

Additional information

Supplementary Information accompanies this paper at http://www.nature.com/naturecommunications

Competing financial interests: The authors declare no competing financial interests.

Reprints and permission information is available online at http://npg.nature.com/reprintsandpermissions/

How to cite this article: Wu, Y. *et al.* Dub3 inhibition suppresses breast cancer invasion and metastasis by promoting Snail1 degradation. *Nat. Commun.* **8**, 14228 doi: 10.1038/ncomms14228 (2017).

Publisher's note: Springer Nature remains neutral with regard to jurisdictional claims in published maps and institutional affiliations.

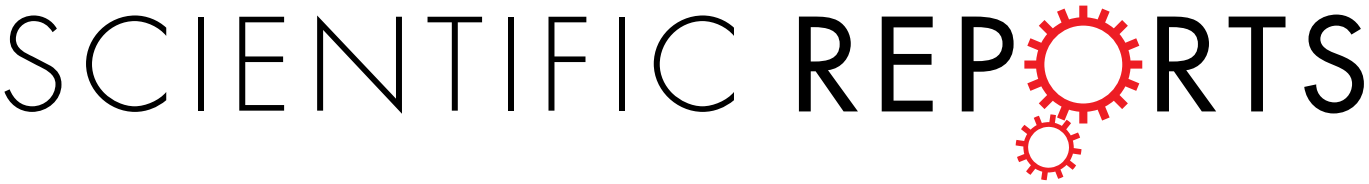

OPEN

Twist-mediated Epithelial-mesenchymal Transition Promotes Breast Tumor Cell Invasion via Inhibition of Hippo Pathway

Received: 14 January 2016
Accepted: 01 April 2016
Published: 20 April 2016

Yifan Wang[1,4,*], Jingyi Liu[2,3,4,*], Xuhua Ying[1], Pengnian Charles Lin[3] & Binhua P. Zhou[4]

Twist is a key transcription factor for Epithelial-mesenchymal transition (EMT), which is a cellular de-differentiation program that promotes invasion and metastasis, confers tumor cells with cancer stem cell (CSC)-like characteristics, and increases therapeutic resistance. However, the mechanisms that facilitate the functions of Twist remain unclear. Here we report that Twist overexpression increased expression of PAR1, an upstream regulator of the Hippo pathway; PAR1 promotes invasion, migration, and CSC-like properties in breast cancer by activating the transcriptional co-activator TAZ. Our study indicates that Hippo pathway inhibition is required for the increased migratory and invasiveness ability of breast cancer cells in Twist-mediated EMT.

Breast cancer is the most common cancer in women worldwide, and approximately 90% of breast cancer deaths are the result of metastasis. Metastasis is the process by which tumor cells detach from a primary tumor and migrate to nearby blood vessels or the lymph system, and are thereby able to spread to other organs in the host[1]. During metastasis, tumor cells acquire a highly motile phenotype through a de-differentiation program known as epithelial to mesenchymal transition (EMT). EMT, a phenomenon traditionally associated with embryonic development, is now accepted as a central mechanism that induces invasion and metastasis of tumors[2,3]. As part of the EMT process, epithelial cells lose their apical-basal polarity and intercellular adhesive property; in proxy, the cells gain mesenchymal properties, including fibroblast-like morphology and increased motility, all of which favor invasion and dissemination. EMT also bestows tumor cells with cancer stem cell (CSC)-like characteristics, and an associated therapeutic resistance.

Breast cancer is a heterogeneous disease in terms of tumor histology, clinical presentation, and response to therapy. There are four major subtypes based on gene expression profiling: luminal A, luminal B, ErbB2, and basal like. Breast cancer undergoes EMT and show a basal-like phenotype, suggesting that EMT occurs within a specific genetic context in breast cancers[4]. A better understanding of the mechanisms that support the EMT program in breast cancer is crucial in order to develop new therapeutic strategies. A hallmark of EMT is the loss of E-cadherin expression[3]. Several transcription factors have been implicated in the transcriptional repression of E-cadherin and function as molecular switches for the EMT program[3,5,6]. Twist and Snail are two transcriptional factors that are crucial to EMT activation, and cooperate to support development of full invasive and metastatic capacity. For example, during the mesoderm formation in *Drosophila*, twist and snail function as positive and negative regulators, respectively; Twist acts as a transcriptional activator to induce mesodermal gene expression, whereas Snail serves as a transcriptional suppressor to prevent expression of genes that belong to ectoderm[7]. Similar cooperative activities suggest that Twist and Snail work synergistically to induce EMT[8].

Protease-activated receptors (PARs) are members of a subfamily of G protein-coupled receptors that play critical roles in development, inflammation and angiogenesis, and cancer. PARs contribute to tumor cell motility and metastasis[9]. PAR1, also known as the coagulation factor II (thrombin) receptor, is a protein encoded by the

[1]Cancer Institute of Integrative Medicine, Zhejiang Academy of Chinese Medicine, Hangzhou, Zhejiang, 310007, China. [2]The State Key Laboratory of Experimental Hematology, Institute of Hematology and Blood Diseases Hospital, Chinese Academy of Medical Sciences and Peking Union Medical College, Tianjin 300020, China. [3]Center for Cancer Research, National Cancer Institute-Frederick, Frederick, MD 21702, USA. [4]Department of Molecular and Cellular Biochemistry, and Markey Cancer Center, the University of Kentucky, College of Medicine, Lexington, KY 40506, United States. *These authors contributed equally to this work. Correspondence and requests for materials should be addressed to B.P.Z. (email: peter.zhou@uky.edu)

F2R gene in humans. PAR1 is thought to be involved in the invasive and metastatic processes of several types of cancer, including breast, colon, lung, pancreas and prostate cancers[10–13]. Recent research shows that the PARs are upstream signals of Hippo pathway[14]. The Hippo signaling pathway, initially discovered by genetic studies in *Drosophila* as a regulator of organ size, plays a crucial role in tissue growth, and in tumorigenesis[15]. PAR1 acts through the $G_{12/13}$ and Rho GTPase to inhibit the Hippo pathway kinases Lats1/2; this kinase activates downstream signaling of YAP/TAZ by decreasing its phosphorylation and increasing nuclear localization[14]. Therefore, Hippo inhibition and the associated YAP/TAZ activation function as a key downstream signaling branch of PAR1 activation. However, the proteases responsible for activating the pro-invasive functions of PAR1 are, to date, not identified.

In this study, we found that the expression of Twist induced EMT in mammary epithelial cells and luminal breast cancer cells, and that PAR1 and TAZ were activated in these Twist-overexpressing transfectants. Knockdown of TAZ expression significantly decreased the expression of connective tissue growth factor (CTGF) and suppressed the invasive properties mediated by Twist. Together, our results indicate that the activation of PAR1 and the inhibition of Hippo pathway are required for the Twist-induced EMT. Therefore, our study not only reveals a critical mechanism underlying metastasis but also has implications for the development of therapeutic strategies for breast cancer.

Results

Overexpression of Snail or Twist induces EMT. To determine the role of Snail and Twist in EMT, we expressed Snail or Twist in immortalized human mammary epithelial cells (HMLE). Expression of Snail or Twist induced morphologic changes in HMLE cells, from a cobble-stone-like epithelial appearance to a spindle-shaped fibroblastic-like phenotype; these cells became elongated in shape and disassociated from their neighboring cells (Fig. 1A). Immunofluorescence staining showed downregulation of the epithelial marker E-cadherin, and upregulation of the mesenchymal marker Vimentin. Western blot analysis confirmed these results (Fig. 1B). We also expressed Snail or Twist in two luminal breast cancer cell lines, T47D and MCF7, that contain little endogenous Snail and Twist. Expression of Snail or Twist induced EMT in these cells, and converted the morphology of luminal cells to a basal-like phenotype (Fig. 2A). In addition, we found downregulation of the luminal epithelial markers E-cadherin and ERα, and the upregulation of the mesenchymal marker N-cadherin by immunofluorescence and western blot analysis (Fig. 2A,B). Long term (over 10 days) expression of Snail in T47D and MCF7 cells led to apoptosis in both cell lines (Table 1), and expression of Twist in MCF7 cells also led to apoptosis in this cell line. Interestingly, overexpression of Twist in T47D cells did not result in apoptosis, but led to the formation of a stable cell line with morphologic changes typical of EMT (Table 1). The mRNA levels of E-cadherin and ERα were dramatically decreased in this transformed cell line (Fig. 2C).

Twist expands the stem cell population. To investigate whether Twist-expression affects proliferation of breast cancer cells, we measured cell growth of T47D-Twist cells by cell counting. T47D-Twist cells did not demonstrate a significant growth difference compared with the vector control cells over the 96-hour interval examined (Fig. 3A). We also examined tumorsphere formation of these cells, which is based on the unique property of stem/progenitor cells to survive and grow in serum-free suspension. Although both T47D-vector and T47D-Twist cell types did form tumorspheres, the size and density of tumorspheres formed by T47D-Twist cells were lightly smaller than those formed by vector control cells under normoxic conditions. Under hypoxic conditions, tumorspheres were sparse in vector control cells. Surprisingly, the size and density of tumorsphere formed by T47D-Twist cells were much bigger than that of control cells (Fig. 3B). These results suggest that expression of Twist promotes induction of CSC-like properties and their growth in T47D cells under hypoxic conditions.

Twist promotes cell migration and invasion. To investigate the migratory and invasive capabilities mediated by Twist, we performed an *in vitro* wound healing assay, which is commonly used to assess the effects of exogenous gene expression on the migration of individual cells. Closure of the scratch wound required significantly less time in T47D-Twist cells than in vector control cells (Fig. 4A). Statistical analysis indicated that migration activity of T47D-Twist cells was about 3-fold higher than that of vector control cells (Fig. 4A). We also used Matrigel-coated Boyden chambers to assess cell invasiveness; the invasion capacity of T47D-Twist cells increased 14-fold compared with that of vector control cells (Fig. 4B).

Twist induces PAR1 activation and Hippo inhibition. To understand the molecular mechanisms associated with Twist-induced EMT, we performed cDNA microarray analysis of HMLE and T47D cells that had undergone Twist-mediated EMT (Figs 1A and 2A). The mRNA of two PARs family genes, PAR1 (*F2R*) and PAR3 (*F2RL2*), were significantly elevated in both cell lines. These results were confirmed by qRT-PCR (Fig. 5A). Recently, these PAR proteins were identified as upstream regulators of the Hippo pathway, and play a crucial role in breast cancer invasion and metastasis. These data suggest that Twist regulates the Hippo pathway by upregulating PAR expression.

Next, we investigated whether Twist expression suppresses the Hippo pathway by examing the expression of TAZ in T47D-Twist cells and the corresponding control vector cells. Since PAR1 inhibits the Lats1/2 kinases, we would expect that a Twist-mediated increase in PAR1 expression would decrease TAZ phosphorylation and increase TAZ activity. We found that TAZ was activated in T47D-Twist cells, and that the level of phosphorylated TAZ was significantly reduced (Fig. 5B). Consistent with this, the expression level of CTGF, a downstream transcriptional target of TAZ, was increased (Fig. 5B). These results support the idea that Twist suppresses the Hippo pathway by upregulating the PAR1 signaling.

If TAZ activation is crucial for the Twist-mediated EMT, depletion of TAZ should reverse the changes induced by Twist. To test this possibility, we employed a luciferase reporter assay to determine if TAZ is required for the

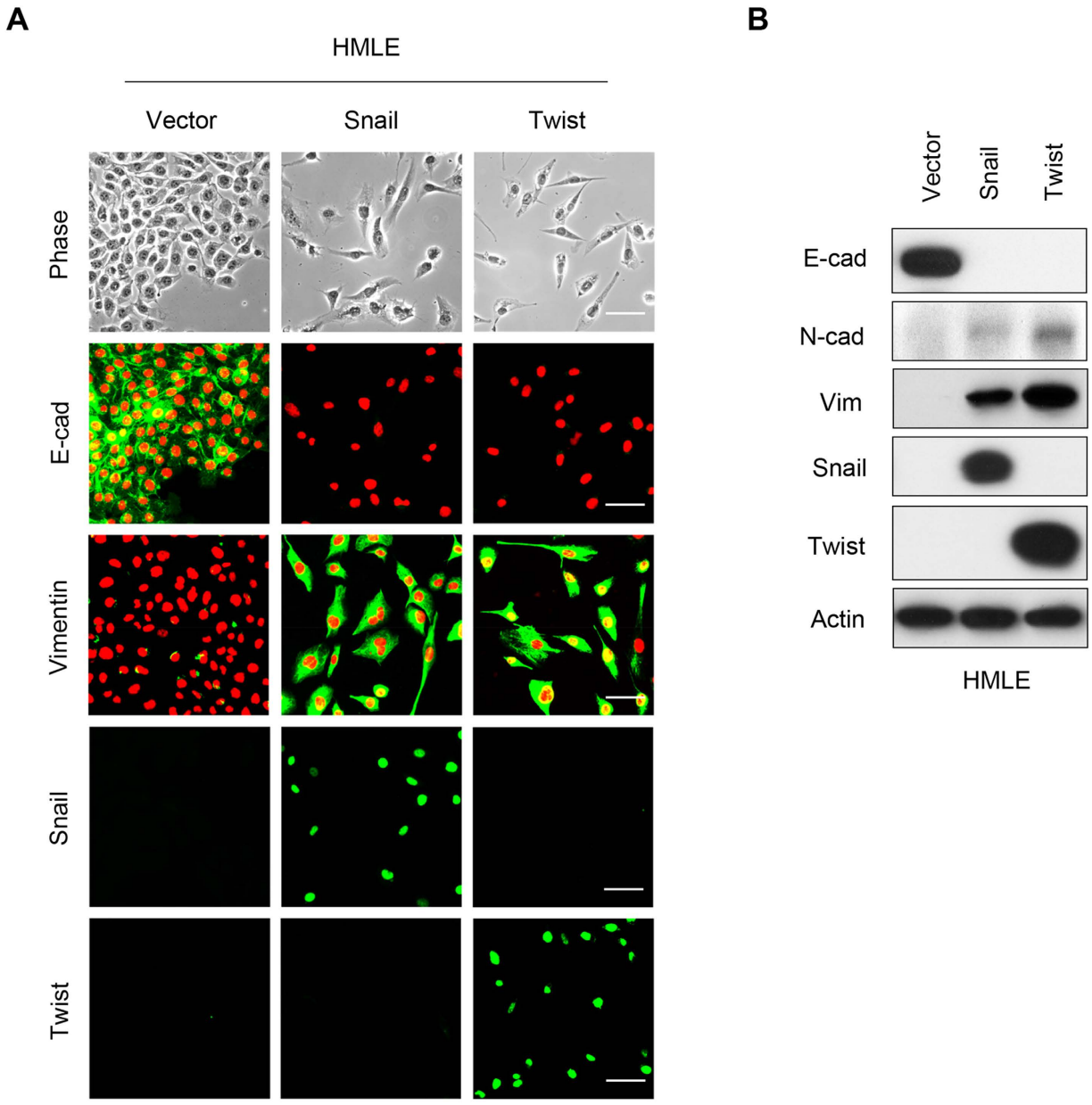

Figure 1. Overexpression of Snail or Twist induces EMT in HMLE cells. (**A**) Representative images show expression of E-cadherin and Vimentin in Snail- or Twist-expressing HMLE cells analyzed by immunofluorescent staining. Nuclei were visualized with DAPI staining (red). The morphologic changes associated with EMT are shown in the representative phase contrast images. Scale bars, 50 μm. (**B**) Expression of E-cadherin, N-cadherin and Vimentin in these cells was assessed by western blot analysis; actin served as a loading control.

Twist-mediated activation of CTGF promoter. We found that expression of Twist increased the promoter activity of CTGF, however, this effect was blocked by knocking down the expression of TAZ (Fig. 5C). Taken together, these results indicate that Twist expression activates TAZ, which leads to an increase in CTGF promoter transactivation as measured by luciferase activity. To further confirm the effect of TAZ, we knocked down the expression of TAZ by siTAZ in T47D-Twist cells and control vector cells (Fig. 5D), and performed wound healing and invasion analyses. We found that the migration induced by Twist in T47D cells was reduced from 3-fold to 1.3-fold (Fig. 6A), and that the invasion capability was reduced from 14-fold to 5-fold (Fig. 6B); these data indicate that Hippo pathway inhibition is required for the increased migratory and invasiveness in Twist-mediated EMT.

Discussion

Accumulating evidence indicates that EMT-associated transcription factors endow cells with malignant traits, such as invasion, migration and therapeutic resistance. In this study, we showed that the exogenous expression of Twist induced EMT not only in normal mammary epithelial cells HMLE, but also in the luminal breast cancer

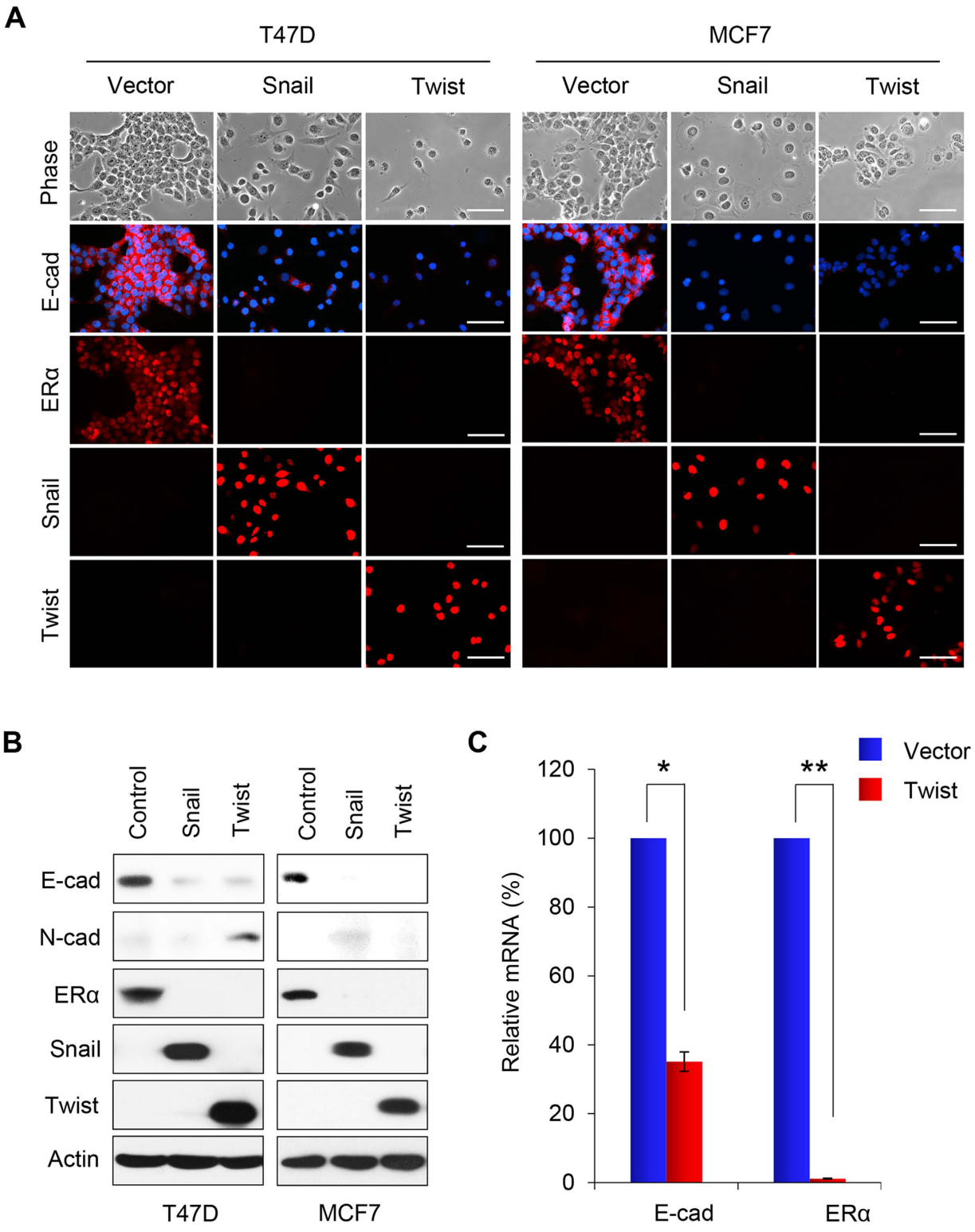

Figure 2. Overexpression of Snail or Twist induces EMT in T47D and MCF7 cells. (**A**) Representative images show expression of E-cadherin and ERα in Snail- or Twist-expressing T47D and MCF7 cells analyzed by immunofluorescent staining. Nuclei were visualized with DAPI staining (blue). The morphologic changes associated with EMT are shown in representative phase contrast images. Scale bars, 50 μm. (**B**) Expression of E-cadherin, N-cadherin and ERα in these cells was assessed by western blot analysis; actin served as a loading control. **(C)** Quantification of the relative mRNA levels of E-cadherin and ERα in Twist expressing T47D cells compared with vector-control cells using real-time PCR. Presented data are the mean ± SD from three separate experiments, with *and **indicate $p < 0.01$ in comparison with that of control.

Cell lines		EMT	Apoptosis	Survival
T47D	control	No	No	Yes
	Snail	Yes	Yes	No
	Twist	Yes	No	Yes
MCF7	control	No	No	Yes
	Snail	Yes	Yes	No
	Twist	No	Yes	No

Table 1. EMT, apoptosis and survival status in T47D and MCF7 cells with Snail/Twist overexpression.

cells T47D. We established a T47D cell line stably expressing Twist, and this cell line displayed a mesenchymal cell phenotype.

Our study demonstrates that Twist-induced EMT in T47D cells is accompanied by functional effects, including increased cell invasion, migration and CSC-like properties under hypoxic conditions. We also established that Twist activates PAR1 and PAR3 gene expressions. The PARs are a unique class of G-protein-coupled receptors that act as high-gain sensors of extracellular protease gradients, allowing cells to react to a proteolytic microenvironment[10]. PARs have been implicated in tumor progression. PAR1 is not expressed in normal breast epithelia but is upregulated in invasive breast carcinomas[16]. The invasive MDA-MB-231 breast cancer cell line express high levels of PAR1[17]. In our study, activation of PAR1 in noninvasive T47D cells accompanied the acquisition of a mesenchymal phenotype and suppression of the Hippo pathway (Fig. 6C).

Major components of the Hippo pathway, including the MST1/2 and Lats1/2 kinases, are highly conserved and play an important role in control of mammalian organ size, cell proliferation, apoptosis, and stem cell differentiation[18]. PARs regulate the Hippo pathway. Activation of PAR1 and other G protein coupled receptors that link to $G_{12/13}$, trigger the activation of Rho GTPase, which works through the actin cytoskeleton to inhibit the Lats1/2 kinase and subsequently activates YAP/TAZ by decreasing its phosphorylation and increasing nuclear localization[14]. PAR3 was speculated to modulate PAR1 signaling by receptor dimerization. PAR3 had been reported functions as an important allosteric modulator of PAR1 signaling. PAR1 heterodimerization with PAR3 alters the PAR1/$G\alpha_{13}$ binding conformation, enhancing $G\alpha_{13}$ signaling[19]. TAZ, a transducer of Hippo pathway, was reported to confer CSC-related traits on breast cancer cells, and was required to sustain self-renewal and tumor-initiation capacities in breast cancer stem cells[20]. We hypothesize that PAR1 overexpression induced by Twist could contribute to breast cancer cell progression by inhibiting Hippo pathway. In our study, we found that the expression level of TAZ was upregulated by Twist expression, while the phosphorylation level of TAZ was downregulated. Dephosphorylated TAZ functions as transcription coactivators for the TEAD family of transcription factors to induce gene expression, thereby promoting cell growth, proliferation, and survival[21–23]. We found that the expression level of CTGF, a known TAZ target gene[15,24], was increased in Twist-expressing T47D cells. The luciferase activity of the CTGF promoter was also enhanced. To further address the role of TAZ in the Twist regulated Hippo pathway, we knocked down the expression of TAZ, and found that clear reversion of luciferase activity was observed by TAZ depletion in Twist-expressing T47D cells. Moreover, TAZ ablation suppressed migration and invasion capability as determined by the wound healing and invasion assays. These results imply that Twist activates TAZ in the Hippo pathway and that TAZ depletion inhibits Twist-induced cell migration and invasion.

In summary, we delineated the cross-talk between Twist-mediated EMT and the Hippo pathway in metastatic breast cancer. We showed that PAR1 was activated by Twist. The induction of PAR1 expression was critical for the Twist-mediated promotion of EMT and cell invasion and migration. Activated PAR1 signaling induced the expression of TAZ by suppressing Hippo pathway, and bestowed breast cancer cells with stem cell properties (Fig. 6C). Together, our experiments revealed a role for PAR1 in promoting EMT and invasive potential of breast cancer cells, suggesting that PAR1 might be a potential therapeutic target for EMT and metastasis of breast cancer.

Methods

Plasmids, siRNA, and Antibodies. Smart pool siRNA against TAZ was obtained from Dharmacon (Chicago, IL). Human Twist and Snail were amplified from a HeLa cDNA library and subcloned into pLenti6.3/V5. Antibodies for Vimentin and ERα were from Neomarkers (Fremont, CA). Antibodies for E-cadherin and TAZ were from BD Transduction Laboratories (San Jose, CA). Antibodies for Twist, YAP, p-YAP and CTGF were purchased from Santa Cruz Biotechnology (Santa Cruz, CA). Snail and N-cadherin antibodies was purchased from Cell Signaling Technology (Danvers, MA) and Upstate (Charlottesville, VA), respectively.

Cell Culture. The MCF7 breast cancer cell line was grown in Dulbecco's modified Eagle's medium (DMEM)/F12 supplemented with 10% fetal bovine serum (FBS). T47D cells were grown in RPMI1640 plus 10% FBS. HMLE was grown in DMEM/F-12 medium plus 10 ng/mL EGF, 10 μg/mL insulin and 0.5 μg/mL hydrocortisone. For establishing stable clones, transfected breast cell lines were selected with puromycin (1 μg/mL) for 4 wks.

Immunostaining and Immunoblotting. Experiments were performed as described previously[25,26]. For immunofluorescent staining, cells grown on chamber slides, were fixed with 4% paraformaldehyde, and incubated overnight with primary antibodies. Secondary antibodies were Alexa Fluor 488 goat anti-mouse IgG (H + L), Alexa Fluor 568 goat anti-mouse IgG (H + L), or Alexa Fluor 568 goat anti-rat IgG (H + L) (Molecular Probe, Carlsbad, CA).

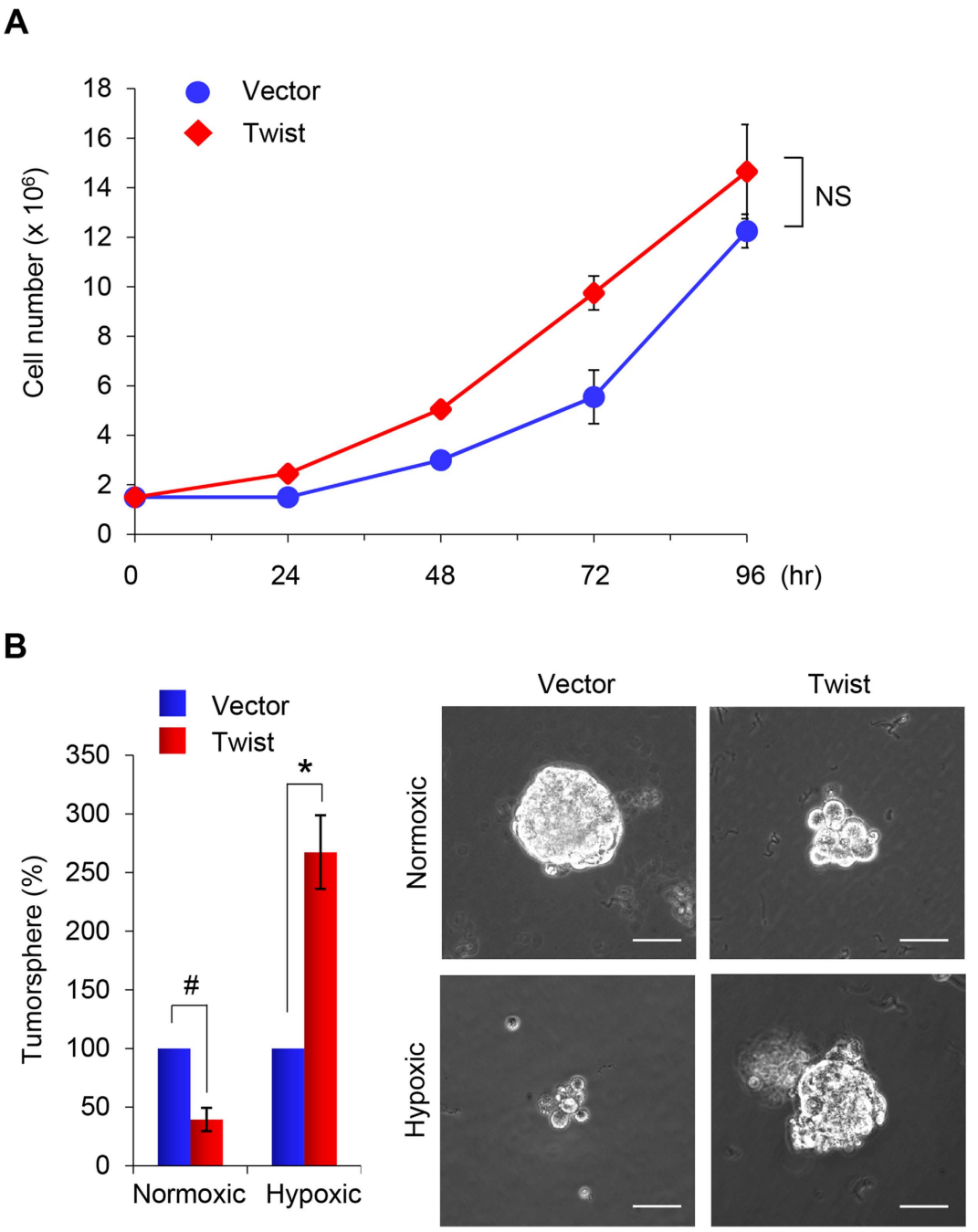

Figure 3. Overexpression of Twist induces CSC-like properties in T47D cells. (**A**) Graphic representation of cell growth rates by T47D cells stably expressing Twist or control vector. Cell counts were obtained daily over a 4 day period. Presented data are the mean ± SD from two independent experiments with triplicate samples. NS stands for statistically non-significant. (**B**) Tumorsphere formation was assessed in T47D cells overexpressing Twist under normoxic or hypoxic conditions. Representative images of tumorspheres are shown in the right panel. Scale bars, 100 μm. Left panel, are graphic representations of tumorsphere number. Presented data are the percentage of control vector values, with mean ± SD of three separate experiments performed in duplicate. $^{\#}p < 0.05$ and $^{*}p < 0.01$ when vector control cells compared with their Twist-expressing clones, respectively.

Quantitative Real-Time PCR. Total RNA was prepared using the RNeasy Mini kit (Qiagen) according to the manufacturer's instructions. Specific quantitative real-time PCR experiments were performed using SYBR Green Power Master Mix following manufacturer's protocol (Applied Biosystems).

Luciferase Reporter Assay. Luciferase reporter assays were performed as described previously[25,27]. Cells grown to 50% confluence in six-well plates were co-transfected with reporter gene constructs using Fugene 6 (Roche, Indianapolis, IN). To normalize transfection efficiency, cells were also co-transfected with pTK-RL

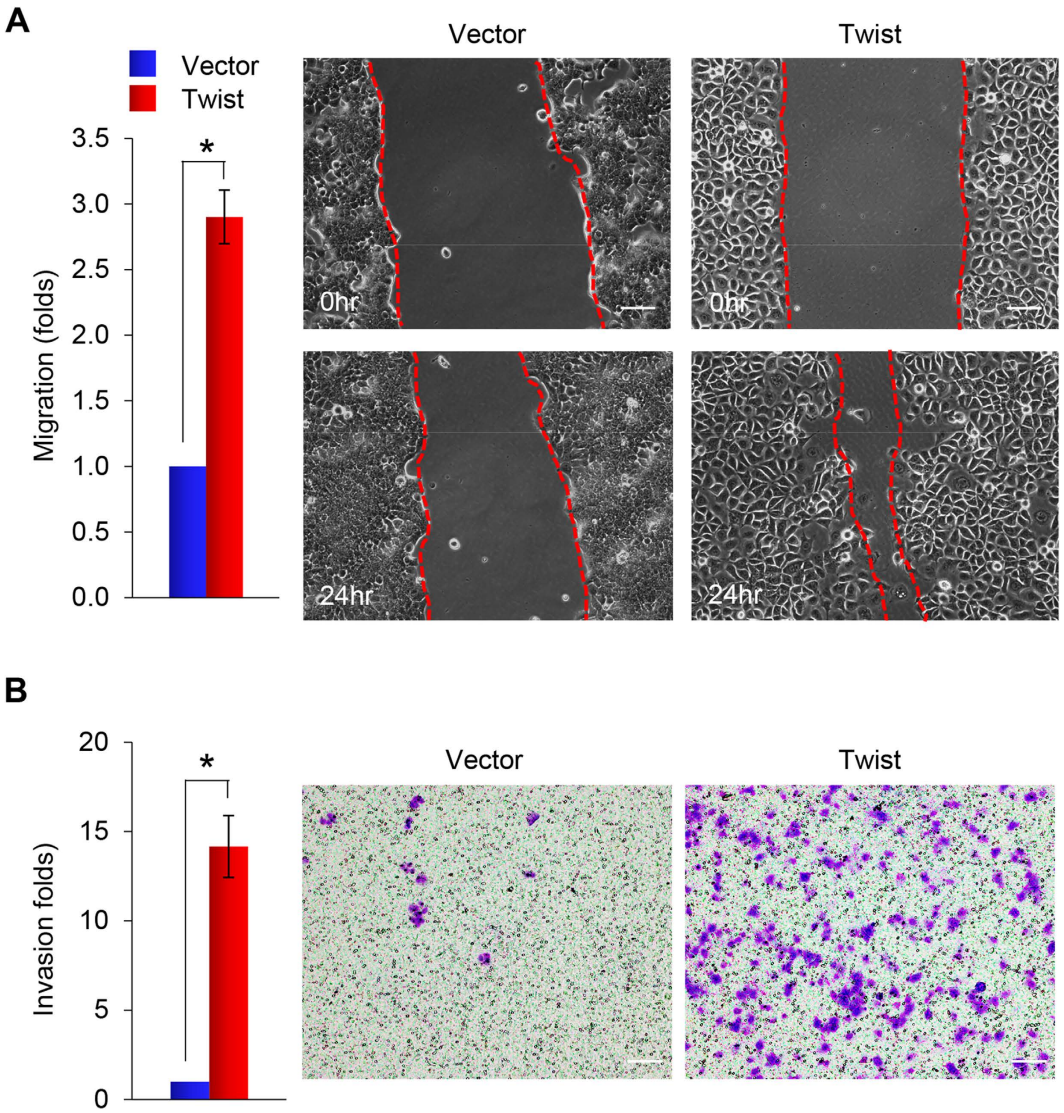

Figure 4. Overexpression of Twist enhances cell migration and invasion of T47D cells. (**A**) Graphic representation of the migratory capability of stably transfected T47D cells expressing either Twist or control vector assessed using a wound healing assay. A scratch ("wound") was inflicted to a cell layer produced 48 hours post-plating, and culture continued for an additional 24 hrs. Wound closures were photographed at 0 and 24 hr. Presented data are the mean ± SD from three independent experiments, with *indicates $p < 0.01$ when comparing with control values. A representative experiment is shown in the right panel. Scale bars, 50 μm. (**B**) Graphic representation of the invasiveness of T47D cells stably expressing Twist or control vector using a modified Boyden Chamber invasion assay as described in the Materials and Methods. Presented data are the mean ± SD from three separate experiments, with *indicates $p < 0.01$ when comparing with control values. A representative experiment is shown in the right panel. Scale bars, 100 μm.

(Renilla luciferase). Cell extracts, prepared 48 hrs after transfection, were assessed for luciferase activity using the Dual-Luciferase Reporter Assay System (Promega, Madison, WI). All experiments were performed three times in triplicate.

Invasion Assay. Invasion assays were performed in Boyden chambers coated with Matrigel as instructed by the manufacturer (BD Biosciences, San Jose, CA). Cancer cells were seeded on top of the Matrigel in the upper chamber, and the bottom chamber was filled with culture medium containing EGF (10 ng/mL) as the chemoattractant. The invasive cancer cells, on the underside of the Boyden chamber membrane, were fixed with paraformaldehyde, stained with crystal violet and counted. All experiments were performed in triplicate.

Tumorsphere Assay. Tumorsphere assays were performed following the protocol previously described[28,29]. Briefly, cells were seeded in single-cell suspension in triplicate into ultra-low attachment 6-well plates (Corning) in DMEM/F12 medium supplemented with 20 ng/mL EGF, 5 mg/mL insulin, 0.5 mg/mL hydrocortisone and 2% B27. After 1 to 2 wks incubation, the presence of spheres (3D multicellular structures greater than 40 μm in

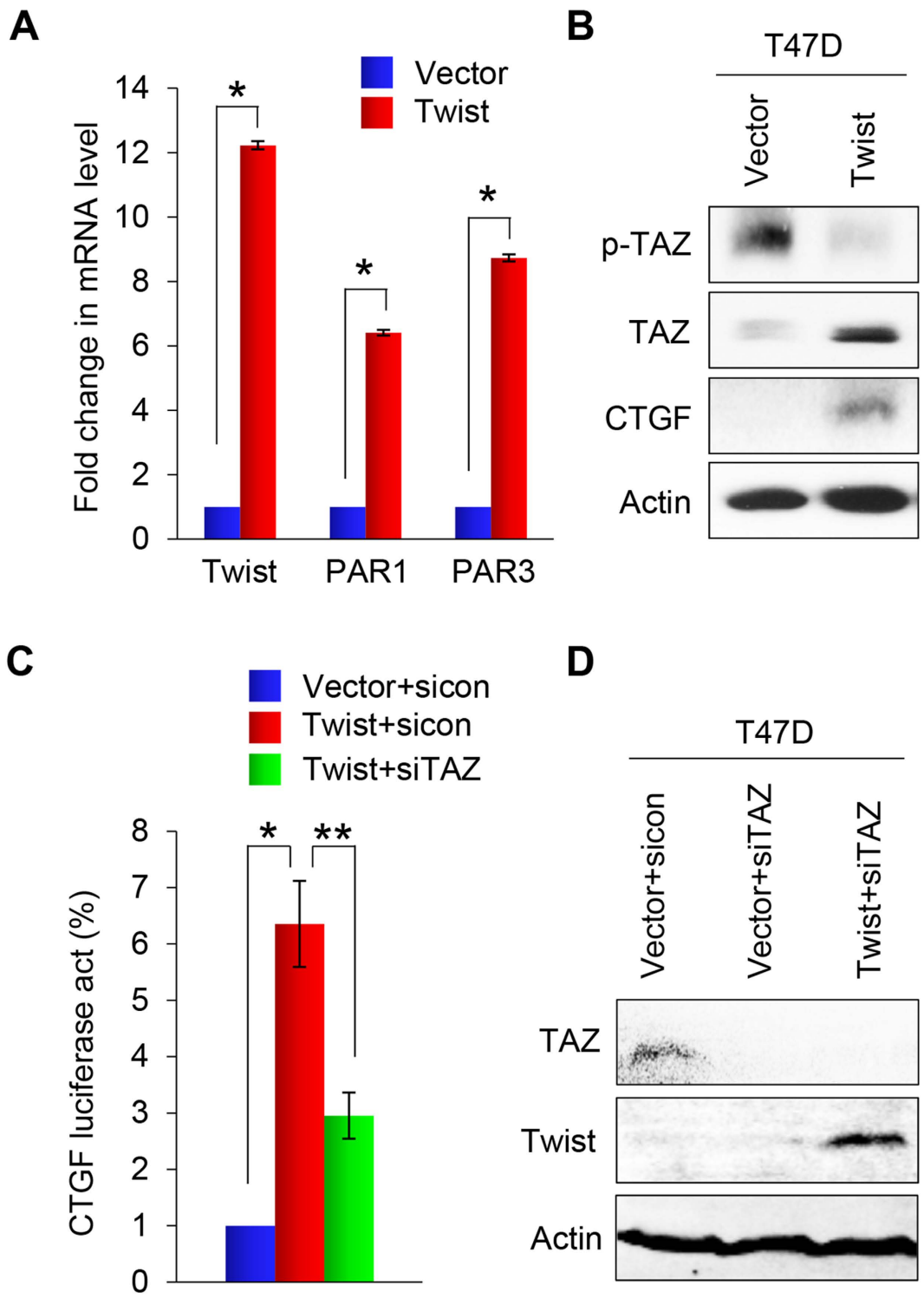

Figure 5. Overexpression of Twist induces the activation of PAR1 signaling. (**A**) Graphic representation of the fold change in mRNA levels of Twist, F2R and F2RL2 in Twist-expressing T47D cells compared with control vector cells by real-time PCR. Presented data are the mean ± SD of three separate experiments, with *indicates $p < 0.01$ when comparing with control values. (**B**) Western blot analysis for p-TAZ, TAZ and CTGF expression in EMT-induced Twist-expressing T47D cells or T47D cells expressing control vector. Actin served as a loading control. (**C**) Effect of TAZ siRNA or NTC siRNA on CTGF promoter luciferase activity in Twist-overexpressing T47D cells and T47D cells expressing control vector. Assessments were made after 48 hours in culture. Presented data are mean ± SD of normalized luciferase activities determined from three separate experiments. *indicates $p < 0.01$ when control siRNA expressed in Twist-T47D cells compared with in vector control cells; and **indicates $p < 0.01$ when compared expression of TAZ siRNA and control siRNA in Twist-T47D cells. (**D**) Effect of TAZ siRNA on TAZ and Twist expression in EMT-induced Twist-expressing T47D cells and in T47D cells expressing control vector by western blot analysis. Actin served as a loading control.

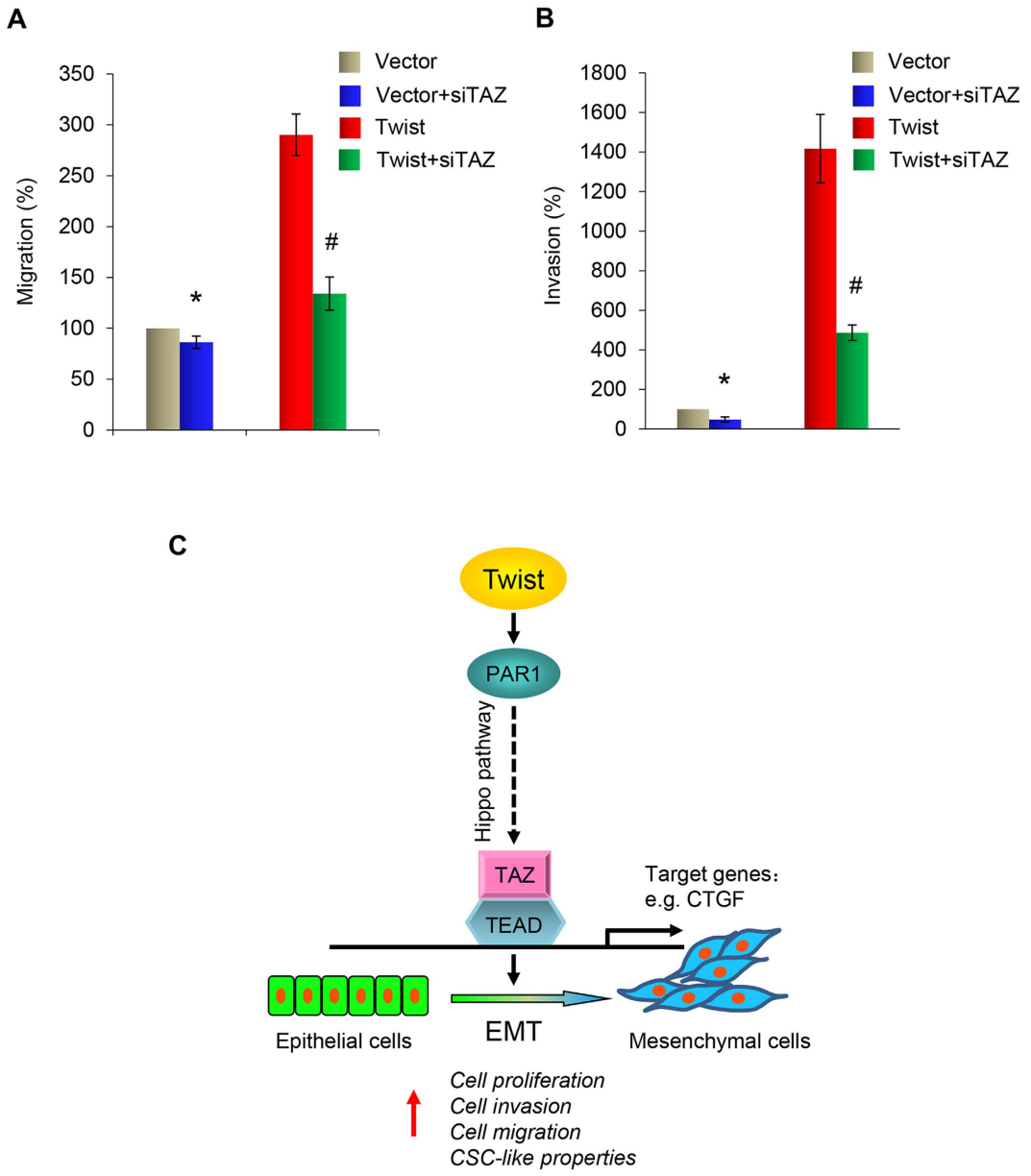

Figure 6. Knockdown of TAZ suppresses Twist-induced cell migration and invasion of T47D cells. (**A**) Effect of TAZ siRNA on cell migrating activity in Twist-overexpressing T47D cells and T47D cells expressing control vector using a wound healing assay. A scratch ("wound") was inflicted to a cell layer produced 48 hours post-plating, and culture continued for an additional 24 hrs. Wound closures were photographed at 0 and 24 hr. Presented data are the mean ± SD from three independent experiments, with *and #indicating significant difference of $p < 0.05$ from control values. **(B)** Effect of TAZ siRNA on cell invasiveness in Twist-overexpressing T47D cells and T47D cells expressing control vector using a modified Boyden Chamber invasion assay as described in the Materials and Methods. Presented data are a graphic representation of the mean ± SD of percentage of invasive cells obtained from three separate experiments, with *and #indicating significant difference of $p < 0.05$ from control values. **(C)** Expression of Twist results in increased expression of PAR1, which promotes invasion, migration, and induces CSC-like properties in breast cancer cells by upregulating the expression of TAZ.

diameter) was assessed by inverted microscopy. Ten random fields for each cell lines were visualized; the number and size of spheres in the 10 fields were calculated as a percentage over that of parent cells.

Statistical Analysis. Experiments were repeated at least twice. Data are presented as mean ± SD. A Student's t-test (two tailed) was used to compare two groups. $p < 0.05$ was considered statistically significant.

References

1. Pantel, K. & Brakenhoff, R. H. Dissecting the metastatic cascade. *Nat Rev Cancer.* **4,** 448–456 (2004).
2. Polyak, K. & Weinberg, R. A. Transitions between epithelial and mesenchymal states: acquisition of malignant and stem cell traits. *Nat Rev Cancer.* **9,** 265–273 (2009).
3. Thiery, J. P., Acloque, H., Huang, R. Y. & Nieto, M. A. Epithelial-mesenchymal transitions in development and disease. *Cell.* **139,** 871–890 (2009).
4. Sarrio, D. *et al.* Epithelial-mesenchymal transition in breast cancer relates to the basal-like phenotype. *Cancer Res.* **68,** 989–997 (2008).
5. Kalluri, R. & Weinberg, R. A. The basics of epithelial-mesenchymal transition. *J Clin Invest.* **119,** 1420–1428 (2009).
6. Yang, J. *et al.* Twist, a master regulator of morphogenesis, plays an essential role in tumor metastasis. *Cell.* **117,** 927–939 (2004).
7. Leptin, M. twist and snail as positive and negative regulators during Drosophila mesoderm development. *Genes Dev.* **5,** 1568–1576 (1991).
8. Zeitlinger, J. *et al.* Whole-genome ChIP-chip analysis of Dorsal, Twist, and Snail suggests integration of diverse patterning processes in the Drosophila embryo. *Genes Dev.* **21,** 385–390 (2007).
9. Shi, X., Gangadharan, B., Brass, L. F., Ruf, W. & Mueller, B. M. Protease-activated receptors (PAR1 and PAR2) contribute to tumor cell motility and metastasis. *Mol Cancer Res.* **2,** 395–402 (2004).
10. Boire, A. *et al.* PAR1 is a matrix metalloprotease-1 receptor that promotes invasion and tumorigenesis of breast cancer cells. *Cell.* **120,** 303–313 (2005).
11. Nierodzik, M. L., Kajumo, F. & Karpatkin, S. Effect of thrombin treatment of tumor cells on adhesion of tumor cells to platelets *in vitro* and tumor metastasis *in vivo*. *Cancer Res.* **52,** 3267–3272 (1992).
12. Heider, I. *et al.* PAR1-type thrombin receptor stimulates migration and matrix adhesion of human colon carcinoma cells by a PKCepsilon-dependent mechanism. *Oncol Res.* **14,** 475–482 (2004).
13. Even-Ram, S. *et al.* Thrombin receptor overexpression in malignant and physiological invasion processes. *Nat Med.* **4,** 909–914 (1998).
14. Mo, J. S., Yu, F. X., Gong, R., Brown, J. H. & Guan, K. L. Regulation of the Hippo-YAP pathway by protease-activated receptors (PARs). *Genes Dev.* **26,** 2138–2143 (2012).
15. Pan, D. The hippo signaling pathway in development and cancer. *Dev Cell.* **19,** 491–505 (2010).
16. Yang, E. *et al.* Blockade of PAR1 signaling with cell-penetrating pepducins inhibits Akt survival pathways in breast cancer cells and suppresses tumor survival and metastasis. *Cancer Res.* **69,** 6223–6231 (2009).
17. Kamath, L., Meydani, A., Foss, F. & Kuliopulos, A. Signaling from protease-activated receptor-1 inhibits migration and invasion of breast cancer cells. *Cancer Res.* **61,** 5933–5940 (2001).
18. Zhao, B., Li, L., Lei, Q. & Guan, K. L. The Hippo-YAP pathway in organ size control and tumorigenesis: an updated version. *Genes Dev.* **24,** 862–874 (2010).
19. McLaughlin, J. N., Patterson, M. M. & Malik, A. B. Protease-activated receptor-3 (PAR3) regulates PAR1 signaling by receptor dimerization. *Proc Natl Acad Sci USA* **104,** 5662–5667 (2007).
20. Cordenonsi, M. *et al.* The Hippo transducer TAZ confers cancer stem cell-related traits on breast cancer cells. *Cell.* **147,** 759–772 (2011).
21. Lei, Q. Y. *et al.* TAZ promotes cell proliferation and epithelial-mesenchymal transition and is inhibited by the hippo pathway. *Mol Cell Biol.* **28,** 2426–2436 (2008).
22. Zhao, B. *et al.* TEAD mediates YAP-dependent gene induction and growth control. *Genes Dev.* **22,** 1962–1971 (2008).
23. Zhao, B., Li, L., Tumaneng, K., Wang, C. Y. & Guan, K. L. A coordinated phosphorylation by Lats and CK1 regulates YAP stability through SCF(beta-TRCP). *Genes Dev.* **24,** 72–85 (2010).
24. Lai, D., Ho, K. C., Hao, Y. & Yang, X. Taxol resistance in breast cancer cells is mediated by the hippo pathway component TAZ and its downstream transcriptional targets Cyr61 and CTGF. *Cancer Res.* **71,** 2728–2738 (2011).
25. Wu, Y. *et al.* Stabilization of snail by NF-kappaB is required for inflammation-induced cell migration and invasion. *Cancer Cell.* **15,** 416–428 (2009).
26. Zhou, B. P. *et al.* Dual regulation of Snail by GSK-3beta-mediated phosphorylation in control of epithelial-mesenchymal transition. *Nat Cell Biol.* **6,** 931–940 (2004).
27. Dong, C. *et al.* G9a interacts with Snail and is critical for Snail-mediated E-cadherin repression in human breast cancer. *J Clin Invest.* **122,** 1469–1486 (2012).
28. Grimshaw, M. J. *et al.* Mammosphere culture of metastatic breast cancer cells enriches for tumorigenic breast cancer cells. *Breast Cancer Res.* **10,** R52 (2008).
29. Smart, C. E. *et al. In vitro* analysis of breast cancer cell line tumourspheres and primary human breast epithelia mammospheres demonstrates inter- and intrasphere heterogeneity. *PLoS One.* **8,** e64388 (2013).

Acknowledgements

We thank Cathy Anthony for critical reading and editing of this manuscript. We also thank Dr. Kunliang Guan for providing CTGF-Luc plasmid for this study. This work was supported in part by grants from NIH (RO1s CA125454 and CA188118), DOD Breakthrough Award (BC140733P1), Mary Kay Ash Foundation (to B.P. Zhou), National Natural Science Foundation of China (No. 81402434 to Y. Wang, and No. 81402432 to J. Liu), and the Zhejiang Provincial Natural Science Foundation of China (No. LQ14H280002) (to Y. Wang).

Author Contributions

Y.W. and J.L. performed experiments, analyzed data, and wrote the manuscript; X.Y. and P.C.L. analyzed data, and wrote the manuscript; B.P.Z. designed the experiments, analyzed the data, wrote the paper, and supervised the project.

Additional Information

Competing financial interests: The authors declare no competing financial interests.

How to cite this article: Wang, Y. *et al.* Twist-mediated Epithelial-mesenchymal Transition Promotes Breast Tumor Cell Invasion via Inhibition of Hippo Pathway. *Sci. Rep.* **6**, 24606; doi: 10.1038/srep24606 (2016).